



**Centro de Investigación Científica de Yucatán, A.C.**

**Posgrado en Materiales Poliméricos**

**“Multifunctional properties of carbon nanotube  
yarns and their use for damage sensing in fiber  
reinforced polymer composites”**

A doctoral dissertation presented by:

**César Antonio Pérez Aranda**

In partial fulfillment of the requirements for the degree of:

**Doctor of Science**

In the subject area of:

**Polymeric Materials**

Mérida, Yucatán, Mexico

February 2024

# DECLARACIÓN DE PROPIEDAD

Declaro que la información contenida en las secciones de: Materiales y Métodos, Resultados y Discusión de este documento, proviene de las actividades de investigación realizadas durante el período que se me asignó para desarrollar mi trabajo de tesis, en las Unidades y Laboratorios del Centro de Investigación Científica de Yucatán, A.C., y que, a razón de lo anterior, y en contraprestación de los servicios educativos o de apoyo que me fueron brindados, dicha información, en términos de la Ley Federal del Derecho de Autor y la Ley Federal de Protección a la Propiedad Industrial, le pertenece patrimonialmente a dicho Centro de Investigación. Por otra parte, en virtud de lo ya manifestado, reconozco que de igual manera los productos intelectuales o desarrollos tecnológicos que deriven o pudieran derivar de lo correspondiente a dicha información, le pertenecen patrimonialmente al Centro de Investigación Científica de Yucatán, A.C., y se registrarán, en todo caso, por lo dispuesto por la Ley Federal del Derecho de Autor y la Ley Federal de Protección a la Propiedad Industrial, en el tenor de lo expuesto en la presente Declaración.



---

César Antonio Pérez Aranda

*CENTRO DE INVESTIGACIÓN CIENTÍFICA DE YUCATÁN, A. C.*  
*POSGRADO EN MATERIALES POLIMÉRICOS*



**RECONOCIMIENTO**

Por medio de la presente, hago constar que el trabajo de tesis de **César Antonio Pérez Aranda**, titulado “**Multifunctional properties of carbon nanotube yarns and their use for damage sensing in fiber reinforced polymer composites**” fue realizado en la Unidad de Materiales, en la línea de investigación de Materiales compuestos y nanomateriales, en los laboratorios de materiales compuestos, fisicoquímica y mecánica del Centro de Investigación Científica de Yucatán, A.C., bajo la dirección del **Dr. Francis Avilés Cetina**, perteneciente al Programa de Posgrado en Materiales Poliméricos de este Centro.

Atentamente,



---

Dra. Cecilia Hernández Zepeda  
Directora de Docencia

Mérida, Yucatán, México, a 15 de febrero de 2024

This thesis is dedicated to my beloved companion and partner in life, Estefanía López Sauri. From the moment we became best friends to the day you became my cherished wife, you have been a constant source of love, support, and inspiration. Your presence in my life has brought immense joy, and your belief in my abilities has fueled my determination in this academic journey. I am forever grateful for your faith in me, and it is with immense gratitude that I dedicate this thesis to you. Your love, encouragement, and support have sustained me throughout this endeavor. Thank you for being my rock and my greatest source of happiness.

# Acknowledgments

I would like to extend my heartfelt gratitude to the following individuals and organizations who played an important role in the completion of this doctoral thesis:

- ❖ To the “Consejo Nacional de Humanidades, Ciencia y Tecnología” (CONAHCYT) for financial support through the Doctoral scholarship (CVU: 816344) and through the award CF-2023-I-926, granted to Dr. Francis Avilés Cetina.
- ❖ To the Office of Naval Research Global (ONRG) for financial support through award number N62909-19-1-2119.
- ❖ To the “Unidad de Materiales Poliméricos” of the “Centro de Investigación Científica de Yucatán” (CICY) for the use of facilities and equipment.
- ❖ To the Applied Mechanics group of the Department of Materials Science and Engineering at “Ångströmlaboratoriet” of the “Uppsala Universitet” (UU) for the use of facilities and equipment during six months, and for providing financial support for accommodation during my research stay.
- ❖ To Dr. Francis Avilés Cetina for his unwavering support, invaluable advice, and guidance. I am profoundly grateful.
- ❖ To Dr. Kristofer Gamstedt for his generous support, technical input, and insightful advice.
- ❖ To Dr. Fernando Hernández Sánchez for his invaluable comments and technical input.
- ❖ To Dr. Pedro Herrera Franco for his technical input during my pre-doctoral examination.
- ❖ To the members of my doctoral examination committee, Dr. Juan Cauich Rodríguez, and Dr. Fabien Léonard, for their invaluable comments and technical input.
- ❖ To the CICY technicians for their technical assistance and lab support, including Miguel Rivero Ayala for his help with atomic force microscopy and mechanical testing, Dr. Hugo Carrillo Escalante for his support and assistance with dynamic mechanical analysis, Rossana Vargas Coronado for her support with Raman spectroscopy, Santiago Duarte Aranda for his assistance with scanning electron microscopy, Dr. Alejandro May Pat for his assistance with atomic force microscopy, Silvia Andrade Canto for her assistance with scanning electron microscopy, Javier Cauich Cupul for his help with cyclic mechanical testing, and Luis Flores Mena for constructing the tensile stage for the Raman equipment and fabricating the support fixture for compression testing.

- ❖ To the faculty and staff of CICY, specifically Gabriel Pool Balam for his support in repairing the digital image correlation equipment, Miriam Juan-Qui Valencia for providing the requested scientific articles, and Nery Arceo García for her diligent help with the administrative procedures.
- ❖ To the faculty and staff of UU, including Dr. Rhodel Bengtsson for his lab support, Dr. León Zendejas Medina for his support in using the Tabletop scanning electron microscopy, Peter Bergkvist for his lab support and invaluable help, Dr. Reza Afshar for providing guidance in digital image processing with ImageJ, and Dr. Mahmoud Mousavi for his invaluable support.
- ❖ To my colleagues and friends, including Raúl Pech Pisté for his support with dynamic mechanical analysis and Raman spectroscopy, Dr. Abraham Balam Mena for designing the tensile stage for the Raman equipment, and Iván Pérez Alcocer his assistance in fabricating the support fixture for the compression testing.
- ❖ To Carlos Falla Chel and Dr. Fidel Gamboa Perera for their work on the development of the electronic board that organizes the connections for the structural health monitoring of the composite panels.
- ❖ To Dr. Aarón Rivas Menchi for providing initial guidance with the Prony series, and to Dulce Romero Quezada and Jhonatan Tzuc Pam for their assistance in programming the Prony series.
- ❖ To my colleagues and friends in FA's group at CICY and in KG's group at UU for their unwavering support and camaraderie.
- ❖ To Estefanía López Sauri for her unwavering support and assistance throughout my entire doctoral journey.

# Contents

<b>Acronyms</b> .....	<b>iv</b>
<b>Nomenclature</b> .....	<b>v</b>
Greek variables .....	v
Latin variables.....	viii
<b>List of figures</b> .....	<b>xii</b>
<b>List of tables</b> .....	<b>xvii</b>
<b>Resumen</b> .....	<b>xviii</b>
<b>Abstract</b> .....	<b>xix</b>
<b>Research objectives</b> .....	<b>xx</b>
<b>Outline of the research</b> .....	<b>xxi</b>
<b>Introduction</b> .....	<b>1</b>
<b>Chapter 1. Background</b> .....	<b>3</b>
1.1. Carbon nanotube yarns .....	3
1.1.1. Methods of production .....	4
1.1.2. Hierarchy and mechanics of load transfer.....	6
1.1.3. Electrical, mechanical, and piezoresistive properties .....	9
1.1.4. Applications.....	12
1.2. Carbon nanotube yarns for structural health monitoring .....	13
<b>Chapter 2. Materials and methods</b> .....	<b>16</b>
2.1. Materials .....	16
2.2. Characterization of carbon nanotube yarns.....	16
2.2.1. Atomic force and scanning electron microscopy.....	16
2.2.2. Measurement of linear density and porosity .....	17
2.2.3. Fourier-transform infrared spectroscopy.....	18
2.2.4. Thermogravimetric analysis .....	18
2.2.5. In situ Raman spectroscopy during tensile electromechanical testing.....	18
2.2.6. In situ scanning electron microscopy during tensile mechanical testing .....	21
2.2.7. Monotonic and cyclic tensile mechanical testing .....	22
2.2.8. Tensile electromechanical testing.....	24
2.2.9. Relaxation testing with in situ electrical monitoring .....	25
2.2.10. Constrained thermoresistive characterization.....	27

2.2.11.	Electrical monitoring during dynamic mechanical testing.....	28
2.2.12.	Tensile electromechanical testing at different temperatures .....	30
2.3.	Modeling for tensile mechanical behavior carbon nanotube yarns .....	31
2.4.	Electromechanical characterization of monofilament composites .....	35
2.4.1.	Manufacturing of monofilament composites .....	35
2.4.2.	Tensile mechanical and electromechanical testing using digital image correlation.....	37
2.5.	Laminated composites panels for structural health monitoring .....	38
2.5.1.	Manufacturing of laminated composites panels .....	38
2.5.2.	Electrical instrumentation and algorithm for structural health monitoring.....	39
2.5.3.	Monotonic compression testing .....	43
2.5.4.	Cyclic compression testing.....	44
2.5.5.	Optical and scanning electron microscopy.....	45
<b>Chapter 3.</b>	<b>Results and discussion.....</b>	<b>47</b>
3.1.	Properties of carbon nanotube yarns .....	47
3.1.1.	Morphological and structural properties .....	47
3.1.2.	Linear density and porosity .....	49
3.1.3.	Fourier-transform infrared analysis .....	50
3.1.4.	Thermogravimetric analysis .....	52
3.1.5.	Raman spectroscopy .....	52
3.1.6.	Correlation between strain, Raman shift, and electrical response .....	55
3.1.7.	Radial contraction ratio .....	59
3.1.8.	Tensile mechanical properties under monotonic loading.....	63
3.1.9.	Cyclic tensile mechanical properties and hysteresis.....	64
3.1.10.	Electromechanical response under tensile loading .....	68
3.1.11.	Stress and electrical relaxation responses under tensile loading .....	70
3.1.12.	Constrained thermoresistive response.....	73
3.1.13.	Dynamic mechanical response .....	75
3.1.14.	Electrical response during dynamic mechanical analysis .....	78
3.1.15.	Electromechanical response under tensile loading at different temperatures .....	80
3.2.	Property-structure relationships inferred from modeling .....	82
3.3.	Tensile mechanical and electromechanical properties of monofilament composites .....	85
3.4.	Structural health monitoring of laminated composite panels under compression loading .....	90
3.4.1.	Compression response and failure mode.....	90

3.4.2.	In situ electrical mapping and damage detection during monotonic compression loading.....	94
3.4.3.	In situ electrical mapping and damage detection during cyclic compression loading....	96
<b>Conclusions and perspectives .....</b>		<b>102</b>
<b>Appendices .....</b>		<b>105</b>
A.	Dynamic mechanical response of carbon nanotube yarns .....	105
A.1.	Effect of static force.....	105
A.2.	Effect of frequency .....	107
A.3.	Effect of preheating .....	107
A.4.	Effect of heating rate.....	109
B.	Diameter distribution of the carbon nanotube yarns .....	110
C.	Variability of Raman spectra in the carbon nanotube yarns as function of location and axial strain .....	111
D.	Parametric analysis of the yarn's tensile model.....	114
D.1.	Tensile modulus and coefficient of friction of the fibrils .....	114
D.2.	Radial packing density .....	115
D.3.	Distribution of compressive transverse stress .....	116
D.4.	Distribution of fibril axial strain.....	117
E.	Critical length for load transfer of the carbon nanotubes and their fibrils.....	117
F.	Summary of the physical properties of the carbon nanotubes yarns .....	119
<b>References .....</b>		<b>122</b>

## Acronyms

Acronym	Meaning
2D	Two-dimensional.
3D	Three-dimensional.
a.u.	Arbitrary units.
AFM	Atomic force microscopy.
CNT	Carbon nanotube.
CNTY	Carbon nanotube yarn.
CVD	Chemical vapor deposition.
DC	Direct current.
DMA	Dynamic mechanical analysis.
FTIR	Fourier-transform infrared spectroscopy.
FWHM	Full width at half maximum.
GFW	Glass fiber weave.
PER	Panel's electrical resistance algorithm.
PERI	Panel's electrical resistance with interpolation algorithm.
RC	Resistive-capacitive.
SEM	Scanning electron microscopy.
SHM	Structural health monitoring.
TGA	Thermogravimetric analysis.
VER	Vinyl ester resin
vol.%	Volume concentration (%).
wt.%	Weight concentration (%).

# Nomenclature

## Greek variables

Symbol	Parameter	Unit
$\beta_i$	Temperature coefficient of resistance of the CNTYs ( $i = 1$ for the $0 \leq \Delta T \leq 50$ K heating range, $i = 2$ for the $130 \text{ K} \leq \Delta T \leq 250$ K heating range, and $i = 3$ for the full cooling range).	$\text{K}^{-1}$
$\beta_{\text{Ph}}^{\text{DMA}}$	Temperature coefficient of resistance of preheated CNTYs for the full temperature range during DMA.	$\text{K}^{-1}$
$\beta_{\text{Pri}}^{\text{DMA}}$	Temperature coefficient of resistance of pristine CNTYs in the $0 \leq \Delta T \leq 50$ K range during DMA.	$\text{K}^{-1}$
$\Delta L$	Displacement.	m
$\Delta R$	Change of electrical resistance.	$\Omega$
$\Delta R/R_0$	Fractional change of electrical resistance.	-
$\Delta r_{\text{ext}}$	Change of radius of the CNTYs.	m
$\Delta T$	Temperature change.	K
$\Delta z$	Displacement in the z-axis direction (out-of-plane) of the laminated composite panels.	m
$\Delta z_{\text{C}}$	Displacement in the z-axis direction (out-of-plane) at the center of the laminated composite panels.	m
$\varepsilon_r$	Radial strain of the CNTYs.	-
$\varepsilon_x$	Strain in the x-axis direction.	-
$\varepsilon_{x_u}^{\text{M}}$	Tensile failure axial (x) strain of the monofilament composites.	-
$\varepsilon_y$	Strain in the y-axis direction.	-
$\varepsilon_{y_u}^{\text{P}}$	Compressive failure strain of the laminated composite panels.	-
$\varepsilon_z$	Axial (z) strain of the CNTYs.	-
$\varepsilon_z^{\text{Max}}$	Maximum axial strain of the CNTYs.	-
$\varepsilon_{z_f}$	Axial strain of the CNTY's fibrils.	-
$\varepsilon_{z_f}^{\text{Max}}$	Maximum axial strain of the CNTY's fibrils.	-
$\varepsilon_{z_u}$	Ultimate (failure) axial tensile strain of the CNTYs.	-
$\varepsilon_{z_f}/\varepsilon_{z_f}^{\text{Max}}$	Normalized axial strain of the CNTY's fibrils.	-
$\theta$	Twist angle of the CNTY (function of the radial position).	$^\circ$

$\theta_{\text{ext}}$	Twist angle of the CNTY at external radius (surface).	°
$\theta_{\text{ext}0}$	Pristine (undeformed) twist angle of the CNTYs at external radius (surface).	°
$\lambda$	Slippage ratio of the CNTY's fibrils.	-
$\mu$	Coefficient of friction of the CNTY's fibrils	-
$\nu_{xy}^M$	Poisson's ratio of the monofilament composites.	-
$\nu_{zr}$	Radial contraction ratio of the CNTYs in the $z$ - $r$ plane.	-
$\nu_{zr\infty}$	Plateau parameter of the exponentially decaying function used to fit the experimental data of the radial contraction ratio of the CNTYs.	-
$\xi$	Electrical conductivity of the CNTYs.	S/m
$\xi/\rho$	Specific electrical conductivity of the CNTYs.	S·cm <sup>2</sup> /g
$\rho$	Volumetric mass density of the CNTYs.	g/cm <sup>3</sup>
$\rho_{\text{CNT}}$	Volumetric mass density of the CNTs that make up the CNTYs.	g/cm <sup>3</sup>
$\rho_L$	Linear density of the CNTYs.	tex
$\rho_r$	Packing density of the CNTYs (function of the radial position).	-
$\rho_r^{\text{Max}}$	Maximum packing density of the CNTYs.	-
$\rho_r/\rho_r^{\text{Max}}$	Normalized packing density of the CNTYs.	-
$\sigma_{z\text{Res}}$	Residual axial tensile stress of the CNTYs.	Pa
$\sigma_x$	Stress in the $x$ -axis direction.	Pa
$\sigma_{x_u}^M$	Tensile strength of the monofilament composites.	Pa
$\sigma_y$	Stress in the $y$ -axis direction.	Pa
$\sigma_{y_u}^P$	Compressive strength of the laminated composite panels.	Pa
$\sigma_z$	Axial stress of the CNTYs.	Pa
$\sigma_z^{\text{Max}}$	Maximum axial stress of the CNTYs.	Pa
$\sigma_{z_f}$	Axial stress of the CNTY's fibrils.	Pa
$\sigma_{z_u}^{\text{CNT}}$	Tensile strength of the CNTs that make up the CNTYs.	Pa
$\sigma_{z_u}^f$	Tensile strength of the CNTY's fibrils.	Pa
$\sigma_z/\rho$	Specific axial stress of the CNTYs.	N/tex
$\sigma_z^{\text{Max}}/\rho$	Maximum specific axial stress of the CNTYs	N/tex

$\sigma_{zRes}/\rho$	Residual specific axial tensile stress of the CNTYs.	N/tex
$\sigma_{zu}/\rho$	Specific axial tensile strength of the CNTYs.	N/tex
$\tau_i$	Relaxation time of the CNTYs corresponding to the $i$ -th Maxwell element of the Prony series.	s
$\tau_{Int}^{CNT}$	Inter-CNT shear strength of the CNTs that make up the CNTYs.	Pa
$\tau_{Int}^f$	Inter-fibril shear strength of the CNTY's fibrils.	Pa
$\Phi_P$	Porosity of the CNTYs.	-
$\varphi$	Tangential direction/position in the CNTYs (orthogonal cylindrical coordinate system).	Rad

## Latin variables

Symbol	Parameter	Unit
$a$	Fitting constant for transverse pressure inside the CNTYs.	Pa/m <sup>6</sup>
$b$	Strain parameter for transverse pressure inside the CNTYs.	-
$A_{SEM}$	Two-dimensional projected area of the CNTYs measured by SEM.	m <sup>2</sup>
$c_1$	First parameter representing the amplitude of the exponentially decaying function used to fit the experimental data of the CNTY's radial contraction ratio.	-
$c_2$	Second parameter representing the amplitude of the exponentially decaying function used to fit the experimental data of the CNTY's radial contraction ratio.	-
$d_1$	First parameter representing the decay rate of the exponentially decaying function used to fit the experimental data of the CNTY's radial contraction ratio.	-
$d_2$	Second parameter representing the decay rate of the exponentially decaying function used to fit the experimental data of the CNTY's radial contraction ratio.	-
$d_{ext}$	Diameter of the CNTYs.	m
$d_{ext0}$	Pristine (undeformed) diameter of the CNTYs.	m
$d_f$	Diameter of the CNTY's fibrils.	m
$d_{S-S}$	Inter-shell distance of the CNTs.	nm
$d_{Out}$	Outer diameter of the CNTs.	nm
$E$	Tensile elastic modulus of the CNTYs.	Pa
$E'$	Storage modulus of the CNTYs.	Pa
$E''$	Loss modulus of the CNTYs.	Pa
$E^M$	Tensile modulus of the monofilament composites.	Pa
$E_C^P$	Compressive modulus of the laminated composite panels.	Pa
$E_f$	Tensile elastic modulus of the CNTY's fibrils.	Pa
$E_{Max}$	Maximum value of tensile elastic modulus of the CNTYs.	Pa
$E/\rho$	Specific tensile modulus of the CNTYs.	N/tex
$E/E_{Max}$	Normalized specific tensile elastic modulus of the CNTYs.	-
$E_i/\rho$	Specific elastic modulus of the CNTYs corresponding to the $i$ -th Maxwell element of the Prony series.	N/tex

$E_{\infty}/\rho$	Equilibrium specific tensile modulus of the CNTYs.	N/tex
$F_y$	Force applied in the y-axis direction.	N
$F_z$	Force applied in the z-axis direction.	N
$F_z^{\text{Max}}$	Maximum value of force applied during DMA in the z-axis direction.	N
$F_z^{\text{Min}}$	Minimum value of force applied during DMA in the z-axis direction.	N
$F_{zD}$	Dynamic force applied in the z-axis direction during DMA.	N
$F_{zS}$	Static force applied in the z-axis direction during DMA.	N
$F_{zu}$	Ultimate (failure) axial tensile force of the CNTYs.	N
$f$	Frequency.	Hz
$GF$	Gage factor.	-
$H$	Mechanical hysteresis loop of the CNTYs under axial tensile loading.	J/g
$H_N$	Normalized hysteresis of the CNTYs under axial tensile loading.	-
$H/\rho$	Dissipated energy density of the CNTYs.	J/cm <sup>3</sup>
$h$	Length of the CNTYs with one turn of twist.	m
$h_0$	Pristine (undeformed) length of the CNTYs with one turn of twist.	m
$I$	Electrical current.	A
$I_D$	Raman intensity of the D band.	a.u
$I_{D'}$	Raman intensity of the D' bands.	a.u.
$I_G$	Raman intensity of the G band.	a.u.
$I_D/I_G$	Relative intensities of the D to G Raman bands	-
$I_{D'}/I_G$	Relative intensities of the D' to G Raman bands.	-
$k$	Slip factor of the CNTYs.	-
$L$	Length of the CNTY samples.	m
$L_c^{\text{CNT}}$	Critical length of the CNTs that make up the CNTYs.	m
$L_c^f$	Critical length of the CNTY's fibrils.	m
$L_f$	Length of the CNTY's fibrils.	m
$L_g$	Gage length of the CNTYs for tensile testing (same as the distance between electrodes for electromechanical testing). It also represents the distance between electrodes for the tensile coupons.	m

$L_{i,j}$	Shortest distance between the $i$ -th and $j$ -th electrodes in the laminated composite panels by following paths that connect electrodes.	m
$L_{SEM}$	Length of the SEM image used to measure the radial contraction ratio of the CNTYs.	m
$m$	Mass.	kg
$n$	Number of CNT walls/number elements in the Prony series.	-
$P$	Compressive transverse stress inside the CNTYs.	Pa
$P_{Max}$	Maximum value of compressive transverse stress inside the CNTYs.	Pa
$P/P_{Max}$	Normalized compressive transverse stress inside the CNTYs.	-
$Q$	Migration cycle of the CNTYs.	m
$R$	Electrical resistance.	$\Omega$
$R_0$	Initial electrical resistance.	$\Omega$
$R_i$	Electrical resistance of the CNTYs corresponding to the $i$ -th Maxwell element of the Prony series.	$\Omega$
$R_{ij}$	Electrical resistance between the $i$ -th and $j$ -th electrodes in the laminated composite panels.	$\Omega$
$R_{Max}$	Maximum value of electrical resistance.	$\Omega$
$R_{N_l}$	Electrical resistance assigned to the $l$ -th node in the laminated composite panels.	$\Omega$
$R_{P_l}$	Electrical resistance assigned to the $l$ -th path that connect electrodes to nodes in the laminated composite panels.	$\Omega$
$R_{P_{i,j}}$	Electrical resistance assigned to central path $i, j$ that connects nodes to nodes in the laminated composite panels.	$\Omega$
$R_\infty$	Equilibrium electrical resistance of the CNTYs in the Prony series.	$\Omega$
$R/R_{Max}$	Normalized electrical resistance of the CNTYs.	-
$r$	Radial direction/position in the CNTYs (orthogonal cylindrical coordinate system).	m
$r_{CNT}$	Radius of the CNTs that make up the CNTYs.	m
$r_{ext}$	Radius of the CNTYs.	m
$r_{ext_0}$	Pristine (undeformed) radius of the CNTYs.	m
$r_f$	Radius of the CNTY's fibrils.	m
$r/r_{ext}$	Normalized radial position of the CNTYs.	-
$T$	Temperature.	$^\circ\text{C}$

$T_0$	Room temperature/initial test temperature.	°C
$\tan(\delta)$	Damping factor.	-
$t$	Time.	s
$V$	Voltage.	V
$x$	Abscissa direction in the Cartesian coordinate system.	m
$y$	Ordinate direction in the Cartesian coordinate system.	m
$z$	Axial direction in the CNTYs (orthogonal cylindrical coordinate system) and depth direction in the composites.	m

# List of figures

**Fig. 1.** Outline of the research. .... xxi

**Fig. 2.** Overview of the research..... xxii

**Fig. 3.** Intelligent structural health monitoring concept applied to a building. Extracted from [1]. ..... 1

**Fig. 1.1.** Conceptual view of a CNT as a graphene sheet rolled along a chiral vector. Modified from [24].  
..... 3

**Fig. 1.2.** Hierarchical structure of a CNTY. Individual scanning electron microscopy images were obtained from [2,13,14]..... 4

**Fig. 1.3.** Schematic of the wet spinning method. Extracted from [43]..... 4

**Fig. 1.4.** Spun process of a CNTY from a CNT forest by the dry spinning method. **(a)** Schematic of the draw-twist process (extracted from [46]), **(b)** formation of a CNTY during the draw-twist process (extracted from [29])..... 5

**Fig. 1.5.** Mechanical response of an aerogel-spun CNTY under uniaxial tensile loading ( $SG$  = specific gravity; 1 tex = 1 g/km). Extracted from [62]. ..... 7

**Fig. 1.6.** Schematic depicting the change in twist angle ( $\theta_{ext}$ ) of a CNTY with increasing axial strain ( $\epsilon_z$ )..... 7

**Fig. 1.7.** Schematic of the strength-twist relationship for yarns. Extracted from [28,52]. ..... 8

**Fig. 1.8.** Effects of porosity in a dry-spun CNTY (extracted from [15]). **(a)** Effect of yarn surface twist angle on the yarn density and porosity, **(b)** effect of yarn porosity on the electrical conductivity and resistivity. .... 10

**Fig. 1.9.** Electrical response of CNTYs under uniaxial tensile loading. **(a)** Effect of twist level (extracted from [52]), **(b)** effect of strain rate (extracted from [91]). ..... 11

**Fig. 1.10.** Applications of CNTYs. **(a)** Self-powered twistron strain sensor woven into a shirt and used for monitoring breathing (extracted from [34]), **(b)** polymer soft-actuator composed of polymer threads and CNTYs (extracted from [38])..... 12

**Fig. 1.11.** Use of a CNTY 2D array (grid) for SHM in IM7/977-3 composite panels (extracted from [94]). **(a)** Schematic of connections of the 12×12 CNTY array, **(b)** normalized change in electrical resistance of the CNTY grid after impact..... 13

**Fig. 1.12.** Delamination detection in laminated composites using CNTYs (extracted from [17]). **(a)** Schematic of the CNTYs configuration, **(b)** electromechanical response. .... 14

**Fig. 2.1.** CNTY specimens for in situ Raman spectroscopy during uniaxial tensile testing. **(a)** Specimen for mechanical testing, **(b)** specimen for electromechanical testing..... 19

<b>Fig. 2.2.</b> Schematic of the test setup for in situ Raman spectroscopy during uniaxial tensile testing. ...	20
<b>Fig. 2.3.</b> In situ SEM of CNTY during axial tensile testing. (a) Test setup, (b) image processing procedure for measuring the effective diameter. Hatched lines correspond to the CNTY. ....	21
<b>Fig. 2.4.</b> CNTY specimen for uniaxial tensile mechanical testing. ....	23
<b>Fig. 2.5.</b> Schematic of the hysteresis parameters used for the uniaxial cyclic tensile test. ....	24
<b>Fig. 2.6.</b> CNTY specimen for tensile electromechanical testing. ....	25
<b>Fig. 2.7.</b> CNTY specimen for stress relaxation testing. ....	26
<b>Fig. 2.8.</b> Wiechert's model. Modified from [105]. ....	27
<b>Fig. 2.9.</b> CNTY specimen for constrained thermoresistive characterization and electrical monitoring during DMA. ....	28
<b>Fig. 2.10.</b> DMA of the CNTYs. (a) CNTY specimen, (b) schematic of the oscillatory force. ....	29
<b>Fig. 2.11.</b> Coaxial helix model of a twisted staple yarn. Modified from [28]. ....	32
<b>Fig. 2.12.</b> Monofilament specimen. (a) Specimen for tensile mechanical testing, (b) specimen for tensile electromechanical testing. ....	36
<b>Fig. 2.13.</b> Schematic of a GFW+CNTY/VER laminated composite panel containing a 2×2 CNTY array for SHM. ....	39
<b>Fig. 2.14.</b> Electrical mapping of the GFW+CNTY/VER panels. (a) Definition of electrical elements used for the SHM algorithm, (b) photograph of electrical connections. ....	41
<b>Fig. 2.15.</b> Setup for compression testing of the laminated composite panels. (a) Schematic of the fixture and DIC measurements, (b) photograph of the actual setup. ....	44
<b>Fig. 2.16.</b> Photograph of the setup for cyclic compression testing of the laminated composite panels. ....	45
<b>Fig. 3.1.</b> Morphology of CNTYs. (a) Representative SEM image of the CNTYs, (b) histogram of CNTY's diameter ( $d_{ext_0}$ ) distribution. ....	47
<b>Fig. 3.2.</b> AFM images of the CNTY's fibrils. (a) 3×3 $\mu\text{m}^2$ 2D view, (b) 5×5 $\mu\text{m}^2$ 2D view, (c) 10×10 $\mu\text{m}^2$ 3D view, (d) histogram of fibril's diameter ( $d_f$ ) distribution. ....	49
<b>Fig. 3.3.</b> Weight measurements to determine the linear density ( $\rho_L$ ) of the CNTYs. ....	50
<b>Fig. 3.4.</b> Representative FTIR of the CNTYs. ....	51
<b>Fig. 3.5.</b> Thermogram of a representative CNTY. ....	52
<b>Fig. 3.6.</b> Raman spectra of the CNTYs. (a) 10 $\mu\text{m}$ line scan, (b) representative Raman spectrum, (c) D band variability, (d) $I_D/I_G$ variability, (e) $I_{D'}/I_G$ variability. ....	53
<b>Fig. 3.7.</b> D band peak position of the CNTYs as a function of axial strain ( $\epsilon_z$ ). ....	57

<b>Fig. 3.8.</b> D band peak position and fractional change in electrical resistance ( $\Delta R/R_0$ ) of a representative CNTY as a function of axial strain ( $\varepsilon_z$ ) and time. ....	59
<b>Fig. 3.9.</b> In situ SEM of a CNTY during tensile testing. (a) CNTY at $\varepsilon_z = 0$ , (b) CNTY at $\varepsilon_z = 12\%$ , (c) CNTY at failure ( $\varepsilon_z = 13\%$ ), (d) close-up of the CNTY at failure, indicated by a dashed rectangle in Fig. 3.9c. ....	60
<b>Fig. 3.10.</b> In situ mechanical response of CNTYs under axial tensile loading with radial contraction measured by SEM. (a) Specific stress in the axial direction ( $\sigma_z/\rho$ ), radial strain ( $\varepsilon_r$ ) and radial contraction ratio ( $\nu_{zr}$ ) of a representative CNTY as a function of axial strain ( $\varepsilon_z$ ), (b) measured $\nu_{zr}$ as a function of $\varepsilon_z$ , including the fitting curve given by Eq. (3.1). ....	62
<b>Fig. 3.11.</b> Mechanical response of CNTYs under uniaxial tensile loading. ....	64
<b>Fig. 3.12.</b> Mechanical hysteresis of a representative CNTY under cyclic tensile loading up to $\varepsilon_z = 1.0\%$ . (a) Tensile response of all 300 cycles, (b) tensile response of selected cycles, (c) residual specific stress ( $\sigma_{zRes}/\rho$ ), (d) normalized hysteresis ( $H_N$ ). ....	65
<b>Fig. 3.13.</b> Mechanical hysteresis of a representative CNTY under incremental strain cyclic tensile loading. (a) Tensile behavior of different cycles, (b) normalized hysteresis ( $H_N$ ), (c) residual specific stress ( $\sigma_{zRes}/\rho$ ). ....	67
<b>Fig. 3.14.</b> Electromechanical response of a representative CNTY under uniaxial tensile loading. ....	70
<b>Fig. 3.15.</b> Specific tensile modulus and electrical resistance relaxations of a representative CNTY under constant axial tensile strain ( $\varepsilon_z = 1.0\%$ ). (a) Normalized specific modulus ( $E/E_{Max}$ ) and normalized electrical resistance ( $R/R_{Max}$ ) as a function of elapsed time ( $t$ ), (b) $E/E_{Max}$ as a function of $t$ and its fitting to Eq. (2.6) with $n = 3$ (continuous line), (c) $R/R_{Max}$ as a function of $t$ and its fitting to the electrical form of Eq. (2.6) with $n = 3$ (continuous line). ....	71
<b>Fig. 3.16.</b> Constrained thermoresistive response of a representative CNTY. ....	75
<b>Fig. 3.17.</b> Tensile DMA response of representative CNTYs. (a) Response as a function of temperature ( $T$ ), (b) response as a function of frequency ( $f$ ). ....	76
<b>Fig. 3.18.</b> Electrical response of representative CNTYs during DMA testing. (a) Pristine CNTY, (b) preheated CNTY (tested after the constrained thermoresistive characterization). ....	79
<b>Fig. 3.19.</b> Electromechanical response of CNTYs under uniaxial tensile loading at different temperatures. (a) Mechanical response, (b) electrical response. ....	81
<b>Fig. 3.20.</b> Tensile mechanical response of CNTYs, obtained from Eq. (2.13). (a) Comparison of modeling results with experimental data, (b) effect of radial contraction ratio ( $\nu_{zr}$ ), (c) effect of slip factor	

(k), (d) effect of coefficient of friction ( $\mu$ ), (e) effect of fibril radius ( $r_f$ ), (f) effect of fibril length ( $L_f$ ). .....	83
<b>Fig. 3.21.</b> Electromechanical response of different monofilament composites under uniaxial tensile loading. (a) Representative mechanical response of the VER specimen, (b) representative electromechanical response of the CNTY/VER+Cu specimen. ....	87
<b>Fig. 3.22.</b> Electromechanical properties of the monofilament composites under uniaxial tensile loading. (a) tensile failure strain ( $\epsilon_{xu}^M$ ), (b) tensile strength ( $\sigma_{xu}^M$ ), (c) tensile modulus ( $E^M$ ), d) Poisson's ratio ( $\nu_{xy}^M$ ). ....	88
<b>Fig. 3.23.</b> Compressive mechanical behavior of the laminated composite panels. (a) Axial compression stress ( $\sigma_y$ ) as a function of strain ( $\epsilon_y$ ), (b) out-of-plane displacement measured at the center of the panel ( $\Delta z_C$ ) as a function of $\epsilon_y$ , (c) failure mode, (d) compression modulus ( $E_C^P$ ), (e) compression failure strain ( $\epsilon_{yu}^P$ ), (f) compression strength ( $\sigma_{yu}^P$ ). ....	91
<b>Fig. 3.24.</b> Post-mortem examination of laminated composite panels after compression testing. (a) Photograph of the GFW+CNTY/VER panel, (b) photograph of the GFW+CNTY/VER-D25 panel, (c) photograph of the GFW/VER-D50 panel, (d) optical microscopy images (GFW+CNTY/VER and GFW/VER-D25), (e) SEM images (GFW+CNTY/VER-D25 and GFW/VER-D50). ....	93
<b>Fig. 3.25.</b> Structural health monitoring of an exemplary GFW+CNTY/VER panel. ....	95
<b>Fig. 3.26.</b> Structural health monitoring of an exemplary GFW+CNTY/VER-D25 panel. ....	96
<b>Fig. 3.27.</b> Mechanical response of a representative GFW+CNTY/VER-D25 panel under cyclic compression loading. ....	97
<b>Fig. 3.28.</b> DIC strain fields ( $\epsilon_y$ ) of a representative GFW+CNTY/VER-D25 panel under cyclic compression loading. ....	98
<b>Fig. 3.29.</b> DIC out-of-plane displacement fields ( $\Delta z$ ) of a representative GFW+CNTY/VER-D25 panel under cyclic compression loading. ....	99
<b>Fig. 3.30.</b> SHM of an exemplary GFW+CNTY/VER-D25 panel under cyclic compression loading. (a) DIC and electrical contour maps during loading (at maximum compression load) of selected cycles, (b) photograph of the backside of the panel after testing and its PERI contour map. ....	101
<b>Fig. A.1.</b> DMA response of a collection of CNTYs as a function of temperature ( $T$ ), using different static forces. (a) Storage modulus ( $E'$ ), (b) loss modulus ( $E''$ ), (c) damping ratio ( $\tan(\delta)$ ). ....	105
<b>Fig. A.2.</b> DMA tensile response of an individual CNTY (at 30 °C) as a function of frequency ( $f$ ) using different static forces. (a) Storage modulus ( $E'$ ), (b) loss modulus ( $E''$ ), (c) damping ratio ( $\tan(\delta)$ ). ....	106

<b>Fig. A.3.</b> DMA response of a collection of CNTYs as a function of frequency ( $f$ ) for different temperatures. (a) Storage modulus ( $E'$ ), (b) loss modulus ( $E''$ ), (c) damping ratio ( $\tan(\delta)$ ).	107
<b>Fig. A.4.</b> DMA tensile response of the CNTYs as a function of temperature ( $T$ ) with and without (pristine) preheating. (a) Storage modulus ( $E'$ ), (b) loss modulus ( $E''$ ), (c) damping ratio ( $\tan(\delta)$ ).	108
<b>Fig. A.5.</b> DMA tensile response of the CNTYs as a function of temperature ( $T$ ) using different heating rates. (a) Storage modulus ( $E'$ ), (b) loss modulus ( $E''$ ), (c) damping ratio ( $\tan(\delta)$ ).	109
<b>Fig. B.1.</b> Probability of the statistical CNTY diameter distributions. (a) Largest extreme value distribution, (b) 3-parameter lognormal distribution, (c) loglogistic distribution, (d) 3-parameter loglogistic distribution.	110
<b>Fig. C.1.</b> Variability of the Raman bands' peak position, intensity and FWHM of the CNTYs. (a) D band, (b) G band, (c) D' band, (d) G' band.	112
<b>Fig. C.2.</b> Raman bands' peak position, intensity and FWHM of the CNTYs as a function of axial strain ( $\varepsilon_z$ ). (a) D band, (b) G band, (c) D' band, (d) G' band.	113
<b>Fig. D.1.</b> Effect of the slip factor ( $k$ ) in the fibril tensile modulus ( $E_f$ ) according to Eq. (2.11).	115
<b>Fig. D.2.</b> Distribution of the normalized packing density ( $\rho_r/\rho_r^{\text{Max}}$ ) along the normalized radial position of the CNTY ( $r/r_{\text{ext}}$ ) for different values of axial strain ( $\varepsilon_z$ ).	116
<b>Fig. D.3.</b> Distribution of the normalized compressive transverse stress ( $P/P_{\text{Max}}$ ) along the normalized radial position of the CNTY ( $r/r_{\text{ext}}$ ) for different values of axial strain ( $\varepsilon_z$ ).	116
<b>Fig. D.4.</b> Distribution of the normalized axial strain of the CNT fibrils ( $\varepsilon_{z_f}/\varepsilon_{z_f}^{\text{Max}}$ ) along the normalized radial position of the CNTY ( $r/r_{\text{ext}}$ ) for different values of axial strain ( $\varepsilon_z$ ).	117

## List of tables

<b>Table 1.1.</b> Selected properties of CNTs and CNTYs. ....	10
<b>Table 2.1.</b> DMA test program. ....	30
<b>Table 2.2.</b> Baseline input parameters of the mechanical model, Eq. (2.13). ....	35
<b>Table 2.3.</b> Type of monofilament specimens. ....	37
<b>Table 3.1.</b> Statistical distribution models of the CNTY diameters*. ....	48
<b>Table 3.2.</b> FTIR band identification for the CNTYs. ....	51
<b>Table 3.3.</b> Features of Raman bands in CNTYs and other carbon nanostructures. ....	54
<b>Table 3.4.</b> Specific (per unit density) dissipated energy of different materials. ....	68
<b>Table 3.5.</b> Prony series elements for the specific tensile modulus and electrical resistance relaxation of a representative CNTY at $\varepsilon_z = 1.0\%$ . ....	72
<b>Table 3.6.</b> Electromechanical tensile properties of the monofilament composites. ....	89
<b>Table 3.7.</b> Mechanical compression properties of the laminated composite panels. ....	92
<b>Table F.1.</b> Summary of physical properties of the CNTYs. ....	119

# Resumen

Los hilos de nanotubos de carbono (CNTYs, por sus siglas en inglés) exhiben propiedades mecánicas notables, capacidad de disipación de energía y características multifuncionales que los posicionan como materiales jerárquicos inteligentes con un inmenso potencial. Esta tesis investiga la relación entre la estructura y las propiedades de los CNTYs y explora su potencial para el monitoreo eléctrico de la salud estructural en materiales compuestos avanzados fibroreforzados. Se emplean experimentos in situ utilizando espectroscopía Raman y microscopía electrónica de barrido para estudiar la evolución estructural de los CNTYs bajo carga de tensión. Los hallazgos revelan que la respuesta mecánica de los CNTYs está gobernada por movimientos estructurales de las fibrillas y grupos de nanotubos de carbono, más que por la elongación de los enlaces C-C. Se observó que los CNTYs fallan por extracción de sus fibrillas, causada por el deslizamiento entre estas. La contribución de la deformación del material (C-C) a la elongación del CNTY solo surge por encima del 0.5 % de deformación, y es evidenciada por un pequeño factor de deformación de desplazamiento Raman de  $-0.30 \text{ cm}^{-1}/\%$ . Estos resultados mostraron que el eslabón más débil de los CNTYs es la resistencia cortante entre fibrillas. Este comportamiento confiere a los CNTYs capacidades excepcionales de disipación de energía, como se observa en su respuesta de histéresis a la tracción bajo carga cíclica y en el módulo de pérdida elevado en el análisis dinámico mecánico. Los CNTYs experimentan una reducción significativa de diámetro y rotación debido a la reorganización de las fibrillas, presentando una elevada contracción radial que disminuye exponencialmente con el aumento de la deformación axial. El modelado de hélice coaxial de los CNTYs destaca la importancia de la razón de contracción radial y su dependencia con la deformación aplicada. El modelo demostró la fuerte influencia del factor de deslizamiento, el radio de fibrilla y la longitud de fibrilla en la respuesta mecánica no lineal de los CNTYs. Todos estos cambios estructurales influyen en la respuesta eléctrica de los CNTYs. Sin embargo, las mediciones simultáneas de la resistencia eléctrica durante las pruebas de relajación indican que la capacitancia y la acumulación de carga eléctrica influyen en la respuesta eléctrica de los CNTYs más allá de la reorganización estructural interna. Finalmente, esta investigación se extiende a la aplicación de los CNTYs en el monitoreo de la salud estructural. Para ello, los CNTYs se integraron en paneles compuestos laminados hechos de tejidos de fibra de vidrio tipo E y resina vinil éster. La técnica de monitoreo utilizada aquí demuestra la efectividad de los CNTYs en la detección y localización de daños en los paneles bajo carga de compresión monótona y cíclica, lo cual se correlacionó con las mediciones de correlación digital de imágenes. Estos resultados indican que los CNTYs tienen un gran potencial para el monitoreo de salud estructural, ofreciendo retroalimentación en tiempo real sobre la concentración de esfuerzos y la detección de daño visible y no visible, lo que puede mejorar significativamente la seguridad y confiabilidad en diversas industrias que utilizan materiales compuestos avanzados.

## Abstract

Carbon nanotube (CNT) yarns (CNTYs) stand out as extraordinary materials, rendering remarkable mechanical properties, energy dissipation capabilities, and multifunctional characteristics that position them as smart hierarchical materials with immense potential. This thesis work investigates the structure-property relationship of CNTYs and explores their potential for structural health monitoring in advanced fiber-reinforced composites. In situ experiments using Raman spectroscopy and scanning electron microscopy are employed to study the structural evolution of CNTYs under tensile loading. The findings reveal that the mechanical response of the CNTYs is governed by structural motions, slippage, and rotations (untwist) of the fibrils and CNT bundles, rather than C-C bond stretching. CNTYs fail through fibril pull-out caused by fibril-to-fibril slippage. The contribution of material (C-C) deformation to the stretching of the CNTY only arises above 0.5 % strain, evidenced by a small Raman shift strain factor of  $-0.30 \text{ cm}^{-1}/\%$ . These results prove that the weakest link of the CNTY is the shear strength between fibrils. This behavior yields CNTYs with exceptional energy-dissipation capabilities, as observed in their tensile hysteresis response under cycling loading and high loss modulus in dynamic mechanical analysis. The CNTYs undergo a significant diameter reduction and rotation (untwist) due to fibril rearrangement, presenting a high radial contraction ratio that decreases exponentially with increasing axial strain. The coaxial helix modeling of CNTYs emphasizes the significance of the radial contraction ratio and its dependence on applied strain. The model demonstrates the strong influence of the slip factor, fibril radius, and fibril length on the nonlinear mechanical response of CNTYs. All these structural changes influence the electrical response of the CNTYs. However, simultaneous measurements of the electrical resistance during relaxation testing indicate that structural relaxation and equilibrium occurred faster than electrical relaxation. This means that capacitive and charge transport effects occur even after structural motions of the fibrils have reached equilibrium. These findings are crucial for their integration into composite materials and as sensors in composite structures. Finally, this research extends the application of CNTYs into structural health monitoring (SHM), wherein an array of CNTYs is integrated into laminated composite panels made of E-glass fiber weaves and vinyl ester resin. The SHM technique used herein proved the effectiveness of CNTYs in detecting and localizing damage in the panels under monotonic and cyclic compression loading, which correlated well with digital image correlation measurements. These results indicate that CNTYs hold remarkable promises for SHM, offering real-time feedback on damage detection, which can significantly improve safety and reliability across diverse composite industries.

## Research objectives

The aim of this research is to investigate the electromechanical response of twisted carbon nanotube yarns to mechanical loading in three hierarchical scales, viz. as individual yarns, as a single filament embedded in a thermosetting matrix, and as part of laminated composites made of glass fiber weaves and a thermosetting resin.

The specific objectives are:

- To characterize the electromechanical and physicochemical properties of carbon nanotube yarns.
- To investigate the electrical response of carbon nanotube yarns subjected to thermo-mechanical stimuli.
- To investigate the property-structure relationships of carbon nanotube yarns subjected to mechanical stimuli using a micromechanical model.
- To investigate the electromechanical response of individual carbon nanotube yarns embedded in thermosetting resins.
- To investigate the electrical response of carbon nanotube yarns as part of a glass fiber weave/vinyl ester laminated composite subjected to compression loading, implementing an algorithm for its proper data reduction.
- To assess the structural health monitoring potential of a carbon nanotube yarn array in a glass fiber weave/vinyl ester composite under cyclic compression loading.

# Outline of the research

This work delves into the investigation of the electromechanical response of carbon nanotube yarns (CNTYs) under mechanical loading in three hierarchical scales, viz. as individual yarns, as a single yarn embedded in a vinyl ester resin (VER) matrix, and as part of laminated composite panels made of E-glass fiber weaves (GFWs) and VER. The research is divided into three main stages, as outlined in Fig. 1. Most of the experiments and model development were carried out at “Centro de Investigación Científica de Yucatán” (CICY). Some experiments were conducted at “Uppsala Universitet” (UU) during a six-month research stay, as indicated.

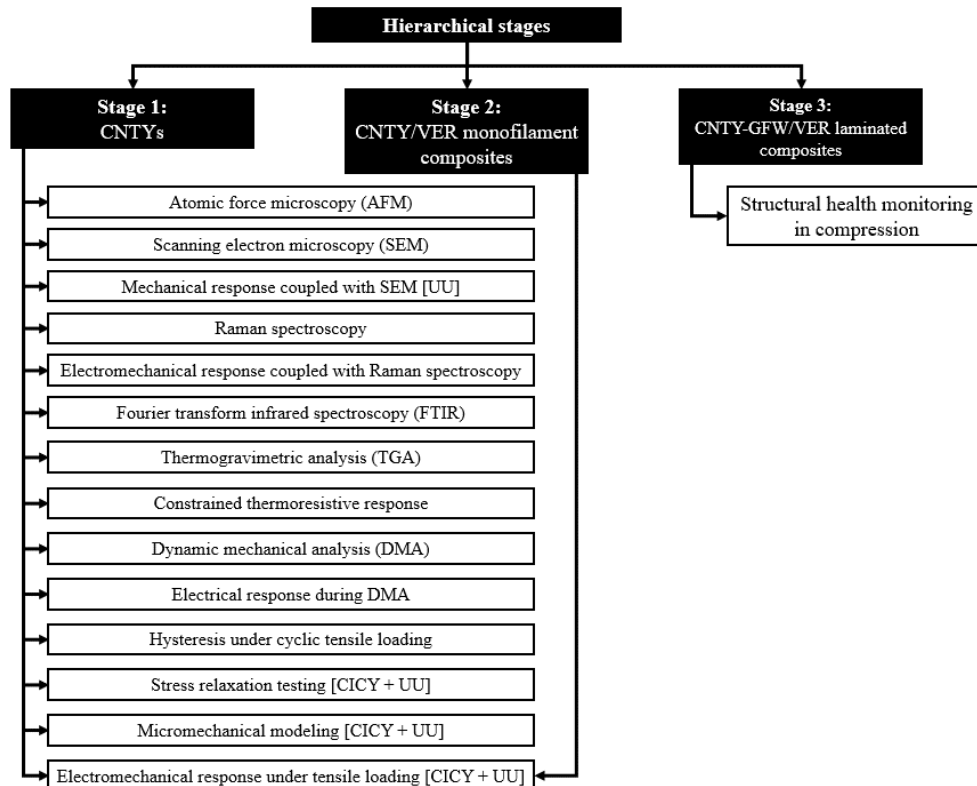
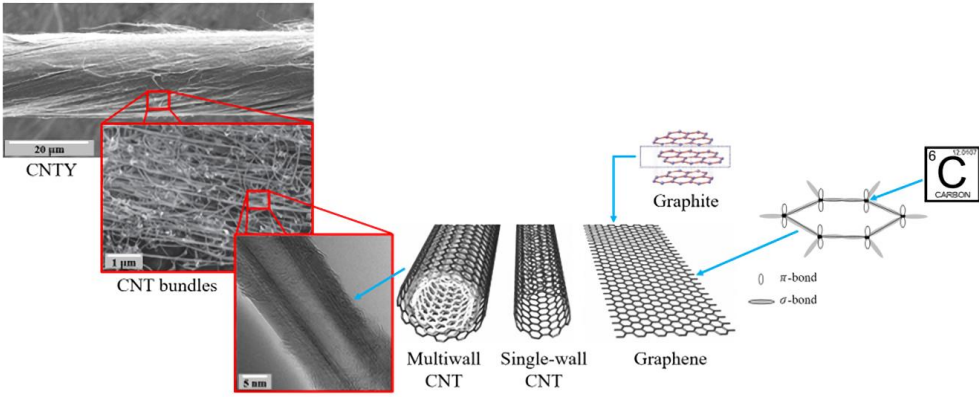
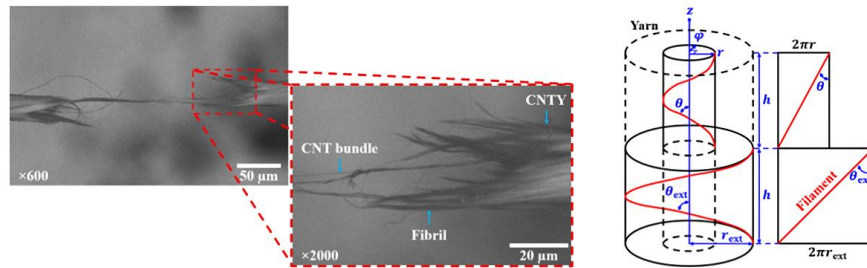
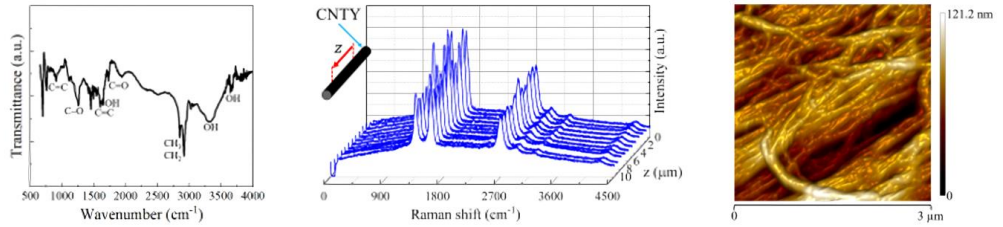


**Fig. 1.** Outline of the research.

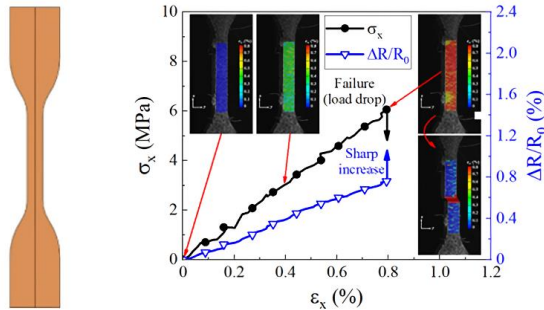
The first stage focuses on the physical and chemical characterization of CNTYs, along with the investigation of their structure-property relationship to understanding the fundamental concepts behind the mechanical and electrical properties of CNTYs. This understanding is essential for designing and developing new high-performance materials with structural health monitoring capabilities. The second stage focuses on the electromechanical characterization of monofilament composites, wherein a single CNTY was embedded into VER to study their electrical behavior for SHM applications. Finally, the third stage focused on the development and validation of a technique to monitor the structural health of the GFW/VER laminated composite panels using CNTYs. The overview of the research is presented in Fig. 2.



Characterization of individual CNTYs



Study of CNTYs in monofilament composites



Evaluation of CNTYs for structural health monitoring of laminated composites panels

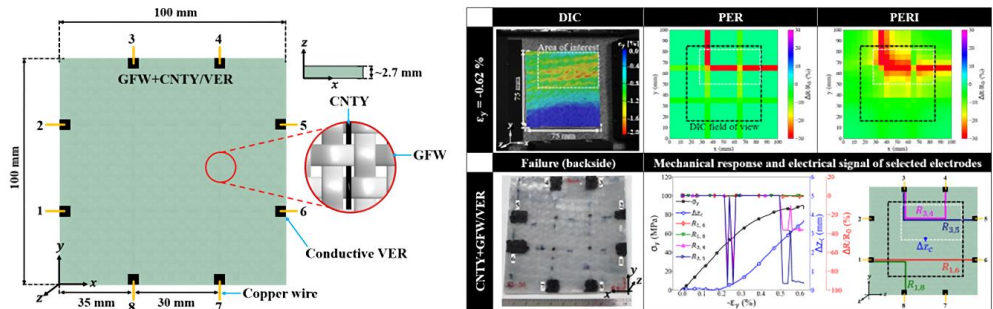
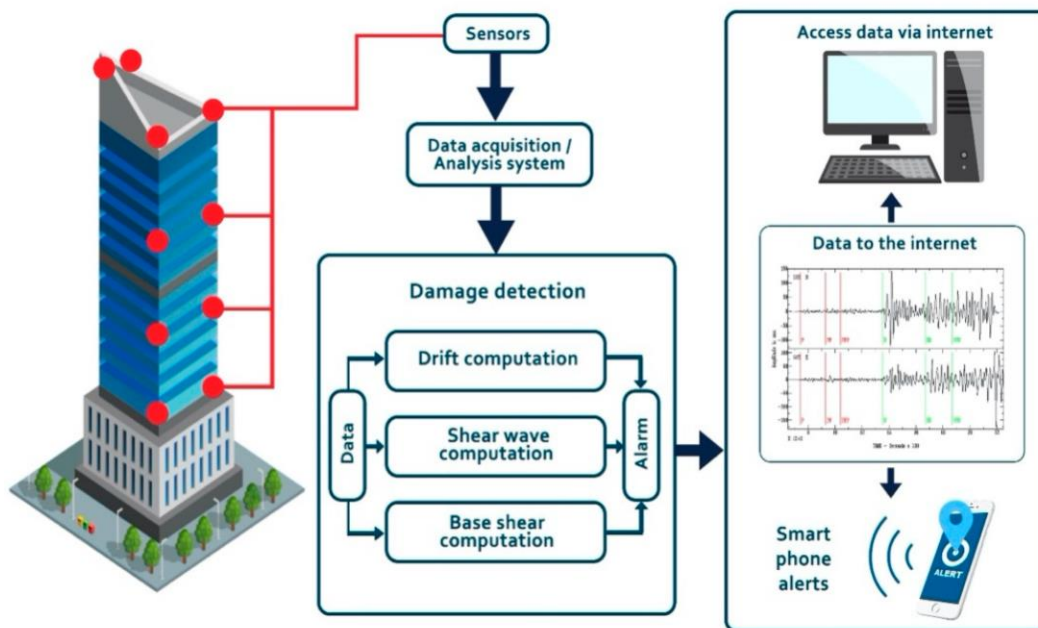


Fig. 2. Overview of the research.

## Introduction

Fiber-reinforced composite materials have been used in various industries including automotive, aircraft, naval, and energy, due to their enhanced properties, which result in reduced weight and increased resistance to extreme conditions. Nevertheless, composites are not immune to wear, corrosion, and degradation. It is often challenging or even impossible to detect when a fiber-reinforced composite material has undergone damage. This is why routine preventive maintenance is conducted for all vehicles and structures. However, unnecessary maintenance can lead to financial waste. Additionally, if such maintenance is not carefully planned, it can result in worse scenarios, such as catastrophic failure of the material. One effective strategy for optimizing this process is the implementation of condition-based maintenance, whereby maintenance is performed only when necessary. This approach involves the continuous monitoring of the real-time structural health of the materials in question. For instance, Fig. 3 depicts the concept of structural health monitoring (SHM) applied to a building [1]. Intelligent materials possessing sensory properties, such as piezoresistivity [2–4] or thermoresistivity [5–7], play a pivotal role in enabling this proactive maintenance strategy. These materials allow structural health monitoring while preserving similar or even superior physical and chemical properties.



**Fig. 3.** Intelligent structural health monitoring concept applied to a building. Extracted from [1].

Polymer composites are attractive materials for the fabrication of smart structural composites [8]. One of the most promising materials to create polymeric composites with SHM capabilities are

carbon nanotubes (CNTs). CNT-based polymeric nanocomposites have successfully demonstrated their use as sensors for strain [2,4,8], temperature [5–7], and various other complex applications, including structural damage detection [9–12]. However, in the particular case of CNT-based nanocomposites, one of the biggest current challenges is their individual dispersion and scaling up for industrial processing. A possible solution to this problem can be the use of CNT yarns (CNTYs), which are twisted fibers made of millions of CNT bundles (groups of interlocking CNTs bonded by van der Waals forces) [13,14]. Hypothetically, CNTYs could reach properties those of the CNTs, which make them very attractive for structural composites. Their outstanding electrical conductivity and multifunctionality makes them suitable for more interesting applications [14–16]. Polymer composites made with CNTYs have been initially tested with very good results in SHM applications [17–20]. Despite this, the study of CNTYs for SHM is yet in its early stages, rendering opportunities for developing new smart structural composite materials. Given this motivation, this work studies the physical, chemical, and electromechanical behaviors exhibited by CNTYs. Then the electrical response of such CNTYs as part of monofilament composites under tensile mechanical loading is investigated. Finally, the capabilities of CNTYs for SHM of laminated composites panels are evaluated, where the yarns are non-invasively integrated into the composites. The integration of the results at all dimensional scales assists in advancing the understanding of property-structure relationships of CNTYs and their fiber-reinforced structural composite materials.

# Chapter 1. Background

## 1.1. Carbon nanotube yarns

Carbon nanotubes (CNTs) are a form of carbon allotropes characterized by a cylindrical structure composed of  $sp^2$  hybridized carbon atoms arranged in a hexagonal lattice [21,22]. Conceptually, CNTs can be visualized as rolled-up sheets of graphene, which consists of a single layer of carbon atoms arranged in a two-dimensional (2D) honeycomb lattice [23,24], as shown in Fig. 1.1. Since the discovery of CNTs [25], they have been widely studied due to their outstanding thermal, electrical, and mechanical properties, as well as their response to interrelated stimuli (thermoelectrical, electromechanical, and thermo-electromechanical). Moreover, CNTs find utility in producing macroscopic carbon assemblies such as CNT arrays [24], films [26], and CNTYs [27].

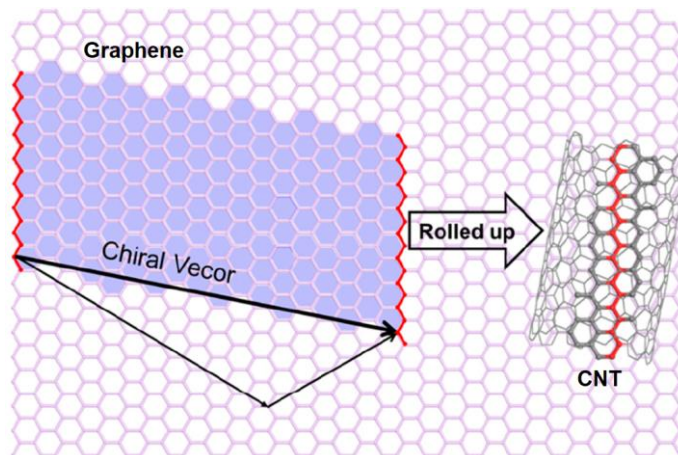


**Fig. 1.1.** Conceptual view of a CNT as a graphene sheet rolled along a chiral vector. Modified from [24].

It is important to point out that the term “CNT yarn” is sometimes used interchangeably with “CNT fiber” in literature, but this may be inaccurate. The main difference between a fiber and a yarn is that a fiber is a single strand, while a yarn is a twisted group of fibers [28]. Therefore, a CNT fiber refers to assemblies where the CNTs are only structured in bundles (groups of CNTs held together by van der Waals forces). A CNTY, on the other hand, refers to assemblies where the CNTs are grouped into bundles, which are entangled, forming fibrils or fibers that make up the yarn [14,16,27,29–32], as shown in Fig. 1.2. This hierarchical structure of the CNTYs renders a very strong property-structure relationship [14,16,27,29–32]. Because of this characteristic, CNTYs find applications across a wide range of fields, such as energy generation/storage [33,34], biomedical applications [35,36], advanced materials [37–39], and multifunctional materials [40,41].

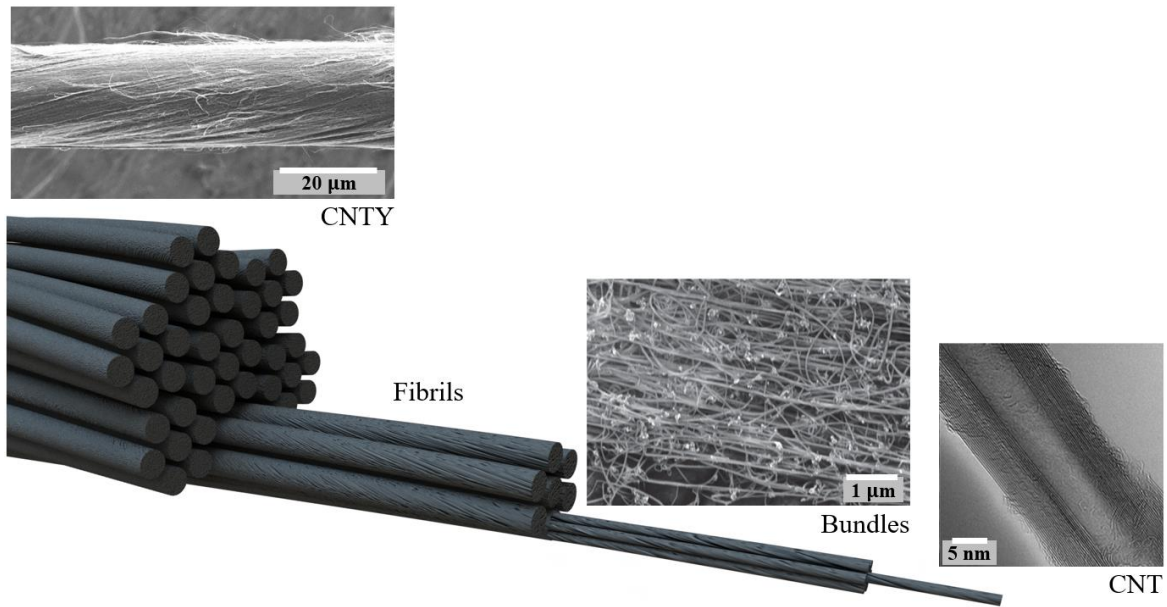


**Fig. 1.2.** Hierarchical structure of a CNTY. Individual scanning electron microscopy images were obtained from [2,13,14].

### 1.1.1. Methods of production

CNTYs can be synthesized by solution state (wet) spinning or solid state (dry) spinning [16,27,42]. In the wet spinning method, the pre-synthesized CNTs are dispersed in surfactant or acidic solvents [16,27,42,43]. Then, the CNT solution is injected through a spinneret into a tank of coagulant solution, as shown in Fig. 1.3. The CNTY is formed as the CNTs pass through the spinneret. The CNTY is subsequently pulled out from the coagulation tank, stretched, and finally collected onto a spool.

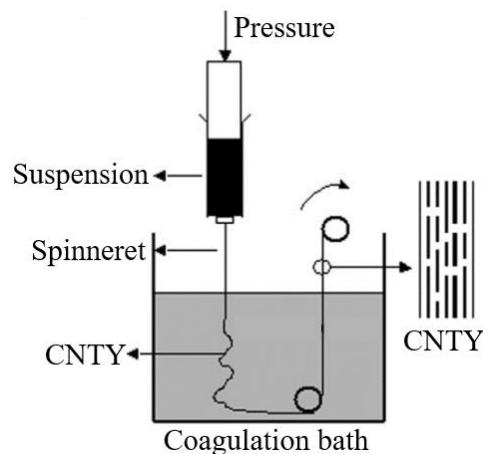


**Fig. 1.3.** Schematic of the wet spinning method. Extracted from [43].

The dry spinning method includes spinning from a vertically aligned CNT array previously grown on a substrate (Fig. 1.4a) [29,44–46], spinning from a CNT aerogel formed in a chemical vapor

deposition (CVD) reactor [47–49], and twisting/rolling from a CNT film [50]. Spinning from a CNT forest comprises two steps, growth of the CNT forest, and drawing from the CNT forest [29,44–46]. Thermal CVD is used to produce spinnable CNT forests, which are grown on flat substrates. A reaction furnace with flowing gaseous carbon feedstock in presence of catalyst on a silicon wafer substrate is used to grow the aligned CNTs. A layer of catalyst particles, e.g., Fe/Al<sub>2</sub>O<sub>3</sub>, is deposited on the silicon wafer, using carrier gas, for example helium, and a carbon source, such as acetylene or ethylene. It is necessary to obtain a high level of CNT alignment in the forest to form a continuous CNTY. Finally, the CNTs are pulled out from the CNT forest in CNT webs to form a continuous yarn, as shown in Fig. 1.4b. These CNT webs can be condensed either by using a solvent, mechanically through twisting or both. The twist is applied to improve the coherency (degree of packing) of the CNTYs [51,52]. The spinning from an aerogel of CNTs is considered a direct spinning method, which is capable of continuously producing CNTYs without length limitation [47–49]. In this process, the CNTs are synthesized in the vapor phase of a vertical reactor and form a porous cluster (carbon aerogel) similar to “cotton candy” [53]. The CNTs are continuously pulled out and twisted to draw a CNTY.

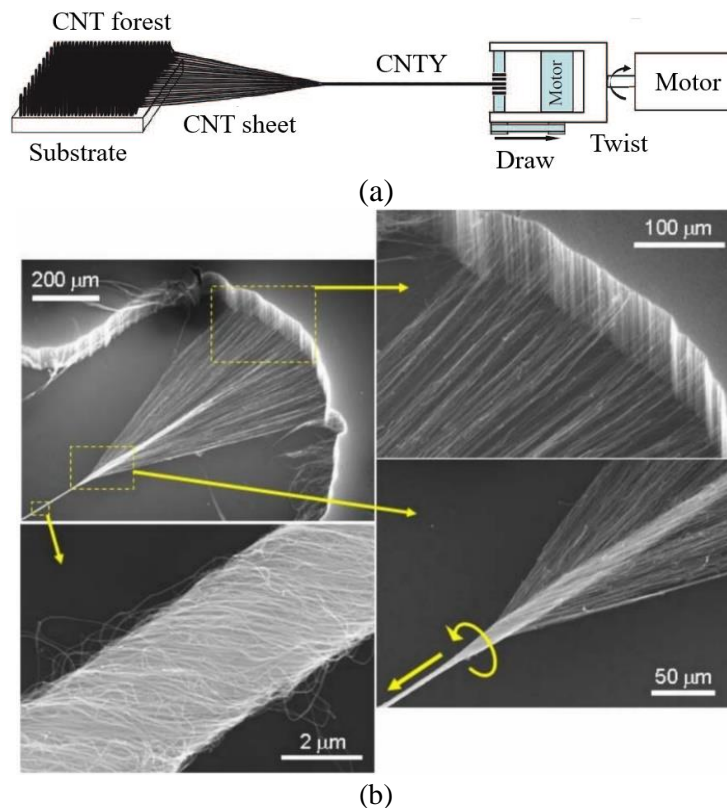


**Fig. 1.4.** Spun process of a CNTY from a CNT forest by the dry spinning method. (a) Schematic of the draw-twist process (extracted from [46]), (b) formation of a CNTY during the draw-twist process (extracted from [29]).

### *1.1.2. Hierarchy and mechanics of load transfer*

The hierarchical structure of the CNTYs (yarn, fibril, bundle, CNT, Fig. 1.2) results in a very strong relationship between their nano/microstructure and their resulting effective properties [14,16,27,29–32]. It is known that load transfer in a CNTY subjected to uniaxial tensile loading occurs hierarchically among its components. The axial load is transferred from the yarn to its fibrils, then from fibrils to the thinner CNT bundles comprising the fibrils, and finally from bundles to CNTs [14,27,32]. The load transfer from one CNT to another occurs through inter-tube interactions, such as van der Waals forces, friction, and entanglement [54–56]. However, the mechanical response of CNTYs is governed by the load transfer mechanisms that occurs at the fibril/bundle level [57]. Therefore, the mechanical response of CNTYs mainly depends on multiple structural parameters, such as twist angle (the angle formed between the direction of twist and the yarn's axial direction) [51,52], porosity (the volume of voids divided by the yarn's total volume) [58], and packing density (the ratio of the total area of the fibrils to the yarn's cross-sectional area) [59]. The test length (gage length) [60] and strain rate [61] also impact the mechanical behavior of CNTYs. All these parameters influence the interaction between fibrils/bundles and hence the mechanical response of CNTYs. The slipping between fibrils/bundles is the main mechanism that influences the overall mechanical response of CNTYs, leading to the reorientation of fibrils/bundles and redistribution of stresses [14,27,32]. For instance, Jung et al. [62] observed that CNTYs can exhibit stretching, untwisting, and a reduction in diameter when subjected to tensile loading. They categorized this strain behavior into two stages of the specific strength vs. strain curve (Fig. 1.5). The strain behavior of the first stage was attributed to the straightening and untwisting of the CNT bundles/fibrils, resulting in a gradual stress increase with strain [62,63]. The second stage was attributed to the slippage of the fibrils/bundles as a result of weak van der Waals interactions [62,63]. The sliding friction generated during the bundle slippage, along with attaching/detaching and zipping/unzipping mechanisms, contributes to the yarn's energy dissipation ability [64–68]. The attaching/detaching mechanism refers to the separation and reconnection of CNTs or their bundles due to the interaction between intermolecular forces [68]. In this mechanism, when CNTs or bundles are separated, energy is released, which helps to dissipate the impact energy (damping). On the other hand, the zipping/unzipping mechanism refers to the sliding motion of CNTs or their bundles against each other due to the friction between them [69]. This friction also improves the damping performance of CNTY.

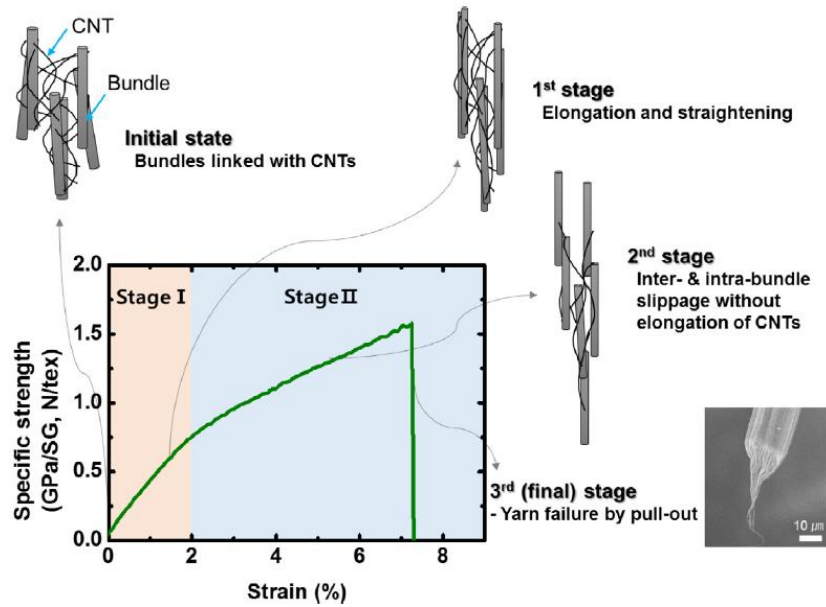


**Fig. 1.5.** Mechanical response of an aerogel-spun CNTY under uniaxial tensile loading ( $SG$  = specific gravity; 1 tex = 1 g/km). Extracted from [62].

Under uniaxial tensile loading, CNTYs experience a decrease in diameter [29,58]. The high porosity and structure of the CNTYs result in high radial contraction ratios. This phenomenon can be attributed to their porosity and structural characteristics, leading to significant radial contraction ratios [29,58], sometimes improperly referred to as “Poisson’s ratio”. This parameter has been reported with values as high as 8.0 for low twist yarns [58], whereas the thermodynamic limit of a continuous solid material is known to be 0.5 [70]. The radial contraction of the CNTYs reduces its porosity and increases its packing density [58]. During this process, the fibrils/bundles slip in the loading direction, which reduces the twist angle ( $\theta_{ext}$ ) [57,63]. The decrease in the initial twist angle ( $\theta_{ext_0}$ ) of a CNTY with increasing the axial strain ( $\epsilon_z$ ) is depicted in Fig. 1.6.

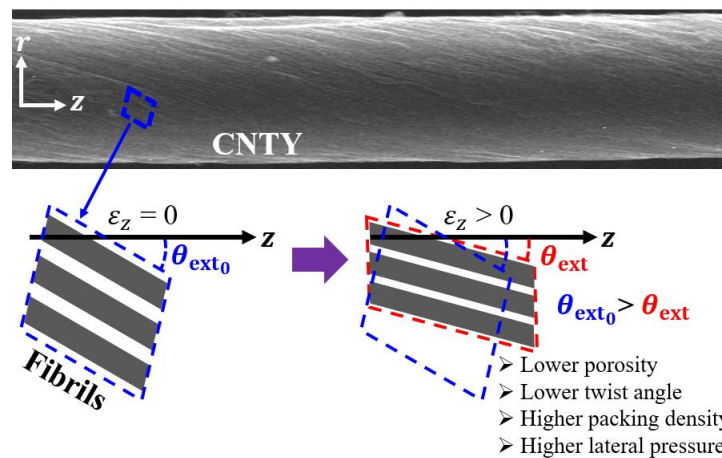


**Fig. 1.6.** Schematic depicting the change in twist angle ( $\theta_{ext}$ ) of a CNTY with increasing axial strain ( $\epsilon_z$ ).

The tensile mechanical strength of a CNTY is closely related to its coherence (the degree to which the fibrils are aligned and bonded together) and its obliquity (the angle between the fibrils and the longitudinal axis of the yarn) [51,52]. These parameters of CNTYs can be modified by twisting. The twist angle in a CNTY increases the packing density, enhancing its resistance to slippage through friction [52]. As the twist angle increases in a CNTY, the strength of such yarn also increases until reaching a maximum value, beyond which the strength decreases [28,52,71], as shown in Fig. 1.7. The twist angle at which a yarn exhibits maximum strength is called the optimum twist. For instance, Anike et al. [52] have found that this optimum twist is about  $30^\circ$  for dry-spun CNTYs with diameters ranging from  $43\ \mu\text{m}$  to  $57\ \mu\text{m}$  and porosity of 0.71–0.80.

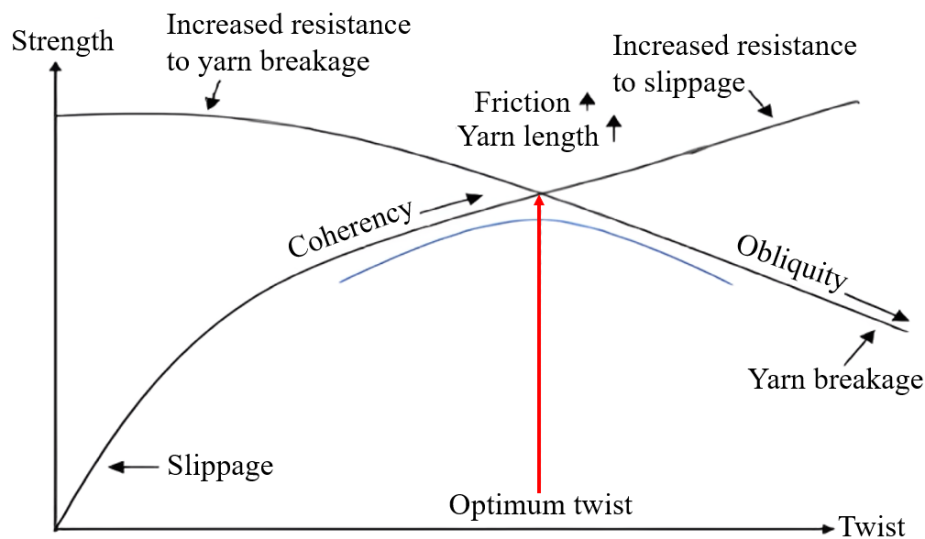


**Fig. 1.7.** Schematic of the strength-twist relationship for yarns. Extracted from [28,52].

Despite the tremendous progress that has been made in understanding the mechanics of CNTYs, there are still several challenges to fully comprehend and characterize their mechanical response and unravel their full scientific and technological potential. However, experimentally studying the relationship between the microstructure of the CNTYs and their mechanical response is often exceedingly challenging. For this reason, computational modeling is a useful tool for the study of CNTYs. Several models have been developed to study their mechanical response under uniaxial tensile loading [72–77]. For example, Vilatela et al. [73] employed an analytical model based on molecular dynamics to calculate the strength of untwisted CNTYs and their CNT bundles under axial tensile loading, using the structural and mechanical properties of their constituent CNTs. They modeled the CNTY as a collection of parallel, rigid rod elements capable of sliding relative to each other, with the tensile stress applied to either end of the yarn. According to this model, the CNT

length and shear strength between CNTs are key parameters that affect the tensile strength of CNTYs. Additionally, they found that the strength of CNTYs also depend on the strength of the network of bundles. In another work, Wei et al. [74] developed a Monte Carlo model that incorporates statistical variation in CNTY strength and a shear load transfer law to simulate interactions between adjacent fibrils. The model's predictions align well with experimental measurements, achieving standard deviations that are smaller than the observed experimental values. They attribute this difference to the simplified nature of the model, which does not account for complexities such as fibril misalignment, entanglement, and waviness. Pirmoz et al. [77] proposed a sequential multiscale finite element model to predict the stress-strain response of CNTYs, considering the randomness of the CNTY structure by the Monte Carlo method. The first step involved a nanoscale model of CNTs comprising bundles; the second step included a mesoscale model of bundles comprising fibrils, while the third step encompassed a microscale model of twisted fibrils comprising the CNTY. This model did not consider slippage and was able to capture the nonlinear tensile mechanical response of the CNTYs by calibrating the elastic properties of their constituent fibrils. These examples demonstrate that the success of predictive models largely depends on the accuracy of the structural and mechanical properties of the CNTY constituents used as input parameters. In addition, they highlight the importance of considering a statistical distribution of these parameters. This randomness makes the true mechanical response of CNTYs a stochastic process. All these structural characteristics and mechanisms also impact the thermal and electrical properties of the CNTYs.

### *1.1.3. Electrical, mechanical, and piezoresistive properties*

CNTs have outstanding thermal, electrical, and mechanical properties, as summarized in Table 1.1. In an ideal scenario, these properties would be inherited by the CNTYs. However, the properties of the CNTYs are lower than those of their individual components, as shown in Table 1.1. This discrepancy arises from the discontinuous hierarchical structure of CNTYs (Fig. 1.2). Thus, the physical properties of the CNTYs depend not only on the CNTs comprising the yarn, but also on the interactions among them and the structural characteristics of the yarn. This is not necessarily a disadvantage, as this structure-property relationship gives rise to exceptional coupled properties, such as electromechanical or thermoelectrical.

**Table 1.1.** Selected properties of CNTs and CNTYs.

Property	CNTs	CNTYs
Elastic modulus [GPa]	100–1800 [8,21,22,78–80]	0.10–397 [14,16,52,81]
Tensile strength [GPa]	11.0–71.0 [82,83]	0.04–8.80 [14,16,52,53,81]
Density [g/cm <sup>3</sup> ]	1.33–2.60 [21,79,84]	0.35–1.55 [52,58,81]
Electrical conductivity [S/m]	10 <sup>2</sup> –10 <sup>7</sup> [14,79,85]	0.10–10 <sup>5</sup> [14–16,53,81]
Thermal conductivity [W/(m·K)]	1750–6000 [14,22,79,86–88]	5.0–80 [14,16]

Porosity plays a crucial role in the thermal, electrical, and mechanical response of CNTYs. The high number of CNTs and CNT-to-CNT contact points present in CNTYs with low porosity allows improved electron transport and, therefore, better electrical conductivity. The porosity of the CNTYs can be controlled during the manufacturing process, through the yarn twist angle [15,52]. The relationship between these parameters (Fig. 1.8a) has been investigated by Miao [15] using dry-spun CNTY made of multiwall CNTs with ~4.0 nm inner diameter, ~10 nm outer diameter, and 350 μm length. The electrical conductivity of the CNTYs is highly dependent on their relative density or porosity, as shown in Fig. 1.8b [15].

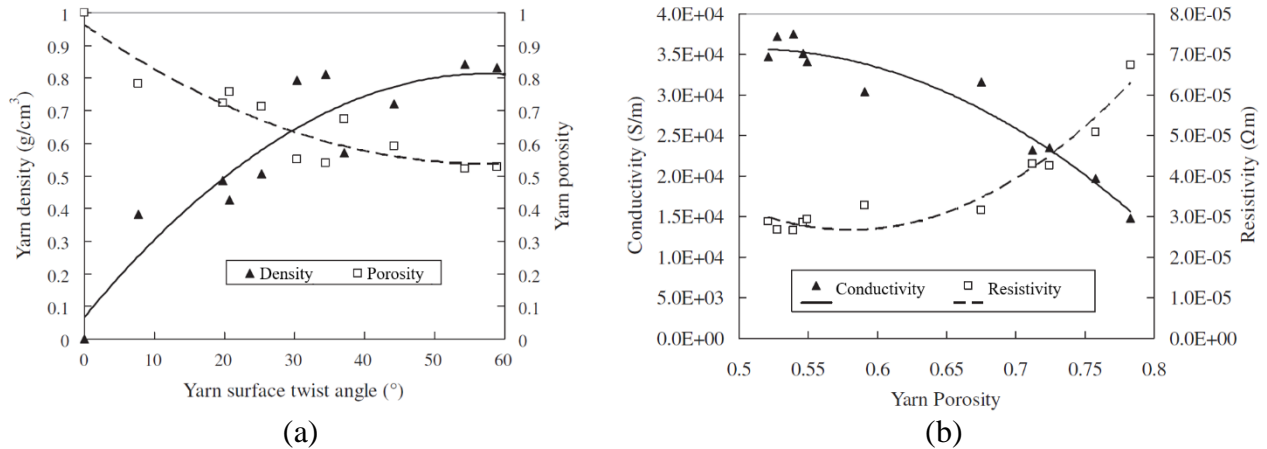


**Fig. 1.8.** Effects of porosity in a dry-spun CNTY (extracted from [15]). (a) Effect of yarn surface twist angle on the yarn density and porosity, (b) effect of yarn porosity on the electrical conductivity and resistivity.

The relationship between twist angle, porosity, and electrical conductivity gives CNTYs an electrical response that depends on strain [52,63,89]. This electromechanical response is commonly

expressed as the fractional change in electrical resistance ( $\Delta R/R_0$ ), which is the ratio between the change in electrical resistance ( $\Delta R$ ) and the reference (initial, unloaded) electrical resistance ( $R_0$ ). CNTYs can exhibit piezoresistive properties, as they recover their initial electrical resistance when the load is removed, provided they have not been loaded to the point of experiencing irreversible structural strain or damage. In this coupling phenomenon, the electrical resistance depends on the strain response of the CNTY [52,90,91]. Anike et al. [52,90,91] have hypothesized that there are two physical phenomena governing the piezoresistive response of CNTYs. The first phenomenon occurs when the CNTY is stretched during loading, generating a decrease in contact length of the CNT bundles, and therefore, an increase in its electrical resistance. The second phenomenon occurs when the CNTY relaxes during the loading segments, presenting inter-CNTs/inter-bundles slippage, and therefore, a decrease in its electrical resistance. When a CNTY is subjected to uniaxial tensile loading and experiences irreversible strain, its electrical resistance typically increases with increased axial strain. This increase in resistance is primarily due to the decreased contact length of the fibrils/bundles during stretching [52,90,91]. Simultaneously, an increase in contact area occurs among the fibrils/bundles due to the radial contraction-induced increase in packing density, resulting in a decrease in the electrical resistance of the CNTY [52,90,91]. These competing phenomena govern the electrical response of CNTYs. It is important to note that these phenomena are highly dependent on the yarn's structure, as depicted in Fig. 1.9a [52]. Since CNTYs show strong property-structure relationships, there is no universal behavior for their electromechanical response. The electromechanical response of CNTYs depends not only on the strain level but also on the strain rate, as shown in Fig. 1.9b [91].

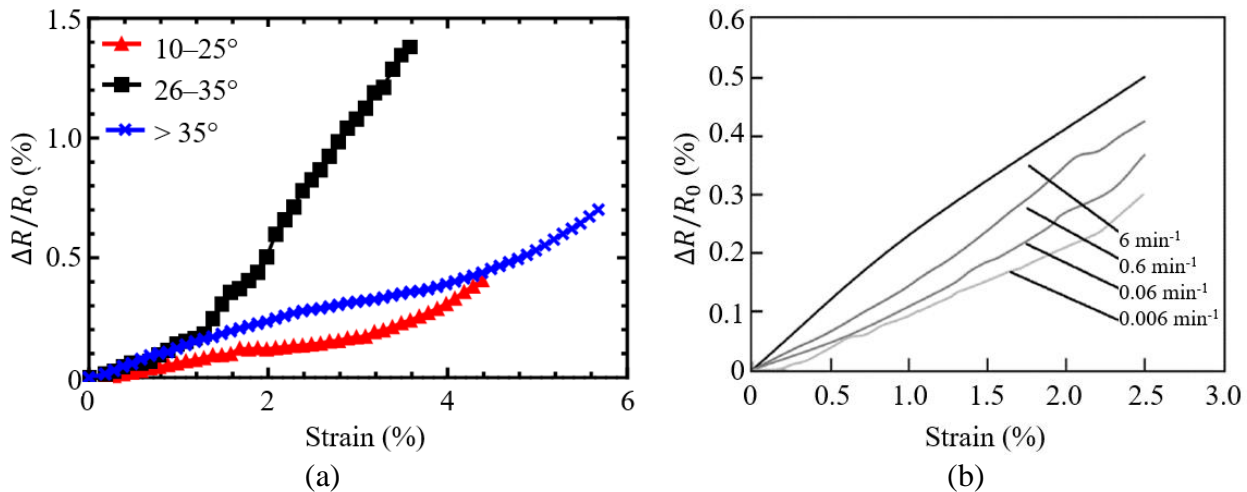


**Fig. 1.9.** Electrical response of CNTYs under uniaxial tensile loading. **(a)** Effect of twist level (extracted from [52]), **(b)** effect of strain rate (extracted from [91]).

#### 1.1.4. Applications

CNTYs have generated substantial attention in the field of materials science due to their extraordinary thermal, electrical, and mechanical, making them promising candidates for a wide range of applications. For example, CNTYs have shown promising results in energy generation and storage applications [33,34,41]. In this context, CNTYs have been integrated into energy-harvesting textiles, serving as self-powered solid-state strain sensors used for monitoring breathing [34], as illustrated in Fig. 1.10a. The biomedical field has also greatly benefited from the unique properties of CNTYs [35,36]. They have been proposed for use as electrodes in deep brain stimulation [35], a neurosurgical procedure involving implanted electrodes and electrical stimulation to treat neurological conditions. Furthermore, CNTYs have been employed as strain sensors to monitor human motion [34,36]. CNTYs can be used to monitor liquid or polymer flow, exothermic reactions, and resin curing kinetics by measuring the change in electrical resistance of the CNTYs [13,92,93]. These capabilities make CNTYs valuable for applications in materials science and manufacturing. In addition, CNTYs have found utility in the development of advanced and smart materials [17,37–39,94–97]. CNTYs have also been proposed as reinforced for pressure vessels and aerospace structures due to their high strength-to-weight ratio and multifunctionality [98,99]. CNTYs are of particular interest for actuators (see [37–39]) and structural health monitoring applications [17,94–97] due to their high specific (per unit weight) mechanical properties and their responsiveness to external stimuli. For instance, CNTYs can be employed as artificial muscles, as demonstrated in Fig. 1.10b.

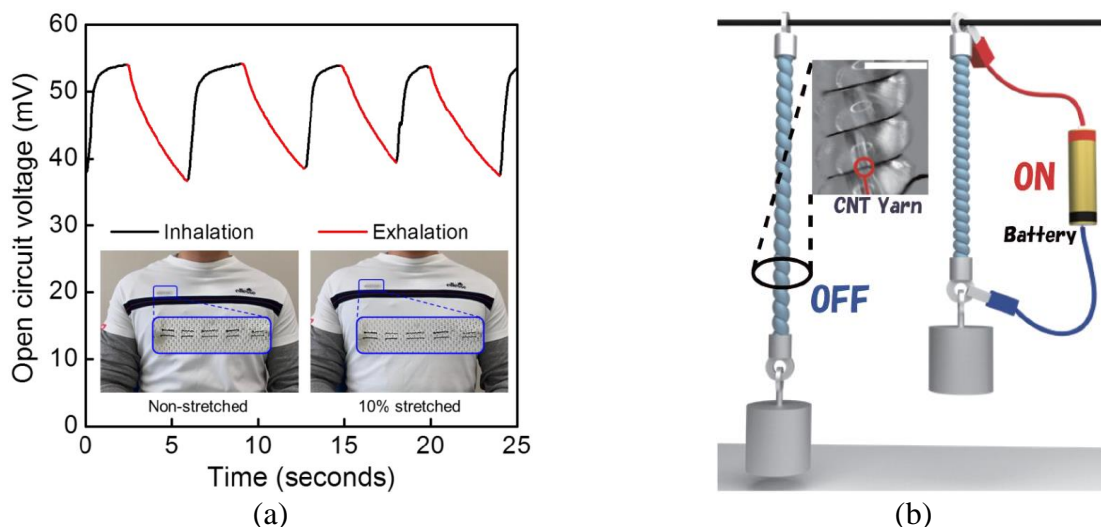


**Fig. 1.10.** Applications of CNTYs. (a) Self-powered twistron strain sensor woven into a shirt and used for monitoring breathing (extracted from [34]), (b) polymer soft-actuator composed of polymer threads and CNTYs (extracted from [38]).

## 1.2. Carbon nanotube yarns for structural health monitoring

Structural health monitoring (SHM) is the process of collecting and analyzing data from a material to assess its condition [100]. This data can be used to detect damage, identify changes in the structure's behavior, and predict its remaining service life. SHM can be applied in various fields, including aerospace, automotive, construction, and more. It is particularly useful for structures that are exposed to harsh environments or are subjected to high loads. In this context, CNTYs are ideal for SHM due to their high sensitivity to changes in strain and temperature, damping properties, flexibility, and lightweight nature. For this purpose, CNTYs can be integrated into composites as a 2D array, where the CNTYs are positioned in rows and columns, forming a grid. This integration allows for SHM of materials by measuring the electrical response of the CNTY array. For example, Song et al. [94] used a  $12 \times 12$  CNTY array to monitor structural damage on  $200 \times 200 \times 2.4$  mm<sup>3</sup> composite panels made of IM7/977-3 (carbon fiber/epoxy) prepreg under impact testing. The CNTY were bonded with epoxy resin onto the composites. The CNTY were organized into groups of three per side, with one end connected to a Wheatstone bridge circuit and the other end connected to a common ground, as shown in Fig. 1.11a. A time-division multiplexing method was used to establish connections between each electrode of the rows (longitudinal direction,  $x$ ) and each electrode of the columns (transverse direction,  $y$ ). This configuration allowed the authors to monitor strain distribution and determine damage location on the IM7/977-3 panels by observing changes in electrical resistance of the CNTY grid. They observed an increment in electrical resistance after the impact, with the effect being more pronounced in the impacted area, as shown in Fig. 1.11b.

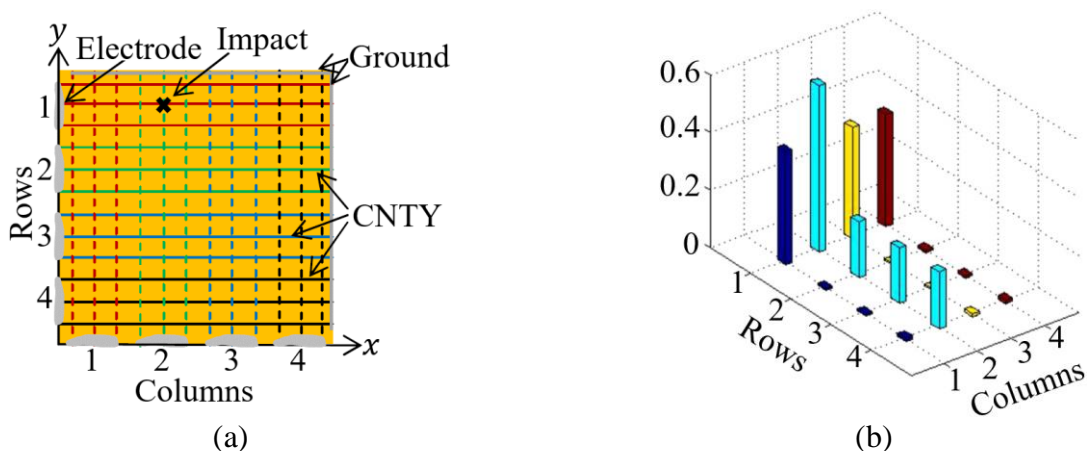


**Fig. 1.11.** Use of a CNTY 2D array (grid) for SHM in IM7/977-3 composite panels (extracted from [94]). (a) Schematic of connections of the  $12 \times 12$  CNTY array, (b) normalized change in electrical resistance of the CNTY grid after impact.

In a different work, Abot et al. [17] embedded CNTYs into laminated composites to monitor damage and delamination. In this case, the CNTYs were arranged in different configurations to sense damage (in-plane strains) and delamination (out-of-plane strains), as shown in Fig. 1.12a. Specimens were tested under three-point bending. Delamination in the composites was identified by a significant peak in the electrical resistance of the CNTYs, as shown in Fig. 1.12b.

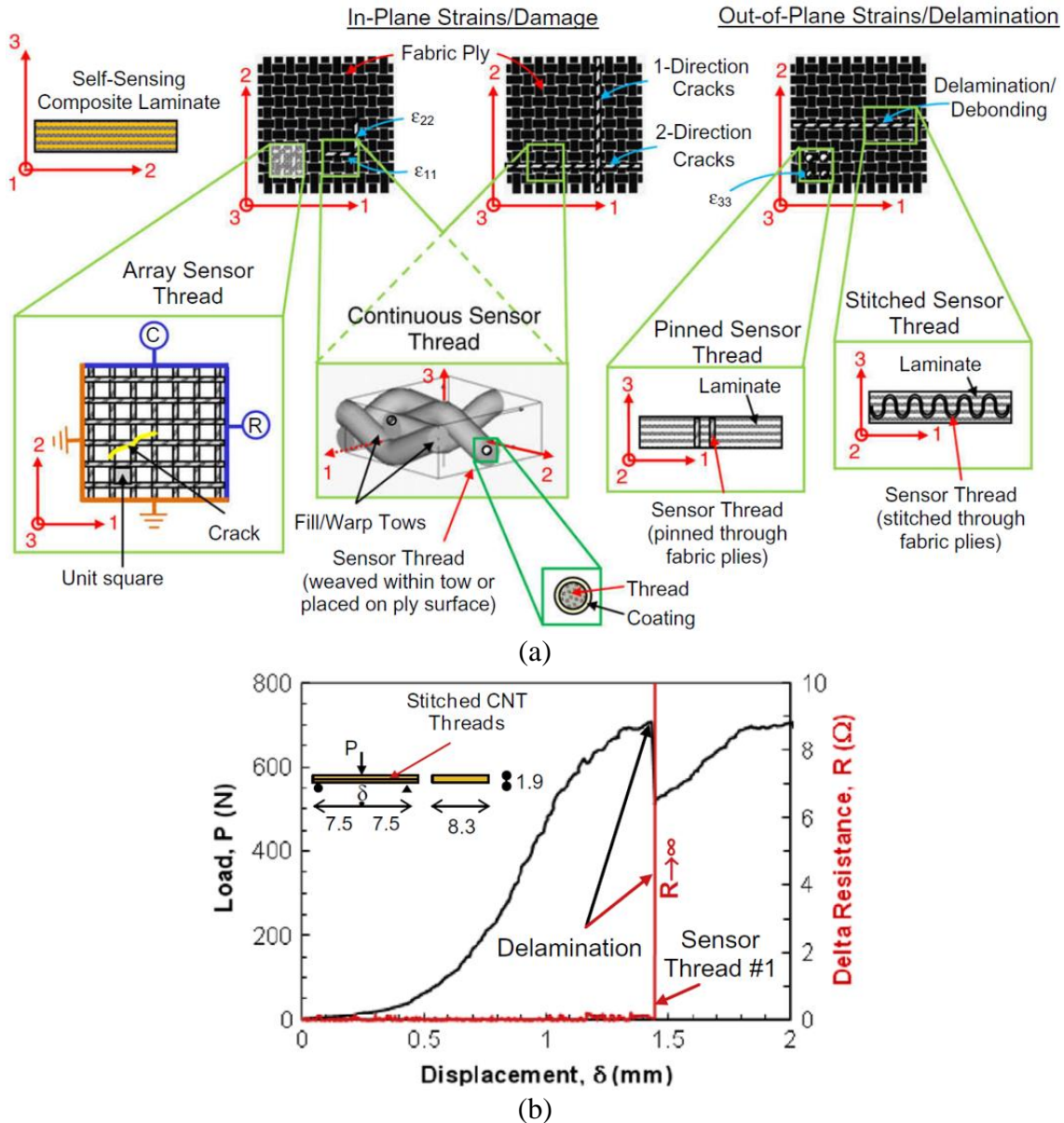


**Fig. 1.12.** Delamination detection in laminated composites using CNTYs (extracted from [17]).  
**(a)** Schematic of the CNTYs configuration, **(b)** electromechanical response.

Using a different approach, Jia and Wan [97] embedded CNTY sensors in three-dimensional (3D) braided composites to detect internal damage and enhance structural health monitoring. Signals from the CNTYs were processed using the dynamic wavelet threshold algorithm to locate damage.

Damage location was estimated based on changes in CNTY resistance, and the quadratic matrix singular value decomposition algorithm simplified data, providing high positioning accuracy with a coordinate error under 1 mm. This work also highlights the significance of the algorithm in accurately determining the location of structural damage when analyzing data from CNTY arrays. All these results demonstrate the effectiveness of CNTYs in detecting delamination and debonding in laminated composite materials without compromising the integrity of the material. They also indicate that the field is not yet fully explored, and there exist research opportunities. Scaling the technique to larger panels is yet a challenge, along with the electrical signal handling, post-processing and on-line distributing. The study of the CNTY electrical response under different loading scenarios is also still very shallowly explored. While it is known that the electrical response of the CNTYs is strongly dependent on their structural changes, there are mechanisms that have not been thoroughly studied. Therefore, understanding the fundamental concepts behind the mechanical and electrical properties of CNTYs is essential for designing and developing new high-performance materials with structural health monitoring capabilities.

## Chapter 2. Materials and methods

### 2.1. Materials

The CNTYs were dry-spun from 500  $\mu\text{m}$ -high vertically aligned CNT arrays grown using water-assisted CVD [45,101]. According to the manufacturer (University of Cincinnati, Cincinnati, USA), the CNTs have two to three walls and outer diameter ranging from 9 to 12 nm [45,101].

A Derakane 470-300 vinyl ester resin (VER) from Ashland (Ashland Inc., Wilmington, USA) was used as polymeric matrix for monofilament composites and laminated composite panels. Cobalt naphthenate with a 6 % volume concentration (vol.%) of active cobalt, and peroxide methyl ethyl ketone with 9 vol.% of active oxygen, both from “Plastiformas de México” (Plastiformas de México S.A. de C.V., Monterrey, Mexico), were used as the polymerization promotor and initiator, respectively. Additionally, a commercial E-type glass fiber weave (GFW) from “Plastiformas de México” was used to manufacture the laminated composite panels.

### 2.2. Characterization of carbon nanotube yarns

#### 2.2.1. Atomic force and scanning electron microscopy

The CNTYs were morphologically characterized using atomic force microscopy (AFM) with a Bruker SPM-8 instrument (Bruker, Kontich, Belgium). Different sections of  $5\times 5\ \mu\text{m}^2$  and  $10\times 10\ \mu\text{m}^2$  of the CNTYs were scanned, using tapping mode (dynamic contact mode) in air. Surface roughness was measured in sub-areas of  $5\times 5\ \mu\text{m}^2$  within the  $10\times 10\ \mu\text{m}^2$  AFM images using the NanoScope Analysis 1.5 software from Bruker. The roughness is reported as the root mean square average of 24 measurements, acquired from six AFM images of three different sections (samples) of the CNTYs (four measurements per image, two images for sample). Furthermore, the diameter of the constituent CNT fibrils comprising the CNTY was digitally measured in the  $5\times 5\ \mu\text{m}^2$  AFM images using the image processor software Image-J from the National Institutes of Health (Bethesda, USA). A total of 100 diameter measurements were obtained from 32 images of four different samples of the CNTYs.

Scanning electron microscopy (SEM) was carried out using a JEOL JSOL-6360-LV microscope (JEOL Ltd., Tokyo, Japan). SEM images were obtained from the longitudinal section of the CNTYs with magnifications of  $500\times$  and acceleration voltages of 20–25 kV. In order to construct a statistical diameter distribution of the CNTYs, a total of 480 values of diameter were digitally

measured from four samples (20 measurements per SEM image and six images per sample) using the Image-J software.

The diameters of both the CNTY ( $d_{\text{ext}}$ ) and their fibrils ( $d_f$ ) are reported as the mean value derived from the best fit statistical distribution. The distribution was chosen based on the results of the Anderson-Darling goodness-of-fit test [102]. The statistical distribution models considered in the analysis included normal, lognormal, 3-parameter lognormal, exponential, parameter exponential, Weibull, 3-parameter Weibull, smallest extreme value, largest extreme value, gamma, 3-parameter gamma, logistic, loglogistic, and 3-parameter loglogistic. The statistical analysis of the data was conducted using the Minitab Software (Minitab LLC, State College, USA).

### 2.2.2. Measurement of linear density and porosity

Four segments of the CNTYs with different lengths (6, 12, 18, and 24 cm) were cut and weighed on the microbalance (0.1  $\mu\text{g}$  resolution) of a PerkinElmer TGA 7 thermogravimetric analyzer (PerkinElmer Inc., Waltham, USA). The smallest CNTY length used was 6 cm, in order to allow sufficient mass in the microbalance. To guarantee uniformity in length between samples and prevent buckling of the fibers, the CNTYs were slightly preloaded using an in-house fixture by attaching a 75 mg mass (fragment of a needle) at the end of the fiber.

The lineal density of the CNTYs ( $\rho_L$ ) is defined as,

$$\rho_L = \frac{m}{L} \quad (2.1)$$

where  $m$  and  $L$  are the mass and length of the CNTYs, respectively. The reported value of linear density is the linear fit (slope, with the intercept set to zero) of the measured mass values for each length. In addition, the porosity of the CNTYs ( $\Phi_p$ ) was estimated by [52,84],

$$\Phi_p = 1 - \frac{\rho}{\rho_{\text{CNT}}} \quad (2.2)$$

where  $\rho$  is the density of the CNTYs, and  $\rho_{\text{CNT}}$  is the volumetric mass density of the CNTs that make up the CNTYs ( $\rho_{\text{CNT}} = 2.10 \text{ g/cm}^3$  [84,103]). The value of  $\rho$  was obtained by dividing  $\rho_L$  by the cross-sectional area of the CNTYs (using the mean diameter of the statistical distribution, see section 3.1.1), while  $\rho_{\text{CNT}}$  was calculated as [104],

$$\rho_{\text{CNT}} = \frac{4}{1315000} \left[ \frac{n}{d_{\text{Out}}} - \frac{2d_{s-s} \sum_{i=0}^{n-1} i}{d_{\text{Out}}^2} \right] \quad (2.3)$$

where  $n$  is the number of CNT walls,  $d_{S-S}$  is the inter-shell distance of the CNTs ( $d_{S-S} = 0.34$  nm) and  $d_{Out}$  is the outer diameter of the CNTs. In this case,  $n = 3$  and  $d_{Out} = 11$  nm were used since they were the most frequently observed values.

### 2.2.3. *Fourier-transform infrared spectroscopy*

Fourier transform infrared spectroscopy (FTIR) was used to identify the chemical composition of the CNTYs. The FTIR was carried out using a Thermo Fisher Scientific Nicolet 8700 FTIR Spectrometer (Thermo Fisher Scientific Inc., Wilmington, USA), in a spectral range of 650–4000  $\text{cm}^{-1}$  at 200 scans per spectrum and resolution of 8.0  $\text{cm}^{-1}$ . An 18 cm long CNTY was spirally wound to form a disk and then placed in the Nicolet 8700 FTIR Spectrometer. In total, two 18 cm long yarn samples were analyzed using the attenuated total reflection sampling Technique. The spectra were baseline corrected.

### 2.2.4. *Thermogravimetric analysis*

Thermogravimetric analysis (TGA) was used to study the mass changes as a function of temperature and the thermal stability of the of the CNTYs. The TGA was carried out using a PerkinElmer TGA 7 thermogravimetric analyzer. CNTYs samples with 60 cm length were analyzed from 50 to 750  $^{\circ}\text{C}$  with a heating rate of 10  $^{\circ}\text{C}/\text{min}$  in nitrogen environment. A preheating from 30 to 400  $^{\circ}\text{C}$  was applied to the CNTYs samples before the test to remove potential moisture and impurities from the CNTY manufacturing method.

### 2.2.5. *In situ Raman spectroscopy during tensile electromechanical testing*

Raman spectroscopy was used to characterize the chemical structure of individual CNTYs. The Raman spectroscopy was carried out with a confocal Renishaw inVia Raman spectrometer (Renishaw plc, Wotton-under-Edge, England), using a 50 $\times$  objective lens, a 532 nm (green) laser of 50 mW (using 1 % of its power), a 60 s exposure time, an 1800 lines/mm grating, and a laser spot size of 1  $\mu\text{m}$ . Furthermore, in situ Raman spectroscopy was used to study the mechanisms that govern the response of the CNTY to uniaxial tensile loading (mechanical test). Additionally, the direct current (DC) electrical response of selected CNTYs was measured during the tests (electromechanical tests) to establish correlations with their mechanical behavior. For this purpose, CNTY specimens were utilized, following the dimensions shown in Fig. 2.1. The orthogonal cylindrical coordinate system (where  $z$ ,  $r$ , and  $\varphi$  denote the axial, radial, and tangential directions, respectively) used for describing the yarn and the applied force in the axial direction ( $F_z$ ) are also

depicted in Fig. 2.1. The CNTY shown in Fig. 2.1a corresponds to the specimen used for the mechanical tests, while the CNTY displayed in Fig. 2.1b corresponds to the specimen employed for the electromechanical tests. In both cases, the specimens were slightly pre-stretched using a very small load ( $\sim 0.73$  mN) to minimize variability in the initial strain state of the CNTYs. This pre-stretching involved attaching a 75 mg mass (fragment of a needle) to one end of the yarn. Subsequently, the yarn was affixed to a cardboard frame with a rectangular internal window, as shown in Fig. 2.1a. The ends of the CNTY were fixed to the frame using cyanoacrylate adhesive, and the frame was cut in the middle before conducting the tests. To measure the electrical resistance of the CNTYs by the four-point probe method, four 38-gauge copper wires were bonded to the CNTY using carbon-based conductive paint (Bare Conductive, London, England), as shown in Fig. 2.1b.

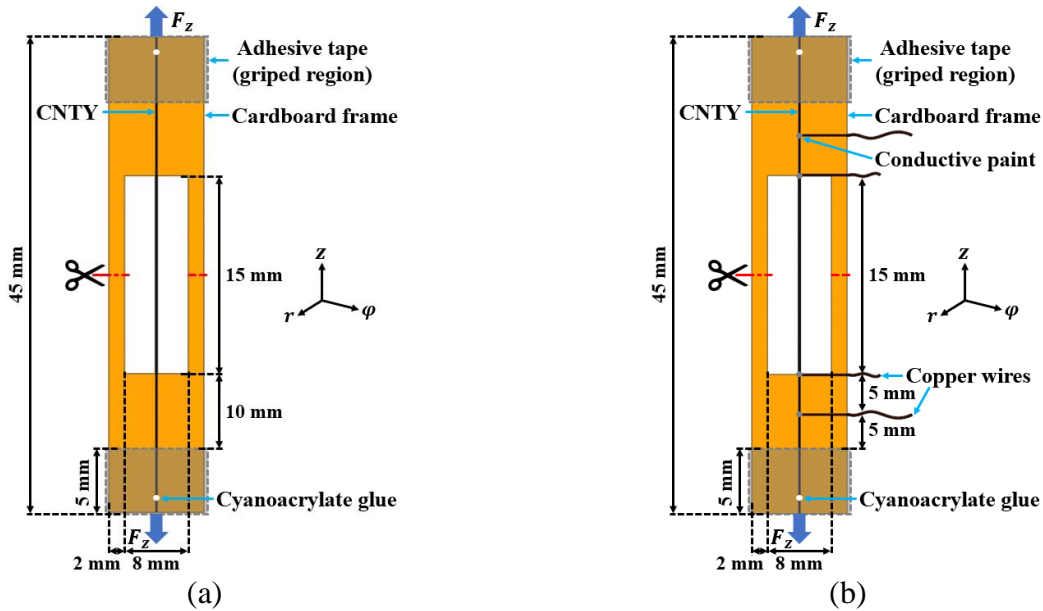


**Fig. 2.1.** CNTY specimens for in situ Raman spectroscopy during uniaxial tensile testing. **(a)** Specimen for mechanical testing, **(b)** specimen for electromechanical testing.

For the in situ Raman spectroscopy analysis during the tensile mechanical testing, the CNTYs were strained in multiple steps using a special tensile stage (rig) designed to that aim (Fig. 2.2). Each strain step deformed the CNTY an amount of  $50 \mu\text{m}$  (corresponding to 0.33 % strain) in about 30 s, until CNTY failure was reached. The strain of the CNTY ( $\epsilon_z$ ) was calculated by dividing the displacement ( $\Delta L$ ) by the gage length of the specimen ( $L_g = 15$  mm, free length in the window of the frames, Fig. 2.1). Prior to the first step (before loading the specimen) and immediately after each strain step, a  $5 \mu\text{m}$  Raman line scan mapping was conducted at the central region of the

specimen and along the axial direction of the CNTY ( $z$ ), as schematized in Fig. 2.2. As the Raman line mapping technique collects information from a broader region compared to a simple point analysis, it was observed that this mapping technique significantly aided in reducing data variability and obtaining more reliable information about the yarn. Each line scan mapping took about 20 min (time between steps) using the automated scanning function of the Raman instrument. The Raman line scan covered  $5\ \mu\text{m}$  with steps of  $1\ \mu\text{m}$ , resulting in a total of six Raman spectra. The Raman peaks were fit to a Lorentzian function to obtain the center position, full width at half maximum (FWHM) and intensity of the Raman bands. The Raman parameters of each line scan were averaged, using the standard deviation as a metric of dispersion.

In the case of the electromechanical testing, the same procedure as described above was performed, but with the added step of continuously recording the electrical resistance ( $R$ ) of the CNTYs throughout the entire duration of the test, concurrently with the Raman spectroscopy. The electrical resistance of was measured at 1 data/s using the four-point probe method. Voltage ( $V$ ) measurements were taken between the inner electrodes (Fig. 2.1b, Fig. 2.2), while electrical current ( $I$ ) was applied to the outer. These measurements were conducted using a Keysight 34980A multifunction switch/measure equipment (Keysight Technologies, Santa Clara, USA), which incorporated a 34921A terminal block module controlled by the BenchLink Data Logger software from Keysight. The change in electrical resistance ( $\Delta R = R - R_0$ ) was divided by the electrical resistance of the CNTYs in the reference state ( $R_0$ ), i.e., at  $\varepsilon_z = 0$ , to obtain the fractional change in electrical resistance ( $\Delta R/R_0$ ). All experiments were conducted at room temperature ( $\sim 25\ ^\circ\text{C}$ ).

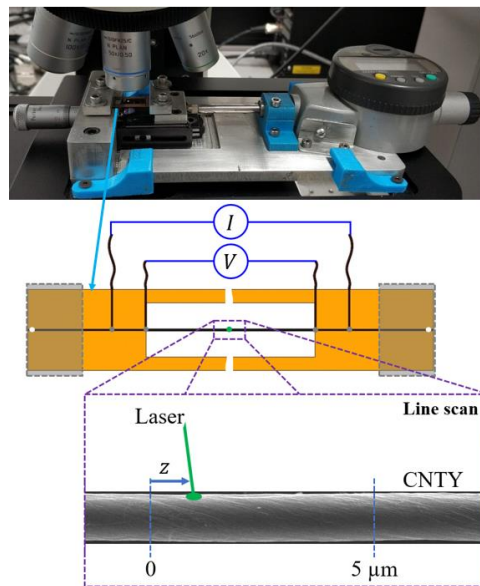


**Fig. 2.2.** Schematic of the test setup for in situ Raman spectroscopy during uniaxial tensile testing.

### 2.2.6. In situ scanning electron microscopy during tensile mechanical testing

In situ tensile tests of individual CNTYs were carried out inside a table-top SEM as shown in Fig. 2.3a. The tensile tests were performed using a Hitachi TM1000 Tabletop SEM (Hitachi Ltd., Tokyo, Japan) operating at 15 kV and using a Deben tensile stage. Samples were studied without gold metallization. The CNTY specimens were prepared as described in section 2.2.5 with the dimensions shown in Fig. 2.3a.

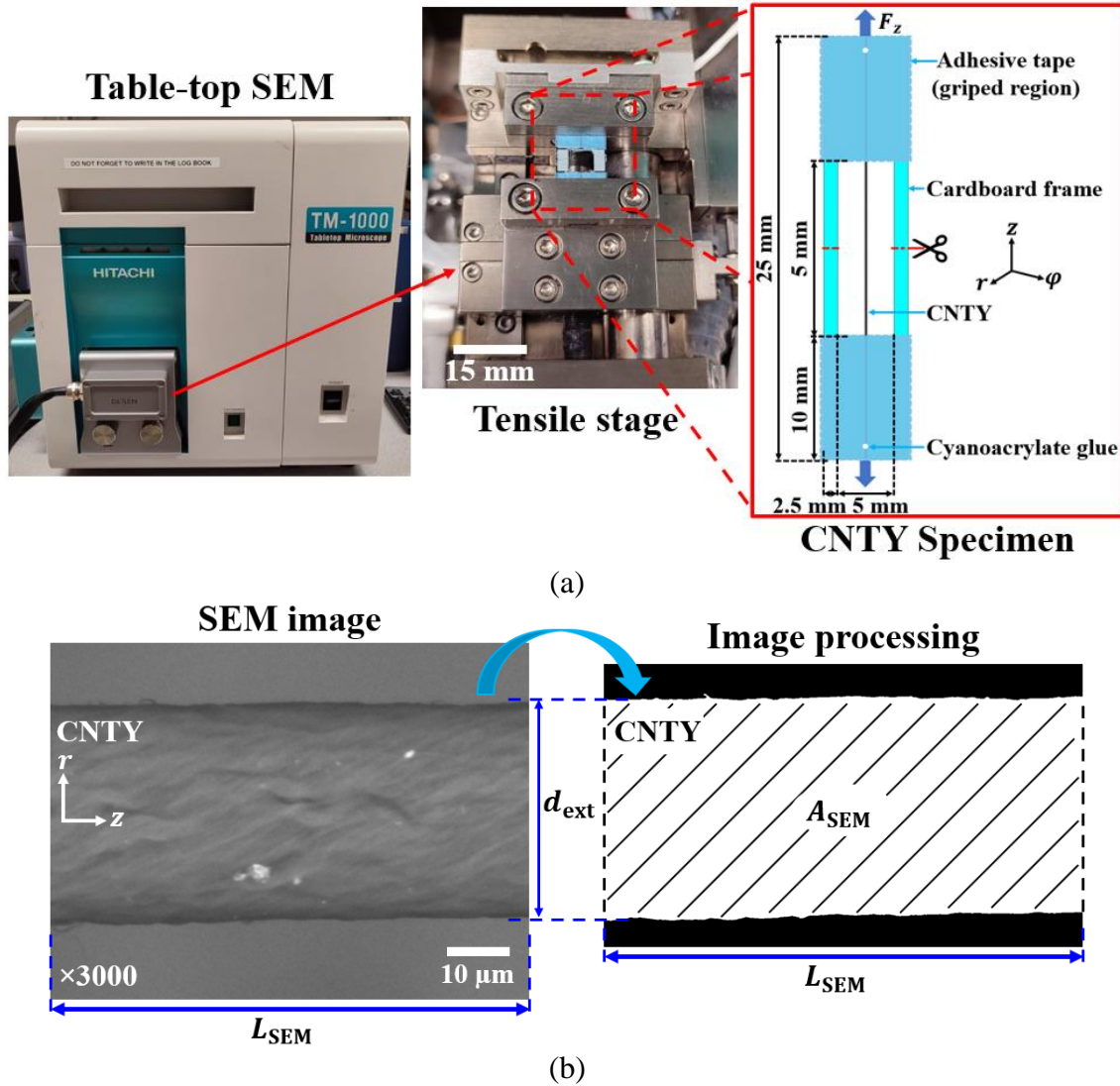


**Fig. 2.3.** In situ SEM of CNTY during axial tensile testing. (a) Test setup, (b) image processing procedure for measuring the effective diameter. Hatched lines correspond to the CNTY.

The CNTYs were axially strained in multiple steps applying a displacement of 0.02 mm (corresponding to  $\varepsilon_z = 0.4\%$ ) at 0.5 mm/min, until failure was reached. A schematic of the CNTY specimen is included in Fig. 2.3a. Before the first loading step and between each load step, an SEM image was taken at the central section of the specimen to measure its change in diameter and to

observe the morphological changes. Each image acquisition took about 3 min (time between steps). The new diameter of the CNTY was imaged and digitally measured using the image processor software “Image-J” from National Institutes of Health (Bethesda, USA). The SEM images of the CNTYs were converted to binary images by adjusting the threshold (relative image lightness) of the original images in order to obtain a mask of the CNTY as depicted in Fig. 2.3b. Each analyzed SEM image has a length of 76  $\mu\text{m}$  ( $L_{\text{SEM}}$ ), and the masking process yields a 2D projected area of the CNTY ( $A_{\text{SEM}}$ ). At each imaged load step,  $L_{\text{SEM}}$  is kept constant but the CNTY diameter reduces, yielding a change in  $A_{\text{SEM}}$ . Thus, for each load step,  $A_{\text{SEM}}$  was digitally measured and divided by the length of the SEM image ( $L_{\text{SEM}} = 76 \mu\text{m}$ ) to obtain the corresponding CNTY effective diameter ( $d_{\text{ext}}$ ), i.e.,  $d_{\text{ext}} = A_{\text{SEM}}/L_{\text{SEM}}$ . This procedure is equivalent to calculating the area under the curve of the profile formed by the diameter contraction in the SEM image. This procedure was preferred over localized point measurements of diameter reduction, since it smears out the calculation yielding an effective yarn diameter for each strain level. It provides an effective CNTY diameter which is homogenized over the entire area (image) measured. This practice proved to render more consistent results than local point measurements of diameter, given the natural variations in the morphology of the CNTYs. Using these SEM measurements, the radial strain of the yarn ( $\varepsilon_r$ ) was calculated as  $\varepsilon_r = \Delta r_{\text{ext}}/r_{\text{ext}_0}$ , where  $r_{\text{ext}_0}$  is the CNTY pristine (undeformed) effective radius,  $\Delta r_{\text{ext}} = r_{\text{ext}} - r_{\text{ext}_0}$ , and  $r_{\text{ext}}$  is the instantaneous radius (after deformation). The radial contraction ratio of the CNTY (analogous to the Poisson’s ratio in a continuous solid material,  $\nu_{zr}$ ) was obtained by the ratio between  $-\varepsilon_r$  and the applied axial strain ( $\varepsilon_z$ ) [28,70], i.e.,

$$\nu_{zr} = -\frac{\varepsilon_r}{\varepsilon_z} \quad (2.4)$$

Ten CNTY specimens were tested for this analysis.

### 2.2.7. *Monotonic and cyclic tensile mechanical testing*

The CNTY specimens detailed in this section were prepared as described section 2.2.5, and their dimensions are depicted in Fig. 2.4. The CNTYs were tested in uniaxial tension, with a monotonically increasing load up to failure, using a Shimadzu AGS-X universal testing machine (Shimadzu Corporation, Kyoto, Japan) with a crosshead displacement of 0.5 mm/min.

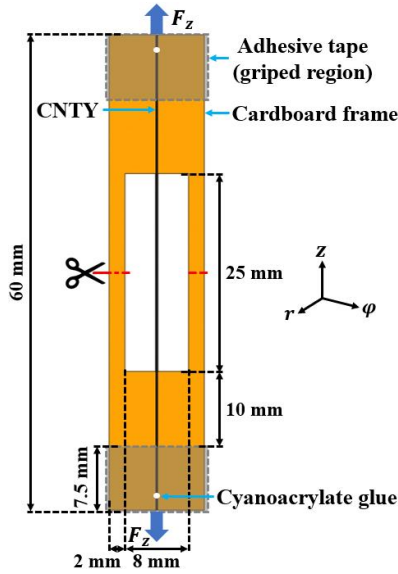


**Fig. 2.4.** CNTY specimen for uniaxial tensile mechanical testing.

Instead of using the volumetric stress ( $\sigma_z$ ) obtained by considering the yarn as a continuous solid, the specific stress (commonly used for textiles) was employed. The specific stress ( $\sigma_z/\rho$ ) was obtained by dividing the applied load ( $F_z$ ) by the linear density of the CNTYs  $\rho_L$ , i.e.,  $\sigma_z/\rho = F_z/\rho_L$ ; where  $\sigma_z/\rho$  is expressed in N/tex (1 tex = 1 g/km). The specific tensile modulus ( $E/\rho$ ) was obtained from the slope of the linear fit of the  $\sigma_z/\rho$  vs.  $\varepsilon_z$  curve in the  $0.2\% \leq \varepsilon_z \leq 1.0\%$  range.

The CNTY specimens (Fig. 2.4) were also tensile tested under strain-controlled cyclic loading by using a Shimadzu AGS-X universal testing machine. Two types of uniaxial cyclic tensile tests were conducted, viz. cycling under constant strain, and cycling under incremental strain. For the first one (constant strain), all test cycles consisted of stretching the specimen to  $\Delta L = 25$  mm ( $\varepsilon_z = 1.0\%$ ), and then returning the specimen to the original position ( $\Delta L = 0$ ). All cycles were carried out with a crosshead displacement speed of 0.5 mm/min, both in the loading and unloading cycles. A total of 300 cycles were performed on each specimen. The second type of cycling testing involved increasing the crosshead displacement by 25  $\mu\text{m}$  ( $\varepsilon_z = 0.1\%$ ) with each new cycle, until  $\Delta L = 400$   $\mu\text{m}$  ( $\varepsilon_z = 1.6\%$ , 16 cycles) was reached.

To quantify the mechanical hysteresis of each cycle, the residual specific axial tensile stress ( $\sigma_{z\text{Res}}/\rho$ ;  $\sigma_{z\text{Res}}$  is the residual axial tensile stress) and the hysteresis loop ( $H$ ) were obtained as depicted in Fig. 2.5. The hysteresis loop (a trajectory function) is the energy dissipated due to internal friction within the material at the molecular or structural level. On the other hand, the residual specific stress (a point function) indicates the amount of specific stress that remains in the

specimen upon unloading, which results from irreversible strain. The hysteresis loop was quantified by the area between the loading and unloading curves, while the residual specific stress was obtained from the difference between  $\sigma_z/\rho$  at the end of each cycle and  $\sigma_z/\rho$  at the end of the first cycle. It should be noted that, for plotting purposes, all curves were slightly shifted a very small constant amount on the vertical axis to avoid surplus negative values. This small force arises from the fine adjustment (preload) of the fiber specimen upon tightening the clamps. Finally, the hysteresis loop was used to calculate the normalized hysteresis parameter ( $H_N$ ) as,

$$H_N = \frac{H}{(\sigma_z^{\text{Max}}/\rho)\varepsilon_z^{\text{Max}}} \quad (2.5)$$

where  $\varepsilon_z^{\text{Max}}$  and  $\sigma_z^{\text{Max}}/\rho$  are the maximum values of strain and specific stress ( $\sigma_z^{\text{Max}}$  is the maximum value of axial stress) of each cycle, respectively (Fig. 2.5). The normalized hysteresis parameter is used to provide a more appropriate metric to compare the path-dependent hysteresis.

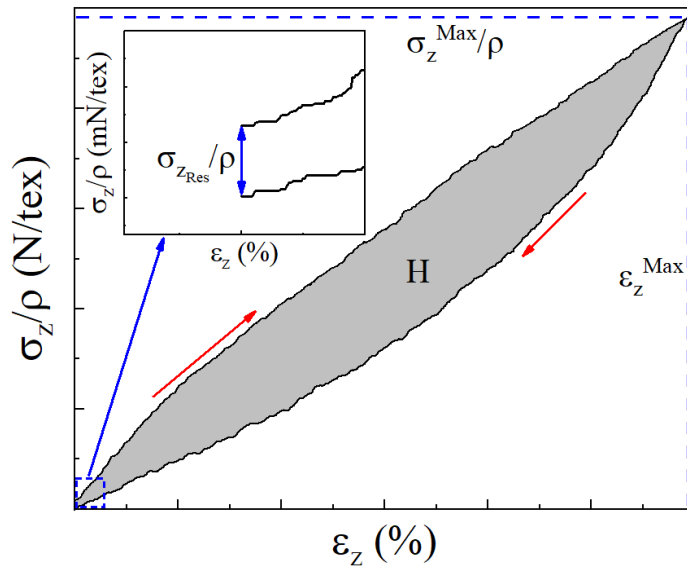


**Fig. 2.5.** Schematic of the hysteresis parameters used for the uniaxial cyclic tensile test.

### 2.2.8. Tensile electromechanical testing

The CNTY specimens tested in uniaxial tension under monotonically increasing loads were prepared as described in section 2.2.5, and their dimensions are depicted in Fig. 2.6. The tests were conducted using a Shimadzu AGS-X universal testing machine with a load cell of 100 N and a crosshead displacement of 0.5 mm/min.

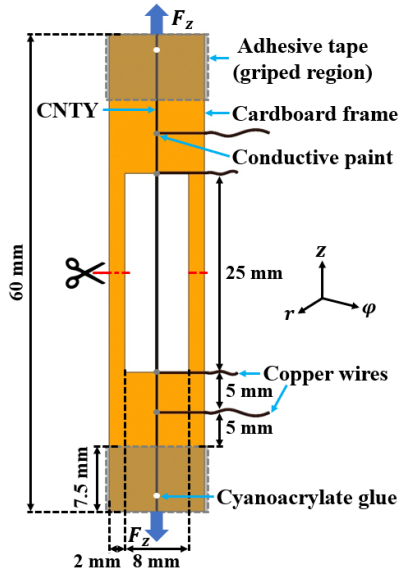


**Fig. 2.6.** CNTY specimen for tensile electromechanical testing.

The electrical resistance ( $R$ ) of the CNTYs was measured in situ (during tensile testing) by the four-point probe method, using a Keysight 34980A multifunction switch/measure equipment, which incorporated a 34921A terminal block module controlled by the BenchLink Data Logger software. The gage factor ( $GF$ ) of the CNTY was obtained from the slope of the linear fit of the  $\Delta R/R_0$  vs.  $\varepsilon_z$  curve within the same strain interval as  $E/\rho$  ( $0.2\% \leq \varepsilon_z \leq 1.0\%$ ). Additionally, the specific electrical conductivity ( $\xi/\rho$ ) of the CNTY was calculated by dividing the distance between electrodes (same as  $L_g$ ;  $L_g = 25$  mm, Fig. 2.6) by the product of  $R_0$  and  $\rho_L$ . All properties of the CNTYs were reported using the arithmetic mean as the nominal value and the standard deviation as a metric of dispersion.

### 2.2.9. Relaxation testing with in situ electrical monitoring

Stress relaxation tests on CNTYs under the application of a constant axial tensile strain were conducted using a Shimadzu AGS-X universal testing machine with a load cell of 10 N. The CNTY specimens were prepared as described in section 2.2.5, with the dimensions shown in Fig. 2.7. The specimens were tensile strained up to  $\varepsilon_z = 1.0\%$  and the strain held constant for 24 h at room temperature ( $\sim 22^\circ\text{C}$ ). During constant strain, the drops in  $F_z$  and  $R$  were simultaneously measured over time at 1 data/s. The electrical resistance of the specimens was measured by the four-point probe method using an Agilent 34401A digital multimeter (Agilent Technologies Inc., Santa Clara, USA). Five replicates were tested for this analysis.

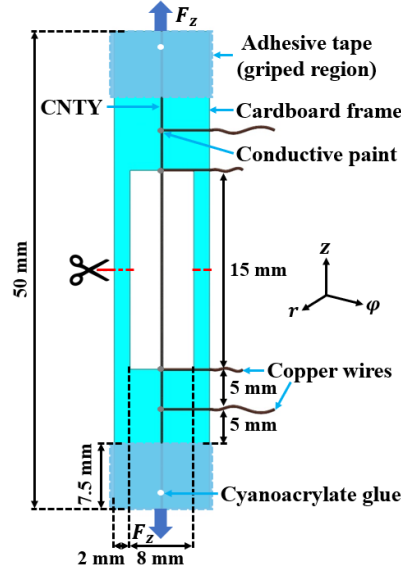


**Fig. 2.7.** CNTY specimen for stress relaxation testing.

A Prony series of the Wiechert's model [105] was used to fit the mechanical and electrical relaxation responses. The Wiechert's model (Fig. 2.8) adds a spring term in parallel to the generalized Maxwell model, which describes the viscoelastic behavior through a parallel system of  $n$  spring and dampers connected in series [105]. The Prony series used to fit either the specific stress or the specific tensile modulus response of the CNTYs ( $E/\rho$ ) is given by [105,106],

$$E/\rho = E_{\infty}/\rho + \sum_{i=1}^n (E_i/\rho) e^{-\left(\frac{t}{\tau_i}\right)} \quad (2.6)$$

where  $E_{\infty}/\rho$  is the equilibrium specific tensile modulus (the residual specific tensile modulus once the material is fully relaxed, i.e., at the plateau stage),  $E_i/\rho$  and  $\tau_i$  are respectively the specific elastic modulus and relaxation time corresponding to the  $i$ -th Maxwell element of the Prony series, and  $t$  is the elapsed time. Notice that the series has been divided by the yarn's density ( $\rho$ ) to incorporate yarn's specific properties, i.e., independent of the cross-sectional area. Additionally, electromechanical equivalences allow the substitution of springs for capacitors and dampers by electrical resistors [107]. Thus, Eq. (2.6) was also used to fit the electrical relaxation curve (the decay of  $R$  over time) by replacing  $E/\rho$  with  $R$ ,  $E_i/\rho$  with  $R_i$ , and  $E_{\infty}/\rho$  with  $R_{\infty}$  (equilibrium electrical resistance). The mechanical and electrical relaxation times ( $\tau_i$ ), however, may differ as they arise from distinct physical mechanisms. Stress relaxation involves structural motion, while electrical relaxation involves the movement and polarization of charges. The best fit procedure

utilized herein uses non-linear least squares optimization to find the best parameters that minimize the difference (residual) between the model predictions and the actual data points.

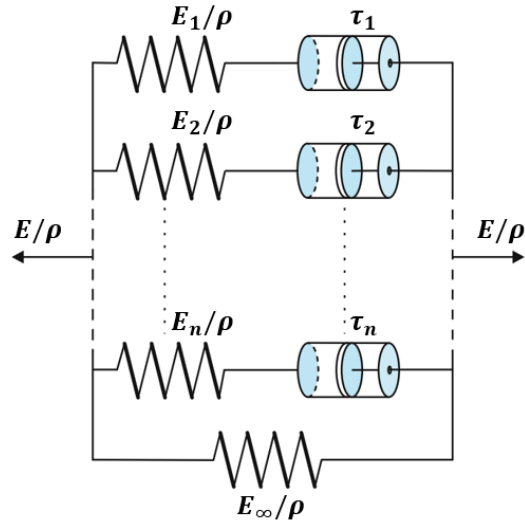


**Fig. 2.8.** Wiechert's model. Modified from [105].

#### 2.2.10. Constrained thermoresistive characterization

The (constrained) thermoresistive characterization of the CNTYs was carried out to better understand the electrical response of the CNTY during dynamic mechanical analysis (DMA) testing, and thus was conducted emulating the test rig conditions of the DMA. The test was conducted by measuring the electrical resistance of the CNTY while heating inside a PerkinElmer DMA 7 dynamic mechanical analyzer. This test was conducted inside the DMA equipment without loading the specimen, i.e., the DMA chamber was initially used just for heating. Since the CNTY is fixed within the DMA tensile clamps (and not free to expand), the test is referred to as “constrained”. The CNTY specimens were prepared as described in section 2.2.5, with the dimensions shown in Fig. 2.9. Instead of using a cardboard frame, a polyimide (Kapton) frame was used. Furthermore, the four 38-gauge copper wires were cemented to the CNTY with silver paint to measure the electrical response of the CNTYs within the DMA equipment. The electrical resistance of the CNTYs was measured by the four-point probe method, using a Keysight 34465A digital multimeter. The DMA setup (Fig. 2.9) requires the application of either a static or a dynamic force (or both) to simulate the experiment and run the heating chamber. The dynamic force was set to zero for this test. To avoid significant loading of the CNTY specimen, the constrained thermoresistive test was conducted keeping the Kapton frame of the specimen (without cutting the side-legs in Fig. 2.9) and applying a very small constant static force of 20 mN. Using strength of

materials concepts, the partition of the total force supported by the CNTY is estimated as  $\sim 1.0$  mN, while the remaining force ( $\sim 19$  mN) is supported by the (uncut) Kapton frame. The force supported by the CNTY (1.0 mN) corresponds to  $\sim 0.68$  % of the CNTY ultimate tensile force (144 mN), so it is deemed negligible for this analysis. During the test, the CNTY was first heated at a rate of  $5$   $^{\circ}\text{C}/\text{min}$  from  $30$  to  $300$   $^{\circ}\text{C}$ . Then, a temperature ( $T$ ) dwell of  $5$  min at  $300$   $^{\circ}\text{C}$  was maintained. Finally, the specimens were cooled down at  $-5$   $^{\circ}\text{C}/\text{min}$  from  $300$  to  $30$   $^{\circ}\text{C}$ . After the thermoresistive tests inside the DMA chamber, conventional DMA testing was performed by cutting the side-legs of the Kapton frame, as discussed in the following section.

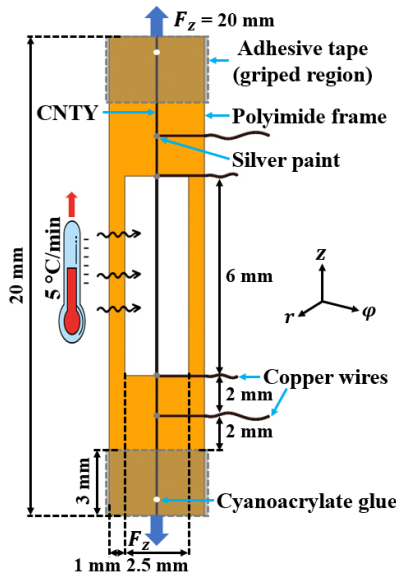


**Fig. 2.9.** CNTY specimen for constrained thermoresistive characterization and electrical monitoring during DMA.

### 2.2.11. Electrical monitoring during dynamic mechanical testing

Dynamic mechanical analysis (DMA) of the CNTYs was carried out using a PerkinElmer DMA 7 dynamic mechanical analyzer. The CNTY specimens were prepared as described in section 2.2.5, using a polyimide (Kapton) frame instead of a cardboard frame, with the dimensions shown in Fig. 2.10a. The CNTYs were subjected to uniaxial tensile cyclic loading, performing temperature and frequency scans. The temperature scans were performed from  $-50$  to  $300$   $^{\circ}\text{C}$ , with a heating rate of  $5$   $^{\circ}\text{C}/\text{min}$  and using an oscillating force at  $1$  Hz. The frequency scans were conducted at  $30$   $^{\circ}\text{C}$  from  $0$  to  $51$  Hz. This maximum frequency ( $51$  Hz) was selected due to equipment limitations. The DMA was performed on pristine CNTYs with a static force ( $F_{z_s}$ ) of  $18$  mN and a dynamic force ( $F_{z_D}$ ) of  $12.6$  mN, resulting in a maximum applied force value ( $F_z^{\text{Max}}$ ) of  $30.6$  mN and a minimum applied force value ( $F_z^{\text{Min}}$ ) of  $5.4$  mN. These DMA parameters were selected based on preliminary analysis

presented in Appendix A. First, temperature and frequency scans were conducted to investigate the effect of  $F_{zS}$  by using different values of this force, viz. 18, 30, 40 and 50 mN (see Appendix A.1). Here,  $F_{zD}$  was always taken as 70 % of the static force, i.e.,  $F_{zD} = 0.7F_{zS}$ , oscillating sinusoidally around  $F_{zS}$  with a certain frequency ( $f$ ), as shown in Fig. 2.10b. In this first analysis, the DMA with temperature scan was performed at 1 Hz from -50 to 300 °C with a heating rate of 5 °C/min, and the DMA with frequency scan was performed at 30 °C from 0 to 51 Hz. Subsequently, the DMA with frequency scans was performed at different constant temperatures ( $T = -50, 30, 50,$  and 100 °C) from 0 to 51 Hz, using  $F_{zS} = 18$  mN, in order to study the effect of temperature (see Appendix A.2). Then, to examine the effect of preheating (see Appendix A.3), two groups of specimens (three specimens per group) were tested with temperature scans at 1 Hz from -50 to 300 °C with a heating rate of 5 °C/min and  $F_{zS} = 18$  mN. The first group consisted of CNTYs that were previously heated to 300 °C (raised to this temperature from 30 °C with a heating rate of 5 °C/min) for 5 min, and the second group consisted of CNTYs without preheating (pristine CNTY). Finally, to study the effect of heating rate (see Appendix A.4), the CNTYs were tested at 1 Hz from 30 to 300 °C, with  $F_{zS} = 18$  mN, using different heating rates, viz. 1, 2, and 5 °C/min. Table 2.1 provides an overview of the test program for DMA, covering both temperature and frequency scanning.

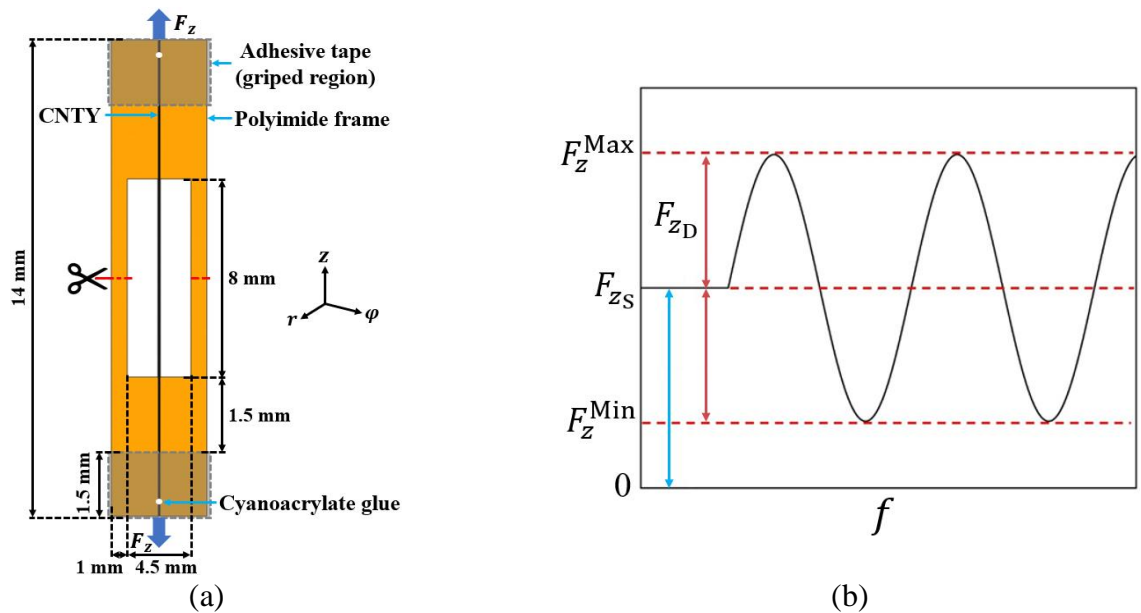


**Fig. 2.10.** DMA of the CNTYs. (a) CNTY specimen, (b) schematic of the oscillatory force.

**Table 2.1.** DMA test program.

$F_{zS}$ (mN)	$F_{zD}$ (mN)	$F_z^{Max}$ (mN)	Temperature scanning		Frequency scanning
			Temperature range (°C)	Heating rate (°C/min)	Temperature (°C)
18.0	12.6	30.6	-50–300	5	-50
					30
			30–300	1	50
					2
30.0	21.0	51.0	30–300	5	30
					50
40.0	28.0	68.0	-	-	30
50.0	35.0	85.0	30–300	5	30
					50

The electrical monitoring during DMA was carried out for two groups of CNTY specimens (Fig. 2.9). The CNTYs of the first group were tested right after they had been characterized for thermoresistivity, as described in section 2.2.10; in this sense, the thermoresistive test acted as an initial preheating cycle for subsequent DMA testing. The second group of CNTYs was tested using pristine CNTYs, i.e., without being previously heated. In both cases, the Kapton frame was cut in the middle before running the DMA test. The CNTYs were tested using the procedure described previously, with  $f = 1$  Hz,  $F_{zS} = 18$  mN, and  $F_{zD} = 12.6$  mN. The test was carried out performing temperature scans from 30 to 300 °C with a heating rate of 5 °C/min. The electrical response of the CNTYs was simultaneously (in situ) measured by the four-point probe method using a Keysight 34465A digital multimeter.

#### 2.2.12. Tensile electromechanical testing at different temperatures

The CNTY specimens (Fig. 2.6) were subjected to uniaxial tension tests under monotonically increasing loads at different temperatures (25, 80, and 120 °C) as described in section 2.2.8. The temperature at 25 °C is the room temperature and was selected as the reference temperature. The 80 and 120 °C temperatures were chosen because the CNTYs exhibited a change in their thermoresistive behavior during the constrained thermoresistive characterization (see sections 2.2.10 and 3.1.12). Tensile electromechanical tests were conducted using a Shimadzu AGS-X universal testing machine with a 100 N load cell and a crosshead displacement of 0.5 mm/min. Before starting the test, the CNTY specimen was placed in the universal testing machine and

enclosed within an in-house chamber that was attached to a hot-air blower. This system was used to heat the specimen and maintain its temperature constant during the tensile test. The temperature ( $T$ ) inside the chamber increased from room temperature ( $\sim 25$  °C) to 80 or 120 °C in  $\sim 1$  h, then remained constant for 1 h, and finally the tensile test was started. It is worth mentioning that the temperature distribution inside the chamber varied up to 8 °C. This temperature distribution was measured at four points inside the chamber, forming a quadrant around the CNTY. The electrical resistance ( $R$ ) of the CNTYs was measured in situ (during tensile testing) by the four-point probe method, using a Keysight 34980A multifunction switch/measure equipment, which incorporated a 34921A terminal block module controlled by the BenchLink Data Logger software.

### 2.3. Modeling for tensile mechanical behavior carbon nanotube yarns

CNTYs are considered here as staple yarns, due to their hierarchical structure which comprises CNTs, CNT bundles, and fibrils making up the yarn [27]. A staple yarn (also known as spun yarn) is a type of strand made by bonding discrete filaments (fibrils) together through twisting, wrapping, and surface friction. Therefore, the mechanical behavior of CNTYs under axial tensile loading can be modeled using classical mechanical theories of yarns, such as the coaxial helix model [27,28]. In this model, the CNTY is assumed to have a circular cross-section with fibrils distributed in a series of concentric cylinders of differing radii  $r$  (radial position), that vary from the center ( $r = 0$ ) to the yarn surface ( $r = r_{\text{ext}}$ ), as shown in Fig. 2.11. The height of each cylinder is defined by the length of the yarn with one turn of twist ( $h$ ), given by [28],

$$h = \frac{2\pi r_{\text{ext}}}{\tan(\theta_{\text{ext}})} \quad (2.7)$$

where  $\theta_{\text{ext}}$  is the yarn's surface twist angle. In the coaxial helix model,  $h$  is used to define the axial strain as  $\varepsilon_z = \Delta h/h_0$ , where  $h_0$  is the length of the yarn with one turn of twist before deformation, and  $\Delta h = h - h_0$ . Therefore, Eq. (2.7) can be rewritten as,

$$h = (1 + \varepsilon_z) \left( \frac{2\pi r_{\text{ext}_0}}{\tan(\theta_{\text{ext}_0})} \right) \quad (2.8)$$

where  $r_{\text{ext}_0}$  and  $\theta_{\text{ext}_0}$  are respectively the external radius and twist angle of the yarn before deformation. Within  $h$ , each fibril follows a uniform helical path with angle  $\theta$  around one of the concentric cylinders described by [28],

$$\theta = \arctan\left(\frac{2\pi r}{h}\right) \quad (2.9)$$

In Eq. (2.9), when  $r = r_{\text{ext}}$  the helical path is  $\theta_{\text{ext}}$ , and therefore  $0 \leq \theta \leq \theta_{\text{ext}}$ . Considering these parameters, the relationship between the axial strain of the yarn ( $\varepsilon_z$ ) and the axial strain of each fibril ( $\varepsilon_{z_f}$ , where  $z_f$  refers to the axial direction,  $z$ , and “f” stands for fibril) can be represented by [28],

$$\varepsilon_{z_f} = [\cos^2(\theta) - \nu_{zr} \sin^2(\theta)]\varepsilon_z \quad (2.10)$$

where  $\nu_{zr}$  is the radial contraction ratio of the CNTY. Notice that, for a yarn,  $\nu_{zr}$  is a structural parameter rather than a material property; therefore, it is not referred herein as “Poisson’s ratio”. Additionally, the relationship between the yarn’s tensile modulus ( $E$ ) and the fibril’s tensile modulus ( $E_f$ ) is given by [28],

$$E_f = \frac{E}{\cos^2(\theta_{\text{ext}_0}) [1 - k \csc(\theta_{\text{ext}_0})]} \quad (2.11)$$

where  $k$  is a slip factor that can be estimated by [28],

$$k = \frac{\sqrt{2}}{3L_f} \sqrt{\frac{r_f Q}{\mu}} \quad (2.12)$$

In Eq. (2.12),  $L_f$ ,  $r_f$ ,  $Q$ , and  $\mu$  are the length, radius, migration cycle, and coefficient of kinetic friction of the fibrils, respectively. The migration cycle is the change in the helical path that a single fibril follows along the yarn’s axial position ( $z$ ). This movement involves a transition from the outside ( $r = r_{\text{ext}}$ ) to the center ( $r = 0$ ) of the yarn and then returning to the outside. According to classical yarn mechanics, the migration cycle can be estimated as  $Q \approx 4h$  [28].

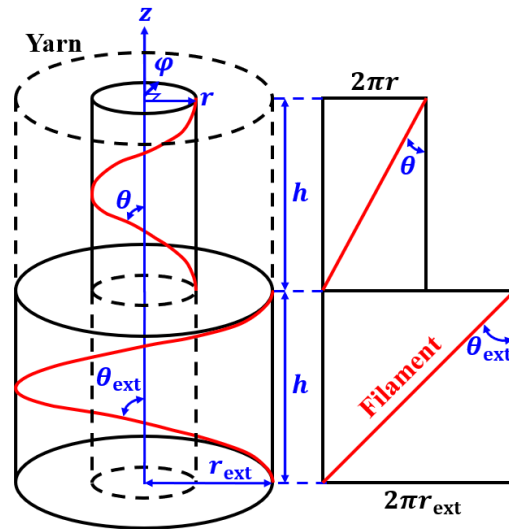


**Fig. 2.11.** Coaxial helix model of a twisted staple yarn. Modified from [28].

Low-twist yarns are a type of yarn that have been spun with a relatively low number of twists per meter, generally less than 6000 twists/m [58]. The CNTYs used in this work have an external radius ( $r_{\text{ext}_0}$ ) of 16.7  $\mu\text{m}$  and a yarn's surface twist angle ( $\theta_{\text{ext}_0}$ ) of 29.9° (see section 3.1.1), which according to Eq. (2.7) yields  $h = 1.82 \times 10^{-4}$  m. This value indicates that the CNTY has approximately 5480 twist/m ( $1/h$ ). Thus, the equations used by Shao et al. [108] to model the tensile mechanical behavior of low-twist staple yarns can also be applied to model the tensile response of the CNTYs. In this case, the total force in the yarn's axial direction ( $F_z$ ) resulting from a tensile strain can be calculated by [108],

$$F_z = 2\pi \int_0^{r_{\text{ext}}} r \rho_r \sigma_{z_f} \cos^2(\theta) dr \quad (2.13)$$

where  $\rho_r$  is the packing density at  $r$  and  $\sigma_{z_f}$  is the average fibril stress in the yarn's axial direction. The packing density of a yarn varies according to its cross-section, decreasing from the center towards the yarn surface [109,110]. Knowing the porosity of the CNTYs ( $\Phi_p = 0.69$ , see section 3.1.2),  $\rho_r$  was assumed to follow the equation,

$$\rho_r = \left[ 1 - \Phi_p \left( \frac{r_{\text{ext}}}{r_{\text{ext}_0}} \right)^2 \right] \left( 1 - \frac{r}{r_{\text{ext}}} \right) \quad (2.14)$$

The first part of Eq. (2.14) describes the space occupied by the fibrils, where the porosity is multiplied by the rate of change of area (equivalent to the squared rate of change in radius) to capture the decrease in porosity with  $\varepsilon_z$ . The second part of the equation refers to the distribution of the packing density as function of  $r$ , with the maximum value occurring at  $r = 0$  and decreasing linearly to zero at  $r = r_{\text{ext}}$ .

Assuming linear elasticity of the fibrils, the average fibril stress can be obtained by [108],

$$\sigma_{z_f} = \left( 1 - \frac{\lambda}{2} \right) E_f \varepsilon_{z_f} \quad (2.15)$$

where  $\lambda$  is the slippage ratio of the fibrils given by [108],

$$\lambda = \frac{r_f E_f \varepsilon_{z_f}}{\mu L_f P} \quad (2.16)$$

In Eq. (2.16),  $P$  is compressive transverse stress (stress perpendicular to the fibril axis), which can be estimated by [108],

$$P = \frac{a(r_{\text{ext}_0}^2 b^2 - r^2)^3 (1 - (1 + \varepsilon_z)^3 b^6)}{(1 + \varepsilon_z)^3 b^{12}} \quad (2.17)$$

where  $a$  is a constant and  $b = r_{\text{ext}}/r_{\text{ext}_0}$ .

Equation (2.13) was used herein to study the tensile response of the CNTY as a function of strain ( $\varepsilon_z$ ). The force,  $F_z$ , resulting from Eq. (2.13), was divided by the linear density of the CNTYs ( $\rho_L = 0.21$  tex, see section 3.1.2) to obtain the specific stress ( $\sigma_z/\rho$ ), since the use of  $\sigma_z/\rho$  is more appropriate for analyzing the tensile response of the CNTYs. It is worth noting that this is a nonlinear evolutionary model in which the geometry ( $\theta, \theta_{\text{ext}}, h, Q, r_{\text{ext}}$ ) and structural properties ( $\mu, \nu_{zr}, \rho_r$ ) of the CNTY are updated for each level of  $\varepsilon_z$ . The parameters  $L_f, r_f, r_{\text{ext}_0}, \theta_{\text{ext}_0}, E$ , and  $\nu_{zr}$  were experimentally measured and used as inputs for the model. The migration cycle was assumed as  $Q = 4h$ . The slip factor ( $k = 0.37$ ) and the coefficient of friction ( $\mu = 1.11Q$ ) were obtained from a parametric analysis described in Appendix D.1. This analysis utilized Eq. (2.11), Eq. (2.12), and a fibril tensile modulus of  $E_f = 30$  GPa, which was selected from the literature [111–113]. The packing density ( $\rho_r$ ) was assumed to follow Eq. (2.14), see Appendix D.2. The constant  $a$  was estimated based on the best fit of the  $\sigma_z/\rho$  vs.  $\varepsilon_z$  curve. The axial strain of the yarn ( $\varepsilon_z$ ) was varied from 0 to 8.1 % to reproduce experimental tests (see sections 2.2.7 and 3.1.8). Table 2.2 shows the values of the input parameters used in the mechanical model described by Eq. (2.13), as well as the source or assumptions used for their calculation. The bounding values listed in the last column correspond to the values for  $\varepsilon_z = 0$  and 8.1 %.

**Table 2.2.** Baseline input parameters of the mechanical model, Eq. (2.13).

Parameter	Source	Value ( $\varepsilon_z = 0$ to 8.1 %)
$\theta(r, \varepsilon_z)$	Calculated by Eq. (2.9).	$[0^\circ, 29.9^\circ]$ to $[0^\circ, 25.8^\circ]$
$\theta_{\text{ext}}(\varepsilon_z)$	Calculated by Eq. (2.9), when $r = r_{\text{ext}}$ .	$29.9^\circ$ to $25.8^\circ$
$\theta_{\text{ext}_0}$	Measured from SEM images (see section 3.1.1).	$29.9^\circ$
$\mu(\varepsilon_z)$	Assumed as $\mu = 1.11Q$ , using a selected value of $k$ in Eq. (2.12), as described in Appendix D.1.	$810 \times 10^{-6}$ to $976 \times 10^{-6}$
$\nu_{zr}(\varepsilon_z)$	Obtained from fitting experimental measurements (see section 3.1.7), Eq. (3.1).	7.91 to 1.12
$\rho_r(r, \varepsilon_z)$	Assumed to decrease linearly with $r$ , Eq. (2.14).	$[0.310, 0]$ to $[0.429, 0]$
$a$	Estimated based on the best fit of the $F_z$ vs. $\varepsilon_z$ curve.	$4.85 \times 10^{39}$ Pa/m <sup>6</sup>
$E$	Measured from tensile mechanical testing (see section 3.1.8).	5.80 GPa
$E_f$	Selected from the literature [111–113] (see Appendix D.1).	30 GPa
$h(\varepsilon_z)$	Calculated by Eq. (2.8).	182 to 197 $\mu\text{m}$
$k$	Obtained using a selected value of $E_f$ in Eq. (2.11), as described in Appendix D.1.	0.37
$L_f$	Height of the vertically aligned CNT arrays used to spin the CNTY.	500 $\mu\text{m}$
$Q(\varepsilon_z)$	Assumed as $Q = 4h$ .	728 to 786 $\mu\text{m}$
$r_{\text{ext}}(\varepsilon_z)$	Calculated from Eq. (2.4); $r_{\text{ext}} = (1 - \nu_{zr}\varepsilon_z)r_{\text{ext}_0}$ .	16.7 to 15.1 $\mu\text{m}$
$r_{\text{ext}_0}$	Measured from SEM images (see section 3.1.1).	16.7 $\mu\text{m}$
$r_f$	Mean value measured from AFM images (see section 3.1.1).	172 nm

## 2.4. Electromechanical characterization of monofilament composites

### 2.4.1. Manufacturing of monofilament composites

In order to study the electrical behavior of the CNTYs for SHM applications, monofilament (single yarn filament) composites were manufactured using an individual CNTY embedded into VER, as shown in Fig. 2.12. The orthogonal Cartesian coordinate system (where  $x$ ,  $y$ , and  $z$  denote the abscissa/axial, ordinate/transversal, and depth directions, respectively) used for describing the

composites is also depicted in Fig. 2.12. Four types of specimens were manufactured to study not only the electrical response of the CNTYs, but also the effect of the addition of the CNTYs and copper electrodes to the VER. Table 2.3 shows the different types of specimens manufactured. The composites labeled as VER correspond to specimens made of neat resin. VER+Cu corresponds to specimens made of VER with copper electrodes, but without CNTY. CNTY/VER corresponds to specimens made of VER and a single CNTY, while CNTY/VER+Cu corresponds to specimens made of VER and CNTY with copper electrodes. The VER was prepared with a 0.5 % weight concentration (wt.%) of cobalt naphthenate and 0.5 wt.% of methyl ethyl ketone peroxide. The cobalt was mixed with the VER and stirred for 5 min. The resulting VER solution was then placed under vacuum for 5 min. Subsequently, the methyl ethyl ketone peroxide was added to the VER solution and stirred for 3 min. Finally, the VER solution was placed under vacuum for an additional 3 min and then poured into a mold of a 1:0.5 downscaled version of a type IV specimen from D638 standard of the American Society for Testing and Materials [114], as shown in Fig. 2.12a. For the monofilament composites, the CNTY was previously placed in the mold using a 75 mg mass (fragment of a needle) to pre-stretch it. In addition, four 38-gauge copper wires were bounded to the CNTY using Bare Conductive paint (before pouring the resin) to measure the electrical response of selected monofilament composites by the four-point probe method, as shown in Fig. 2.12b. After 24 h at room temperature ( $\sim 25^\circ\text{C}$ ), the specimen was demolded and post-cured during 2 h at  $120^\circ\text{C}$  using a convection oven.

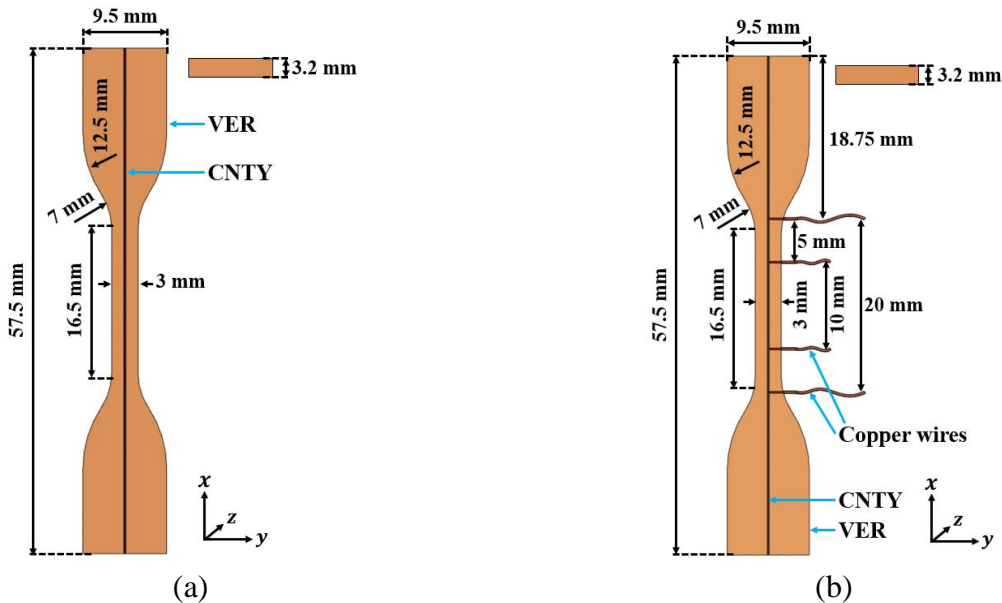


**Fig. 2.12.** Monofilament specimen. (a) Specimen for tensile mechanical testing, (b) specimen for tensile electromechanical testing.

**Table 2.3.** Type of monofilament specimens.

Specimen	Description
VER	Specimen shown in Fig. 2.12a, made only of VER.
VER+Cu	Specimen shown in Fig. 2.12b, made of VER with the copper electrodes, but without the CNTY.
CNTY/VER	Specimen shown in Fig. 2.12a made of VER and the CNTY.
CNTY/VER+Cu	Specimen shown in Fig. 2.12b, made of VER and the CNTY with the copper electrodes.

#### 2.4.2. Tensile mechanical and electromechanical testing using digital image correlation

Monofilament composite specimens (Fig. 2.12) were tensile tested using a Shimadzu AGS-X universal testing machine, with a load cell of 1 kN and a crosshead displacement of 0.8 mm/min. The strain of the specimens was measured with a digital image correlation (DIC) technique, using a GOM ARAMIS 5M, 5M LT DIC system (GOM Metrology, Braunschweig, Germany) with cameras of 2448×2050 pixels (5 Mpx) and Schneider 35 mm lens. For this, a speckle pattern was painted on one surface (referred to as the “front” surface) of the specimens to measure the field of strain in the axial direction ( $\varepsilon_x$ ) and in the transversal direction ( $\varepsilon_y$ ) of the specimens. The DIC system was calibrated using a CP20/30×24 calibration object for three-dimensional field measurements, covering a field of view of 35×29 mm<sup>2</sup> with a depth of 1.5 mm. The system’s configuration included a camera-to-camera distance of 98 mm, a camera angle of 25°, a camera-to-specimen distance of 310 mm, and an aperture of f/8.0 (focal length/number). The electrical resistance of the specimens was measured by the four-point probe method, using an Agilent 34401A digital multimeter.

The tensile modulus of the monofilament composites ( $E^M$ ) was obtained from the slope of the linear fit of the tensile stress in the axial direction ( $\sigma_x$ ) vs.  $\varepsilon_x$  curve in the 0.2 %  $\leq \varepsilon_x \leq$  1.0 % range. Similarly, the Poisson’s ratio of the monofilament composites ( $\nu_{xy}^M$ ) was obtained from the slope of the  $-\varepsilon_y$  vs.  $\varepsilon_x$  curve in the same strain interval. The gage factor ( $GF$ ) of the CNTY inside the monofilament composites was obtained from the slope of the linear fit of the  $\Delta R/R_0$  vs.  $\varepsilon_x$  curve in the same strain interval as  $E^M$ . In addition, the specific electrical conductivity ( $\xi/\rho$ ) of the CNTY inside the monofilament composites was calculated by dividing the distance between electrodes ( $L_g = 10$  mm, Fig. 2.12b) by the product of  $R_0$  and  $\rho_L$ , i.e.,  $\xi/\rho = L_g/(R_0\rho_L)$ . All properties were

obtained from at least five replicates for each type of specimen (Table 2.3), reporting the arithmetic mean as the nominal value and the standard deviation as a metric of dispersion.

## **2.5. Laminated composites panels for structural health monitoring**

### *2.5.1. Manufacturing of laminated composites panels*

Laminated composite panels were manufactured using five GFW layers with initial square lateral dimensions of 110 mm (trimmed to  $100 \times 100 \text{ mm}^2$  after manufacturing), with VER serving as the polymeric matrix. The five layers of GFWs were stacked on top of each other and gently pressed. To monitor the structural health of the panels in a non-invasive fashion, four CNTYs were woven into the third GFW layer (central layer), creating a  $2 \times 2$  CNTY array, as depicted in Fig. 2.13. Each CNTY was stitched in a zigzag pattern between the GFW bundles, as illustrated in the inset of Fig. 2.13. The intersections between the CNTYs were adhered with Bare Conductive paint (Bare Conductive, London, England). To avoid crushing the CNTYs placed at the edges, they were stitched 10 mm away from the edge of the GFW and passed between the upper layers, emerging on the top surface, as shown in Fig. 2.13. In the inset of Fig. 2.13, the CNTYs are shown emerging  $\sim 5$  mm from the edge instead of 10 mm. This is because the missing 5 mm were cut during panel trimming to achieve a final size of  $100 \times 100 \text{ mm}^2$ . It is important to mention that the CNTYs were stitched before reaching the edges to prevent them from being end-crushed during compression testing. The VER was prepared as described in section 2.4.1. A highly concentrated mixture of CNT/VER ( $\sim 9.1$  wt.% CNTs) was used to create a conductive area on the panel's surface, enabling the measurement of electrical resistance in the CNTYs. After preparing the VER, 300 mg of VER was mixed with 30 mg of CNTs and hand-stirred for 1 min. Subsequently, the conductive CNT/VER was spread onto small regions of the GFW where the CNTYs protrude, forming six  $\sim 10 \times 10 \text{ mm}^2$  areas of conductive CNT/VER (Fig. 2.13). These  $\sim 10 \times 10 \text{ mm}^2$  conductive areas served as contact points for electrical connections between the CNTYs and the copper wires after panel manufacturing. Then, the VER was infused into the GFWs, concomitant with curing of the small spots of CNT/VER. The fact that the same VER is used for the home-made conductive resin and cures at the same time reinforces the non-invasive character of this technique. For this purpose, vacuum-assisted resin infusion was employed to introduce the VER into the GFWs. Vacuum-assisted resin infusion is a manufacturing process that uses vacuum pressure to drive resin into a laminate composite. In this case, the resin infusion process lasted about 30 min at a flow rate of approximately  $2.6 \text{ cm}^3/\text{min}$ . After being kept under vacuum at room temperature ( $\sim 25 \text{ }^\circ\text{C}$ ) for 24

h, the specimens were post-cured for 4 h at 120 °C using a convection oven. The specimens were then cut into square panels using a diamond saw disc. The resulting laminated composite panels had a thickness of ~2.7 mm and lateral dimensions of 100 mm, as shown in Fig. 2.13. Finally, 38-gauge copper wires were attached to each of the small areas of conductive CNT/VER in the panel using Bare Conductive paint, to measure the electrical resistance of the CNTY array.

Additionally, selected panels were fabricated with a localized structural failure (an artificial debond) at their center, following the same procedure described above. The artificial debond was created by inserting a ~0.2 μm-thick circular Teflon sheet with a diameter of either 25 mm or 50 mm. The debond was placed between the second and third layer of the GFWs. This Teflon sheet was gently set in place aided by a small drop of cyanoacrylate adhesive. The panels without debond were labeled as GFW/VER for the panel does not include the CNTY array and GFW+CNTY/VER for those containing the array of CNTYs. Those containing a central debond were labeled as GFW/VER-D# (or GFW+CNTY/VER-D#), where the label “#” indicates the diameter (in mm) of the circular debond. For example, GFW+CNTY/VER-D25 is a GFW/VER panel containing the array of CNTYS and 25 mm circular debond. CNTYs were included only in panels with no debond and with a 25 mm debond.

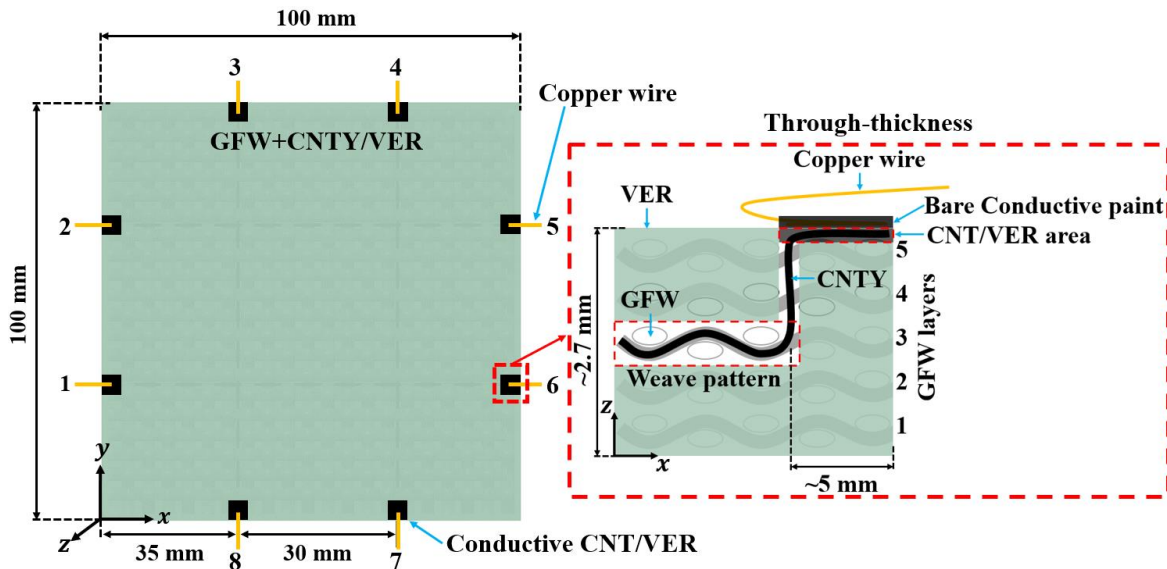


**Fig. 2.13.** Schematic of a GFW+CNTY/VER laminated composite panel containing a 2×2 CNTY array for SHM.

### 2.5.2. Electrical instrumentation and algorithm for structural health monitoring

The electrical resistance of the CNTY array was measured between the ends of the individual CNTYs, which were numbered from 1 to 8 as shown in Fig. 2.14a. The electrical measurements

were carried out in a combinatorial manner. The electrical resistance between electrodes  $i$  and  $j$  is represented by  $R_{i,j}$ , with  $i$  ranging from 1 to  $n - 1$ , and  $j$  ranging from  $i + 1$  to  $n$ , where  $n = 8$  (total number of electrodes in the panel). Thereby, 28 measurements of  $R_{i,j}$  (two-combination of an eight set) were conducted per load step, i.e., every 2 s. These electrical measurements were conducted in situ (during compression testing) by the four-point probe method, using a Keysight 34980A multifunction switch/measure instrument, which incorporated two 34921A terminal block modules controlled by the BenchLink Data Logger software. This equipment allowed a set of 28 electrical measurements every 2 s. The electrodes of the panel (Fig. 2.14) were connected to an electronic board (division board) that organized the connections into combinatorial pairs and distributed them across the inputs of the Keysight's terminal blocks, see Fig. 2.14b. The electrodes were connected from the panel to the terminals of the division board using a single copper wire (see section 2.5.1). This implies that the connections of  $V$  and  $I$  for the four-point probe method were made at the same point. Subsequently, the acquired data underwent post-processing using an algorithm to construct electrical resistance maps that could be used to correlate structural damage. To create a contour (color) map of the panels, an algorithm was programmed in Python (Python Software Foundation, Wilmington, USA) to first assign an electrical resistance value to each path (P#) within the CNTY array. In this context, a path (link) refers to a section of CNTY that connects either electrodes to nodes or nodes to other nodes within the CNTY array, as shown in Fig. 2.14a. Each node (N#) represents the union point (bonded with Bare Conductive paint) between two CNTYs in the array (see section 2.5.1). The electrical resistance assigned to the paths was determined by averaging the weighted values of all  $R_{i,j}$  that correspond to their respective paths. The weighted values, which multiply each  $R_{i,j}$ , were calculated by dividing the path's length by the distance between electrodes ( $L_{i,j}$ ). The distance between electrodes is the shortest electro-conductive distance (i.e., containing CNTY) between electrodes, obtained by summing the lengths of the paths connecting the two electrodes. It was assumed that each path has an equal length, allowing the paths between electrodes to be divided into fractions of  $L_{i,j}$ . For example, consider the distance between electrodes 1 and 2 ( $L_{1,2}$ ). This distance is obtained by summing the lengths of three electro-conductive paths (P1, P3-8, and P2, as shown in Fig. 2.14a), each with length  $L_{1,2}/3$ . Consequently, the weighted value of  $R_{1,2}$  in path 1 is calculated as  $(R_{1,2}L_{1,2})/3L_{1,2} = R_{1,2}/3$ . Therefore, the electrical resistance assigned to path 1 ( $R_{P_1}$ ) was obtained as,

$$R_{P_1} = \frac{1}{7} \left( \frac{R_{1,8}}{2} + \frac{R_{1,2} + R_{1,3} + R_{1,6} + R_{1,7}}{3} + \frac{R_{1,4} + R_{1,5}}{4} \right) \quad (2.18)$$

Thus, for the electrical resistance assigned to paths that connect electrodes to nodes ( $R_{P_l}$ , paths 1 to 8 in Fig. 2.14), Eq. (2.18) can be generalized into two equations:

$$R_{P_l} = \frac{1}{7} \left( \frac{R_{l,l+7}}{2} + \frac{R_{l,l+1} + R_{l,l+2} + R_{l,l+5} + R_{l,l+6}}{3} + \frac{R_{l,l+3} + R_{l,l+4}}{4} \right); \quad l = \text{Odd} \quad (2.19a)$$

$$R_{P_l} = \frac{1}{7} \left( \frac{R_{l,l+1}}{2} + \frac{R_{l,l+2} + R_{l,l+3} + R_{l,l+6} + R_{l,l+7}}{3} + \frac{R_{l,l+4} + R_{l,l+5}}{4} \right); \quad l = \text{Even} \quad (2.19b)$$

where Eq. (2.19a) is used for odd values of  $l$  (integer) and Eq. (2.19b) is used for even values of  $l$  ( $1 \leq l \leq n$ ).

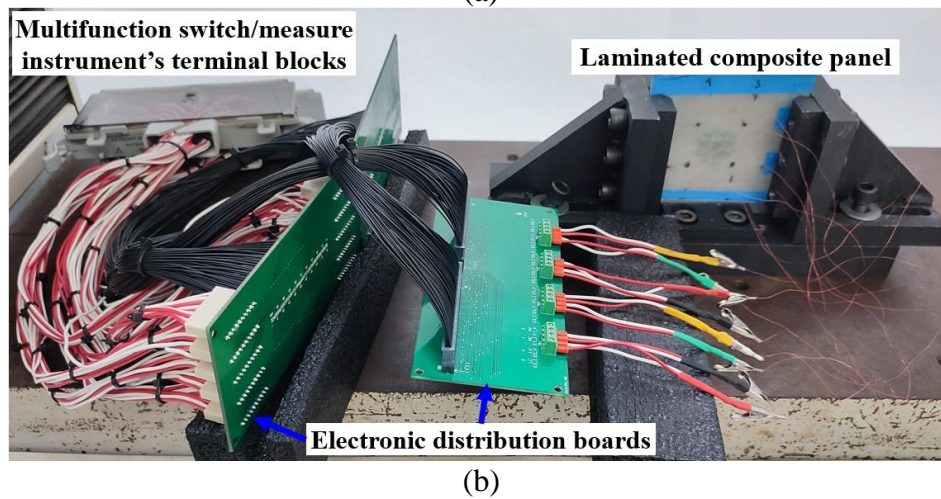
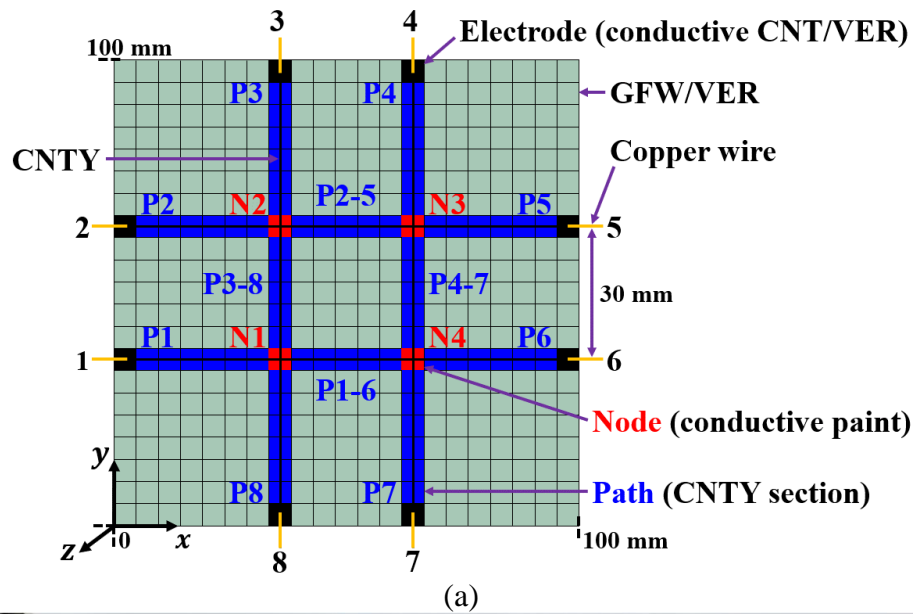


**Fig. 2.14.** Electrical mapping of the GFW+CNTY/VER panels. (a) Definition of electrical elements used for the SHM algorithm, (b) photograph of electrical connections.

The central paths (P#-#) need special consideration. This is because in the central paths, the electrical current that flows from the electrodes is divided among all the paths, as they are interconnected by conductive paint. The numbers in the label P#-# correspond to the number of electrodes forming the path through the continuous CNTY in the array. Therefore, for the case of the electrical resistance assigned to central paths that connect nodes to nodes ( $R_{P_{i,j}}$ , paths 1-6, 2-5, 3-8, and 4-7 in Fig. 2.14a),  $R_{P_{i,j}}$  is given by,

$$R_{P_{l-l+5}} = \frac{1}{12} \left( \frac{R_{l,l+5} + R_{l,l+6} + R_{l+5,l+7} + R_{l+6,l+7}}{3} + \frac{R_{l,l+3} + R_{l,l+4} + R_{l+1,l+5} + R_{l+1,l+6}}{8} + \frac{R_{l+2,l+5} + R_{l+2,l+6} + R_{l+3,l+7} + R_{l+4,l+7}}{8} \right); \quad l = 1, 3 \quad (2.20a)$$

$$R_{P_{l-l+3}} = \frac{1}{12} \left( \frac{R_{l,l+2} + R_{l,l+3} + R_{l+1,l+2} + R_{l+1,l+3}}{3} + \frac{R_{l,l+4} + R_{l,l+5} + R_{l+1,l+4} + R_{l+1,l+5}}{8} + \frac{R_{l+2,l+6} + R_{l+3,l+6} + R_{l+7,l+2} + R_{l+7,l+3}}{8} \right); \quad l = 2, 4 \quad (2.20b)$$

where Eq. (2.20a) is used for  $l = 1$  and  $3$ , and Eq. (2.20b) is used for  $l = 2$  and  $4$  ( $l = 1, 2, 3$ , and  $4$ ). Notice that in Eqs. (2.19) and (2.20), if a subindex of  $R_{i,j}$  exceeds the number of electrodes ( $n = 8$ ),  $n$  is subtracted from the corresponding index, i.e.,  $i = i - n$  if  $i > n$ , and  $j = j - n$  if  $j > n$ . This ensures that the result always provides a valid value of  $R_{i,j}$  ( $R_{i,j} = R_{j,i}$ ,  $i \neq j$ ). Then, the electrical resistance assigned to the nodes ( $R_{N_l}$  where  $l = 1, 2, 3$ , and  $4$ , Fig. 2.14a) was determined by averaging the electrical resistance of the surrounding four paths connecting the respective node. Finally, to assign electrical resistance values to discrete zones of the panel, the panel was hypothetically divided into  $21 \times 21$  grid as shown in Fig. 2.14a. Each  $4.76 \times 4.76$  mm<sup>2</sup> square element represents a small subregion of the panel, and their 441 resistance values populate a square resistance matrix. The electrical resistance assigned to the 361 elements of the panel where the CNTYs are not passing (Fig. 2.14a) was set to zero. This algorithm would then produce values of  $R$  different to zero only along the 12 (blue) paths shown in Fig. 2.14a, and it is hereafter referred to as the ‘‘panel’s electrical resistance algorithm’’ (PER).

The discrete and extremely localized character of the PER data post-processing method bears some limitations regarding the spatial localization of damage. Therefore, as an extension of the PER method, a second algorithm was used which assigns non-zero  $R$  values to the 361 matrix elements where there is no CNTY present. To do so, the electrical resistance assigned to these elements was interpolated among their neighbor elements. This allowed to smear out and spread the conductivity

in a more continuous fashion along the surface of the panel, as opposed to the overly localized and discrete plots obtained by assigning values of  $R$  only to the actual CNTY paths. For this purpose, the electrical resistance assigned to each element of the panel which does not contain a CNTY (light green elements in Fig. 2.14a) was determined by the weighted sum of the surrounding paths. The weight assigned to paths surrounding a particular element is determined by the number of elements between the paths and the given element. The weight assigned to a vertical path is given by the reciprocal of the number of elements in the  $x$ -direction between the path and the given element. Similarly, the weight assigned to a horizontal path is given by the reciprocal of the number of elements in the  $y$ -direction between the path and the given element. In both cases, the number of elements between the paths and the given element is increased by two units to avoid division by zero or one. For example, the element located at the origin of the panel's coordinate system in Fig. 2.14a is surrounded by paths P1 and P8. There are 6 elements in the  $y$ -direction between this element and path P1, and thus, the electrical resistance value of P1 ( $R_{P_1}$ ) is divided by 8 (number of elements + 2). Similarly, there are 6 elements in the  $x$ -direction between the element and path P8, and thus,  $R_{P_8}$  is divided by 8. Therefore, the electrical resistance assigned to this element is given by the sum of these values, i.e.,  $\frac{1}{8}R_{P_1} + \frac{1}{8}R_{P_8}$ . This algorithm is hereafter referred to as the “panel's electrical resistance with interpolation algorithm” (PERI).

The electrical resistance map of the laminated composite panels is presented as the fractional change in electrical resistance ( $\Delta R/R_0$ ), using  $R_0$  as the electrical resistance matrix (21×21 elements) assigned to the 4.76×4.76 mm<sup>2</sup> square elements at the reference stage (initial stage at zero strain).

### 2.5.3. Monotonic compression testing

The laminated composite panels (100×100×2.7 mm<sup>3</sup>, Fig. 2.13) were subjected to uniaxial monotonic compression loading using a Shimadzu AG-I universal testing machine with a load cell of 100 kN and a crosshead displacement speed of 1 mm/min. The panels were placed in a specially designed fixture, as shown in Fig. 2.15a, to ensure proper panel alignment and prevent any movement during the application of the compression force ( $F_y$ ). The support fixture construction was based on an ASTM D7137/D7137M standard [115]. The strain of the specimens was measured using a GOM ARAMIS 5M, 5M LT DIC system with cameras of 2448×2050 pixels (5 Mpx) and Schneider 35 mm lens. The DIC system was calibrated using a CP20 90×72 calibration object for

three-dimensional field measurements, covering a field of view of  $125 \times 100 \text{ mm}^2$  with a depth of 77 mm. The system's configuration (Fig. 2.15a) included a camera-to-camera distance of 222 mm, a camera angle of  $25^\circ$ , a camera-to-specimen distance of 590 mm, and an aperture of f/8.0. Five replicates of each panel type (without debond or with debond of 25 or 50 mm diameter) without CNTYs were tested to investigate their mechanical properties and failure modes. The compression modulus ( $E_C^P$ ) was calculated as the slope of a linear fit to the compression stress ( $\sigma_y$ ) vs. axial strain ( $\varepsilon_y$ ) curve in the  $-0.2\% < \varepsilon_y < 0$  interval. The averaged values of the mechanical properties are reported, along with one standard deviation as a metric of dispersion.

Electrical SHM of composite panels was conducted during the compression test of the panels that include CNTYs, measuring the electrical resistance as described in section 2.5.2. The 28 measurements of  $R_{i,j}$  were recorded every 2 s. A picture of the experimental setup is shown in Fig. 2.15b. In this case, four replicates of the GFW+CNTY/VER and GFW+CNTY /VER-D25 panels were tested.

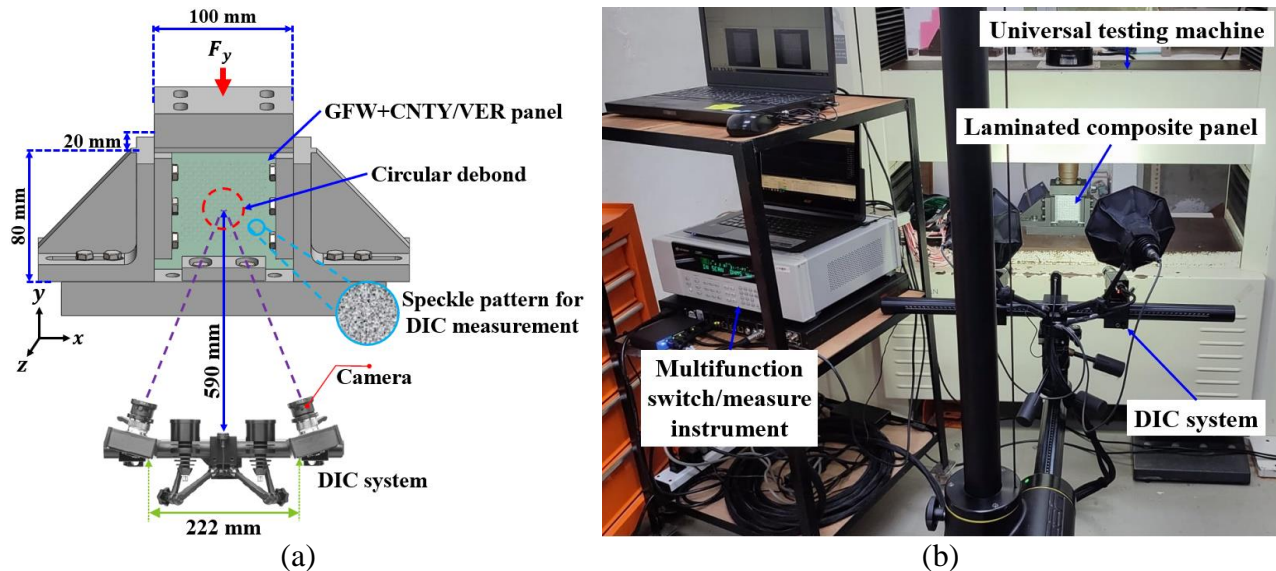


**Fig. 2.15.** Setup for compression testing of the laminated composite panels. (a) Schematic of the fixture and DIC measurements, (b) photograph of the actual setup.

#### 2.5.4. Cyclic compression testing

Cyclic compression tests were conducted on the GFW+CNTY/VER-D25 panels to assess their performance for monitoring progressive damage, see Fig. 2.16. A total of five panels were subjected to uniaxial cyclic compression loading using an MTS Landmark 370 servohydraulic test system (MTS Systems Corporation, Berlin, Germany) with a load cell of 100 kN. Cyclic tests were conducted only on the GFW+CNTY/VER-D25 panels. The force was applied in sinusoidal cycles

from 0 to 16.4 kN over 15000 cycles. The maximum force was set as 80 % of the failure force of the panels tested quasi-statically until failure (see section 3.4.1). The panels were placed in the same compression fixture as those tested under monotonic load until failure (Fig. 2.15). For the cyclic tests, C-shaped aluminum liners were fit tight at the top and bottom edges of the panel to mitigate end-crushing during load introduction, arising from the difference in rigidity between the fixture and the panel. The strain of the specimens was measured using a GOM ARAMIS 5M, 5M LT DIC system with cameras of 2448×2050 pixels (5 Mpx) and Schneider 35 mm lens. The DIC system was calibrated using a CP20 90×72 calibration object for three-dimensional field measurements, covering a field of view of 125×100 mm<sup>2</sup> with a depth of 77 mm. The system's configuration (Fig. 2.15a) included a camera-to-camera distance of 222 mm, a camera angle of 25°, a camera-to-specimen distance of 590 mm, and an aperture of f/8.0. The DIC measurements were taken every 1000 cycles, capturing 4 images/s during 30 s. Electrical SHM of panels with CNTYs was conducted during the cyclic compression test, measuring the electrical resistance as described in section 2.5.2. The 28 measurements of  $R_{i,j}$  were recorded every 2.5 s.

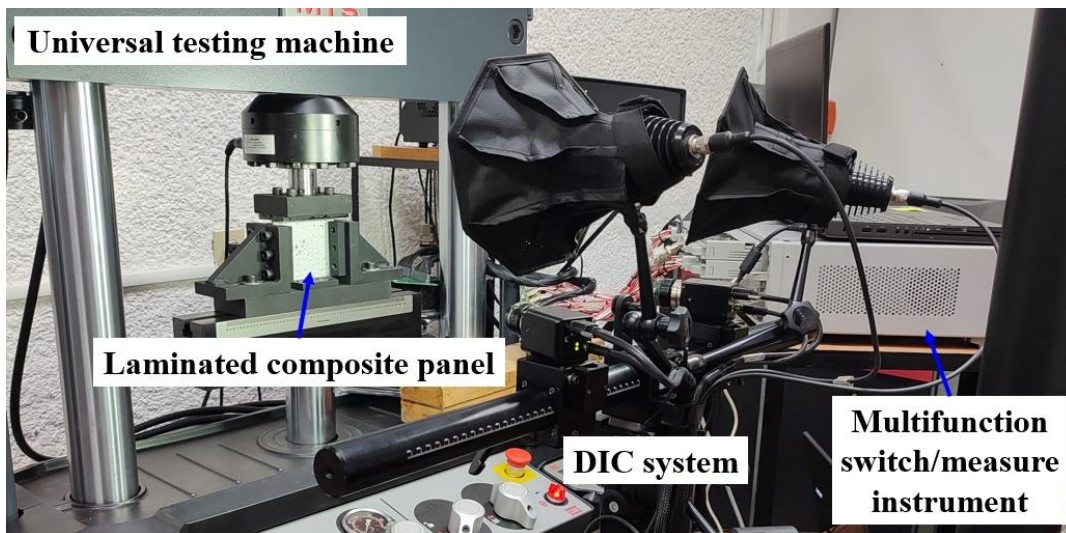


**Fig. 2.16.** Photograph of the setup for cyclic compression testing of the laminated composite panels.

#### 2.5.5. *Optical and scanning electron microscopy*

In order to evaluate damage and failure mechanisms in post-mortem panels, optical and SEM images were acquired at selected zones of the laminated composite panels. Optical microscopy images were captured using a Leica DM LM optical microscope (Leica Microsystems, Wetzlar, Germany). SEM images were obtained using a JEOL JSOL-6360-LV microscope with magnifications of 100× and acceleration voltages of 20 kV. The SEM images were taken from the

outer surface of the composite panels to avoid alterations caused by the cutting process of the samples. The samples were sputtered with gold during 60 s using a Denton Vacuum Desk-II sputtering equipment (Denton Vacuum LLC, Moorestown, USA). The resulting gold layer had a thickness of ~15 nm.

# Chapter 3. Results and discussion

## 3.1. Properties of carbon nanotube yarns

### 3.1.1. Morphological and structural properties

The morphology of the carbon nanotube yarns (CNTYs) is shown in Fig. 3.1a. It is evident that CNTYs are made up of thinner fibrils. These fibrils exhibit an inclination (twist angle) relative to the longitudinal direction of the CNTY. Additionally, the CNTYs present variations in diameter along the length of the continuous yarn. These diameter variations are attributed to the synthesis processes employed for CNTY production. The measured diameter distribution of the CNTYs is shown in Fig. 3.1b and summarized in Table 3.1. Probability plots of the distribution models can be found in Appendix B. To determine the best statistical distribution that fits the diameter distribution of the CNTYs, two statistical tests were employed: the p-value test and the Anderson-Darling test. The p-value is a probability that measures the evidence against the null hypothesis. For an Anderson-Darling test, the null hypothesis is that the data follow the distribution. Therefore, the p-value test assesses how well a given statistical distribution fits the observed data, where a low p-value indicates a poor fit, while a high p-value suggests a better fit. The Anderson-Darling test provides a single-value statistic based on the discrepancies between the observed data and the expected values from the distribution. A lower Anderson-Darling statistic indicates a better fit. According to the Anderson-Darling test, the best-fitting diameter distribution is the 3-parameter loglogistic distribution, which has an Anderson-Darling value of 1.34 (see Table 3.1).

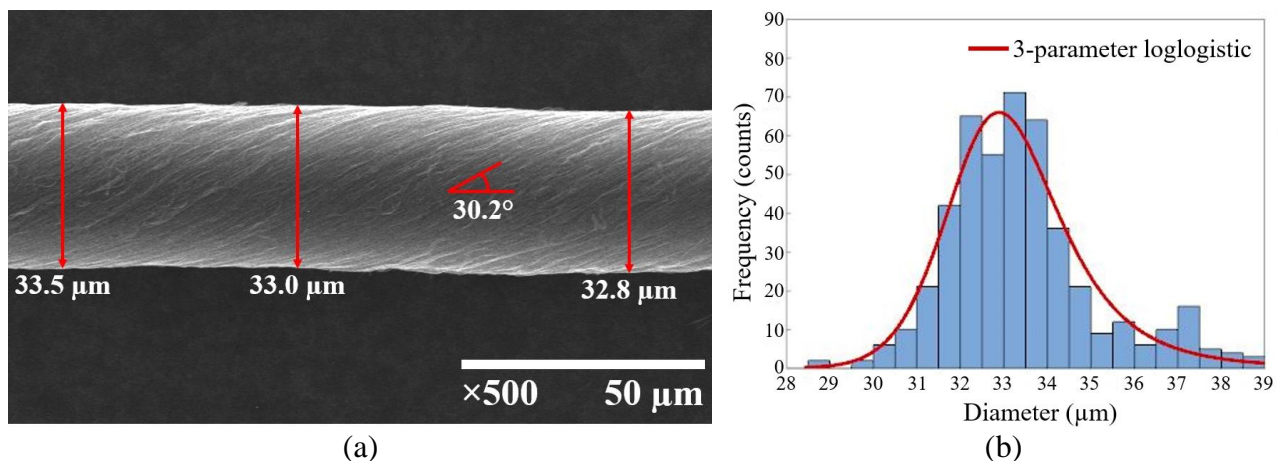


**Fig. 3.1.** Morphology of CNTYs. **(a)** Representative SEM image of the CNTYs, **(b)** histogram of CNTY's diameter ( $d_{ext_0}$ ) distribution.

**Table 3.1.** Statistical distribution models of the CNTY diameters\*.

Distribution	Distribution parameters				Goodness of fit		Estimate diameter [mean $\pm$ standard deviation] ( $\mu\text{m}$ )
	Location ( $\mu\text{m}$ )	Shape	Scale ( $\mu\text{m}$ )	Threshold ( $\mu\text{m}$ )	Anderson- Darling	Mean p-value	
Normal	33.3	-	1.70	-	8.34	< 0.005	33.3 $\pm$ 1.7
Lognormal	3.50	-	0.050	-	6.54	< 0.005	33.3 $\pm$ 1.7
3-parameter lognormal	2.12	-	0.195	24.8	3.22	-	33.3 $\pm$ 1.7
Exponential	-	-	33.3	-	191	< 0.003	33.3 $\pm$ 33.3
2-parameter exponential	-	-	4.65	28.7	91.6	< 0.010	33.3 $\pm$ 4.7
Weibull	-	17.7	34.2	-	22.0	< 0.010	33.2 $\pm$ 2.3
3-parameter Weibull	-	2.97	5.43	28.5	8.44	< 0.005	33.3 $\pm$ 1.8
Smallest extreme value	34.2	-	1.97	-	25.2	< 0.010	33.1 $\pm$ 2.5
Largest extreme value	32.5	-	1.47	-	3.28	< 0.010	33.4 $\pm$ 1.9
Gamma	-	393	0.085	-	7.10	< 0.005	33.3 $\pm$ 2.8
3-parameter gamma	-	15.9	0.419	26.7	3.80	-	34.3 $\pm$ 2.8
Logistic	33.2	-	0.914	-	4.58	< 0.005	33.2 $\pm$ 1.7
Loglogistic	3.50	-	0.027	-	3.60	< 0.005	33.2 $\pm$ 1.6
3-parameter loglogistic	1.90	-	0.132	26.4	1.34	-	33.3 $\pm$ 1.7

\***Descriptive statistics:** Data = 480, mean = 33.3  $\mu\text{m}$ , standard deviation = 1.7  $\mu\text{m}$ , median = 33.1  $\mu\text{m}$ , minimum = 28.7  $\mu\text{m}$ , maximum = 38.6  $\mu\text{m}$ .

The 3-parameter loglogistic distribution is plotted in Fig. 3.1b along with the measured data. This distribution estimates a diameter of 33.3 ( $\pm$  1.7)  $\mu\text{m}$ , which will be used herein to describe the diameter of the CNTYs ( $d_{\text{ext}_0}$ ). In the case of the twist angle ( $\theta_{\text{ext}_0}$ ), twenty measurements of the twist angle indicated average and standard deviation of  $29.9^\circ \pm 5.3^\circ$ .

The topography of the CNTYs is shown in Fig. 3.2a-c. It is observed that the surface of the CNTYs is very porous, comprised of fibrils/bundles which are generally parallel oriented in direction of the twist angle. However, some fibrils are entangled or intertwined. The fibrils comprising the

CNTY exhibit a wide range of diameters in a distribution that goes from 137 to 827 nm, as shown in the histogram of Fig. 3.2d. A wide range of fibril and CNT bundle diameter distribution is common for CNTYs (e.g., 11–28 [113] or 10–100 nm [116]) given their synthesis conditions. The Anderson–Darling goodness-of-fit test with a 95 % confidence interval level indicated that the fibril diameter distribution exhibited the best fit to a 3-parameter Weibull distribution (solid line in Fig. 3.2d) among the tested distribution functions. The 3-parameter Weibull distribution yields an expected (mean) value of 343 nm. This value was used as input for the fibril diameter ( $d_f = 343$  nm) in the model for tensile mechanical behavior (see section 2.3). The root mean square roughness of the CNTYs in this case is 62.2 ( $\pm 12.5$ ) nm.

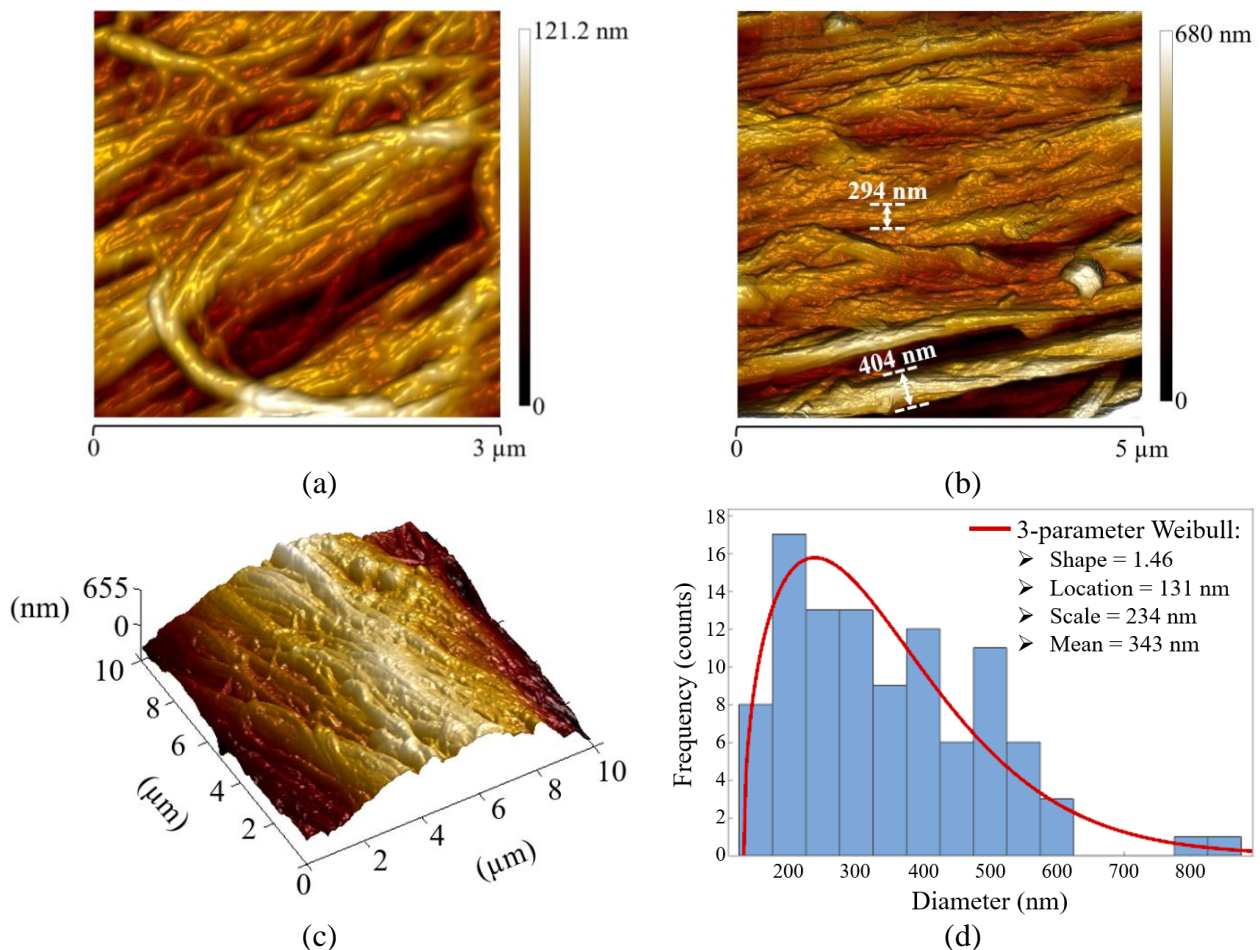


**Fig. 3.2.** AFM images of the CNTY’s fibrils. (a)  $3 \times 3 \mu\text{m}^2$  2D view, (b)  $5 \times 5 \mu\text{m}^2$  2D view, (c)  $10 \times 10 \mu\text{m}^2$  3D view, (d) histogram of fibril’s diameter ( $d_f$ ) distribution.

### 3.1.2. Linear density and porosity

The measured mass ( $m$ ) of CNTYs of different lengths ( $L = 6, 12, 18,$  and  $24$  cm) are shown in Fig. 3.3. It is observed that the mass increases with the length of the CNTYs in a linear fashion.

Thus, a linear density ( $\rho_L$ ) can be calculated from the slope of the linear fit of the data [15], yielding  $\rho_L = 0.21$  tex. The linear density of CNTYs strongly depends on their diameter and porosity. Values of  $\rho_L$  between 0.01–0.40 tex (untwisted) and 0.10–0.82 tex (twisted) have been reported for dry-spun CNTYs [15,29,52,58,117,118]. Values of  $\rho_L$  between 0.03 and 1.40 tex have also been reported for direct spinning CNTYs [31,118,119]. By using the mean diameter determined from the statistical analysis in section 2.2.1 ( $d_{ext_0} = 33.3 \mu\text{m}$ ), and assuming a solid cross section, the volumetric mass density of the CNTYs ( $\rho$ ) yields  $\rho = 0.25 \text{ g/cm}^3$ . According to the supplier [101], the majority of the CNTs that comprise the CNTYs have a diameter of  $\sim 11 \text{ nm}$ , being double- and triple-wall CNTs. Transmission electron micrographs provided by the supplier (not shown) indicate dominance of triple-wall CNTs. Thus, according to Eq. (2.3), and considering  $n = 3$ , the volumetric mass density of the CNTs is  $\rho_{\text{CNT}} = 0.78 \text{ g/cm}^3$ . Using Eq. (2.2), the calculated porosity of the CNTY ( $\Phi_P$ ) is 0.69. This indicates that 31 % of the yarn is composed of CNTs and the rest corresponds to empty spaces. On the other hand, if double-wall CNTs are considered ( $n = 2$ ),  $\rho_{\text{CNT}} = 0.54 \text{ g/cm}^3$  and  $\Phi_P = 0.54$ . Porosities of several other types of CNT fibers and yarns have been reported in the range of 0.40–0.90 [15,52,58].

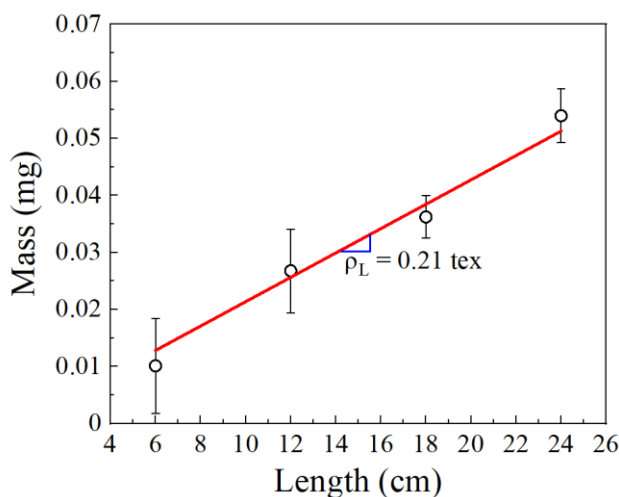


**Fig. 3.3.** Weight measurements to determine the linear density ( $\rho_L$ ) of the CNTYs.

### 3.1.3. Fourier-transform infrared analysis

A representative transmittance FTIR spectrum (in arbitrary units, a.u.) of the CNTY is shown in Fig. 3.4. Table 3.2 shows a summary of the FTIR bands. The FTIR spectrum of the CNTYs arises from their individual CNTs and their mutual interactions. The CNTs that comprise the CNTYs have been synthesized using a water-assisted CVD growth technique that utilizes argon (Ar), hydrogen ( $\text{H}_2$ ), and water vapor ( $\text{H}_2\text{O}$ ) as carrier gases, along with ethylene ( $\text{C}_2\text{H}_4$ ) as the carbon

(C) precursor gas [45]. The transmittance peak  $\sim 3,320\text{ cm}^{-1}$  (stretching vibration modes [120,121]) arises from the hydroxyl (OH) groups from intermolecular hydrogen bonding OH:OH of the CNTs. Part of this transmittance peak could also be attributed to adsorbed moisture [120,122]. The transmittance peak at  $\sim 1640\text{ cm}^{-1}$  arises from the bending vibration modes of these hydroxyl groups [120,121]. The carbonyl groups (C=O) at  $\sim 1730\text{ cm}^{-1}$  (stretching vibration mode of C=O [120]) are by-products of ethylene and water vapor. Finally, the transmittance peak at  $\sim 900\text{ cm}^{-1}$  arises from the backbone of the CNTs due to the stretching vibration mode of C=C [120,123].

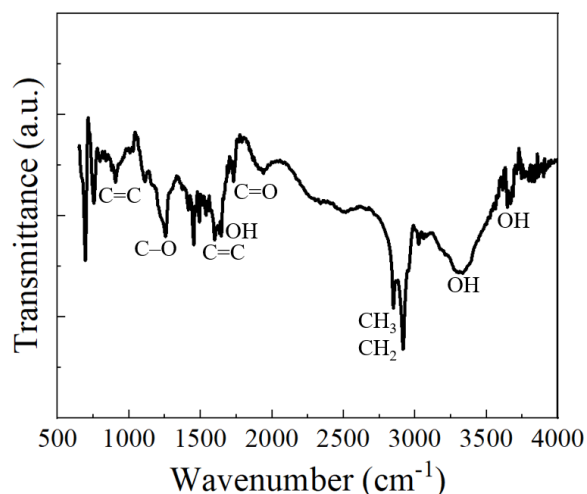


**Fig. 3.4.** Representative FTIR of the CNTYs.

**Table 3.2.** FTIR band identification for the CNTYs.

Wavenumber (cm <sup>-1</sup> )	Assignment	Characteristic vibration mode	Ref.
$\sim 3,320$	Stretching vibration mode of OH	Hydroxyl groups from intermolecular hydrogen bonded OH:OH, adsorbed water or surface carboxylic and phenolic groups.	[120,122]
2840–2920	Stretching vibration mode of CH	CH <sub>2</sub> and CH <sub>3</sub> alkyl chain.	[120]
$\sim 1730$	Stretching vibration mode of C=O	Carboxyl, lactone and/or ketone groups.	[120]
$\sim 1640$	Bending or deformation of OH	Hydroxyl groups.	[120,121]
$\sim 1600$	Stretching vibration mode of C=C	CNT skeletal vibration mode originating from the sp <sup>2</sup> -hybridized Carbon.	[120]
$\sim 1250$	Stretching vibration mode of C-O	Phenols and lactones.	[120–122]
$\sim 900$	Stretching vibration mode of C=C	CNT backbone.	[120,123]

### 3.1.4. Thermogravimetric analysis

A representative thermogram of the CNTY including preheating is shown in Fig. 3.5. The CNTY was first preheated from 30 to 400 °C (red curve with solid triangles) to remove moisture and possible byproducts from the synthesis, followed by the complete heating from 50 to 750 °C (indicated in the plot as “TGA”). During the preheating, the CNTY lost up to ~13 % in weight. This weight loss can be attributed to the evaporation of acetone (used to densify the yarns) and trapped moisture, and, to less extent, burning of amorphous carbon [124]. For the case of the second heating run (labeled as TGA in Fig. 3.5), the CNTY lost negligible weight until ~300 °C, temperature at which appreciable mass loss started. A steep mass loss is observed around 550 °C, with a weight loss of ~10 %. The high thermal stability is attributed to the aromatic bonding of the carbon atoms comprising the CNTY structure; the number of walls and defects within CNTs, the presence and composition of the catalyst, and the presence of other materials (e.g., amorphous carbon, graphite particles) play an important role in thermal stability [124,125]. From ~550 °C, the CNTYs experiment a rapid loss of mass until reaching a maximum rate of thermal decomposition at ~650 °C (obtained from the peak of the negative derivative). It has been reported that decomposition of the multiwall CNTs may vary from 400 to 700 °C [125–127].

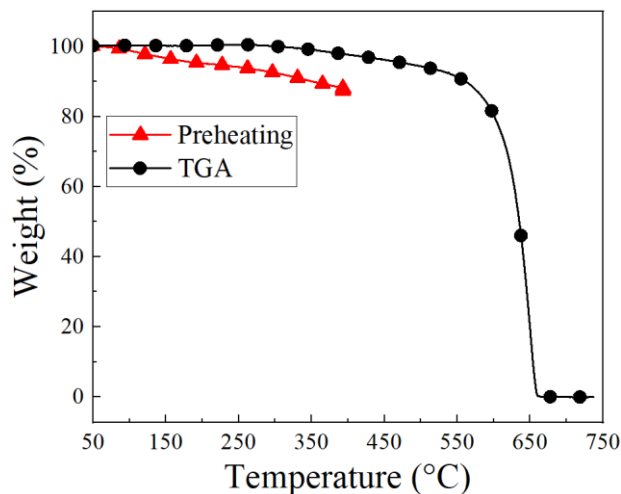


**Fig. 3.5.** Thermogram of a representative CNTY.

### 3.1.5. Raman spectroscopy

The Raman spectra of a 10  $\mu\text{m}$  region along the longitudinal direction of the CNTY ( $z$ ) without loading ( $\epsilon_z = 0$ ) are shown in Fig. 3.6a. Data were collected at 1  $\mu\text{m}$  intervals, resulting in the 11 Raman spectra plotted in Fig. 3.6a. These spectra exhibit homogeneity throughout the CNTY, with only small variations. Each of these Raman spectra displays the same characteristic peaks as those

seen in Fig. 3.6b, which represents a Raman spectrum from a random location along the CNTY. The Raman spectrum retains the fundamental features of the CNTs that compose the CNTY, although a few bands may have experienced slight shifts due to CNT pre-stressing within the yarn.

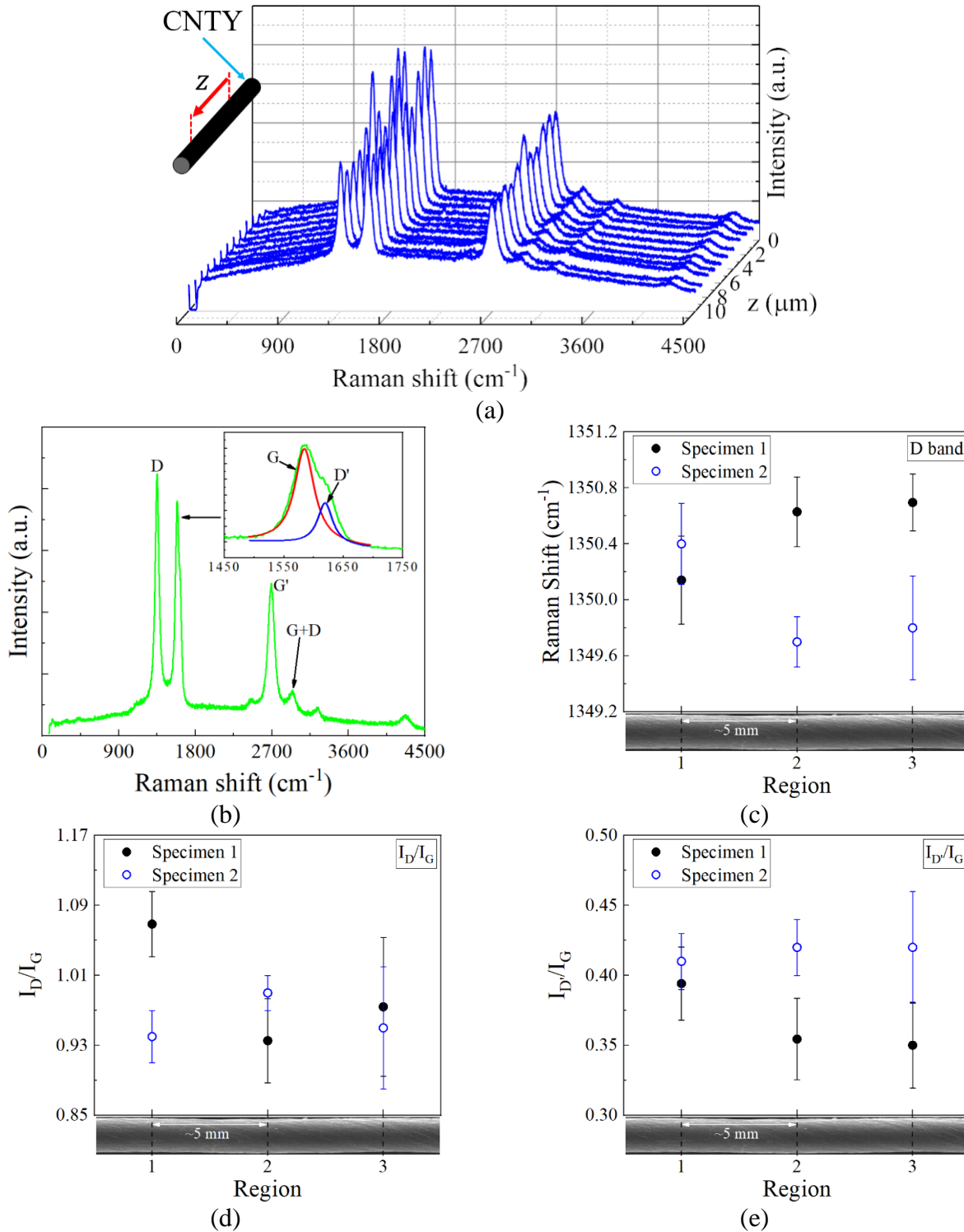


**Fig. 3.6.** Raman spectra of the CNTYs. (a) 10 μm line scan, (b) representative Raman spectrum, (c) D band variability, (d)  $I_D/I_G$  variability, (e)  $I_{D'}/I_G$  variability.

The band at  $\sim 1350\text{ cm}^{-1}$  corresponds to the so-called D band (disordered induced), which arises from the in-plane breathing vibrations of the aromatic ring structures. The D band is induced by the presence of disorder of the crystalline structure of the CNTs or vacancies in the graphitic structure through double Raman resonance processes [128–133]. The band at  $\sim 1585\text{ cm}^{-1}$  corresponds to the G band (graphitic), which arises from the in-plane bond stretching motion of pairs of  $\text{sp}^2$  hybridized carbon atoms [131–133]. The G band is asymmetric towards lower Raman shift values, which confirms the presence of CNTs with few walls [134]. It has also being pointed out that the Raman shift position of the G band can be used to determine residual strains induced in the CNTs during the CNTY assembly process [134]. The peak at  $\sim 2694\text{ cm}^{-1}$  is the so-called G' band. The G' band (or 2D band) is an overtone of the D band, i.e., a second-order two-phonon process [130–133]. A relatively high intensity value of the G' band is an indicative of the metallic feature of the CNTs [135]. The G+D band at  $\sim 2930\text{ cm}^{-1}$  is caused by two-phonon defect-assisted processes due to the presence of symmetry-breaking defects in the CNTY [132,133]. Table 3.3 compares the Raman features of the CNTYs studied in this work with carbon nanostructures and other CNTYs reported in the literature.

**Table 3.3.** Features of Raman bands in CNTYs and other carbon nanostructures.

Material	Raman band								$I_D/I_G$	Ref.
	D		G		D'		G'			
	Peak ( $\text{cm}^{-1}$ )	FWHM ( $\text{cm}^{-1}$ )	Peak ( $\text{cm}^{-1}$ )	FWHM ( $\text{cm}^{-1}$ )	Peak ( $\text{cm}^{-1}$ )	FWHM ( $\text{cm}^{-1}$ )	Peak ( $\text{cm}^{-1}$ )	FWHM ( $\text{cm}^{-1}$ )		
CNTY (Dry spinning)	1350.2 $\pm$ 0.3	46.0 $\pm$ 1.4	1584.6 $\pm$ 0.4	40.1 $\pm$ 1.3	1619.3 $\pm$ 0.8	30.8 $\pm$ 2.2	2694.0 $\pm$ 1.3	70.7 $\pm$ 2.0	0.98 $\pm$ 0.05	This work
CNTY (Direct spinning)	1353	64	1584	52	-	-	-	-	0.748	[136]
Multiwall CNT	1334.3	48.6	1585.7	46.2	1620.6	29.6	-	-	1.67	[2]
Multiwall CNT	$\sim$ 1350	50.7	$\sim$ 1580	57.1	-	-	$\sim$ 2700	72.1	0.71	[137]
Multilayer graphene sheets	$\sim$ 1350	51.1	$\sim$ 1580	25.1	-	-	$\sim$ 2700	77.0	0.25	[137]

In order to distinguish the uncertainty in the Raman parameters (peak position, intensity, and FWHM) arising from the natural variability of CNTY, three 10  $\mu\text{m}$  line scans were performed on two CNTY specimens. Each specimen was divided into three sections separated by 5 mm. The variability of the D band peak position and the relative intensities of the D to G band ( $I_D/I_G$ ) and D' to G ( $I_{D'}/I_G$ ) of a 10  $\mu\text{m}$  region along the z-axis of two different CNTY specimens is shown in Fig. 3.6c-e. The variability of the remaining Raman bands' peak position, as well as the intensity and the FWHM along the CNTYs is shown in Appendix C. It is observed that, even for the same specimen, the CNTYs present a scattering in the D band peak position, which is indicative of structural inhomogeneity. This variability is mainly due to the hierarchical structure and current synthesis methods of the CNTYs. Such a strong property-structure relationship may yield not only batch-to-batch property variations, but some structural properties may also vary within the same (continuously long) yarn [61,134]. The relative intensities  $I_D/I_G$  (Fig. 3.6d) and  $I_{D'}/I_G$  (Fig. 3.6e) can be ascribed to a high number of symmetry-breaking features in the CNTs comprising the yarn, most likely induced during the CNTY manufacturing process. In addition, the relative intensity  $I_D/I_G$  can provide information on the degree of disorder in  $\text{sp}^2$  carbon materials [128,132], and can be used to further assess the homogeneity of the composition of the CNTY. The FWHM (see Appendix C), on the other hand, presents larger scattering along the scanned line (10  $\mu\text{m}$ ), indicating variations in the structural composition of the yarn. The FWHM provides information about the crystalline structure of the CNTYs, and can also be related to axial strains of the fiber [138]. It has been argued that given the different CNTs that typically comprise a yarn (single-, double-, and multi-wall CNTs), the Raman fingerprint of a CNTY could vary from position to position [134]. During CNTY manufacturing, CNTs may also be pre-stressed [134] and the degree of this pre-stress may vary from position to position within the yarn.

### 3.1.6. Correlation between strain, Raman shift, and electrical response

In situ Raman experiments were conducted as described in section 2.2.5. The CNTYs (Fig. 2.1) were strained in multiple steps of 50  $\mu\text{m}$  (corresponding to  $\epsilon_z = 0.33\%$ ), until failure was reached. Prior to the first step and immediately after each strain step, a 5  $\mu\text{m}$  Raman line scan mapping was conducted at the central region and along the axial direction of the CNTY. In the case of electromechanical testing, the electrical resistance of the CNTYs was continuously recorded throughout the entire duration of the test. Among the Raman parameters of the CNTYs studied in this work, only the D band peak position (located at  $\sim 1350\text{ cm}^{-1}$ ) exhibited a statistically significant

correlation with the applied axial strain (see Appendix C). One of the key features of this detailed Raman analysis is to distinguish the uncertainty in the band position due to the natural variability of the CNTY (see section 3.1.5 and Appendix C) from changes in the D band position due to strain. Averaging 11 Raman spectra from the line mapping turned to be a great tool to capture more spatially broad information and assess the uncertainty in this task; such results comprise the scattering bars in Fig. 3.7. Thus, the mean values of the D band peak position were obtained from six Raman spectra plots from each 5  $\mu\text{m}$  Raman line scan, The D band peak position of a representative CNTY as function of axial strain ( $\varepsilon_z$ ) is shown in Fig. 3.7. At small strains ( $\varepsilon_z \leq 0.5$  %), the shift in the D band position with strain cannot be distinguished from the experimental scattering inherent to the measurement. This implies that, below  $\varepsilon_z = 0.5$  %, the CNTY only undergoes structural changes in its constitutive fibrils and CNT bundles, and any C-C bond stretching is negligible. As seen in Fig. 3.7, above this level of strain, the CNTs that make up the CNTY suffer C-C bond stretching upon tensile loading, which is seen by a blue shift in the D band with strain. For  $\varepsilon_z > 0.5$  %, the peak position of the D band is shifted towards lower wavenumbers as the strain increases. This change in the peak position of the D band is approximately linear, with a Raman shift strain factor (sensitivity) obtained from the slope of the linear fit of  $-0.30 \text{ cm}^{-1}/\%$ . This value of Raman shift with strain factor is very small. It is at least one order of magnitude smaller than the one observed for other carbon-based materials such as carbon fibers ( $\sim 18.8 \text{ cm}^{-1}/\%$  for the  $2660 \text{ cm}^{-1}$  band [139]), aramid (Kevlar) fibers ( $\sim 4.85 \text{ cm}^{-1}/\%$  for the  $1610 \text{ cm}^{-1}$  band [140]), and graphene deposited on a flexible substrate ( $\sim 64 \text{ cm}^{-1}/\%$  for G' band [141]). This means that, because of the twist and hierarchical architecture of the yarn, C-C bond stretching is limited as mechanism of deformation and strain transfer, and most of the strain energy is dissipated by the relative motion between the fibrils/bundles. In this sense, Raman spectroscopy suggests that tensile loading of the CNTY is strongly governed by structural changes of the fibrils/bundles comprising the yarn, and this information is of great assistance in understanding the mechanics of the yarn. It has been argued that when subject to tensile loading, CNTYs experiences slippage and stretching within its fibrils and bundles, resulting in a reduction of diameter and untwisting [62,63,75]. As the strain increase, the slippage of the fibrils/bundles increases, and therefore the slippage of the CNTs [62,63,142]. Since breaking or deforming the C-C bonds requires more energy than breaking the secondary bonds (van der Waals, dipolar, hydrogen bonding) between the CNTs, the secondary bonds break earlier, leading to a rearrangement of the CNTY structure. Most CNTs are grouped in

bundles and fibrils, which behave as single structure in the CNTY, in analogy to the behavior of a single filament in a conventional yarn. This hinders the C-C bond stretching of individual CNTs, as the strain is initially transferred from the CNTY to the fibrils, then to bundles, and finally to the CNTs. All this strain transfer process occurs through secondary bonds [14,27,32]. Therefore, only a small fraction of the strain applied to the yarn is transferred to individual CNTs within the bundles [142]. For this reason, the G band shift that typically occurs when a CNT is subjected to tension [143] was not observed in this study. However, there was a slight shift in the D band peak position with strain, indicating some stretching of the C-C bonds, although minimal. The strain-induced shifts of the D and G bands depend strongly on the chirality of the CNTs [143]. The D band can be influenced by loss of symmetry in the crystalline structure of the CNTs or by modifications on the CNT walls, such as the introduction of defects or the attachment of different chemical species on the CNTs [132,144,145]. In this case, the change of the D band peak position can be attributed to the reduction in sidewall and torsion experienced by the CNTs during stretching [146,147]. The stress relaxation of the CNTY (see section 3.1.11) due to the relatively long measurement times between each deformation (~20 min) could also affect the peak position of the D band.

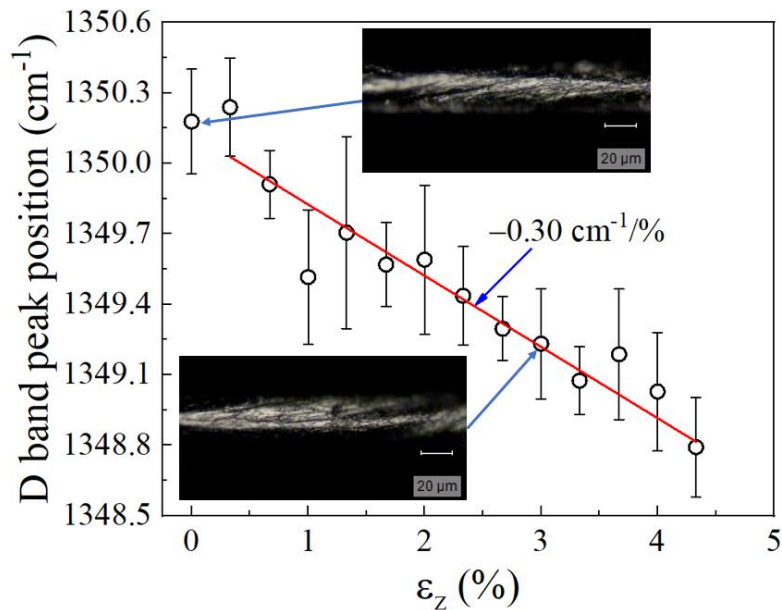


**Fig. 3.7.** D band peak position of the CNTYs as a function of axial strain ( $\epsilon_z$ ).

The D band peak position of the CNTYs as a function of  $\epsilon_z$  and the fractional change of electrical resistance ( $\Delta R/R_0$ ) as function of elapsed time are shown in Fig. 3.8. The inserts are optical microscopy images taken with the Raman microscope during testing times. The mean values of the D band peak position shown in Fig. 3.8 were placed in the plot at the instant of time when the

CNTY was strained. Similar to what was observed in Fig. 3.7, the D band peak position in Fig. 3.8 tends to shift towards lower wavenumbers as the strain increases. However, in this case, the trend is not as clear as in Fig. 3.7. This could be due to the electrical field applied during the measurement of electrical resistance to the CNTYs (see section 2.2.5) affecting the Raman vibrational response. It has been reported that the electric field/current applied can influence the vibrational frequencies and modes of the C-C bonds of the CNTs [148–150]. Additionally, the heat generated by the electric field may play a role in facilitating the rupture of secondary bonds and promoting slipping between CNTs, leading to reduced stretching of the C-C bonds within the CNTs. The relaxation of the CNTYs due to the relatively long measurement times between each deformation may also play an important role. In Fig. 3.8, the discrete load application steps are identified as zones where  $\Delta R/R_0$  exhibited an increase corresponding to the rise in  $\varepsilon_z$ . The zones that presented a nearly constant value or a small decay of  $\Delta R/R_0$  with elapsed time correspond to the periods during which  $\varepsilon_z$  was held constant for the Raman measurements (~20 min). The mechanical tensile response of the CNTY is strongly governed by structural changes at fibrils/bundle level. This indicates that the increase in  $\Delta R/R_0$  mainly depends on these structural changes. During the time where  $\varepsilon_z$  was held constant, the stress in the CNTY relaxes, leading to a slight reduction (relaxation) in  $\Delta R/R_0$ . However, as will be discussed in section 3.1.11, the relaxation of the electrical resistance of the CNTYs is influenced not only by the restructuring of the fibrils, bundles, and CNTs. These opposite effects govern the non-monotonic trend in  $\Delta R/R_0$  and lead to a change in the trend towards an increasing behavior (positive slope) of  $\Delta R/R_0$  for  $\varepsilon_z > 2.0\%$ . Beyond this strain level, the CNTYs experience fibril detachment, as shown in insert B of Fig. 3.8. This detachment/rupture of the fibrils leads to an increase in the electrical resistance and, therefore, in  $\Delta R/R_0$ . This trend is maintained until the CNTY specimen fails (see insert D of Fig. 3.8).

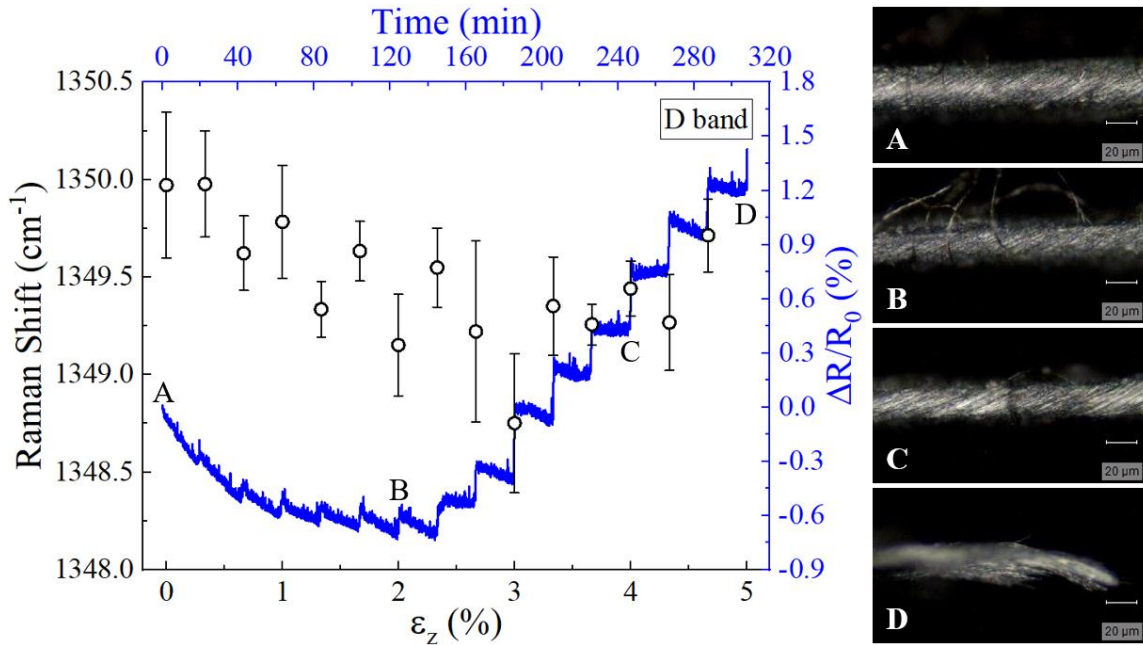


**Fig. 3.8.** D band peak position and fractional change in electrical resistance ( $\Delta R/R_0$ ) of a representative CNTY as a function of axial strain ( $\epsilon_z$ ) and time.

### 3.1.7. Radial contraction ratio

In situ SEM imaging of CNTYs (Fig. 2.3a) was carried out during tensile testing, as described in section 2.2.6. The CNTYs were strained in multiple steps of 0.02 mm (corresponding to  $\epsilon_z = 0.4$  %), until failure was reached. Before the first loading step and between each load step, an SEM image was taken at the central section of the CNTY to measure its change in diameter and to observe the morphological changes. Subsequently, the radial contraction ratio of the CNTYs was calculated. Figure 3.9 shows representative SEM images of the same CNTY depicting undeformed (Fig. 3.9a) and axially strained (Fig. 3.9b,  $\epsilon_z = 12$  %) stages. It is observed that the diameter of the CNTY decreases as  $\epsilon_z$  increases, and that the yarn's fibrils rotate as the axial strain is applied. Taking the white mark (small debris) on the CNTY surface as a reference (signaled with an arrow), it is observed that the marked particle not only moves in the yarn's axial direction ( $z$ ) due to stretching, but also rotates in the yarn's radial direction ( $r$ ). This is due to the rearrangement of the fibrils, which are initially oriented at a twist angle with respect to  $z$  ( $\theta_{\text{ext}_0} = 29.9^\circ$ ). In this process, the fibrils slip in the loading direction, untwisting and causing the observed rotation of the yarn [57,63].

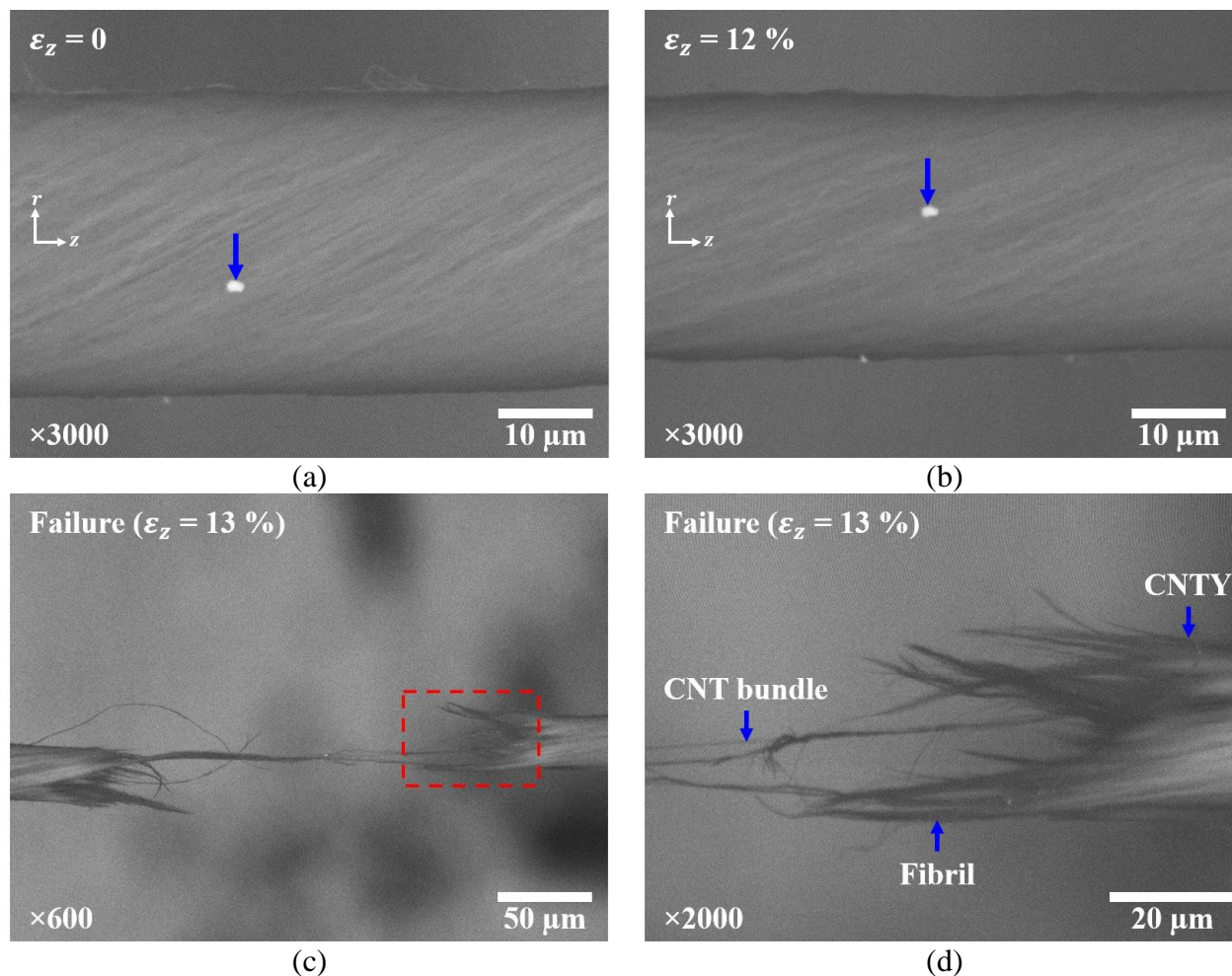


**Fig. 3.9.** In situ SEM of a CNTY during tensile testing. (a) CNTY at  $\epsilon_z = 0$ , (b) CNTY at  $\epsilon_z = 12\%$ , (c) CNTY at failure ( $\epsilon_z = 13\%$ ), (d) close-up of the CNTY at failure, indicated by a dashed rectangle in Fig. 3.9c.

The failure mode of the CNTY is shown in Fig. 3.9c. It is observed that the CNTYs fail due to fibril pull-out (close-up in Fig. 3.9d) after extensive slipping and untwisting of their fibrils. It is well known that a staple yarn may fail either because the individual fibrils slip completely over each other, or because the individual filaments break [28]. In this case, the failure of the CNTYs occurs by pulling-out due to slippage of the fibrils and their bundles. This is due to the weak interaction between fibrils, bundles, and CNTs [55,151,152]. At the CNT level, the secondary bonds (van der Waals, dipolar, hydrogen bonding) and friction that hold the CNTs together in bundles are in total weaker than the assembly of covalent C-C bonds of the CNTs, resulting in the CNTs slipping before breaking [142,153]. The slipping between CNTs in this context is dominated by stick-slip motions [154]. However, as evidenced by the correlation between the Raman spectra of the CNTYs and their axial strain in section 3.1.6, only a small fraction of the strain applied to

the CNTY is transferred to the individual CNTs. Therefore, the mechanical response of the CNTYs is governed by the slippage of the fibrils/bundles. At the fibril/bundle level, the slipping or breaking of the fibrils/bundles is determined by friction, which is influenced by obliquity (angular orientation of individual fibrils within the yarn) and cohesion [28]. The inter-CNT shear strength has been reported ranging between 0.05 and 1.40 GPa [154,155]. Deng et al. estimated that the inter-CNT shear strength is between 3.7 to 33 times higher than the inter-fibril shear strength [151]. This indicates that slipping between fibrils is favored over slipping between CNTs [151], as is observed herein. This argument can also be supported by estimating the critical length of the CNTs and fibrils necessary for effective load transfer within the yarn, as described in Appendix E. According to these estimations and considering the large spread of the data reported in the literature, the critical length of the CNTs comprising the yarn ranges between 35.4 nm and 8.52  $\mu\text{m}$ . Considering that the actual length of the CNTs comprising the CNTYs herein is 500  $\mu\text{m}$  (see section 2.1), the CNTYs should have failed at the tensile strength of the CNTs, which is reported between 11 and 71 GPa [82,83]. However, the CNTYs of this work actually failed around 249 MPa (obtained from the product of  $\rho = 250 \text{ kg/m}^3$  and the specific tensile strength of 994 mN/tex, see section 3.1.10). This value is several orders of magnitude lower than the tensile strength of the CNTs and even lower than the tensile strength of CNT bundles, which has been reported ranging from 1.50 to 52 GPa [112,113,156]. The calculations of Appendix E reinforce this idea. They show that the critical length of the fibrils is about 27 to 2179 times than that of the CNTs. This means that the load transfer is less efficient at the fibril level. Given these arguments, it is clear that failure of the twisted CNTYs examined here is determined by the (weak) inter-fibril shear strength.

The specific stress in the axial direction ( $\sigma_z/\rho$ , solid line), the negative of the radial strain ( $\varepsilon_r$ , solid circles), and the radial contraction ratio ( $\nu_{zr}$ , hollow triangles) of a representative CNTY as a function of the applied axial strain ( $\varepsilon_z$ ) are shown in Fig. 3.10a.  $\sigma_z/\rho$  increases with increased  $\varepsilon_z$ . After an initial adjustment in the test rig, such a relationship is fairly linear for  $\varepsilon_z < 5.0 \%$ . Nonlinearity is observed for  $\varepsilon_z \geq 5.0 \%$ . On the other hand, the negative value of  $\varepsilon_r$  increases (i.e., radial contraction) in a nonlinear fashion. This leads to the observed nonlinear behavior of  $\nu_{zr}$ , which decreases from a maximum of 5.43 ( $\pm 2.48$ ) to 1.08 ( $\pm 0.23$ ) at  $\varepsilon_z = 12.8 \%$ . The radial contraction ratio of the CNTYs is significantly higher than the Poisson's ratio of conventional solid materials such as metals, polymers, and ceramics, which is in the range between 0.2 and 0.5 [70,157,158]. As a material property, the thermodynamic limit of the Poisson's ratio is 0.5 for an

isotropic material. However, it is important to point out that the radial contraction ratio of a CNTY is not an intrinsic (material) property since it depends not only on the yarn's material but also on its porosity and structural properties. The measured values qualitatively agree with Hearle's observation that yarns would exhibit high radial contraction ratios when the twist angle is small and the ratio between the fibril's tensile modulus to the yarn's bulk tensile modulus is large [28]. Furthermore, this value of  $\nu_{zr}$  compares reasonably with the very few values reported for other CNTYs. For example, Zhang et al. [29] obtained values of up to 2.7 for draw-twist CNTYs with diameters between 1.0 and 10  $\mu\text{m}$ , comprising multiwall CNTs with diameter ranging from 5.0 to 8.0 nm. In another study, Miao et al. [58] measured  $\nu_{zr}$  values as high as 8.0 for dry-spun CNTYs with a diameter of 33.1  $\mu\text{m}$ , twist angle of 22.6°, and CNTs consisting of approximately eight walls with an outer diameter of  $\sim 10$  nm and a length of 350  $\mu\text{m}$ . This value of  $\nu_{zr} = 8.0$  was obtained at an axial strain of  $\sim 3.0\%$  [58]. The high radial contraction ratio of the CNTYs is mainly due to their high porosity, which depends on the twist angle [58].

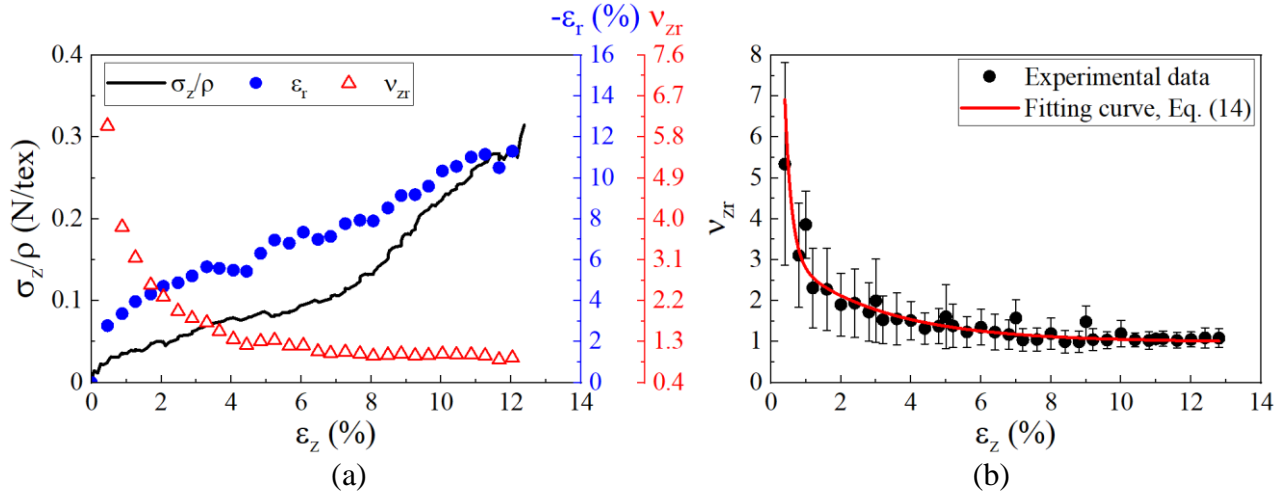


**Fig. 3.10.** In situ mechanical response of CNTYs under axial tensile loading with radial contraction measured by SEM. **(a)** Specific stress in the axial direction ( $\sigma_z/\rho$ ), radial strain ( $\epsilon_r$ ) and radial contraction ratio ( $\nu_{zr}$ ) of a representative CNTY as a function of axial strain ( $\epsilon_z$ ), **(b)** measured  $\nu_{zr}$  as a function of  $\epsilon_z$ , including the fitting curve given by Eq. (3.1).

During axial loading, the fibrils stretch and slip in the direction of the applied load, which generates untwisting (decrease in twist angle, Fig. 1.6) and lateral compression, pressing the fibrils together. This closes the gaps between fibrils and thus reduces the diameter of the CNTY. However, there is a limit to the relative motion of the fibrils due to packing and friction among them. At low axial tensile strain ( $\epsilon_z < 2.0\%$ ), the fibrils have more motion freedom due to the higher porosity, which causes a high radial contraction ( $\epsilon_r$ ) and hence high  $\nu_{zr}$ . As the axial tensile strain increases the

fibrils have progressively less motion freedom due to compaction, which yields a smaller rate of radial contraction. It is noteworthy that the degree of packing also depends on the distribution of fibril diameter, see e.g., [159]. Therefore, the behavior of  $v_{zr}$  as a function of  $\varepsilon_z$  is highly nonlinear, attaining lower and more stable values at larger strains (Fig. 3.10b). This behavior can be fit using an exponentially decaying function given by,

$$v_{zr} = v_{zr\infty} + c_1 e^{-\frac{\varepsilon_z}{d_1}} + c_2 e^{-\frac{\varepsilon_z}{d_2}} \quad (3.1)$$

where  $v_{zr\infty} = 0.992$ ,  $c_1 = 30.1$ ,  $d_1 = 1.96 \times 10^{-3}$ ,  $c_2 = 2.33$ , and  $d_2 = 27.7 \times 10^{-3}$ . Equation (3.1) results in the continuous line fitting the experimental data of  $v_{zr}$  in Fig. 3.10b. In addition, this equation was used as an evolutive input parameter in the model for tensile mechanical behavior discussed in section 2.3. For the model input, the values of  $v_{zr}$  for  $\varepsilon_z < 0.36$  % were fixed at 7.91 since there are not measured data beneath this point, and Eq. (3.1) largely overshoots the first measured value for lower strains.

### 3.1.8. Tensile mechanical properties under monotonic loading

The mechanical response of five CNTY specimens subjected to tensile loading is shown in Fig. 3.11. It is observed that mechanical response of CNTYs is nonlinear and exhibits increasing variability beyond a 0.5 % strain. The CNTYs possess a specific tensile modulus ( $E/\rho$ ) of 17.2 ( $\pm 2.8$ ) N/tex. The ultimate (failure) strain ( $\varepsilon_{z_u}$ ) and the specific tensile strength ( $\sigma_{z_u}/\rho$ ) also exhibit variability, with mean values of  $\varepsilon_{z_u} = 5.75$  ( $\pm 1.00$ ) % and  $\sigma_{z_u}/\rho = 677$  ( $\pm 68$ ) mN/tex. In the case of  $\varepsilon_{z_u}$ , the variability is more apparent, ranging from 4.2 % to 7.0 %. In the literature, the mechanical response of the CNTYs for small strains (ca.  $\varepsilon_z < 1.0$  %), has been attributed to straightening and untwisting of the fibrils/bundles [62,63]. This was confirmed by the correlation between the D band peak position of the CNTYs and their axial strain (see section 3.1.6), where below  $\varepsilon_z = 0.5$  % the D band exhibit negligible peak shifting. For  $\varepsilon_z \geq 0.5$  %, the mechanical response of the CNTYs can be attributed to slippage of the fibrils/bundles (see sections 3.1.6 and 3.1.7). However, CNTYs exhibit a complex mechanical response that depends not only on the properties of the fibrils, bundles and CNTs that make up the yarn but also on structural parameters [160]. Parameters such as the test length (gage length) of the yarn [60] and strain rate [61] also impact its mechanical behavior.

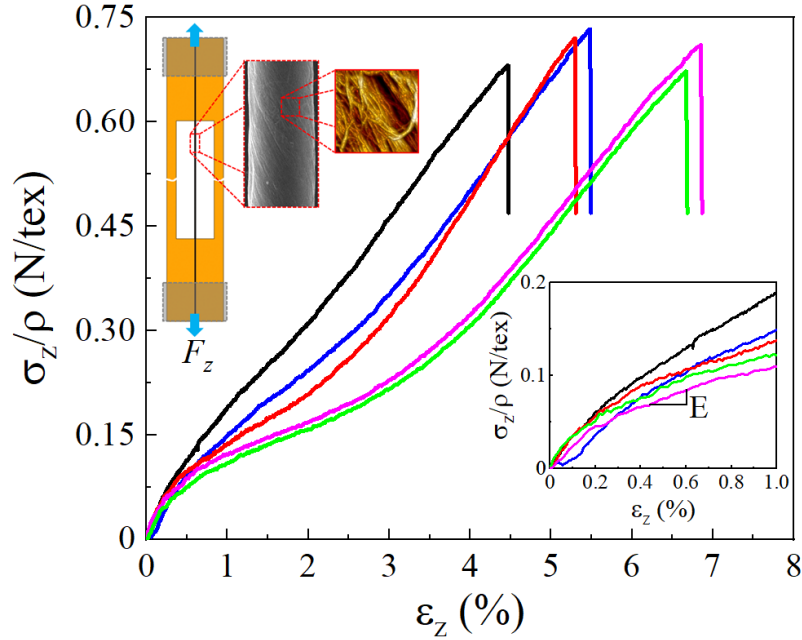


**Fig. 3.11.** Mechanical response of CNTYs under uniaxial tensile loading.

### 3.1.9. Cyclic tensile mechanical properties and hysteresis

The mechanical response of a representative CNTY subjected to cyclic tensile loading up to  $\varepsilon_z = 1.0\%$  is shown in Fig. 3.12a. For increased clarity, the response of selected cycles (1, 100, 200, and 300) is shown in Fig. 3.12b. It is observed that as the number of cycles increases, the  $\sigma_z/\rho$  vs.  $\varepsilon_z$  curves move towards higher values of specific stress. Similarly, as the number of cycles increases, the separation between the loading and unloading curves decreases, i.e., the area between loading and unloading curves (the hysteresis loop,  $H$ ) decreases. Figure 3.12c shows that the residual specific stress ( $\sigma_{z_{Res}}/\rho$ ) of the CNTYs presents some variations from cycle to cycle, but overall presents an increasing trend that stabilizes after cycle  $\sim 230$ . When a CNTY is stretched beyond certain strain, its structure changes irreversibly, and if this is repeated cyclically continuous structural changes are expected. The analysis of the in situ Raman spectra during tensile testing (see section 3.1.6) suggests that deformation of the C-C bonds of the CNTs is very small or negligible for small strain levels (1.0% in this case). Thus, the residual specific stress is attributed to the structural rearrangement of the fibrils and bundles within the CNTY. In addition, it is expected that the CNTY present residual stresses in their fibrils/bundles due to the twisting that is applied when they are spun. This explains why the residual value of  $\sigma_{z_{Res}}/\rho$  upon unloading to zero strain is different for each cycle. However, above cycle 230 the residual specific stress stabilizes around 0.06 N/tex.

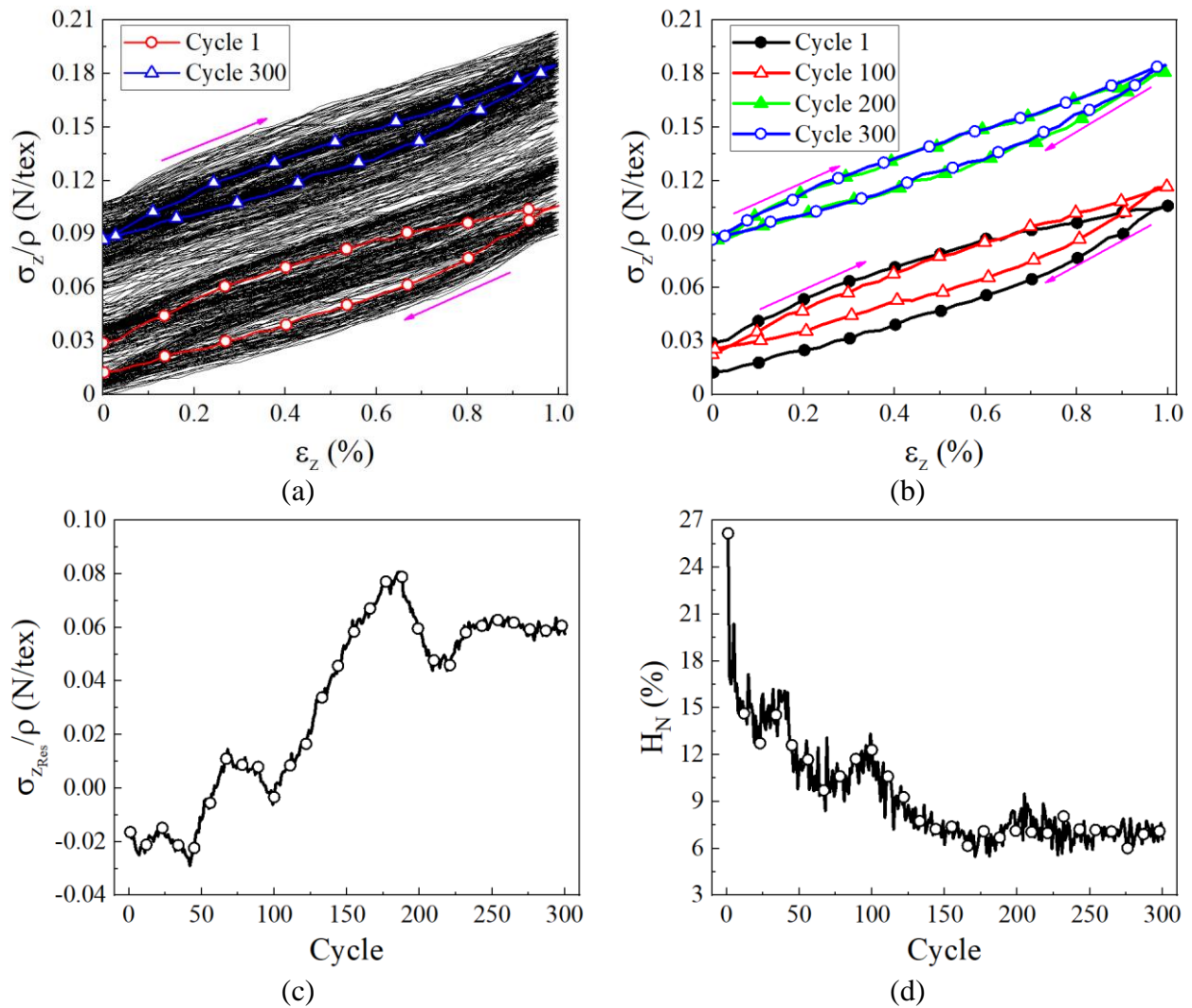


**Fig. 3.12.** Mechanical hysteresis of a representative CNTY under cyclic tensile loading up to  $\varepsilon_z = 1.0\%$ . (a) Tensile response of all 300 cycles, (b) tensile response of selected cycles, (c) residual specific stress ( $\sigma_{zRes}/\rho$ ), (d) normalized hysteresis ( $H_N$ ).

It has been demonstrated that CNTYs exhibit internal slippage and stretching of their fibrils/bundles, as well as untwisting and reduction in diameter under uniaxial tensile loading (see sections 3.1.6 and 3.1.7). As the CNTY is stretched, their fibrils slip and align with the loading direction. However, unlike a monotonic tensile test where the stretching and alignment of the fibrils are continuous and constant, in the cyclic tensile test the rearrangement and alignment of the fibrils is discontinuous and not constant. This could lead to the oscillations in the residual specific stress observed in Fig. 3.12c. With each loading cycle, the fibrils and CNT bundles slip and rearrange, breaking some of the secondary bonds (van der Waals, dipolar, hydrogen bonding) between them, and forming new ones [68,69,161,162]. On the other hand, with each unloading cycle, the fibrils/bundles that have kept their original secondary bonds during the loading cycle might return

to their initial position, while the fibrils/bundles that formed new secondary bonds move to a new location or rearrange [68,69,161,162]. The rate of occurrence of these phenomena has a degree of randomness and could be the reason for the oscillatory behavior between subsequent cycles in Fig. 3.12c. Because of this reason, the normalized hysteresis parameter ( $H_N$ ) shown in Fig. 3.12d also presents some oscillations among subsequent cycles, but the decreasing trend with the cycle number is marked.  $H_N$  starts at ~26 % and decays rapidly with each cycle, until leveling off at ~7.0 %, above cycle 230. During cycling tensile loading/unloading, the CNT network comprising the CNTY changes through attaching/detaching and zipping/unzipping mechanisms [66–68], which may contribute to the energy dissipation observed in  $H_N$ . The process of unzipping between CNTs consumes energy to overcome the van der Waals bonds [69,162], while the zipping process does not require energy consumption [162]. Unlike the zipping/unzipping mechanism, the attaching/detaching mechanism irreversibly changes the CNT network morphology during each loading/unloading cycle [67–69]. Thus, the decrease in  $H_N$  with the number of cycles could be due to the decrease in the number of fibrils that are rearranging (irreversible changes) in the CNTY. Therefore, the fact that the hysteresis remains constant above cycle 230 suggests that there are no longer irreversible changes in the internal structure of the CNTY, leaving only the energy dissipation by friction.

Additional cycling experiments were performed, increasing the strain by 0.1 % after each cycle until reaching a strain of 1.6 % (16 cycles in total). The response of a representative CNTY subjected to cyclic tensile loading under incremental strain is shown in Fig. 3.13a. Although the test plan involves 16 cycles, for clarity, the tensile response is shown only for cycles 4, 8, 12, and 16. It is observed that the stiffness of the CNTY slightly decreases with each cycle, which is due to redistribution of the fibrils/bundles after each incremental loading cycle. In addition, as the cycles and strain increase, the area between the loading and unloading curves (i.e., the hysteresis loop,  $H$ ) also increases. This energy dissipation loop reaches 0.68 J/g (tex = g/km; N/tex = kJ/g) or 0.17 J/cm<sup>3</sup> (obtained by dividing  $H$  by the volumetric mass density of the CNTYs,  $\rho = 0.25$  g/cm<sup>3</sup>) for the last cycle (cycle 16, corresponding to  $\varepsilon_z^{\text{Max}} = 1.6$  %).

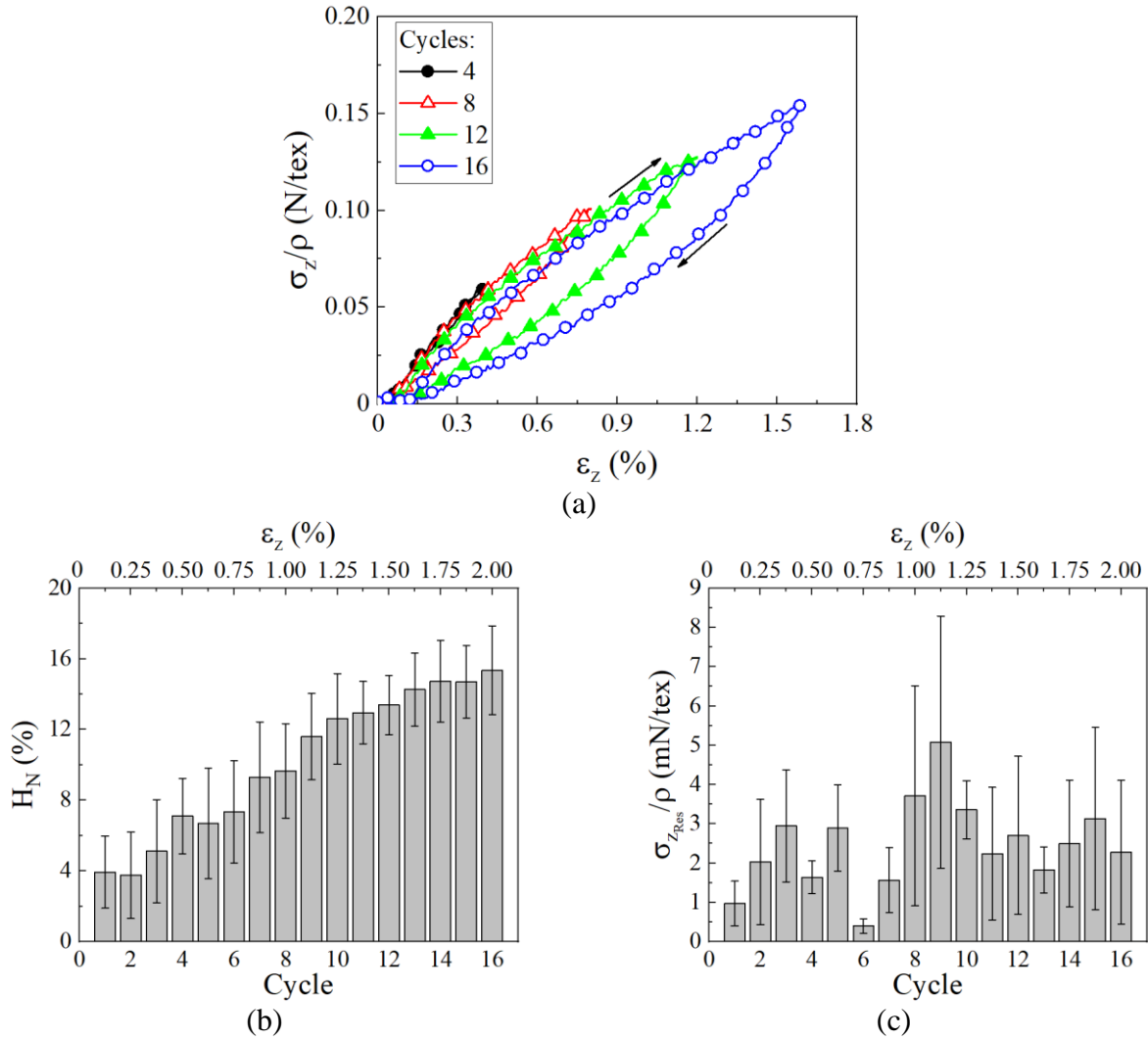


**Fig. 3.13.** Mechanical hysteresis of a representative CNTY under incremental strain cyclic tensile loading. (a) Tensile behavior of different cycles, (b) normalized hysteresis ( $H_N$ ), (c) residual specific stress ( $\sigma_{zRes}/\rho$ ).

The increment of the energy dissipation leads to an increase in  $H_N$ , as shown in Fig. 3.13b, reaching  $15.4 (\pm 2.5)$  % for the last cycle (16). The energy dissipation of the CNTYs leads to a maximum value of residual specific stress of  $5.06 (\pm 3.20)$  mN/tex (at cycle 9,  $\epsilon_z^{Max} = 0.9$  %, Fig. 3.13c). For this test, the behavior of  $\sigma_{zRes}/\rho$  varied randomly throughout all the cycles, as shown in Fig. 3.13c. The increase in  $H_N$  indicates that there is an increase of the irreversible changes in the internal structure (rearrangement of fibrils and CNT bundles) of the CNTY. This supports the hypothesis that the drop in  $H_N$  in the cycles with constant deformation is due to the decrease of the irreversible changes in the internal structure of the CNTY, and that the remaining hysteresis is due to the energy dissipation by friction. In terms of the dissipated energy density ( $H/\rho$ ), the CNTYs reaches a value

of  $0.06 \text{ J/cm}^3$  during the first cycle ( $H = 0.24 \text{ J/g}$ ;  $N/\text{tex} = \text{kJ/g}$ ), and above cycle 230,  $H/\rho$  remains constant around  $0.03 \text{ J/cm}^3$  ( $H = 0.12 \text{ J/g}$ ). Table 3.4 compares the dissipated energy per unit weight of the CNTYs to that of other materials. In Table 3.4, dissipated energy per unit weight of the CNTYs was chosen at cycle 250 because at this point both  $\sigma_{z\text{Res}}/\rho$  and  $H_N$  remain constant. Such a comparison suggests that CNTYs are materials with extraordinary energy dissipation capabilities, whose specific energy dissipation capability (per unit weight) is comparable to that of carbon steel.

**Table 3.4.** Specific (per unit density) dissipated energy of different materials.

Material	Dissipated energy per unit weight (J/g)	Description	Ref.
CNTYs	0.12	Obtained by cyclic tensile tests at cycle 250. $\varepsilon_z^{\text{Max}} = 1.0 \%$ .	This work
Carboxylated nitrile rubber	$1.89 \times 10^{-4}$	Obtained by cyclic tensile tests. The dissipated energy ( $237.7 \text{ J/m}^3$ ) was divided by the density ( $1.26 \text{ g/cm}^3$ ). $\varepsilon_z^{\text{Max}} = 5.0 \%$ .	[163]
A-516 Gr. 70 carbon steel	0.23	Obtained by cyclic tensile tests. The dissipated energy ( $1.79 \text{ J/cm}^3$ ) was divided by the density ( $7.85 \text{ g/cm}^3$ ).	[164]
Segmented poly(urethane-urea) fibers	0.60	Obtained by cyclic tensile tests. The dissipated energy ( $0.75 \text{ J/cm}^3$ ) was divided by the density ( $1.25 \text{ g/cm}^3$ ).	[165]
Sisal fiber/polyester composite	$3.26 \times 10^{-3}$	Obtained by cyclic tensile tests. The dissipated energy ( $4.6 \text{ mJ/cm}^3$ ) was divided by the density ( $1.41 \text{ g/cm}^3$ ).	[166]

### 3.1.10. Electromechanical response under tensile loading

Before tensile testing, the specific electrical conductivity of the CNTYs ( $\xi/\rho$ ) at  $\varepsilon_z = 0$  and room temperature ( $\sim 25 \text{ }^\circ\text{C}$ ) was measured from the tensile coupons, using the distance between electrodes ( $L_g = 25 \text{ mm}$ , Fig. 2.6), yielding  $1211 (\pm 37) \text{ S}\cdot\text{cm}^2/\text{g}$ . The electrical conductivity of the CNTYs is governed by the conductivity of the individual CNTs as well as the degree of electrical contact (by physical contact or by tunnel effect due to their proximity) between the CNTs and among all hierarchical entities comprising the yarn [27,167].

The piezoresistive response of the CNTYs subjected to monotonic tensile loading is shown in Fig. 3.14. The  $\sigma_z/\rho$  vs.  $\varepsilon_z$  response (solid circles) starts with a small linear zone and approximately around  $\varepsilon_z = 0.5 \%$  presents some degree of nonlinearity. The correlation between the D band peak

position of the CNTYs and their axial strain (see section 3.1.6) showed that the mechanical response for  $\varepsilon_z < 0.5\%$  is due to structural changes in the CNTY caused by the straightening and untwisting of the fibrils/bundles. Due to the inherent structural variability of the CNTYs, there was some variability in  $\varepsilon_{z_u}$  among the five replicates tested, reaching values between 2.4% and 6.3% and presenting a mean value of  $\varepsilon_{z_u} = 4.55 (\pm 1.77)\%$ . The CNTYs exhibited values for  $\sigma_{z_u}/\rho$  ranging from 0.84 N/tex to 1.21 N/tex, with a mean value of  $\sigma_{z_u}/\rho = 994 (\pm 140)$  mN/tex. The specific tensile modulus ( $E/\rho$ ) of the CNTYs is  $23.2 (\pm 8.9)$  N/tex. Regarding the piezoresistive response observed in Fig. 3.14 (empty circles), it is observed that for  $\varepsilon_z \leq 1.0\%$ , the fractional change of electrical resistance increases almost linearly with increased strain. The gage factor ( $GF$ ) obtained in the range of  $0.2\% \leq \varepsilon_z \leq 1.0\%$  was  $0.36 \pm 0.13$ . For  $\varepsilon_z > 1.0\%$ , the rate of increase of the fractional change of electrical resistance ( $\Delta R/R_0$ ) increases rapidly and suddenly peaks close to failure. Therefore, it is expected that structural changes of the fibrils/bundles within the CNTY due to the applied strain play a paramount role in its piezoresistive response. Since CNTYs are hierarchical materials with a strong property-structure dependence, there is not a universal piezoresistive response for CNTYs. As discussed in section 3.1.7, when a CNTY is subjected to tensile loading, its fibrils/bundles stretch and slip in the direction of the applied load, leading to a decrease in twist angle and, consequently, a reduction in diameter (Fig. 3.10). This decrease in diameter results in reduced porosity (increased packing density), increasing lateral contact between fibrils/bundles and decreasing the electrical resistance of the CNTY [52,90,91]. However, the slipping of the fibrils/bundles also decreases the length of the lateral contact between them, thereby increasing the electrical resistance [52,90,91]. Additionally, the increased distance between electrodes implies a higher electrical resistance. These are the phenomena that govern the electromechanical response of the CNTYs under uniaxial tensile loading, resulting in increased electrical resistance with increased strain. These competing factors can also explain why the electrical response of CNTYs is nonlinear, despite their mechanical behavior under tension being quite linear. However, in addition to the internal structural rearrangement, the electrical response of the CNTYs is also influenced by capacitance and electrical charge accumulation, as discussed in section 3.1.11.

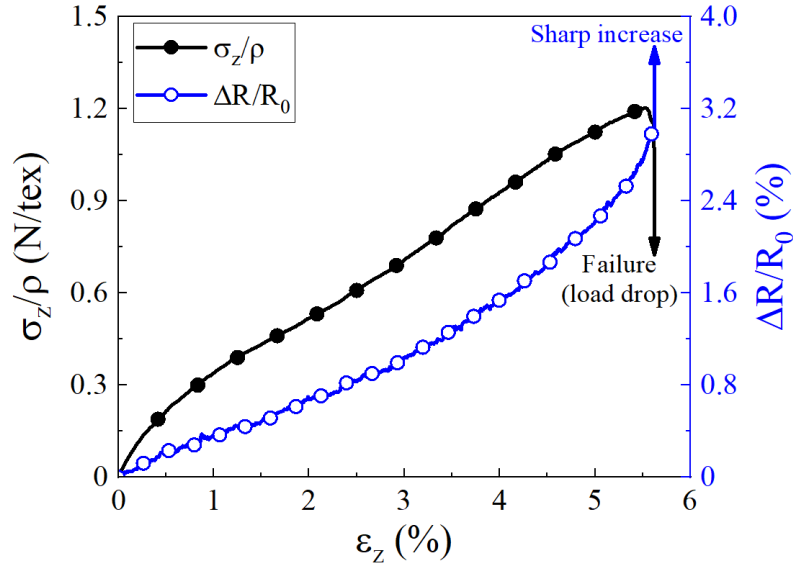
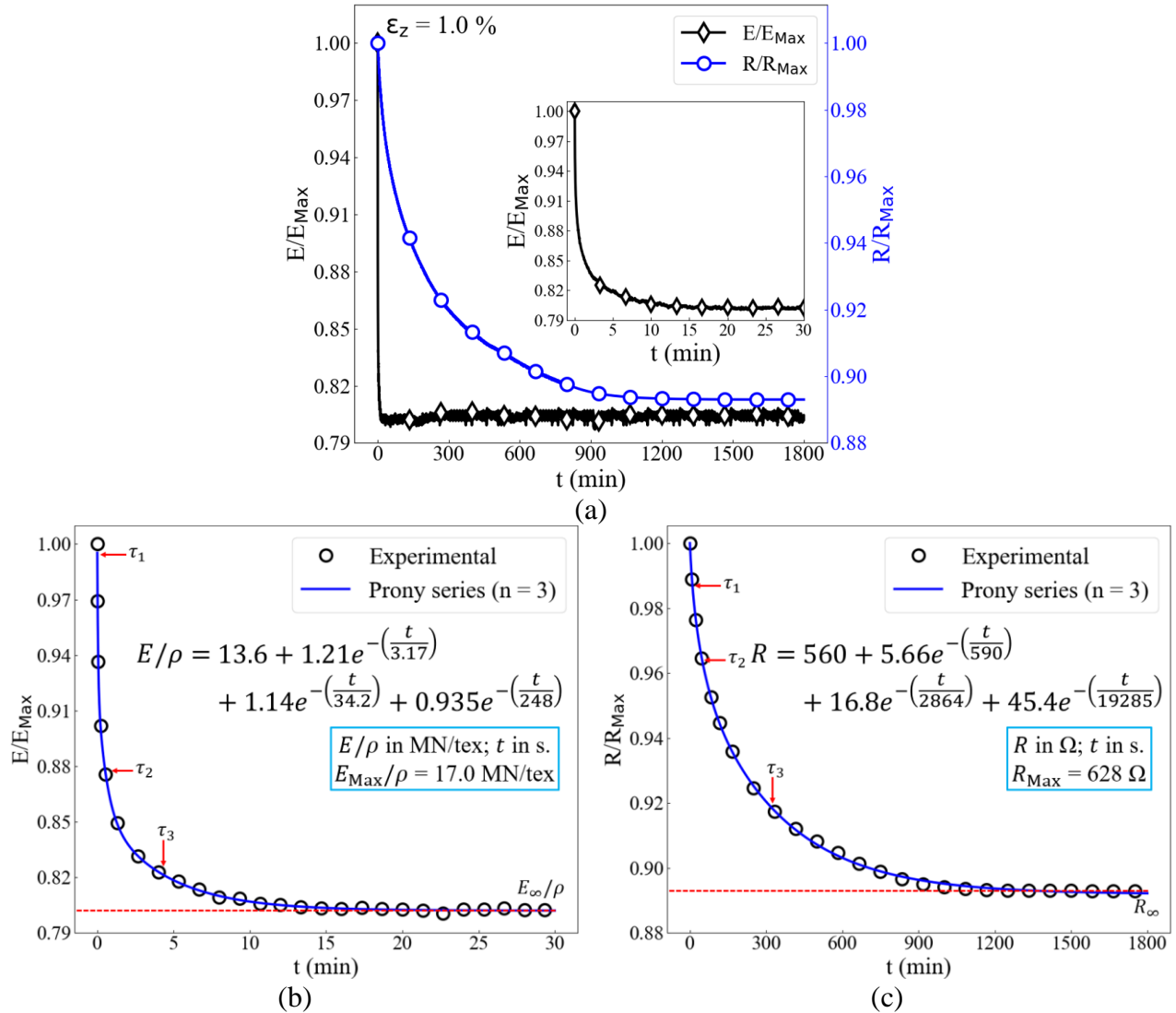


Fig. 3.14. Electromechanical response of a representative CNTY under uniaxial tensile loading.

### 3.1.11. Stress and electrical relaxation responses under tensile loading

The normalized specific tensile modulus ( $E/E_{\text{Max}}$ , where  $E_{\text{Max}}$  is the maximum value of  $E$ ) and the normalized electrical resistance ( $R/R_{\text{Max}}$ , where  $R_{\text{Max}}$  is the maximum value of  $R$ ) as a function of elapsed time ( $t$ ) of a representative CNTY under constant axial tensile strain ( $\epsilon_z = 1.0\%$ ) are shown in Fig. 3.15a. Only measured data are plotted in Fig. 3.15a. Data were measured at a rate of 1 data/s, so the experimental curves look continuous; the few skipped diamond and circle symbols shown in the plots are only included to ease identification. The time  $t = 0$  corresponds to the instant where  $\epsilon_z = 1.0\%$  was first reached and held constant, i.e., where the relaxation test began. It is observed that  $E/E_{\text{Max}}$  drops rapidly during the first 5 min (inset in Fig. 3.15a), decreases at a lower rate until  $t \sim 20$  min, and then remains nearly constant.



**Fig. 3.15.** Specific tensile modulus and electrical resistance relaxations of a representative CNTY under constant axial tensile strain ( $\epsilon_z = 1.0\%$ ). (a) Normalized specific modulus ( $E/E_{Max}$ ) and normalized electrical resistance ( $R/R_{Max}$ ) as a function of elapsed time ( $t$ ), (b)  $E/E_{Max}$  as a function of  $t$  and its fitting to Eq. (2.6) with  $n = 3$  (continuous line), (c)  $R/R_{Max}$  as a function of  $t$  and its fitting to the electrical form of Eq. (2.6) with  $n = 3$  (continuous line).

To obtain the relaxation times, the Prony series of Eq. (2.6), was fit to the CNTY relaxation curves (Fig. 3.15b and c). In such figures, some measured points (experimental data) have been skipped for the sake of clarity in the presentation of the curves. Curve fitting using Eq. (2.6) was initially carried out increasing the number of elements ( $n$ ). The final fitting curves shown were obtained using a Prony series with three elements ( $n = 3$ ), since the variation obtained by using additional elements was less than 1.0%. The fitting curve of  $E/E_{Max}$  as a function of  $t$  is shown in Fig. 3.15b, while Table 3.5 shows the three elements ( $i$ ) of this Prony series. The first two relaxation times ( $\tau_i$ ,

$i = 1, 2$ ), correspond to the first 4 min, indicating that the main structural changes due to relaxation occur within this time.

**Table 3.5.** Prony series elements for the specific tensile modulus and electrical resistance relaxation of a representative CNTY at  $\varepsilon_z = 1.0\%$ .

$i$	Mechanical parameters		Electrical parameters	
	$E_\infty/\rho = 13.6 \text{ MN/tex}$		$R_\infty = 560 \Omega$	
	$E_i/\rho \text{ (MN/tex)}$	$\tau_i \text{ (s)}$	$R_i \text{ (}\Omega\text{)}$	$\tau_i \text{ (s)}$
1	1.21	3.17	5.66	590
2	1.14	34.2	16.8	2864
3	0.935	248	45.4	19,285

During axial loading, the fibrils are stretched, untwisted, and slipping occurs, reorganizing the yarn's structure and generating irreversible conformational changes. This rearrangement is not instantaneous but requires some time. Therefore, when the strain is held constant, it is expected that some CNTs, bundles, and fibrils continue rearranging for a certain time. This process is stochastic, as it involves a random progression of inter-fibril/bundle slipping between neighbours. However, the most stretched fibrils at the yarn's surface are expected to be the first to slip. This is due to the lower packing density and lower compressive transverse stress experienced by the fibrils at the yarn's surface, compared to the fibrils at the center of the yarn (see Appendices D.2 and D.3). As a result, compressive transverse stress is relieved at the inner sections of the yarn. The release of compressive transverse stress allows the internal fibrils to slip as well, since the packing density decreases, therefore decreasing the friction between fibrils. This occurs as a rapid chain reaction. This process results in the rapid stress relaxation of the CNTY, where the tensile modulus drops up to 20 % during the first 5 min, and then drops only  $\sim 2.0\%$  more for the next 10 min. In the case of  $R/R_{\text{Max}}$  (Fig. 3.15c), the electrical resistance decreases as the stress reduces, but it does not decrease at the same rate as the normalized specific tensile modulus (horizontal axes of Fig. 3.15b and c). According to Fig. 3.15, the structural rearrangement occurs faster than the electrical one, and electrical equilibrium takes longer than the structural one. The electrical resistance keeps on decreasing exponentially even after the specific tensile modulus has reached a plateau. For instance, the specific tensile modulus reaches  $\sim 67\%$  ( $1/e$ ) of its total relaxation within 33 s,

whereas the electrical resistance reaches the same percentage of its total relaxation after ~189 min. This decrease in electrical resistance persists for around 20 h, and then levels off. The fitting curve of  $R/R_{\text{Max}}$  as a function of  $t$  is shown in Fig. 3.15c and the fitting coefficients are shown in Table 3.5. In Table 3.5, all relaxation times of  $R$  are far greater than those for  $E/\rho$ . In this case, the first two relaxation times ( $\tau_i, i = 1, 2$ ), correspond to the first 48 min, and during this time  $R$  has fallen only around 4.0 %. This behavior implies that not only internal restructuring of the fibrils, bundles, and CNTs affects the electrical resistance of the CNTYs. The radial contraction during stretching (see section 3.1.7) and its gradual relaxation is expected to affect the electrical response of CNTYs. At the bundle level, frictional sliding between fibrils occurs over time, which causes relaxation. Furthermore, at smaller scales, stretched and untangled CNTs and their bundles may also break their secondary bonds over time. However, the fact that electrical relaxation times are far longer than mechanical ones implies that not only internal restructuring of the fibrils and CNTs affects the electrical resistance of the CNTYs. According to the Wiechert's model used, CNTYs exhibit a resistive-capacitive (RC) behavior, where the electrical conductivity of the effective RC circuit decreases exponentially over time. This is because the electrical properties of bundles of CNTs are different to those of individual CNTs [168]. CNT bundles accumulate electrical charge, and this leads to electrical charge polarization and charge carrier relaxation phenomena. In CNTYs, groups of CNT bundles and fibrils are separated by empty spaces that could be filled with amorphous carbon, air, moisture, or residues of catalyst particles. This effectively create micro- and meso-capacitors, inducing polarization and influencing their time-dependent charge transport properties [169].

### 3.1.12. Constrained thermoresistive response

The constrained (inside the DMA tensile test rig) thermoresistive response of a representative CNTY is shown in Fig. 3.16. It is observed that the fractional change of electrical resistance ( $\Delta R/R_0$ ) of the CNTY decreases linearly with temperature ( $T$ ) up to ~100 °C during heating. Around this temperature (100–160 °C), there is a marked step upwards in  $\Delta R/R_0$  towards positive values (which was present in all replicates tested) that continues until ~160 °C. The thermoresistive curve continues with a similar negative slope thereafter. According to the TGA reported in section 3.1.4, the CNTY loses up to ~13 % in weight during heating from 30 to 400 °C. Important mass losses (~5.0 %) occur between 100 and 160 °C which is the temperature interval where a marked step in  $\Delta R/R_0$  is observed in Fig. 3.16. Mass losses at temperatures below 400 °C are attributed to

evaporation of the densifier (acetone) used in the CNTY synthesis and adsorbed moisture [170], and probably to the degradation of amorphous carbon and other carbonaceous forms [170–172]. The evaporation of functional groups and byproducts (mass loss) of the CNTY likely causes rearranging of their CNT bundles and changes in porosity, leading to a sudden change in electrical resistance. Decrease in the electrical resistance of the CNTYs with temperature is a negative thermoresistive response, which has been previously observed for unconstrained CNTYs [173,174]. As temperature increases, the density and mobility of electric charge carriers also increase, resulting in a quasilinear drop in the electrical resistance of individual CNTs that make up the CNTY [27,173]. This mechanism has also been proposed as the governing thermoresistive mechanism of pitch-based carbon fibers [33,36,46]. In order to quantify the thermoresistive sensitivity of the CNTYs, the temperature coefficient of resistance ( $\beta_i$ ) was obtained from the slope of the linear fit of the  $\Delta R/R_0$  vs. temperature changes ( $\Delta T = T - T_0$ , where  $T_0 = 30$  °C) curve in the three temperature intervals indicated in Fig. 3.16. In the  $0 \leq \Delta T \leq 50$  K range, the CNTYs present a value of  $\beta_1 = -8.63 \times 10^{-4} (\pm 0.79 \times 10^{-4}) \text{ K}^{-1}$ . After the step in  $\Delta R/R_0$ ,  $\beta_2 = -7.78 \times 10^{-4} (\pm 1.80 \times 10^{-4}) \text{ K}^{-1}$  is measured in the  $130 \text{ K} \leq \Delta T \leq 250 \text{ K}$  interval. This means that the thermoresistive response is indeed very similar in the full temperature range examined, except in the interval between 100 °C and 160 °C, where the sudden step is observed. Additionally, the cooling curve exhibits a linear behavior throughout the entire range, with  $\beta_3 = -7.26 \times 10^{-4} (\pm 0.05 \times 10^{-4}) \text{ K}^{-1}$ . The proximity of the numerical results for  $\beta_1$ ,  $\beta_2$  and  $\beta_3$  reinforces the observation of a quasi-linear thermoresistive behavior of the CNTY for the full temperature range, upon heating and cooling. The average values of the temperature coefficient of resistance,  $\beta_1$ ,  $\beta_2$  and  $\beta_3$ , are comparable (a bit smaller) to those reported for similar CNTYs under unconstrained (free) conditions, e.g.,  $-9.46 \times 10^{-4} \text{ K}^{-1}$  [173] and  $-12 \times 10^{-4} \text{ K}^{-1}$  [175]. The difference may be ascribed to the boundary conditions (constrained or not) used in each experiment.

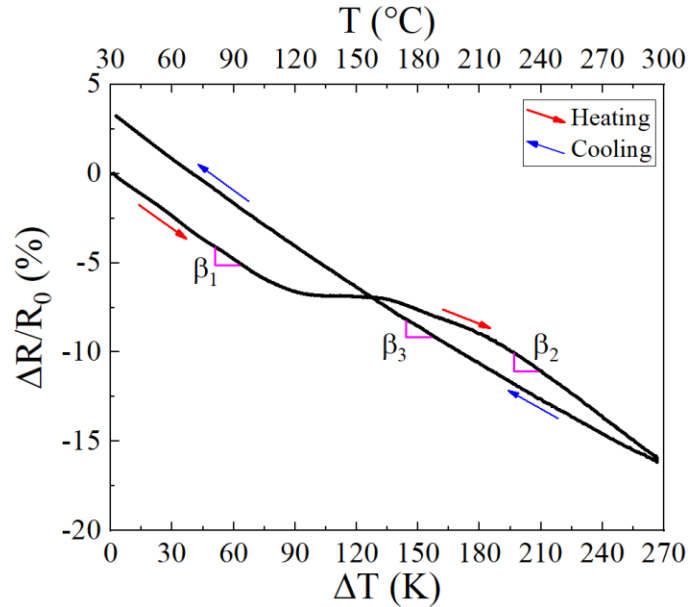


**Fig. 3.16.** Constrained thermoresistive response of a representative CNTY.

### 3.1.13. Dynamic mechanical response

The DMA tensile response of the CNTYs as a function of temperature ( $T$ ) is shown in Fig. 3.17a. The DMA test shown in Fig. 3.17a was conducted under uniaxial tensile cyclic loading at 1 Hz, with a heating rate  $5\text{ }^{\circ}\text{C}/\text{min}$  and a static force ( $F_{z_s}$ ) of 18 mN. The effects of static force, frequency, preheating, and heating rate are discussed in Appendix A. It is observed that the storage modulus ( $E'$ ) decreases from  $\sim 100\text{ GPa}$  (specific storage modulus,  $E'/\rho = 0.27\text{ N/tex}$ ) to  $\sim 15\text{ GPa}$  ( $E'/\rho = 0.04\text{ N/tex}$ ). The loss modulus ( $E''$ ) varies between  $7.0\text{ GPa}$  (specific loss modulus,  $E''/\rho = 0.02\text{ N/tex}$ ) and  $18\text{ GPa}$  ( $E''/\rho = 0.05\text{ N/tex}$ ). From  $-50$  to  $\sim 130\text{ }^{\circ}\text{C}$ ,  $E'$  decreases rapidly with increasing temperature. After  $130\text{ }^{\circ}\text{C}$ ,  $E'$  remains almost constant. This quick decrease in  $E'$  at low temperatures is different from other materials such as polymers, where  $E'$  typically decreases slowly until the glass transition temperature of the polymer [66]. This is because in the glassy state, polymer segments become more mobile given the softening of the material [176]. In the case of CNT assemblies (CNTYs), the change in  $E'$  with temperature is due to restructuring at the CNT and CNT bundle level [65–67]. For the same range of temperatures, the loss modulus ( $E''$ ) remains nearly constant, which yields a damping ratio ( $\tan(\delta) = E''/E' = (E''/\rho)/(E'/\rho)$ ) which increases steadily from  $\sim 0.2$  to  $\sim 0.6$  up to  $60\text{ }^{\circ}\text{C}$ , and then oscillates around  $\sim 0.6$  for higher temperatures. Notice that 30 DMA tests were conducted in the whole test plan (see Table 2.1). Only selected results are shown, and the results showed some degree of specimen-to-specimen scattering (see

Fig. A.1). The variability observed in the dynamic mechanical response is associated with the non-homogeneous fiber architecture, due to the current state of the art of synthesis methods.

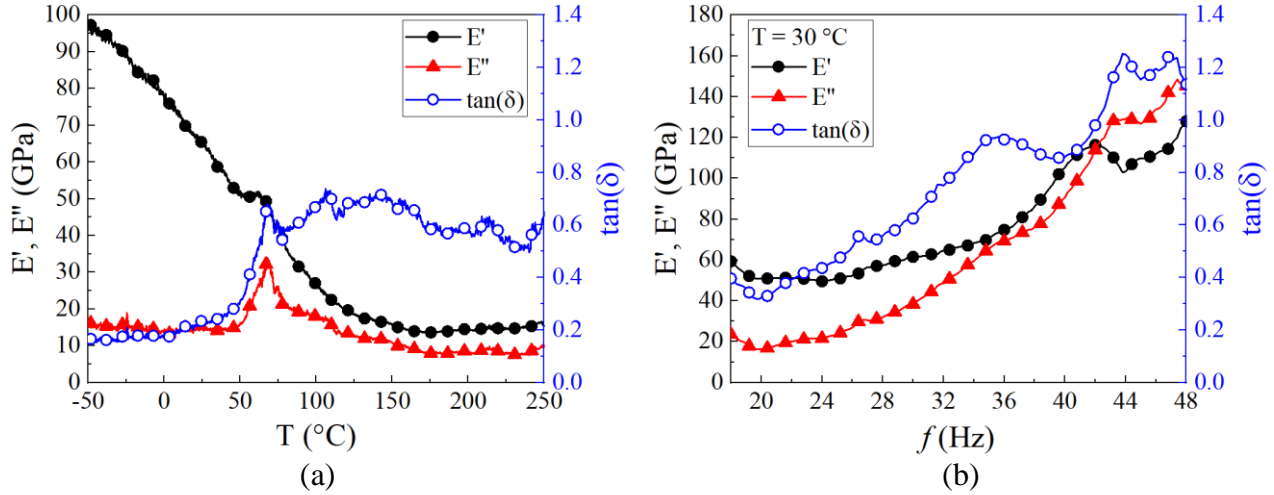


**Fig. 3.17.** Tensile DMA response of representative CNTYs. (a) Response as a function of temperature ( $T$ ), (b) response as a function of frequency ( $f$ ).

It is well known that the damping ratio of traditional materials such as polymers and metals is temperature-dependent, due to phase changes (e.g., glass or melt transitions). However, the damping ratio of CNT assemblies, such as CNTYs, depends chiefly on structural changes of its hierarchical structure [66,67]. According to the TGA in Fig. 3.5, the onset of CNT thermal degradation occurs around 550 °C, so the sharp changes in  $E'$  below 130 °C cannot be explained by material property degradation. Instead, alignment and rearranging of the bundles and fibrils comprising the yarn, sliding and slippage between bundles/fibrils (stick-slip motions), and zipping/unzipping at CNT connections have been recognized as mechanisms affecting the dynamic mechanical response of CNT assemblies [65,66]. As evidenced by the correlation between the Raman spectra of the CNTYs and their axial strain in section 3.1.6, the C-C bond stretching is small. Thus, tensile loading of the CNTY should be governed by the structural mechanisms discussed in sections 3.1.6 and 3.1.7. This is because less energy is required to break the secondary bonds and disentangle the fibrils/bundles, than to break the C-C bonds of the CNTs. All these mechanisms are expected to be affected by temperature. TGA (see section 3.1.4) also shows that, if the yarn is not preheated, certain byproducts suffer thermal degradation below 130 °C. Therefore, the thermal transformation of such byproducts may be further affecting the structural changes expected at the bundle level and changing the porosity of the yarn. This phenomena may facilitate CNT bundles relaxation through slipping [67]. As a result, CNT bundles (and CNTs) begin to orient parallel to the loading direction (the twist angle decreases), decreasing the contacts between CNT

bundles and, therefore, the inter-bundle friction. This causes  $E'$  to decrease since the load transfer between two adjacent bundles is affected by the number of contacts between them [177]. On the other hand,  $E''$  remains almost constant or with a slightly increasing trend, until a temperature of  $\sim 65$  °C is reached. This is explained by attachment-detachment of the CNTY bundles originated by the increase and decrease of contact points, until a relative stable value is reached. Once this critical temperature is reached ( $T > 65$  °C in this case), the bundles reach the maximum level of relaxation, so  $E''$  levels off. It may also be possible that some large hydrocarbon chains reside on the surface of the CNTs grown by chemical vapor deposition, and they start to flow around this temperature.

The DMA tensile response of the CNTYs as a function of frequency ( $f$ ) for  $T = 30$  °C is shown in Fig. 3.17b. Frequency responses for different temperatures are shown in Appendix A.2. Results indicate a shift of  $E'$  towards lower values and of  $E''$  towards higher values as the temperature increases, consistent with the results of Fig. 3.17a. A frequency-independent response of the yarn with only random oscillations was observed for frequencies smaller than 18 Hz (results not shown). After 18 Hz, both  $E'$  and  $E''$  increase with increased frequency, indicating a frequency-stiffening behavior. The results indicate that energy dissipation mechanisms become more prominent as  $f$  increases.  $E''$  has a higher rate of increase (up to  $\sim 700$  % at 48 Hz) than  $E'$  (up to  $\sim 250$  % at 48 Hz), which results in the increase of  $\tan(\delta)$  with increased  $f$ . The damping ratio goes from  $\sim 0.40$  at 18 Hz to 1.20 at 48 Hz. This is a very high damping ratio, indicating that the CNTY is an outstanding energy dissipation material. Materials with high energy dissipation capabilities have been reported with damping ratios of 0.42 at 200 Hz for CNT arrays [65],  $\sim 0.10$  at 50 Hz for ethylene glycol-densified CNT fibers [67], and  $\sim 0.09$  at 10 Hz for nylon yarns [67]. The energy dissipation mechanisms are governed by structural (rather than material) mechanisms (see section 3.1.6). During tensile loading/unloading cycles, the CNTs within the bundles are reversibly attached and detached through zipping/unzipping mechanisms [66,69,162]. This mechanism is one of the causes of energy dissipation since the process of unzipping between CNTs and their bundles/fibrils consume energy to overcome the van der Waals forces [69,162], while the zipping process does not require energy consumption [162]. Another mechanism that likely contributes to dissipate energy in the CNTY is the detaching/attaching process [67,69]. Unlike the zipping/unzipping mechanism, the detaching/attaching mechanism irreversibly changes the CNT network morphology during each loading/unloading cycle. The inter-bundle friction plays a very

important role in the energy dissipation mechanisms. As contact between fibrils/bundles increases (e.g., by increasing the twist angle or decreasing the porosity), slipping dissipation increases [66,67]. This mechanism is also strain rate-dependent [61]. For low strains rates (i.e., low frequency), the CNT bundles have enough time to align longitudinally and relax [61]. As the frequency increases, the CNTs and CNT bundles relaxation through slipping turns into a slow process compared with the loading rate, and therefore, the strain re-distribution becomes more difficult [61].

#### *3.1.14. Electrical response during dynamic mechanical analysis*

The coupled DMA and electrical response of representative pristine (Fig. 3.18a) and preheated (Fig. 3.18b) CNTYs during DMA testing are shown in Fig. 3.18 as a function of temperature ( $T$ ). From Fig. 3.18a, it is observed that the storage modulus ( $E'$ ) of the pristine CNTYs decreases up to ~70 % with increasing temperature from 30 to ~170 °C, while the loss modulus ( $E''$ ) decreases up to ~80 % with increasing temperature from 30 to ~90 °C. From 90 °C,  $E''$  decreases more gradually and tends to level off. On the other hand, the loss modulus of the preheated CNTY (Fig. 3.18b) remains almost constant with increasing temperature, while the storage modulus decreases up to ~40 % at 120 °C. After ~120 °C,  $E'$  remains almost constant.  $E'$  of the pristine CNTY is ~2.8 times higher than that of the preheated yarns at 30 °C, but the pristine CNTYs broke at ~170 °C, while preheated CNTYs did not break during DMA testing. The explanation of the DMA response of the CNTY may be assisted by TGA (see section 3.1.4). They indicated that, when they are not previously heated, the CNTYs continuously lose mass during heating up to 350 °C. As the temperature increases, the thermal transformation of the hydrocarbon functional groups and byproducts in the CNTY may further affect the structural changes at the bundle level and porosity of the yarn, which facilitates the CNT bundles relaxation through slipping [67]. This may explain why the preheated CNTYs have a lower  $E'$  at the beginning of the DMA. At the same time, the loading/unloading cycles gradually changes the structure of the CNTY (twist angle, porosity, diameter, etc.), and this dynamic/friction effect convoluted with the thermal degradation of synthesis byproducts may yield the faster decrease in  $E'$  during the low temperature range of the DMA test. The analysis of tensile hysteresis (see section 3.1.9) and the in situ Raman spectroscopy during tensile testing (section 3.1.6) showed that the CNTYs undergo irreversible structural changes during the loading/unloading cycles. In this sense, the thermal degradation of

hydrocarbons could be contributing to the hysteresis increase of the CNTYs, and therefore, causing its breakdown at lower temperatures.

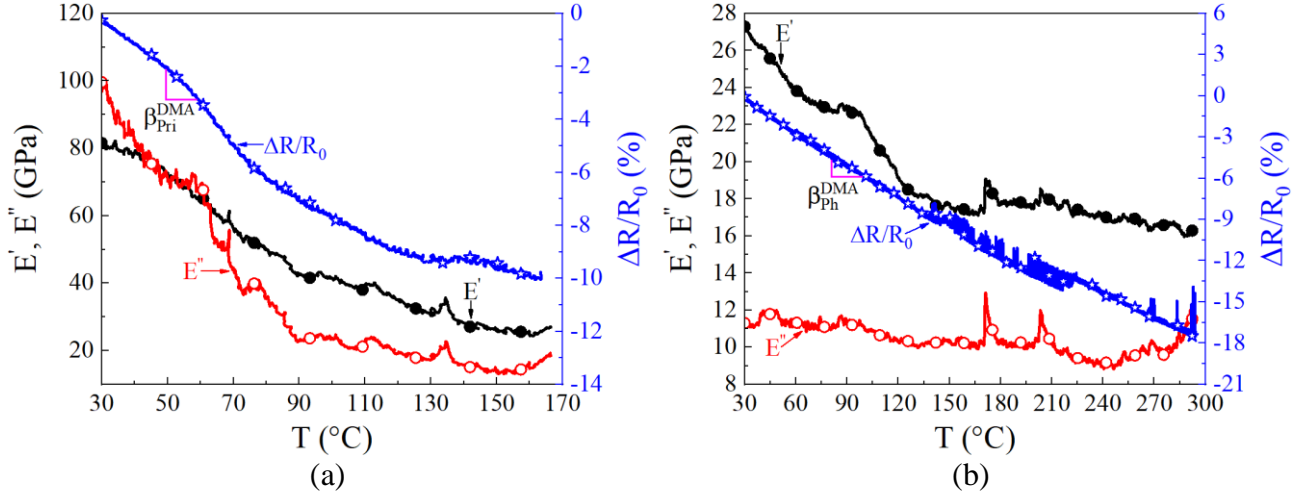


**Fig. 3.18.** Electrical response of representative CNTYs during DMA testing. (a) Pristine CNTY, (b) preheated CNTY (tested after the constrained thermoresistive characterization).

During DMA testing, the fractional change of electrical resistance ( $\Delta R/R_0$ ) of the CNTY decreases as the temperature increases, following the trend of  $E'$  (Fig. 3.18a). Notice that  $\Delta R/R_0$  exhibits small oscillatory variations in the readings, which were observed in all DMA tests but not observed in the thermoresistive response (Fig. 3.16). Thus, it is believed that these oscillations in  $\Delta R/R_0$  are related to experimental noise associated with the oscillatory character of the DMA test, and the large electrical sensitivity of the CNTY (see section 3.1.10).

To assess the contribution of thermoresistivity to the electrical response of the CNTY during DMA testing, the temperature coefficients of resistance were also obtained from the  $\Delta R/R_0$  vs.  $\Delta T$  curves of the DMA in Fig. 3.18. The temperature coefficient of resistance of the pristine CNTYs obtained during DMA testing in the  $0 \leq \Delta T \leq 50$  K range, was  $\beta_{\text{Pri}}^{\text{DMA}} = -9.83 \times 10^{-4} (\pm 3.25 \times 10^{-4}) \text{ K}^{-1}$ . The temperature coefficient of resistance of the preheated CNTYs during DMA testing was obtained in the full temperature range as  $\beta_{\text{Ph}}^{\text{DMA}} = -6.92 \times 10^{-4} (\pm 0.55 \times 10^{-4}) \text{ K}^{-1}$ . Both are numerically similar to  $\beta_1 = -8.63 \times 10^{-4} (\pm 0.79 \times 10^{-4}) \text{ K}^{-1}$  and  $\beta_3 = -7.26 \times 10^{-4} (\pm 0.05 \times 10^{-4}) \text{ K}^{-1}$  calculated from the thermoresistive response of Fig. 3.16. This fact indicates that the decrease in electrical response of CNTY during DMA testing is governed by its negative thermoresistivity, with small oscillations in  $\Delta R/R_0$  superimposed given the oscillatory nature of the DMA test.

### 3.1.15. Electromechanical response under tensile loading at different temperatures

The mechanical response of the CNTYs subjected to monotonic tensile loading at different temperatures ( $T = 25, 80, \text{ and } 120 \text{ }^\circ\text{C}$ ) is shown in Fig. 3.19a. Only the upper and lower curves, which enclose the behavior of the other specimens at their respective temperatures, are included in Fig. 3.19. It is observed that the mechanical response varies depending on temperature. The ultimate (failure) axial tensile load of the CNTYs ( $F_{z_u}$ ), and thus the specific tensile strength ( $\sigma_{z_u}/\rho$ ), decrease at higher temperatures, but the ultimate (failure) axial tensile strain of the CNTYs ( $\varepsilon_{z_u}$ ) increases. Additionally,  $E/\rho$  (calculated in the  $0.2\% \leq \varepsilon_z \leq 1.0\%$  range) decreases from  $23.2 (\pm 8.9) \text{ N/tex}$  at room temperature ( $\sim 25 \text{ }^\circ\text{C}$ ) to  $6.55 (\pm 0.98) \text{ N/tex}$  at  $120 \text{ }^\circ\text{C}$ . As was observed in TGA (Fig. 3.5), the CNTY lose mass during heating up to  $300 \text{ }^\circ\text{C}$ . As the temperature increases, the thermal transformation of the hydrocarbon functional groups and by-products in the CNTY may further affect the structural changes at the fibril/bundle level and porosity of the yarn, which facilitates the fibril/bundles relaxation through slipping [67]. This slipping and relaxation of fibrils and bundles at elevated temperature may explain why  $E/\rho$  decreases at higher temperature. The evaporation of densifier (acetone) and moisture (see section 3.1.4) with temperature allows the fibrils/bundles to have more space to rearrange, allowing the CNTYs to achieve greater values of  $\varepsilon_{z_u}$ . Regarding the piezoresistive response observed in Fig. 3.19b, it is observed that the fractional change of electrical resistance ( $\Delta R/R_0$ ) increases with the strain. However, the curves are noisy, and a conspicuous material response is hard to distinguish. At room temperature ( $\sim 25 \text{ }^\circ\text{C}$ ), the CNTYs have a gage factor ( $GF$ ) of  $0.36 (\pm 0.13)$  in the  $0.2\% \leq \varepsilon_z \leq 1.0\%$  range. For  $\varepsilon_z > 1.0\%$ ,  $\Delta R/R_0$  increases rapidly and suddenly peaks close to failure. Therefore, it is expected that structural changes of the fibrils/bundles within the CNTY due to the applied strain play a paramount role in its piezoresistive response. Since CNTYs are hierarchical materials with a strongly property-structure dependence, there is not a universal piezoresistive response for CNTYs. When a CNTYs is stretched, an increase in the number of contacts between fibrils/bundles is expected due to the decrease in diameter (see section 3.1.7) and porosity, which generates a decrease in electrical resistance. This phenomenon causes negative piezoresistivity, which has also been observed for very low strain rates [91]. However, during stretching the distance between electrodes also increases, and thus the contact length of the fibrils/bundles decreases [52,90,91]. This is the physical phenomenon that governs the piezoresistive response of the CNTYs in our case. When the CNTYs are tested at a higher temperature, a slight tendency to increase  $\Delta R/R_0$

with temperature is also observed. However, the electrical response for 80 and 120 °C is noisy, making it difficult to draw clear conclusions. Therefore, only the  $GF$  at 25 °C is reported. A summary of all the physical properties of the CNTYs obtained in this work can be found in Table F.1 of Appendix F.

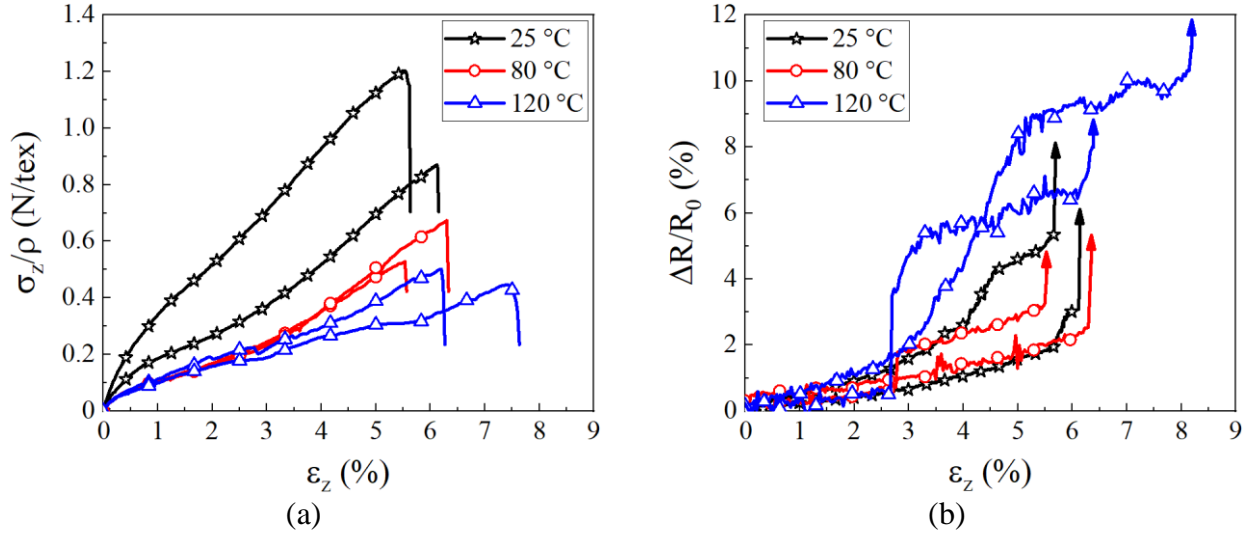


**Fig. 3.19.** Electromechanical response of CNTYs under uniaxial tensile loading at different temperatures. **(a)** Mechanical response, **(b)** electrical response.

The specific electrical conductivity of the CNTYs ( $\xi/\rho$ ) at zero strain was measured at different temperatures in the specimens for tensile testing, using the distance between electrodes ( $L_g = 25$  mm, Fig. 2.6). At room temperature ( $\sim 25$  °C),  $\xi/\rho = 1211 (\pm 37)$  S·cm<sup>2</sup>/g, but it increases with increasing temperature, up to 1237 ( $\pm 18$ ) S·cm<sup>2</sup>/g at 120 °C. The electrical conductivity of the CNTYs is dictated by the conductivity of the individual CNTs as well as the degree of electrical contact (by physical contact or by tunnel effect due to their proximity) between the CNTs and all the hierarchical entities comprising the yarn [27,167]. In addition, the thermoresistive of the CNTYs also plays an important role in the specific electrical conductivity. As temperature increases, the density and mobility of electric charge carriers also increase, resulting in a quasilinear drop in the electrical resistance of individual CNTs that make up the CNTY [27,173]. This mechanism has also been proposed as the governing thermoresistive mechanism of pitch-based carbon fibers [33,36,46].

### 3.2. Property-structure relationships inferred from modeling

The specific stress response in the axial direction ( $\sigma_z/\rho = F_z/\rho_L$ ) of a CNTY subjected to axial tensile strain ( $\varepsilon_z$ ) obtained using Eq. (2.13) with the input parameters shown in Table 1.1 is compared here to the results of a tested CNTY presented in Fig. 3.20a. The experimental curve was selected from the five replicate tests shown in Fig. 3.11. The axial tensile test corresponds to CNTYs of 33.3  $\mu\text{m}$  diameter with a gage length of 25 mm and strain rate of 0.5 mm/min, as describe in section 2.2.7. The model successfully captures the overall tensile nonlinear response of the CNTY. However, it does not fully reproduce the sudden changes in slope observed in the  $\sigma_z/\rho$  vs.  $\varepsilon_z$  curve. This discrepancy could be attributed to the modeling assumptions, unmeasured input parameters, and the current limitations of the analytical deterministic model. Additionally, it is important to consider the natural variability of the mechanical response of CNTYs, as the model only utilizes mean values. The CNTs, bundles, and fibrils that constitute a CNTY have randomly varying structural dimensions and material properties, statistical distribution of lengths, and some of them have different orientations with respect to the twist angle within the yarn (see section 3.1.1). Additionally, each fibril has a different number of bundles and CNTs. This randomness makes the true mechanical response of CNTYs a stochastic process, which has been simulated using, for example, by using Monte Carlo approaches [74,77]. Nevertheless, the close agreement between the results obtained using Eq. (2.13) and experimental data indicates that the model is effective in capturing the fundamental aspects of the mechanical response of CNTYs. Therefore, it can be utilized to analyze the parameters that are the most influential on the axial mechanical response of CNTYs.

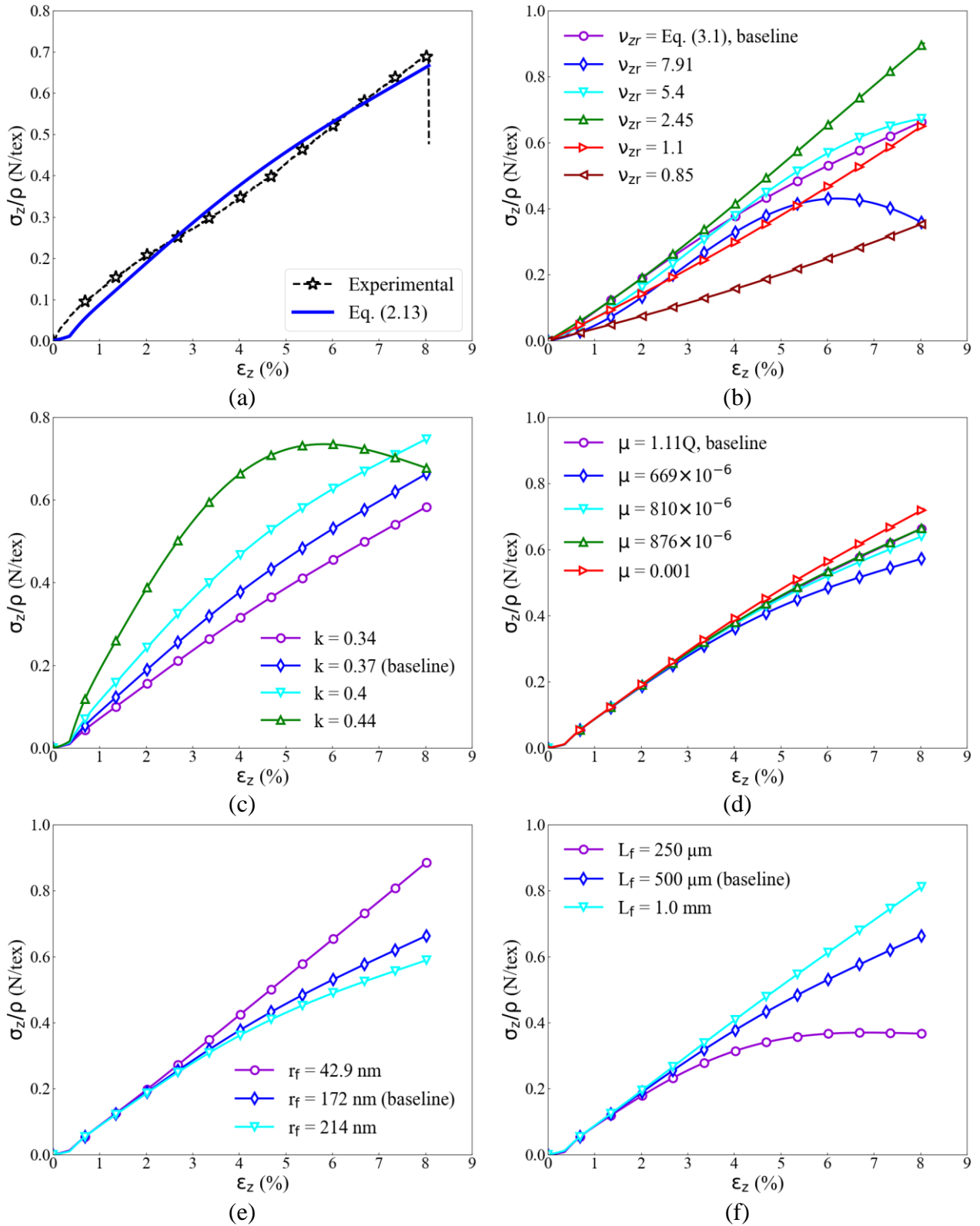


**Fig. 3.20.** Tensile mechanical response of CNTYs, obtained from Eq. (2.13). **(a)** Comparison of modeling results with experimental data, **(b)** effect of radial contraction ratio ( $\nu_{zr}$ ), **(c)** effect of slip factor ( $k$ ), **(d)** effect of coefficient of friction ( $\mu$ ), **(e)** effect of fibril radius ( $r_f$ ), **(f)** effect of fibril length ( $L_f$ ).

The effect of the radial contraction ratio ( $v_{zr}$ ), slip factor ( $k$ ), coefficient of friction ( $\mu$ ), fibril radius ( $r_f$ ), and fibril length ( $L_f$ ) are shown in Fig. 3.20b–f. The curves depicted in these figures were generated by using the baseline parameters listed in Table 1.1 and varying only the specified parameter at the time within physically plausible ranges. In Fig. 3.20b, five additional curves were obtained using constant values of the radial contraction ratio. Those values were selected between the lower and upper bounds listed in Table 1.1. As  $v_{zr}$  increases, the response curve exhibits a more pronounced nonlinear behavior. The specific stress reached at a given strain level first increases with increased  $v_{zr}$ , but reaches a maximum for  $v_{zr} = 2.45$ . For higher values of  $v_{zr}$ , the specific stress gradually decreases with further increments of  $v_{zr}$ . This indicates that complex competing phenomena influence the mechanical response of the CNTYs. On the one hand, higher values of  $v_{zr}$  imply greater radial contraction as  $\varepsilon_z$  increases. This leads to higher values of packing density ( $\rho_r$ , Eq. (2.14)) and, consequently, higher compressive transverse stress ( $P$ , Eq. (2.17)), which in turn reduces the slippage ratio of the fibrils ( $\lambda$ , Eq. (2.16)). As a result, this increases the stress in the fibrils ( $\sigma_{zf}$ ), and therefore, increases  $\sigma_z/\rho$  with increased  $v_{zr}$ . On the other hand, higher values of  $v_{zr}$  means lower  $r_{ext}$ . According to Eq. (2.13) this means a lower  $F_z$ , which yields reduced specific stress ( $\sigma_z/\rho = F_z/\rho_L$ ). The result of these competing parameters give rise to the nonlinear and nonmonotonic behavior of  $\sigma_z/\rho$  with  $v_{zr}$  observed in Fig. 3.20b. From a modeling perspective, the ideal (more realistic) approach involves using an experimentally fit equation for  $v_{zr}$  such as Eq. (3.1), which updates the value of  $v_{zr}$  at each value of applied strain. If the actual measurement of  $v_{zr}$  as a function of applied strain is not carried out, based on the findings of Fig. 3.20b, it is recommended to use  $v_{zr}$  close to 5.4 to achieve more accurate results, at least for this type of twisted yarns.

The slip factor (Fig. 3.20c) also has a strong influence on the mechanical response of the yarn. The CNTY stiffness increases with increased slip factor. Additionally, the nonlinearity of the response increases with increased slip factor, resulting in a decrease in specific stress at high values of strain for  $k = 0.44$ . As  $k$  approaches 0.50, the fibril tensile modulus increases (see Appendix D.1), resulting in an increase in the stiffness of the CNTY. By substituting the slippage ratio from Eq. (2.16) into Eq. (2.15), it is observed that the fibril stress is a quadratic function of the fibril tensile modulus and of the axial tensile strain. Therefore, it is expected that once a certain level of strain is reached, the specific stress ceases to increase due to an increase in fibril slip. This is because the fibrils slip along their interface and are more likely pulled out rather than fully stretched or broken,

given their high modulus/strength and weak interfacial strength [55,151,152]. In the case of the coefficient of friction of the fibrils ( $\mu$ ), the curves shown in Fig. 3.20d were obtained using constant values of  $\mu$ , selected from their lower and upper bounds in the model. This includes a smaller and a higher value to encompass the potential range of the coefficient of friction. The slip factor ( $k$ ) is related to the coefficient of friction ( $\mu$ ) through Eq. (2.12). It is also important to mention that, for the sake of examining the effect of  $\mu$ , the value of  $k$  was fixed at 0.37 for the parametric analysis (see Table 1.1). Given that  $k$  was held constant, a weak dependence of  $\mu$  is observed for  $\varepsilon_z < 4.0$  %. However, for higher levels of strain,  $\sigma_z/\rho$  increases as  $\mu$  increases. Thus, for the parametric analysis varying the fibril radius (Fig. 3.20e) and fibril length (Fig. 3.20f),  $k = 0.37$  and  $\mu = 1.16Q$  were used (see Table 1.1). From Fig. 3.20e and f it is seen that the decrease in fibril radius and increase in fibril length leads to a stronger and stiffer mechanical response. According to Eq. (2.16), as the fibril radius decreases, the slippage ratio also decreases due to the increased surface area between the fibrils. This enhances load transfer between fibrils. Similarly, longer fibrils enable more efficient load transfer, as it is well known for short-fiber reinforced composites.

The effect of varying the radial packing density, compressive transverse stress, and fibril axial strain through the radius of the CNTYs are shown in Appendices D.2, D.3, and D.4, respectively. According to the analysis of this section, the radial contraction ratio ( $v_{zr}$ ) and the slip factor ( $k$ ) are the parameters that have the most impact on the mechanical response of the CNTYs.

### **3.3. Tensile mechanical and electromechanical properties of monofilament composites**

As the second hierarchical level of study, monofilament composites (Fig. 2.12) were manufactured as described in section 2.4.1. These composites were divided into four types of specimens, as outlined in Table 2.3. The composites labeled as VER correspond to specimens made of neat resin. VER+Cu corresponds to specimens made of VER with copper electrodes, but without CNTY. CNTY/VER corresponds to specimens made of VER and a single CNTY, while CNTY/VER+Cu corresponds to specimens made of VER and CNTY with copper electrodes. Before tensile testing (see section 2.4.2), the specific electrical conductivity of the CNTYs ( $\xi/\rho$ ) in the monofilament composites at zero strain was measured, using the distance between electrodes (10 mm, Fig. 2.12b), in order to study the impact of the VER on the electrical properties of the CNTYs. The specific electrical conductivity of the CNTYs decreased from 1211 ( $\pm 37$ ) S·cm<sup>2</sup>/g (see section 3.1.10) to 1065 ( $\pm 30$ ) S·cm<sup>2</sup>/g, once the CNTY became part of the monofilament composites. This 12.1 %

decrease in  $\xi/\rho$  (corresponding to  $\Delta R/R_0 = 13.7\%$ , taking  $R_0$  as the electrical resistance of the individual CNTYs) is mainly attributed to resin infiltration. Similar increases of  $\Delta R/R_0$  ( $\sim 9\%$ ) have been observed when the CNTY was embedded in epoxy resin [13,93]. The change in  $\Delta R/R_0$  of CNTYs resulting from their integration into polymeric resins depends on various factors, such as the type of resin and the curing program [93]. When the VER in its liquid state and is poured into the mold along with the CNTY during the manufacturing of monofilament specimens (see section 2.4.1), VER infiltrates through the CNTY pores. In this process, the VER fills the empty spaces within the yarn yielding slight yarn swelling by opening fibril/bundle junctions [92]. This leads to an increase in electrical conductivity due to the tunnel effect in the CNTY, as the potential barrier between CNT bundles increases. The residual stresses in the VER after curing also affect the electrical resistance of the CNTYs [13,93].

The mechanical behavior of a VER specimen and the electromechanical response of a CNTY/VER+Cu under axial tensile strain ( $\varepsilon_x$ ) are shown in Fig. 3.21a and b, respectively. It is observed that the axial stress ( $\sigma_x$ ) increases with a linear tendency with  $\varepsilon_x$ . The strain fields on the specimens (inserts in Fig. 3.21a and b) are uniform. The specimens exhibited brittle failure failing in the central zone, without showing evident gradients in the strain fields. However, the VER+Cu and the CNTY/VER+Cu specimens predominantly failed in the areas where the internal electrodes were fixed. In Fig. 3.21b, it is observed that  $\Delta R/R_0$  increases linearly with the increase in  $\varepsilon_x$ , following the mechanical behavior of the CNTY/VER+Cu specimens. This indicates a correlation between the electrical response of the CNTYs and the mechanical response of the composites, with the CNTYs exhibiting a gage factor of  $0.41 (\pm 0.06)$ . This value is slightly higher than the  $GF$  presented by the individual CNTYs ( $0.36 \pm 0.13$ , see section 3.1.10). This demonstrates the initial usefulness of the concept of CNTYs for structural health monitoring applications in polymeric composites.

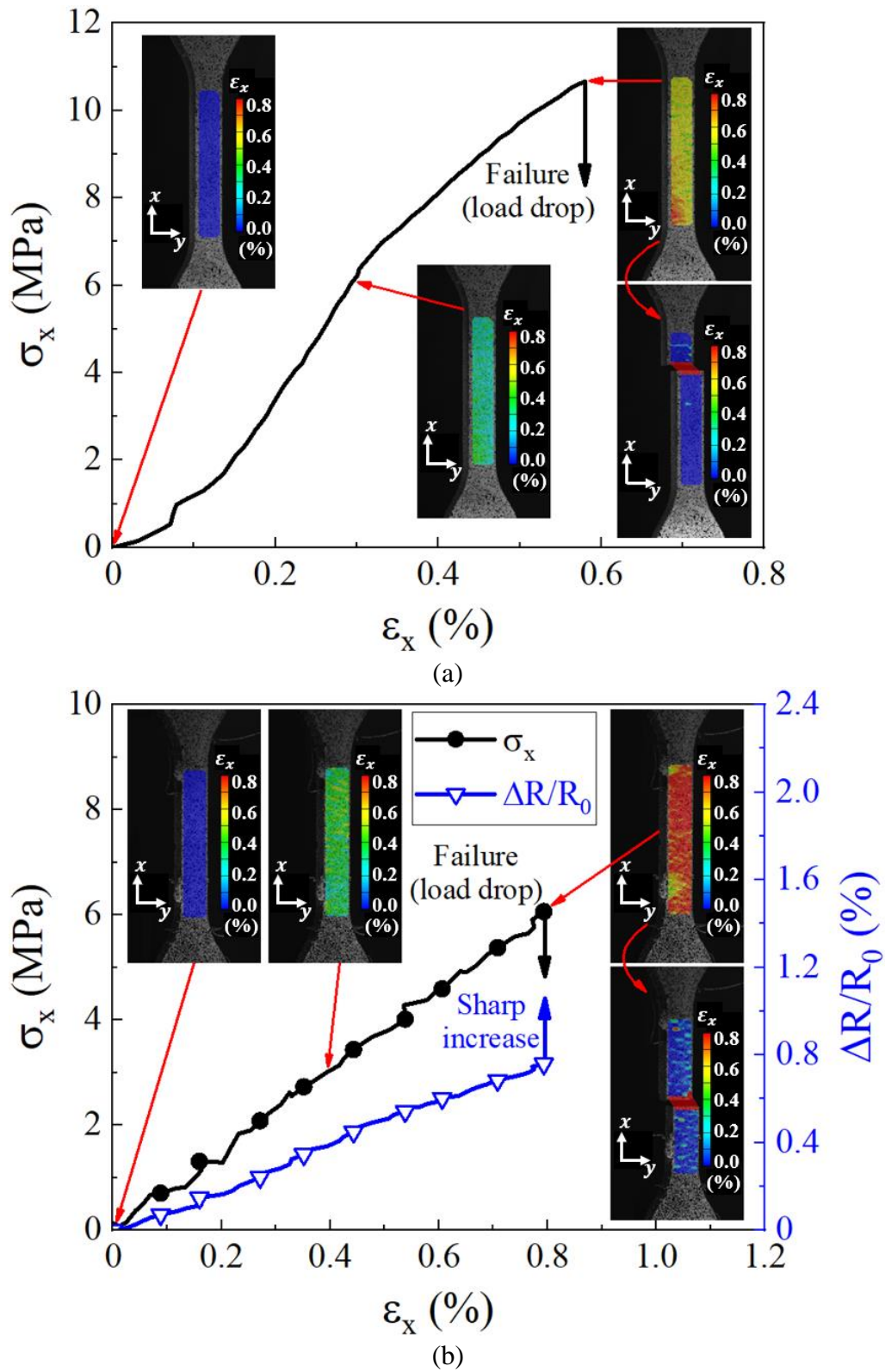


**Fig. 3.21.** Electromechanical response of different monofilament composites under uniaxial tensile loading. (a) Representative mechanical response of the VER specimen, (b) representative electromechanical response of the CNTY/VER+Cu specimen.

The tensile failure strain ( $\epsilon_{x_u}^M$ ) and the tensile strength ( $\sigma_{x_u}^M$ ) of the specimens are shown in Fig. 3.22a and b. It is observed that the addition of the CNTYs and the electrodes does not decrease the mechanical properties of the composites. The same applies to the tensile modulus ( $E^M$ , Fig. 3.22c) and the Poisson's ratio ( $\nu_{xy}^M$ , Fig. 3.22d). This demonstrates that the inclusion of the CNTYs as sensors for structural monitoring applications does not compromise the mechanical properties of the composites. Table 3.6 summarizes the electromechanical properties of the monofilament composites.

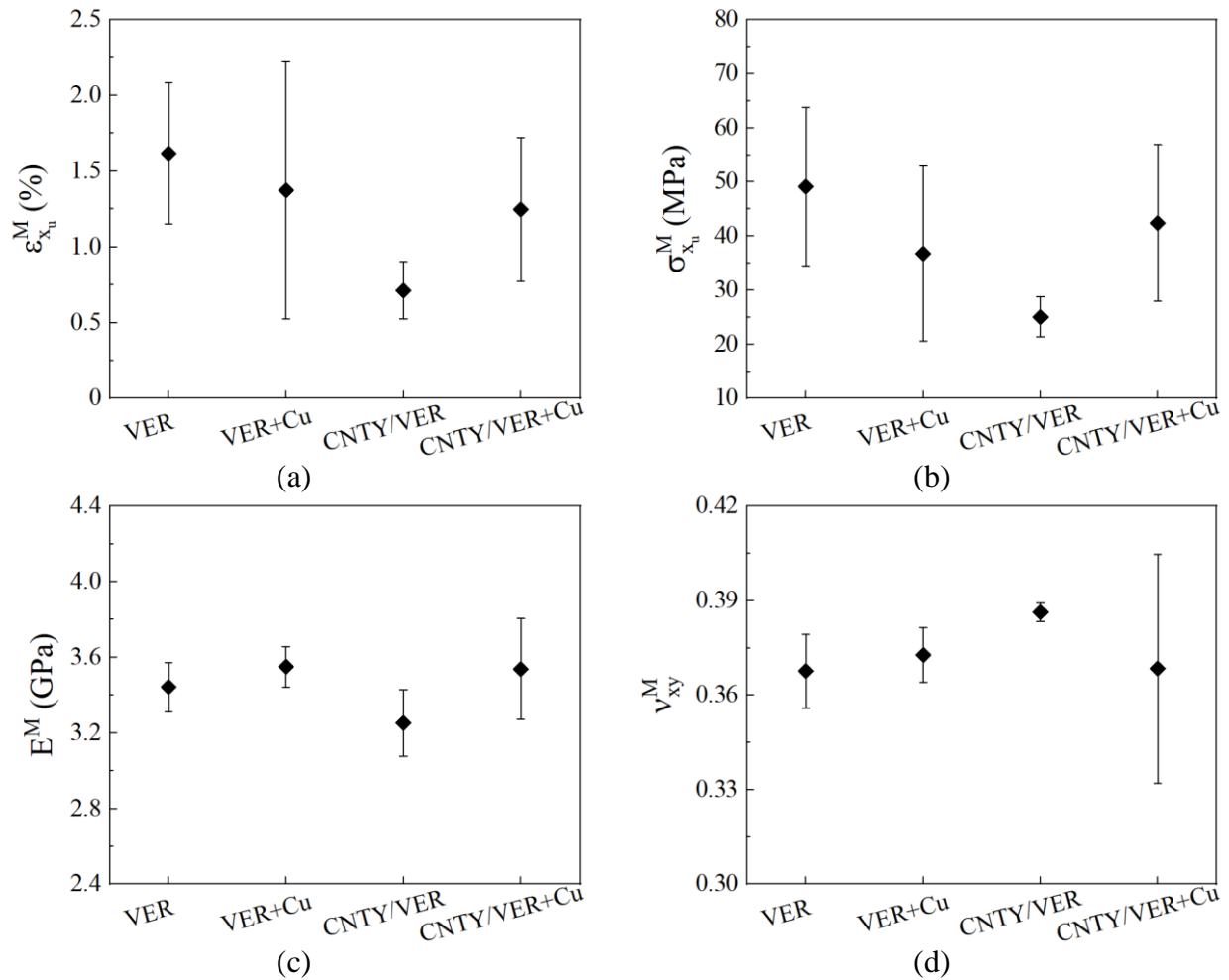


**Fig. 3.22.** Electromechanical properties of the monofilament composites under uniaxial tensile loading. (a) tensile failure strain ( $\epsilon_{x_u}^M$ ), (b) tensile strength ( $\sigma_{x_u}^M$ ), (c) tensile modulus ( $E^M$ ), d) Poisson's ratio ( $\nu_{xy}^M$ ).

**Table 3.6.** Electromechanical tensile properties of the monofilament composites.

Specimen	Property	Mean value (standard deviation)
VER	$\varepsilon_{x_u}^M$	1.62 ( $\pm$ 0.47) %
	$\sigma_{x_u}^M$	49.1 ( $\pm$ 14.6) MPa
	$E^M$	3.44 ( $\pm$ 0.13) GPa
	$\nu_{xy}^M$	0.368 ( $\pm$ 0.012)
VER+Cu	$\varepsilon_{x_u}^M$	1.37 ( $\pm$ 0.85) %
	$\sigma_{x_u}^M$	36.8 ( $\pm$ 16.2) MPa
	$E^M$	3.55 ( $\pm$ 0.11) GPa
	$\nu_{xy}^M$	0.373 ( $\pm$ 0.009)
CNTY/VER	$\varepsilon_{x_u}^M$	0.71 ( $\pm$ 0.19) %
	$\sigma_{x_u}^M$	25.1 ( $\pm$ 3.7) MPa
	$E^M$	3.25 ( $\pm$ 0.18) GPa
	$\nu_{xy}^M$	0.386 ( $\pm$ 0.003)
CNTY/VER+Cu	$\varepsilon_{x_u}^M$	1.48 ( $\pm$ 0.29) %
	$\sigma_{x_u}^M$	50.2 ( $\pm$ 6.9) MPa
	$E^M$	0.42 ( $\pm$ 0.04) GPa
	$\nu_{xy}^M$	0.413 ( $\pm$ 0.048)
	$\xi$	266 ( $\pm$ 7) S/cm
	$\xi/\rho$	1065 ( $\pm$ 30) S·cm <sup>2</sup> /g
	$GF$	0.46 ( $\pm$ 0.11)

### 3.4. Structural health monitoring of laminated composite panels under compression loading

#### 3.4.1. Compression response and failure mode

The CNTYs were integrated into laminated composites panels (Fig. 2.13) made of GFW and VER to assess their performance for SHM applications, as described in section 2.5.1. The labels GFW/VER correspond to the panels without debonding, GFW/VER-D25 correspond to the panels with a circular debond of 25 mm diameter, and GFW/VER-D50 correspond to the panels with a circular debond of 50 mm diameter. If the label includes the term “+CNTY”, it indicates that the panel has the CNTY array for SHM. The mechanical response of the laminated composite panels under compression loading is shown in Fig. 3.23a. It is observed that the compression stress ( $\sigma_y$ ) of all the panels, whether with or without debond, increases in an approximately linear fashion with the axial strain ( $\epsilon_y$ ). During testing, the panels experienced buckling, as is shown in Fig. 3.23b. The out-of-plane displacement ( $\Delta z_C$ ) depicted in Fig. 3.23b was measured at the center of the panels using DIC. All the panels exhibited similar  $\Delta z_C$  response, with values reaching up to 5.4 mm before fully losing their load-bearing capacity. Figure 3.23c illustrates the buckling failure of a GFW/VER-D50 panel, serving as a representative example. The buckling experienced by the panels can be attributed to their high slenderness ratio, according to the Euler buckling theory [178,179]. The panels also exhibited similar compression modulus ( $E_C^P$ ), with mean values of 17.1 ( $\pm 3.3$ ) GPa, 15.6 ( $\pm 1.5$ ) GPa, and 16.4 ( $\pm 0.2$ ) GPa for the GFW/VER, GFW/VER-D25, and GFW/VER-D50, respectively, as shown in Fig. 3.23d. The GFW/VER panels exhibited a compressive failure strain ( $\epsilon_{y_u}^P$ ) of 0.69 ( $\pm 0.08$ ) % and a compressive strength ( $\sigma_{y_u}^P$ ) of 102 ( $\pm 11$ ) MPa. With the introduction of debonding, both  $\epsilon_{y_u}^P$  and  $\sigma_{y_u}^P$  decreased to 0.50 ( $\pm 0.02$ ) % and 82.9 ( $\pm 5.5$ ) MPa, respectively, for the GFW/VER-D50 panels. The comparison of  $\epsilon_{y_u}^P$  and  $\sigma_{y_u}^P$  is shown in Fig. 3.23e and f, respectively. Table 3.7 summarizes the compression properties of the laminated composites panels. The compressive strength of laminated panels of similar architecture, fiber and matrix has been measured as  $\sim 380$  MPa [180]. According to our estimation of stability of simply-supported rectangular plates under uniform compression [181], using the elastic properties of this composite measured in [182], the buckling stress is  $\sim 165$  MPa. This value is approximately 43 % of the expected compressive strength for this composite ( $\sim 380$  MPa), confirming that panel buckling is expected earlier than compression failure in the tested panels.

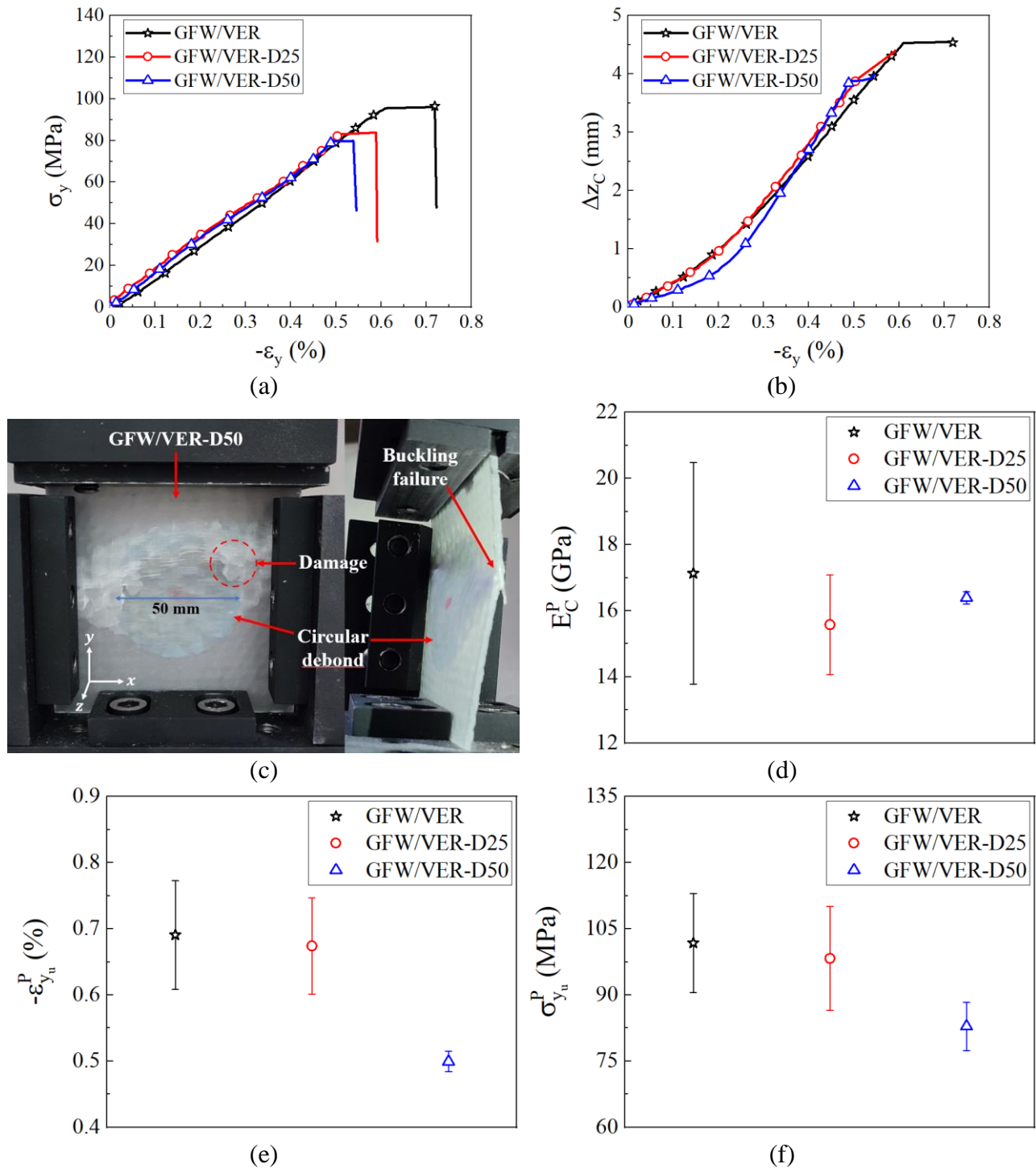


**Fig. 3.23.** Compressive mechanical behavior of the laminated composite panels. **(a)** Axial compression stress ( $\sigma_y$ ) as a function of strain ( $\epsilon_y$ ), **(b)** out-of-plane displacement measured at the center of the panel ( $\Delta z_c$ ) as a function of  $\epsilon_y$ , **(c)** failure mode, **(d)** compression modulus ( $E_C^P$ ), **(e)** compression failure strain ( $\epsilon_{y_u}^P$ ), **(f)** compression strength ( $\sigma_{y_u}^P$ ).

**Table 3.7.** Mechanical compression properties of the laminated composite panels.

Specimen	Property	Mean value (standard deviation)
GFW/VER	$\epsilon_{y_u}^P$	0.69 ( $\pm$ 0.08) %
	$\sigma_{y_u}^P$	102 ( $\pm$ 11) MPa
	$E_C^P$	17.1 ( $\pm$ 3.3) GPa
GFW/VER-D25	$\epsilon_{y_u}^P$	0.67 ( $\pm$ 0.07) %
	$\sigma_{y_u}^P$	98.3 ( $\pm$ 11.8) MPa
	$E_C^P$	15.6 ( $\pm$ 1.5) GPa
GFW/VER-D50	$\epsilon_{y_u}^P$	0.50 ( $\pm$ 0.02) %
	$\sigma_{y_u}^P$	82.9 ( $\pm$ 5.5) MPa
	$E_C^P$	16.4 ( $\pm$ 0.2) GPa
GFW+CNTY/VER	$\epsilon_{y_u}^P$	0.27 ( $\pm$ 0.32) %
	$\sigma_{y_u}^P$	79.8 ( $\pm$ 8.6) MPa
	$E_C^P$	36.7 ( $\pm$ 15.6) GPa
GFW+CNTY/VER-D25	$\epsilon_{y_u}^P$	0.31 ( $\pm$ 0.34) %
	$\sigma_{y_u}^P$	75.8 ( $\pm$ 13.8) MPa
	$E_C^P$	29.2 ( $\pm$ 13.8) GPa

Post-mortem photographs of the backside of the GFW+CNTY/VER, GFW+CNTY/VER-D25, and the GFW/VER-D50 panels after tested under compression loading are shown in Fig. 3.24a-c, respectively. There are areas on the panel's surface where damage is clearly visible. The visible damage is more pronounced in the panels with debonds, particularly in the one with the larger debond (GFW/VER-D50, Fig. 3.24c). The GFW/VER panels exhibited damage predominantly near the top edge (end-crushing), where the load was introduced, as shown in Fig. 3.24a. Panels without debond were more susceptible to failure in this area. In contrast, the GFW/VER-D25 panels (Fig. 3.24b) and the GFW/VER-D50 panels (Fig. 3.24c) exhibited greater damage in proximity to the debond, because of the tendency of the failure mechanism to switch from end-crushing to debond buckling. In the case of the GFW/VER-D25 panels, delamination took place around the debond or in the region between the center and the top (load introduction) edge of the panels.

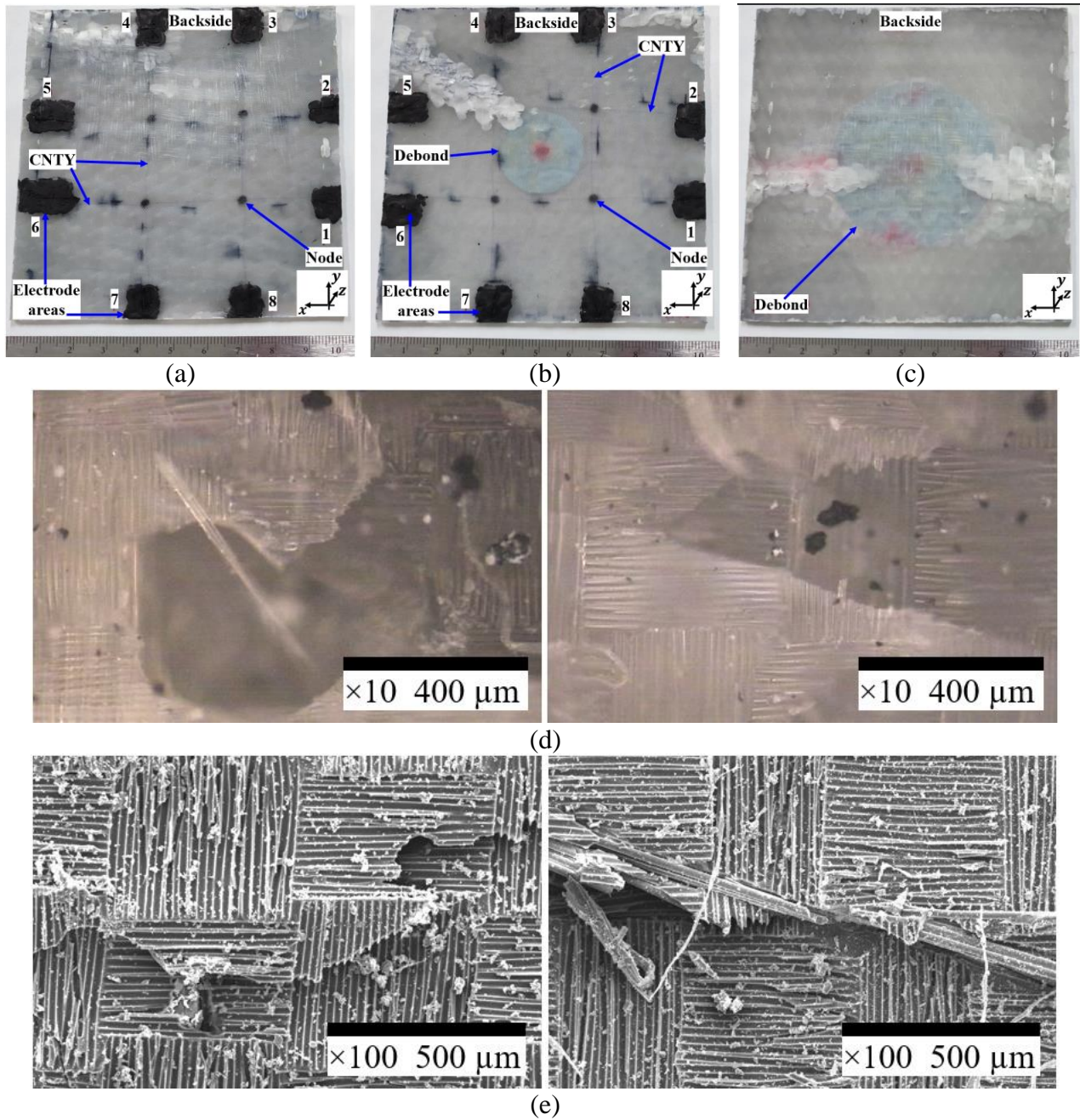


**Fig. 3.24.** Post-mortem examination of laminated composite panels after compression testing. (a) Photograph of the GFW+CNTY/VER panel, (b) photograph of the GFW+CNTY/VER-D25 panel, (c) photograph of the GFW/VER-D50 panel, (d) optical microscopy images (GFW+CNTY/VER and GFW/VER-D25), (e) SEM images (GFW+CNTY/VER-D25 and GFW/VER-D50).

The optical microscopies (Fig. 3.24d) and SEM images (Fig. 3.24e) of the damaged surfaces of the panels present evidence of matrix cracking, fiber breakage, and delamination. The images in Fig. 3.24d and e are shown as representative, as all the panels exhibited similar surface damage. Under compression loading, the panels undergo buckling after reaching Euler's critical load [178,179].

Buckling leads to matrix cracking and delamination, ultimately resulting in fiber breakage and structural collapse.

### 3.4.2. *In situ electrical mapping and damage detection during monotonic compression loading*

The structural health monitoring (SHM) of an exemplary pristine (without debond) GFW+CNTY/VER composite panel is shown in Fig. 3.25. Electrical mapping of the panels was obtained as described in section 2.5.2. The upper part of Fig. 3.25, from left to right, shows the strain field on the panel's surface measured by DIC just before failure (left), followed by a contour map of the panel's electrical resistance using the data post-processing algorithm both without (PER, center image), and with data interpolation (PERI, right image). The electrical resistance plotted as "PER" was calculated by Eqs. (2.19) and (2.20), while those for "PERI" correspond to Eq. (2.21). The lower part of Fig. 3.25 shows an actual photograph of the backside of the failed panel (left), where numbers in the blue tags indicate the electrodes. Notice that the front ( $xy$ ) surface of the panel (not shown) contained the DIC speckle pattern, which hinders visualization of cracks and failure features. Consequently, in this photograph, the failure features must be compared in mirror reflection to the DIC and electrical contour maps. This photograph is followed in the lower-center part of Fig. 3.25 by a plot of the compression stress ( $\sigma_y$ ), out-of-plane displacement at the center of the panel ( $\Delta z_C$ ), and the fractional change of electrical resistance ( $\Delta R/R_0$ ) as a function of compressive strain ( $\varepsilon_y$ ). The paths of the plotted electrodes are shown in the schematic on the lower right. The DIC measurements shown in Fig. 3.25 reveal that there is a strain concentration located in the region between the center and the top of the panel. This behavior is attributed to the load introduction, leading to end-crushing. All CNTY+GFW/VER panels failed at their upper half, presenting the failure mechanisms described in section 3.4.1. During the compression tests, the panels undergo buckling due to their structural geometry, resulting in sequential failure through matrix cracking, delamination, and fiber breakage (see Fig. 3.24d and e). It is also observed that the failure of the panel (see photograph of the panel's backside in Fig. 3.25) occurred in the area where DIC showed higher  $\varepsilon_y$ . The damaged region was identified through monitoring of the panel's electrical resistance, as depicted in the PER contour map in Fig. 3.25. It is evident that the electrical resistance measured for the paths successfully identifies the areas where DIC indicates strain/stress concentration and failure. Large strain gradients in these areas results in higher  $\Delta R/R_0$  of the paths at the same corresponding regions. The electrical resistance of the CNTY arrays ( $R_{i,j}$ )

crossing through the area with large strain gradients (e.g.,  $R_{3,4}$ ,  $R_{3,5}$ ; see plot and schematic in Fig. 3.25) presents higher  $\Delta R/R_0$  than that corresponding to sections away from this region (e.g.,  $R_{1,6}$ ,  $R_{1,8}$ ). In addition,  $R_{3,4}$  and  $R_{3,5}$  presented peaks of  $\Delta R/R_0$  at around 0.20, 0.25, and 0.5 % strain, as shown in Fig. 3.25. These peaks in  $\Delta R/R_0$  observed in the plot also coincided with audible failures, providing further real-time indication of structural health. The contour map obtained by the PER method is further enhanced by interpolating the electrical resistance of the paths, as observed in the PERI contour map in Fig. 3.25. The PERI method matched the area of higher strain gradients measured by DIC, offering a better overview of structural damage.

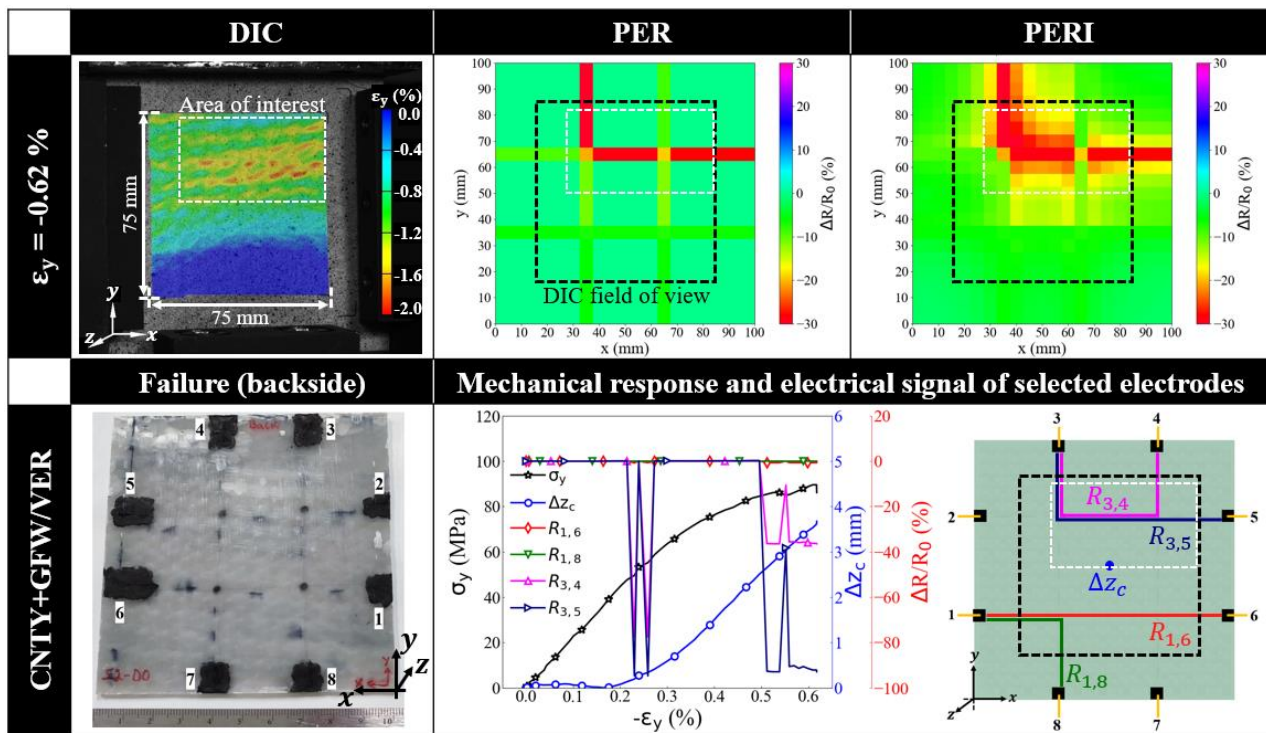


**Fig. 3.25.** Structural health monitoring of an exemplary GFW+CNTY/VER panel.

The SHM of an exemplary GFW+CNTY/VER-D25 composite panel is shown in Fig. 3.26. Unlike the GFW+CNTY/VER panel, in this case, DIC measurements reveal that the strain concentrations arise around the central debond. The GFW+CNTY/VER-D25 panels still undergo buckling, leading to matrix cracking, delamination, and fiber breakage. However, the introduction of a debond in these panels caused a shift in the strain concentration zone with respect to panels without debond, triggering the onset of failure at the debonded region (see photograph of the panel's backside in Fig. 3.26). Once again, the areas where DIC indicates the highest strain/stress concentration and failure were successfully identified by the PER contour map in Fig. 3.26. Here, all

resistance paths ( $R_{i,j}$ ) exhibited a noticeable change in their electrical resistance, as the major damage is located at the center of the panel. However, the  $R_{i,j}$  paths near the area of stress concentration showed a higher change in electrical resistance (see e.g.,  $R_{1,6}$  in Fig. 3.26). The PERI contour map in Fig. 3.26 provides a more comprehensive insight into the extent of damage, with better matches the DIC findings. All these results demonstrate the effectiveness of the technique used herein for SHM applications, highlighting the capability of CNTYs to effectively detect and locate damage in the composite panels.

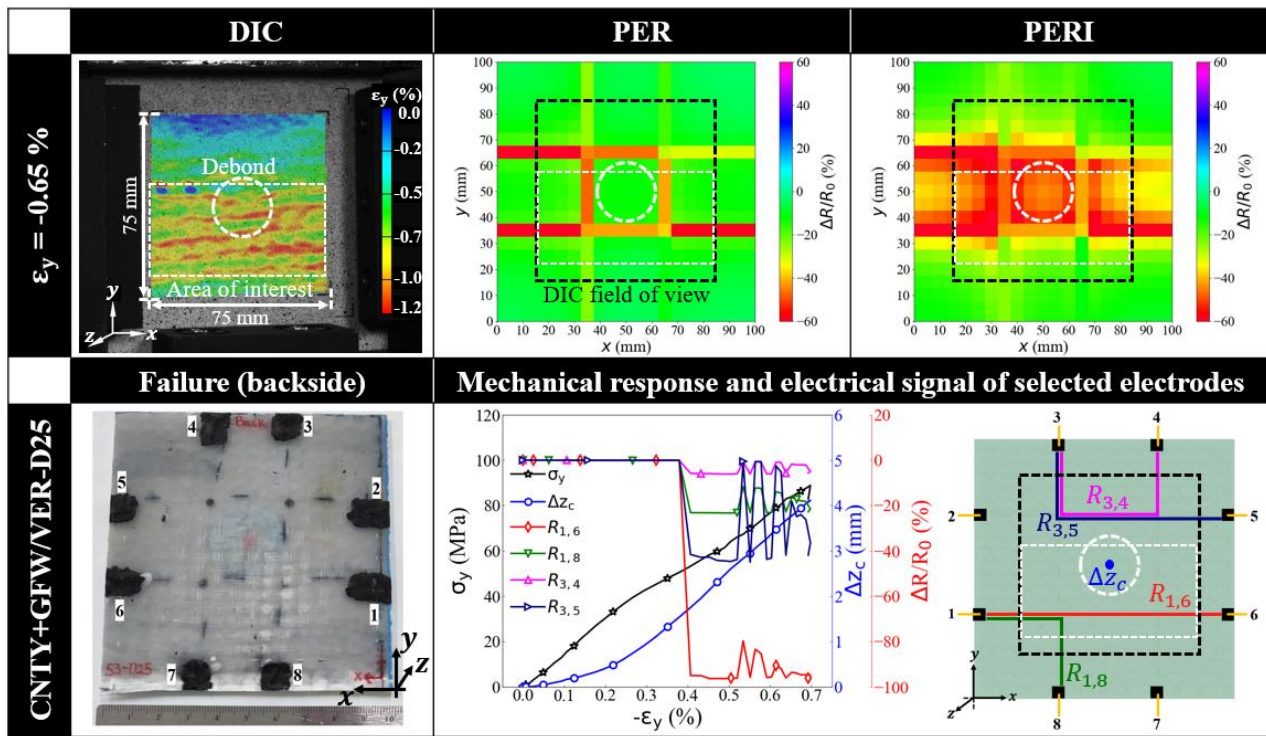


**Fig. 3.26.** Structural health monitoring of an exemplary GFW+CNTY/VER-D25 panel.

### 3.4.3. *In situ electrical mapping and damage detection during cyclic compression loading*

The mechanical response of a representative GFW+CNTY/VER-D25 panel under cyclic compression loading up to 15000 cycles is shown in Fig. 3.27. The test was force-controlled reaching a constant maximum force of 16.4 kN, equivalent to  $\sim 60.7$  MPa. It is observed that  $\epsilon_y$  presented a very slight increment throughout all cycles. The panels also exhibited notable buckling from the first cycle, with  $\Delta z_c$  around 1.40 mm. At this level of load and strain, the panels tested in monotonic compression already displayed significant buckling (Fig. 3.23b). This buckling is attributed to the high slenderness ratio of the panels. In this case, there is a notable increase in  $\Delta z_c$  over the cycles, reaching  $\sim 2.0$  mm at cycle 14997.

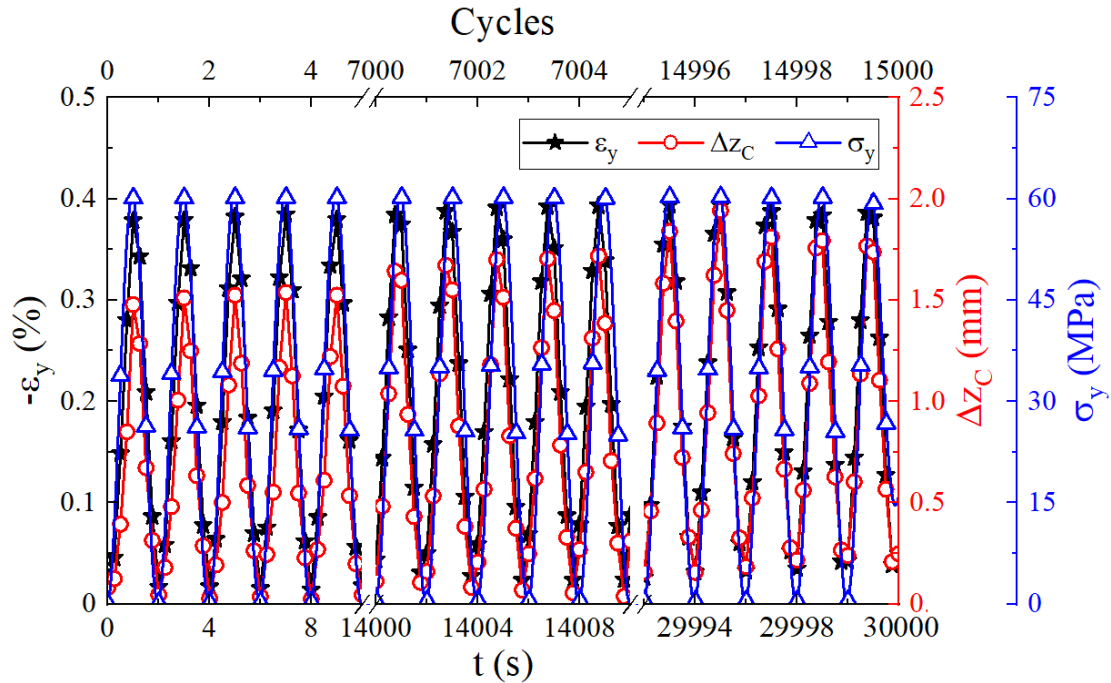


**Fig. 3.27.** Mechanical response of a representative GFW+CNTY/VER-D25 panel under cyclic compression loading.

The strain fields obtained by DIC during the unloading/loading states at cycles 1, 7000, and 15000 are shown in Fig. 3.30. The left column shows the loading stage while the right one shows the corresponding unloading stage belonging to the same cycle. It is observed that there are only small strain concentrations of  $\varepsilon_y$  in the vicinity of the debond at the center of the panel during the first cycle. The strain in this region increases with the number of cycles, initiating from the center of the specimen and propagating toward the top edge. This indicates an accumulation of damage in this area of the panel. It is also observed that there is some remaining permanent damage in the panel, as evidenced by the residual strain observed in the strain field of the panel during the unloading states at cycles 7000 and 15000.

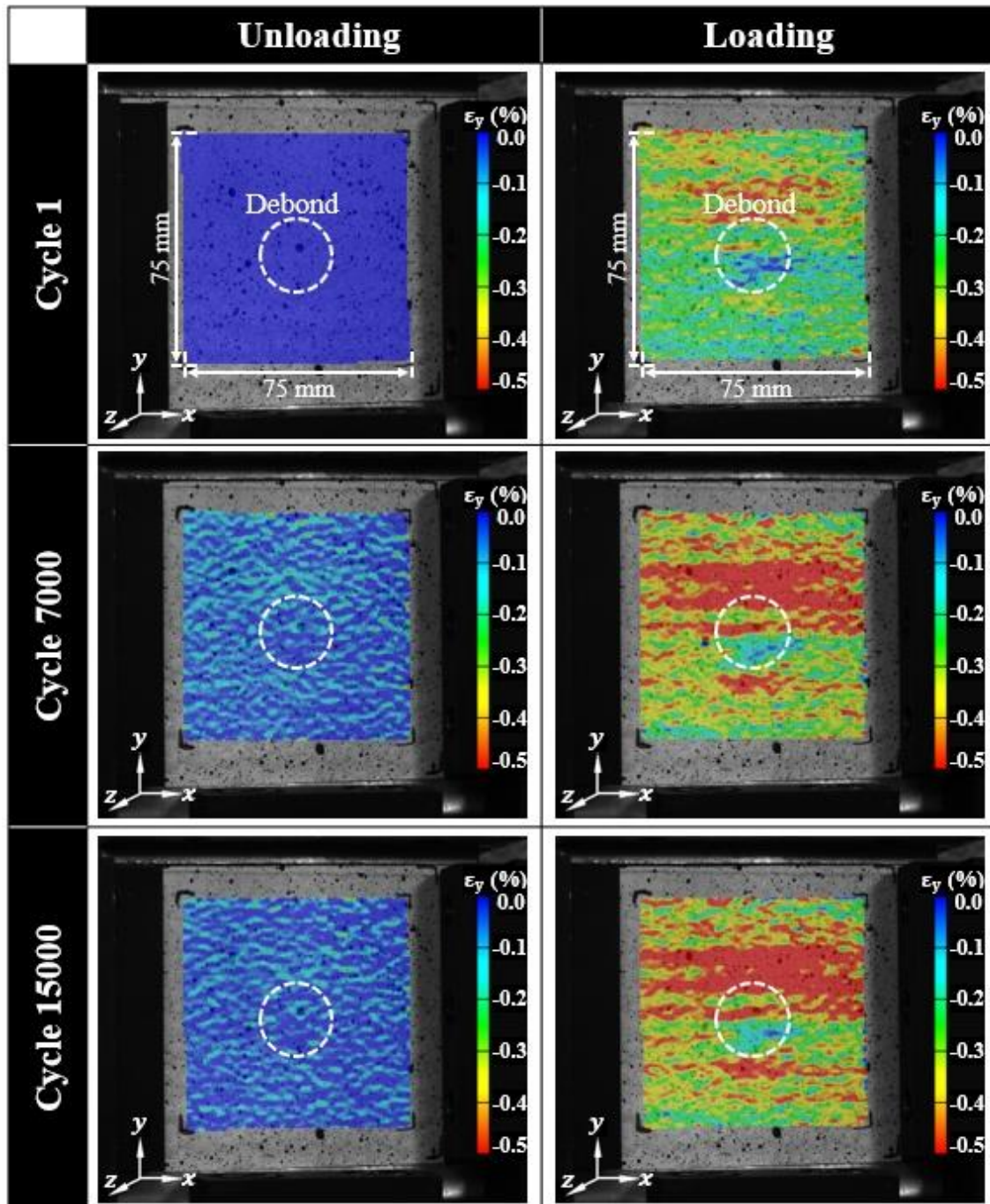


Fig. 3.28. DIC strain fields ( $\epsilon_y$ ) of a representative GFW+CNTY/VER-D25 panel under cyclic compression loading.

The out-of-plane displacement ( $\Delta z$ ) fields obtained by DIC during the unloading/loading states at cycles 1, 7000, and 15000 are shown in Fig. 3.29. It is observed that the panel exhibited somewhat uniform  $\Delta z$  in the whole area due to buckling. This behavior is characteristic of the first buckling mode. However, some panels exhibited also  $\Delta z$  strain fields which correspond to the second

buckling mode. Panel buckling increased gradually during testing, as shown in Fig. 3.27. Nevertheless, none of the panels collapsed during testing, showing residual strength.

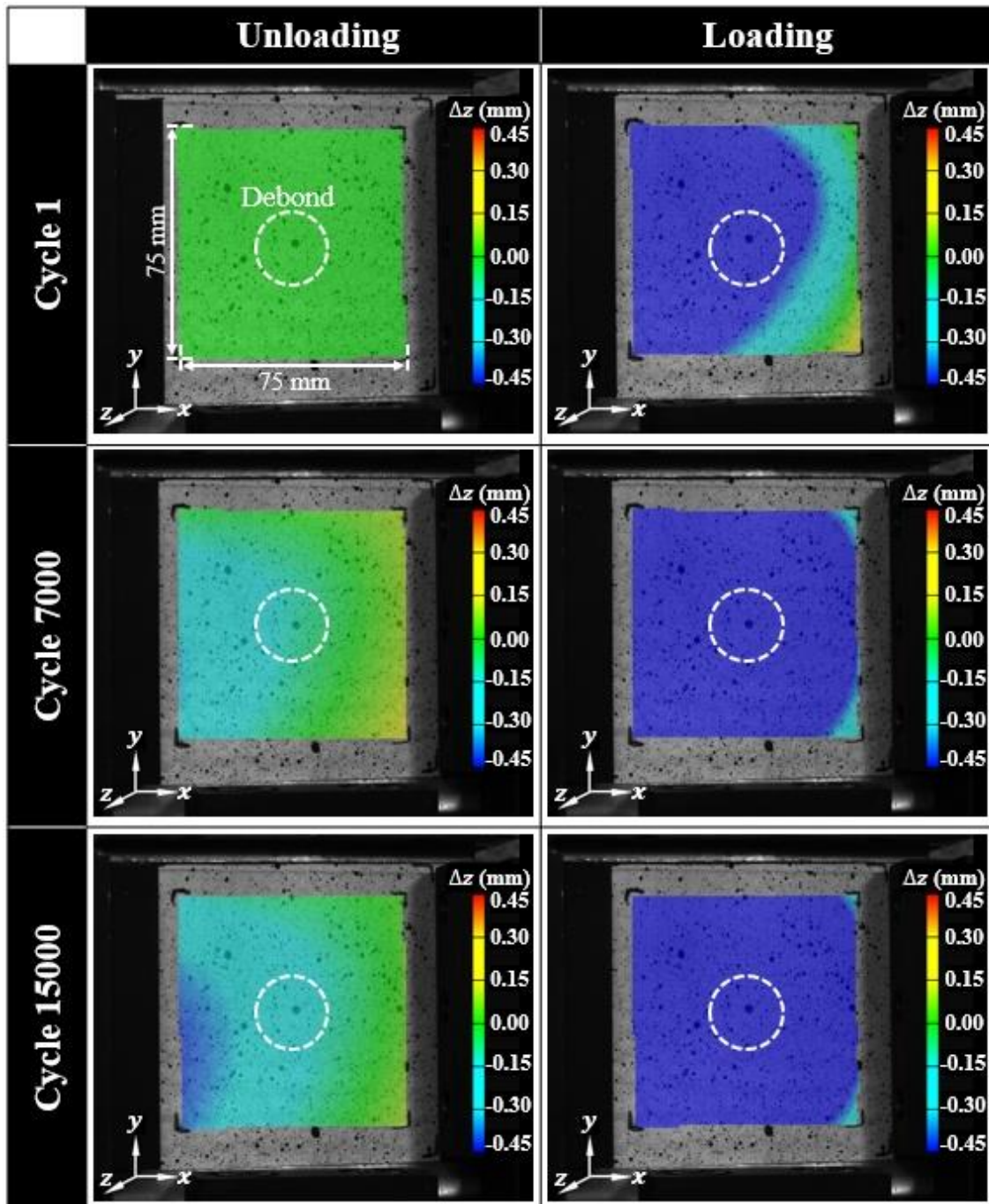
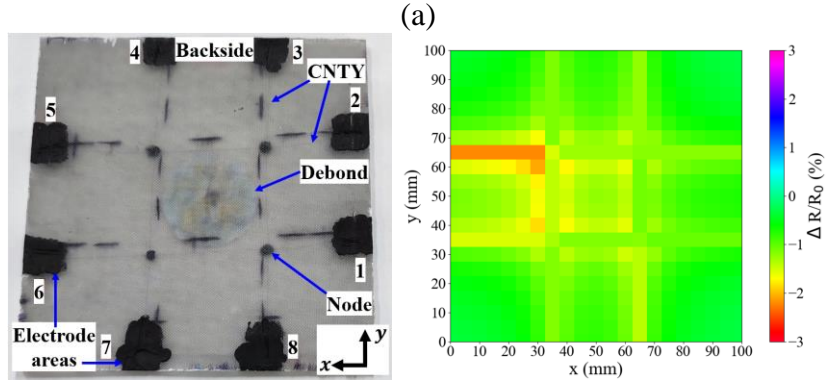
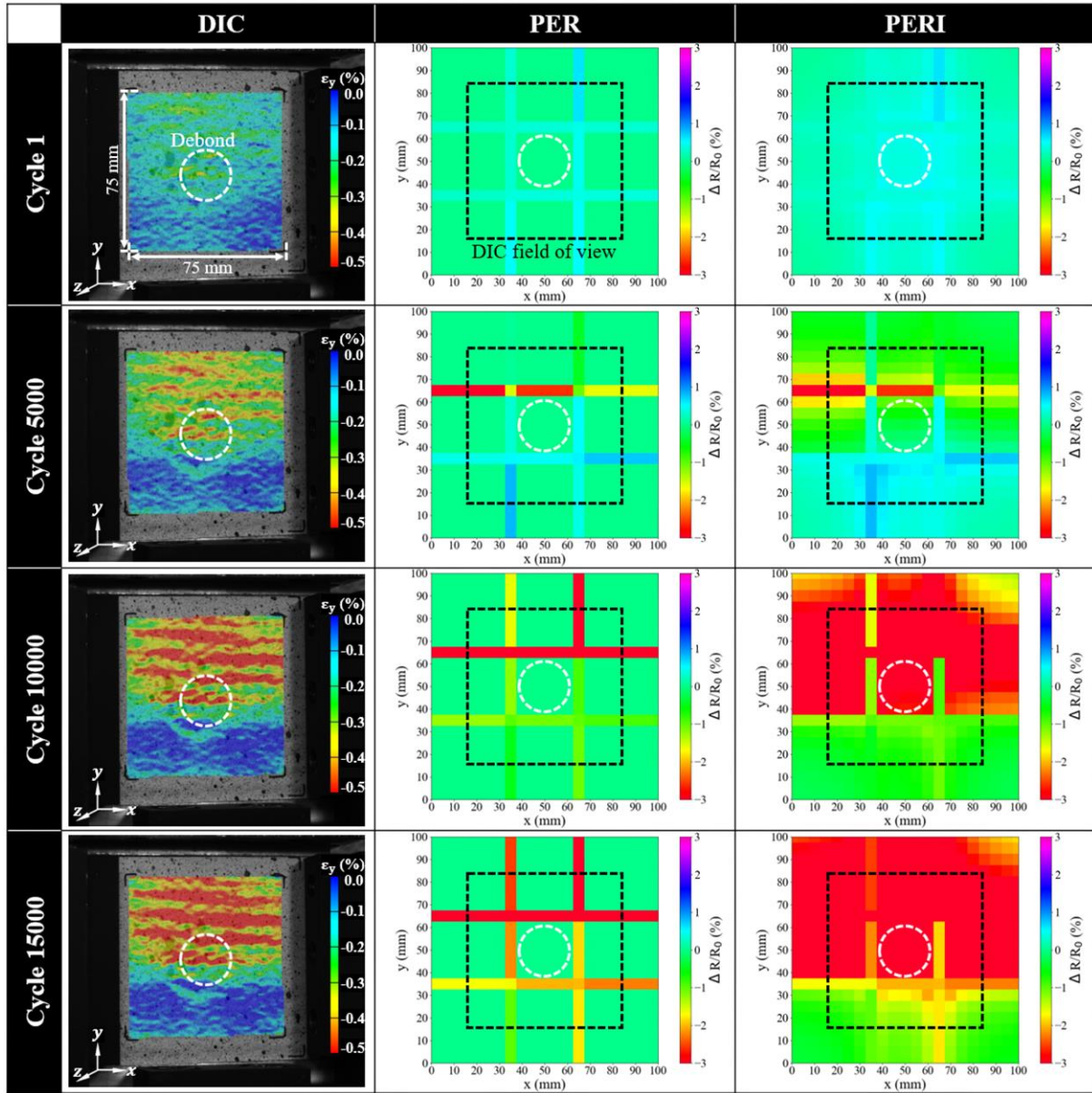


Fig. 3.29. DIC out-of-plane displacement fields ( $\Delta z$ ) of a representative GFW+CNTY/VER-D25 panel under cyclic compression loading.

DIC and electrical contour plots of an exemplary GFW+CNTY/VER-D25 panel under cyclic compression loading is shown in Fig. 3.30a, showing snapshots of selected cycles. The DIC images were taken at the maximum compression load during the cycle. The PER contour maps show that

the electrical resistance of the specimen increases as the strain damage progresses. This increase in  $\Delta R/R_0$  correlates with the strain concentration measured by DIC. The paths passing through the strain concentration area presented the highest values of  $\Delta R/R_0$ . This method enables to pinpoint regions exhibiting the most substantial damage by following the paths that exhibited a greater change in  $\Delta R/R_0$ . This effect was significantly enhanced with the PERI contour maps. This method smeared out the  $\Delta R/R_0$  measured response and captured the panorama of the damage more clearly, better matching the DIC observations. Despite the observed increase in  $\varepsilon_y$  (Fig. 3.28) and in  $\Delta z$  (Fig. 3.29) during cyclic compression testing, the GFW+CNTY/VER-D25 panels did not exhibit visible damage on their surface after testing, as shown in Fig. 3.30b. However, the electrical contour map of the panel after testing (Fig. 3.30b) reveals that there is internal damage. This ability of CNTYs to effectively detect and locate non-visible damage in laminated composite panels demonstrates their great potential for application in structural health monitoring. This potential has also been pinpointed in other studies where the CNTYs were introduced into laminated composites, e.g., [17,19,94]. However, most of these studies were limited to investigating only the electrical response of the CNTYs, without employing algorithms to generate structural damage maps. In this context, artificial intelligence algorithms could be used to enhance the sensing and localization of structural damage in CNTY arrays. Thus, there is still room for improvement, not only in the development of threads but also in the development of advanced algorithms for data management. Therefore, CNTYs represent a cutting-edge solution for the development of advanced, high-performance smart materials. Additionally, it opens up a wealth of possibilities across multiple sectors, promoting safety, efficiency, and longevity in various applications.



**Fig. 3.30.** SHM of an exemplary GFW+CNTY/VER-D25 panel under cyclic compression loading. (a) DIC and electrical contour maps during loading (at maximum compression load) of selected cycles, (b) photograph of the backside of the panel after testing and its PERI contour map.

## Conclusions and perspectives

Carbon nanotube (CNT) yarns (CNTYs) exhibit remarkable mechanical properties, energy dissipation capabilities, and multifunctional characteristics, positioning them as smart hierarchical materials with vast potential. In situ experiments using Raman spectroscopy and scanning electron microscopy have provided evidence of the dominance of structural modifications of the CNTY fibrils over material stretching in CNTYs during tensile loading. In situ Raman spectroscopy showed that the peak position of the D band is only slightly shifted towards lower wavenumbers as the axial strain of the CNTYs increases. This small Raman shift indicates that the mechanical response of the CNTY is governed by structural motions, slippage, and rotations of the fibrils and CNT bundles, rather than to C-C bond stretching. The contribution of material (C-C) deformation to the stretching of the CNTY only arises above 0.5 % strain, evidenced by a small Raman shift strain factor of  $-0.30 \text{ cm}^{-1}/\%$ . This structural behavior yields CNTYs with very high energy-dissipation capabilities, which are reflected in their tensile hysteresis response under cycling loading and high loss modulus in dynamic mechanical analysis. The normalized hysteresis of these CNTYs decreases with each cycle until leveling off around cycle 230. This indicates that, in addition to the energy dissipated by friction, there is a contribution of the dissipated energy due to irreversible changes in the structure of the CNTYs. The specific (per unit weight) dissipated energy of these CNTYs is comparable to that of carbon steels. An average piezoresistive gage factor of 0.36 was measured for the CNTYs. The thermoresistive response under end-clamped conditions (i.e., mechanically constrained) was nearly linear and similar for heating and cooling, with an average coefficient of thermoresistive sensitivity of  $-7.26 \times 10^{-4} \text{ K}^{-1}$ . Both the thermoresistive response and the DMA temperature scans are affected by the initial condition of the CNTY. This means that thermal decomposition of hydrocarbons and possibly other volatile species remaining from the synthesis may affect the DMA thermal and thermoresistive responses. The electrical response of the CNTYs during DMA testing is governed by their thermoresistive response. In situ SEM imaging of CNTYs subjected to axial tensile loading revealed that the CNTYs undergo a significant diameter reduction and rotation (untwist) due to fibril rearrangement. The failure of CNTYs is attributed to fibril pull-out caused by fibril-fibril slippage. The radial contraction ratio of the CNTYs decreases exponentially with increasing axial strain, primarily due to their high porosity. Higher radial contractions occur in the early loading stages. For the type of CNTYs investigated herein, the measured radial contraction ratio decreased from  $\sim 5.4$  (for strains of 0.4

%) to ~1.1 (for strains above 7.0 %). These findings emphasize the significance of the radial contraction effects in the axial mechanical response of CNTYs. The coaxial helix model offers insights into the nonlinear mechanical response of CNTYs, highlighting the importance of the radial contraction ratio and its dependence on applied strain. The mechanical response of the CNTY is strongly influenced by the slip factor, fibril radius, and fibril length. The results showed that the weakest link of the CNTY is the shear strength between fibrils. Increasing such inter-fibril shear strength is crucial for achieving the ultimate goal of high load-bearing CNTYs. All these structural changes influence the electrical response of the CNTYs. However, simultaneous measurements of the electrical resistance during relaxation testing indicates that capacitance and electrical charge accumulation influence the electrical response of CNTYs beyond the internal structural rearrangement of CNTs, bundles, and fibrils. Upon stress relaxation, the electrical resistance of CNTYs decreases exponentially over time, but it does so at a significantly slower rate than the specific stress. Structural relaxation and equilibrium occurred faster than electrical relaxation. This means that capacitive and charge transport effects occur even after structural motions of the fibrils have reached equilibrium. These findings are crucial for their integration into composite materials and as sensors in composite structures.

The structural health monitoring technique with non-invasively integrated CNTYs used herein enabled the detection and localization of internal damage in the laminated composite panels made of glass fiber weaves and vinyl ester resin under monotonic and cyclic compression loading. Dedicated post-processing algorithms were developed to analyze the electrical resistance signals concurrently acquired from a grid of four CNTYs arranged in the form of the “tic-tac-toe” game placed inside a  $100 \times 100 \times 2.7 \text{ mm}^3$  glass fiber weave/vinyl ester panel tested in edgewise compression. The tested panels failed due to delamination, matrix cracking, and fiber breakage caused by buckling, which was attributed to the panels’ high slenderness ratio. The localization of critically damaged zones by the electrical technique correlated well with digital image correlation measurements. Monitoring progressive damage under cyclic compression loading demonstrated the effectiveness of CNTYs for structural health monitoring in advanced fiber-reinforced polymeric composite materials.

All these findings indicate that CNTYs hold remarkable promises for the development of advanced, high-performance smart materials. These materials could find applications in aerospace, automotive, biomedical, and civil engineering, where strong, multifunctional lightweight materials

are in high demand. In this context, the CNTYs can be integrated into composite materials for structural health monitoring applications without sacrificing mechanical performance, offering real-time feedback on stress concentration and damage detection. This capability can significantly improve safety and reliability in various engineering industries. The potential of CNTYs to enhance condition-based maintenance, economic savings, and safety standards underscores the importance of continued research and development in this field. Therefore, future study efforts could focus on refining the synthesis processes of CNTYs to optimize their electromechanical performance. Moreover, efforts should be concentrated on the structural design of CNTY-based composites to maximize their mechanical and multifunctional performance. Future steps in this direction could involve further refining the integration techniques of CNTYs, exploring additional sensor functionalities, and developing advanced algorithms (e.g., artificial intelligence algorithms) for more accurate and comprehensive damage assessment. Therefore, continued research and development efforts are essential to unlock the full potential of CNTYs and translate their remarkable properties into practical solutions for various engineering challenges.

# Appendices

## A. Dynamic mechanical response of carbon nanotube yarns

### A.1. Effect of static force

The DMA with temperature ( $T$ ) scan was performed from 30 to 300 °C, with a heating rate of 5 °C/min, frequency ( $f$ ) of 1 Hz, and using different static forces ( $F_{z_s}$ ). The temperature scan of a collection of CNTY replicas are shown in Fig. A.1. It is observed that the CNTYs exhibited significant experimental dispersion, which can be attributed to structural variations among CNTYs. However, the variations observed when using different  $F_{z_s}$  fall within the range of experimental scatter for 18 and 30 mN. With 50 mN, the majority of CNTYs experienced premature failure.

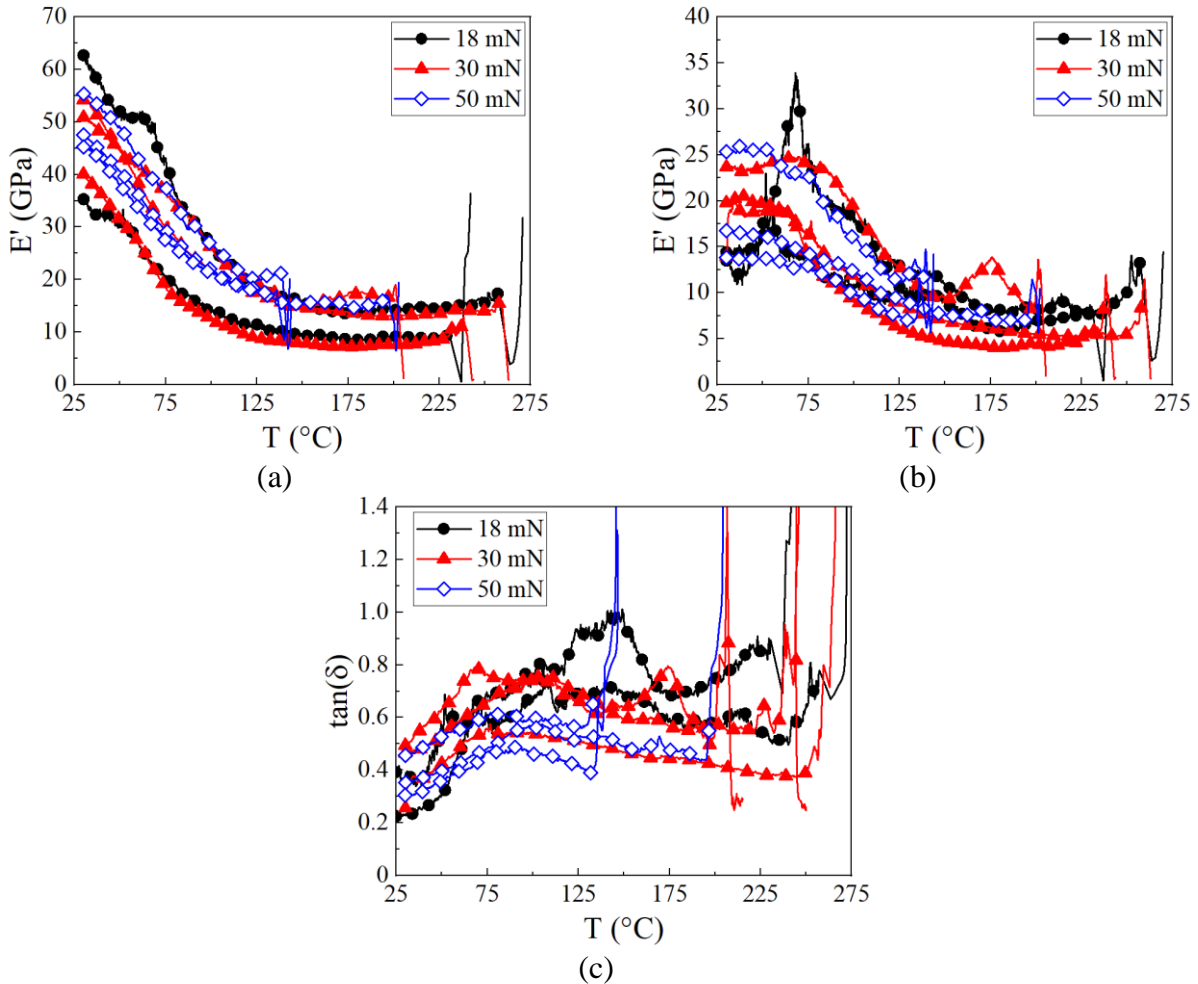


**Fig. A.1.** DMA response of a collection of CNTYs as a function of temperature ( $T$ ), using different static forces. (a) Storage modulus ( $E'$ ), (b) loss modulus ( $E''$ ), (c) damping ratio ( $\tan(\delta)$ ).

The frequency scans from 0 to 51 Hz of the CNTYs at 30 °C with different  $F_{z_s}$  are shown in Fig. A.2. A frequency-independent response of the yarn with only random oscillations around a constant value was observed for frequencies smaller than 18 Hz, and thus results are not shown within that frequency range. After 18 Hz, both  $E'$  and  $E''$  increase with increased frequency, indicating frequency-stiffening behavior. For all static forces, the storage modulus increases almost linearly with frequency. For low strains rates (i.e., low frequency), the CNT bundles have enough time to align longitudinally and relax [61]. As the frequency increases, the CNTs and CNT bundles relaxation through sliding turns into a slow process compared with the loading, and therefore, the strain re-distribution becomes more and more difficult [61].

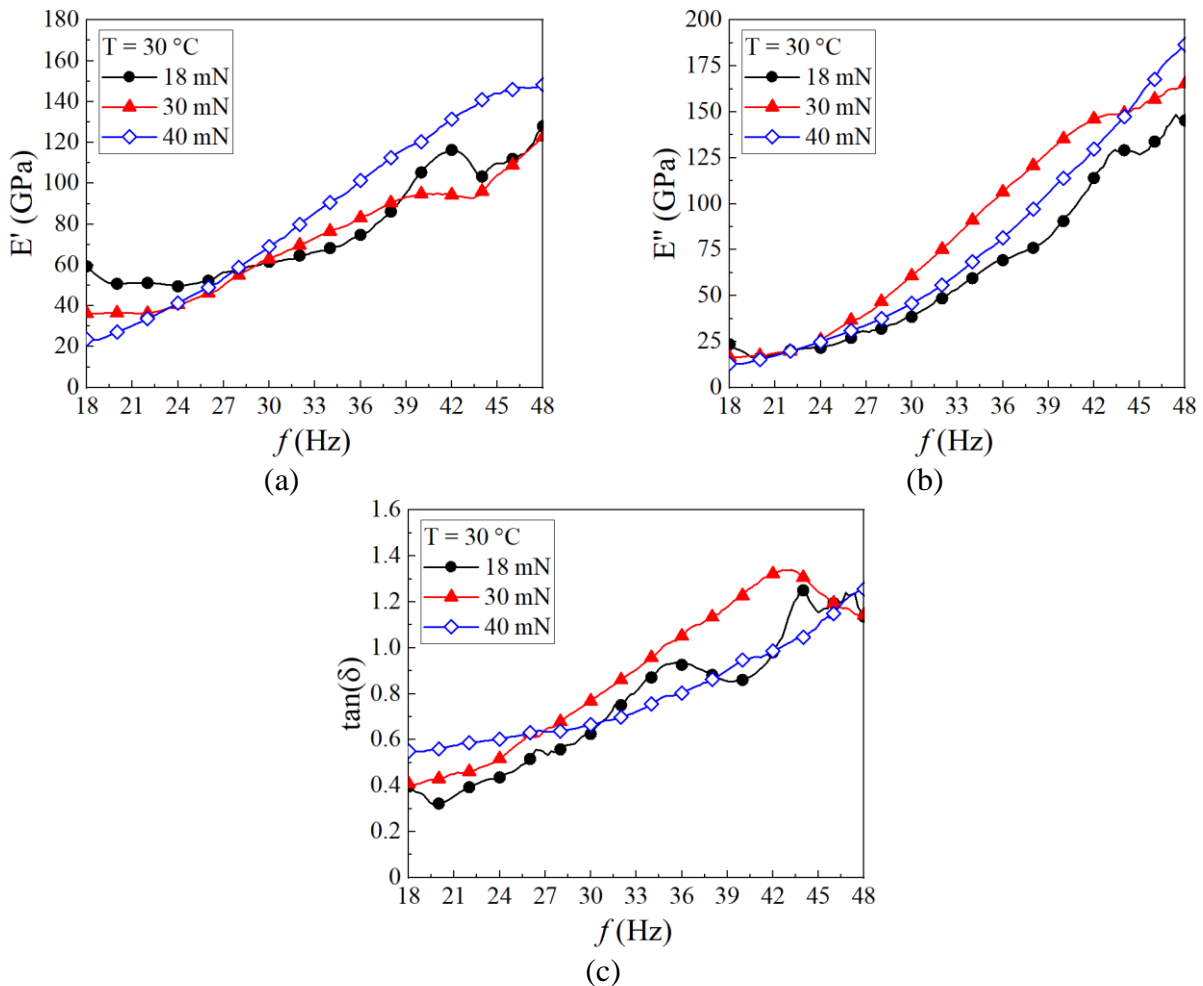


**Fig. A.2.** DMA tensile response of an individual CNTY (at 30 °C) as a function of frequency ( $f$ ) using different static forces. (a) Storage modulus ( $E'$ ), (b) loss modulus ( $E''$ ), (c) damping ratio ( $\tan(\delta)$ ).

### A.2. Effect of frequency

The DMA of CNTYs with frequency scans from 0 to 51 Hz was performed using  $F_{zs} = 18$  mN at different constant temperatures are shown in Fig. A.3. The specimen-to-specimen variability is also large, but conspicuous trends of the material response are captured. The trend in increasing  $E'$ ,  $E''$ , and  $\tan(\delta)$  with increased frequency is consistent for all temperatures examined.

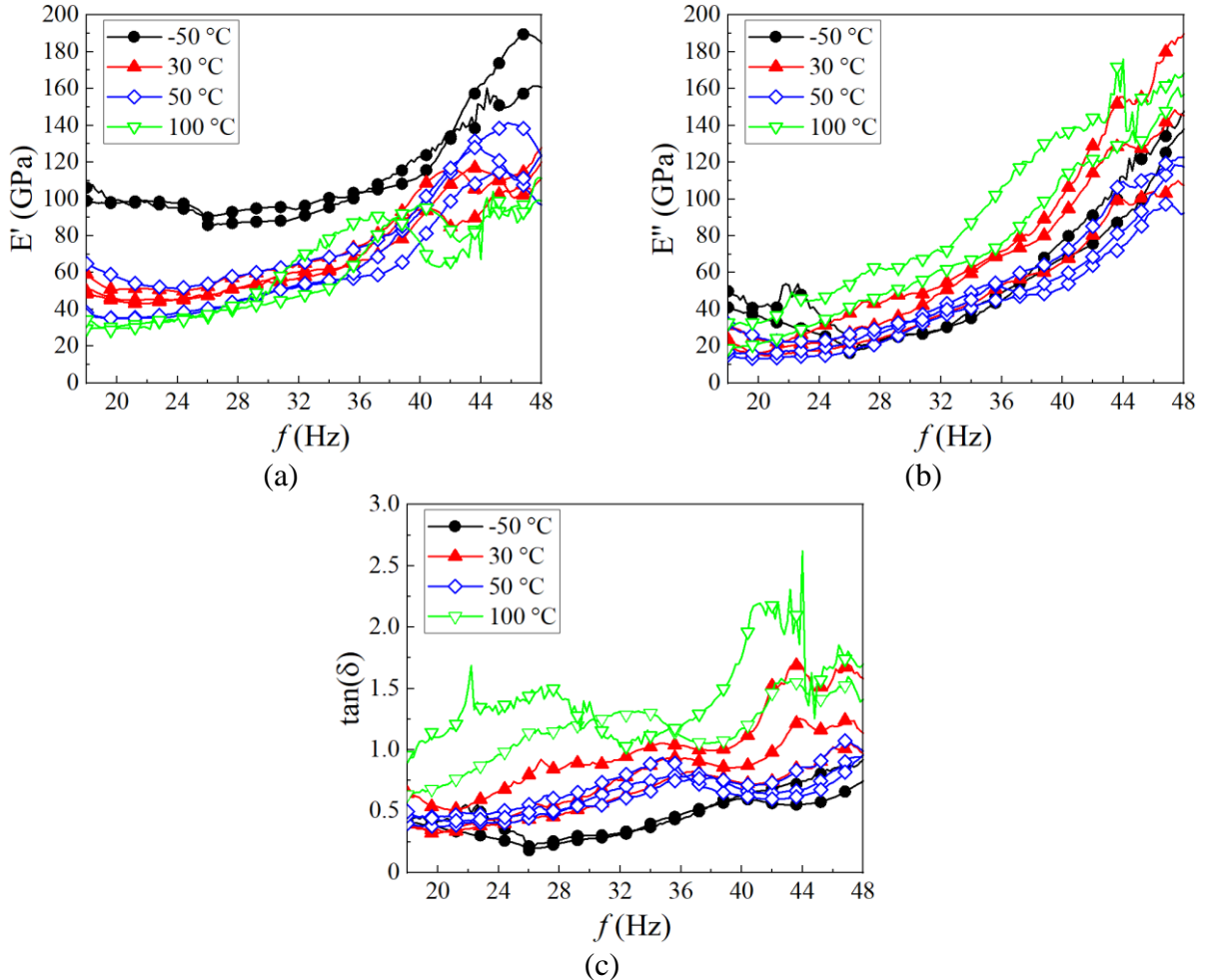
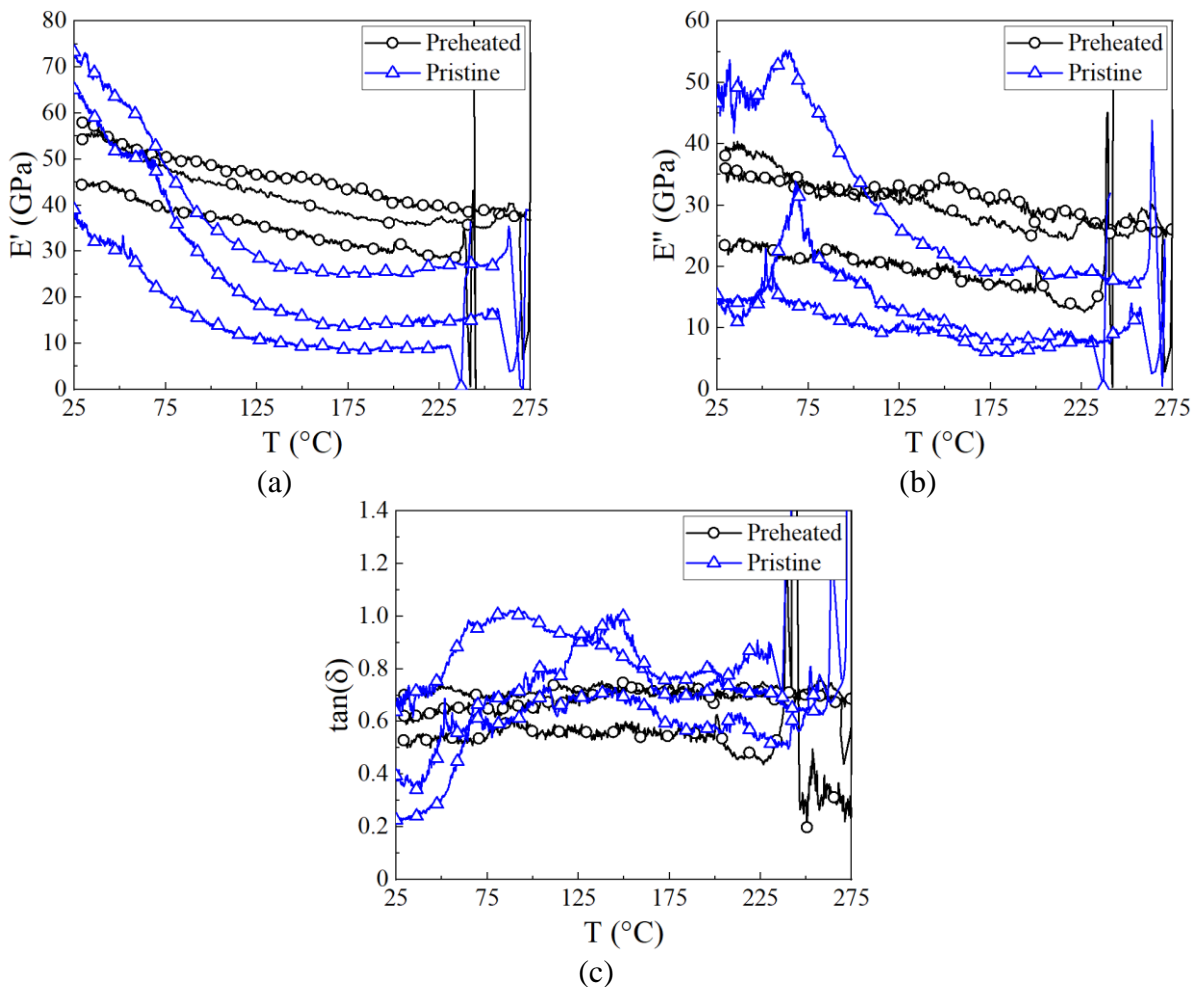


**Fig. A.3.** DMA response of a collection of CNTYs as a function of frequency ( $f$ ) for different temperatures. (a) Storage modulus ( $E'$ ), (b) loss modulus ( $E''$ ), (c) damping ratio ( $\tan(\delta)$ ).

### A.3. Effect of preheating

The DMA tensile response of non-dried (pristine) and preheated CNTYs as a function of temperature is shown in Fig. A.4. The temperature scan was performed from 30 °C to 300 °C, with a heating rate of 5 °C/min,  $F_{zs} = 18$  mN, and  $f = 1$  Hz. It is observed that  $E'$  (Fig. A.4a) of the pristine CNTYs decreases rapidly with increasing temperature from 30 to ~130 °C, after which  $E'$  remains almost constant. The preheated CNTYs show a more linear and smaller rate of decrease in

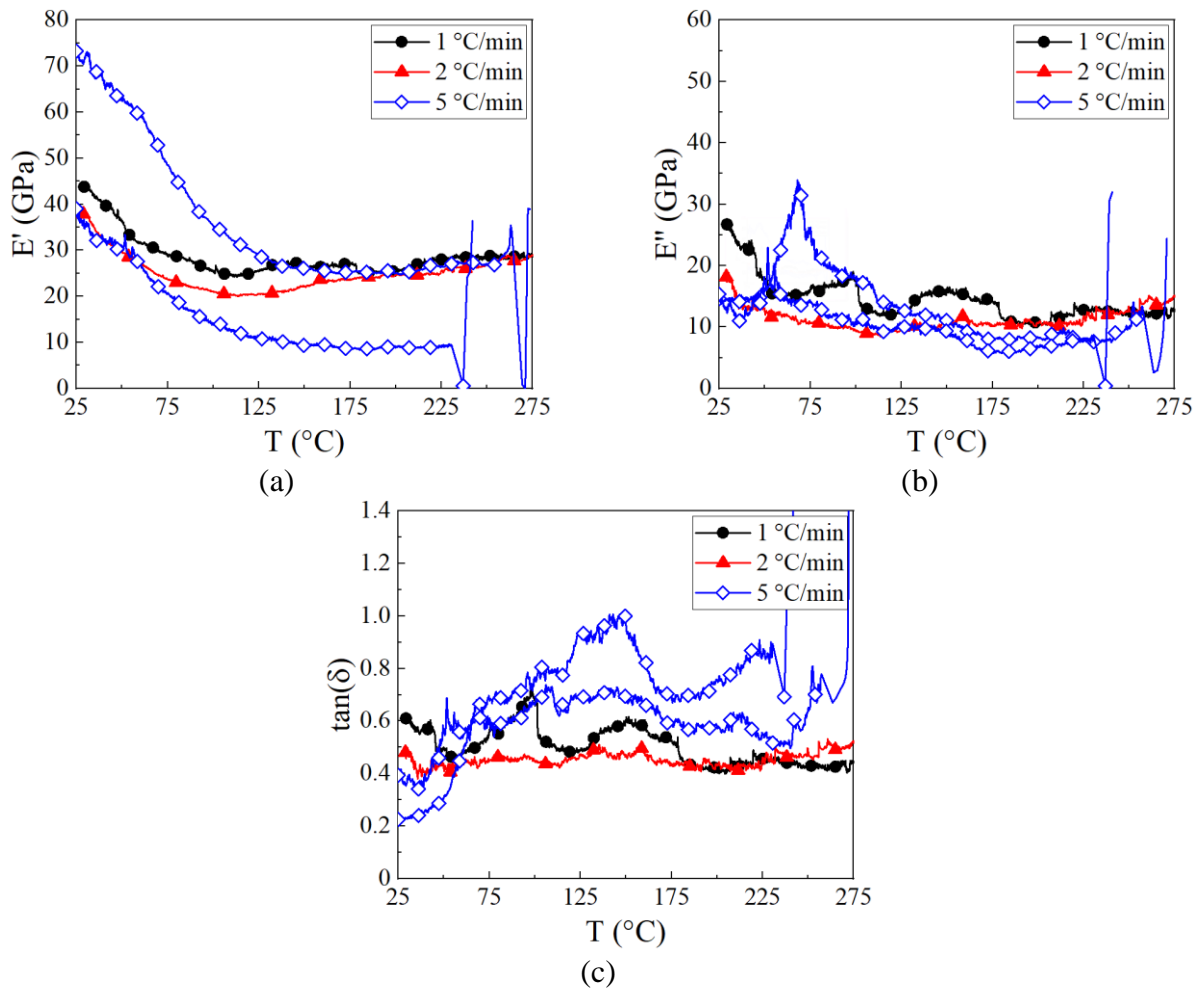
$E'$  with increased temperature. For the same temperature range,  $E''$  (Fig. A.4b) of the pristine CNTYs exhibit a slight increase, while the preheated CNTYs decrease almost linearly until reaching  $T \sim 65$  °C, from where  $E''$  decreases and then remains almost constant. This yields in pristine CNTYs having a  $\tan(\delta)$  (Fig. A.4c) which increases steadily from  $\sim 0.2$  to  $\sim 0.6$ , up to 60 °C, and then oscillates around  $\sim 0.6$  for higher temperatures. The preheated CNTYs exhibit nearly constant damping over almost the entire range. TGA showed that the CNTYs lose weight during the preheating (see section 3.1.4). Once the synthesis byproducts and amorphous carbonaceous materials within the CNTYs are eliminated during preheating, mainly the CNTs that make up the yarn remain. However, if the yarn is not preheated, some byproducts and possibly nonstructured carbon may undergo thermal degradation below 130 °C. Therefore, the thermal transformation of such byproducts may further affect the structural changes, which facilitates the fibril/bundle relaxation through slipping [67].



**Fig. A.4.** DMA tensile response of the CNTYs as a function of temperature ( $T$ ) with and without (pristine) preheating. **(a)** Storage modulus ( $E'$ ), **(b)** loss modulus ( $E''$ ), **(c)** damping ratio ( $\tan(\delta)$ ).

#### A.4. Effect of heating rate

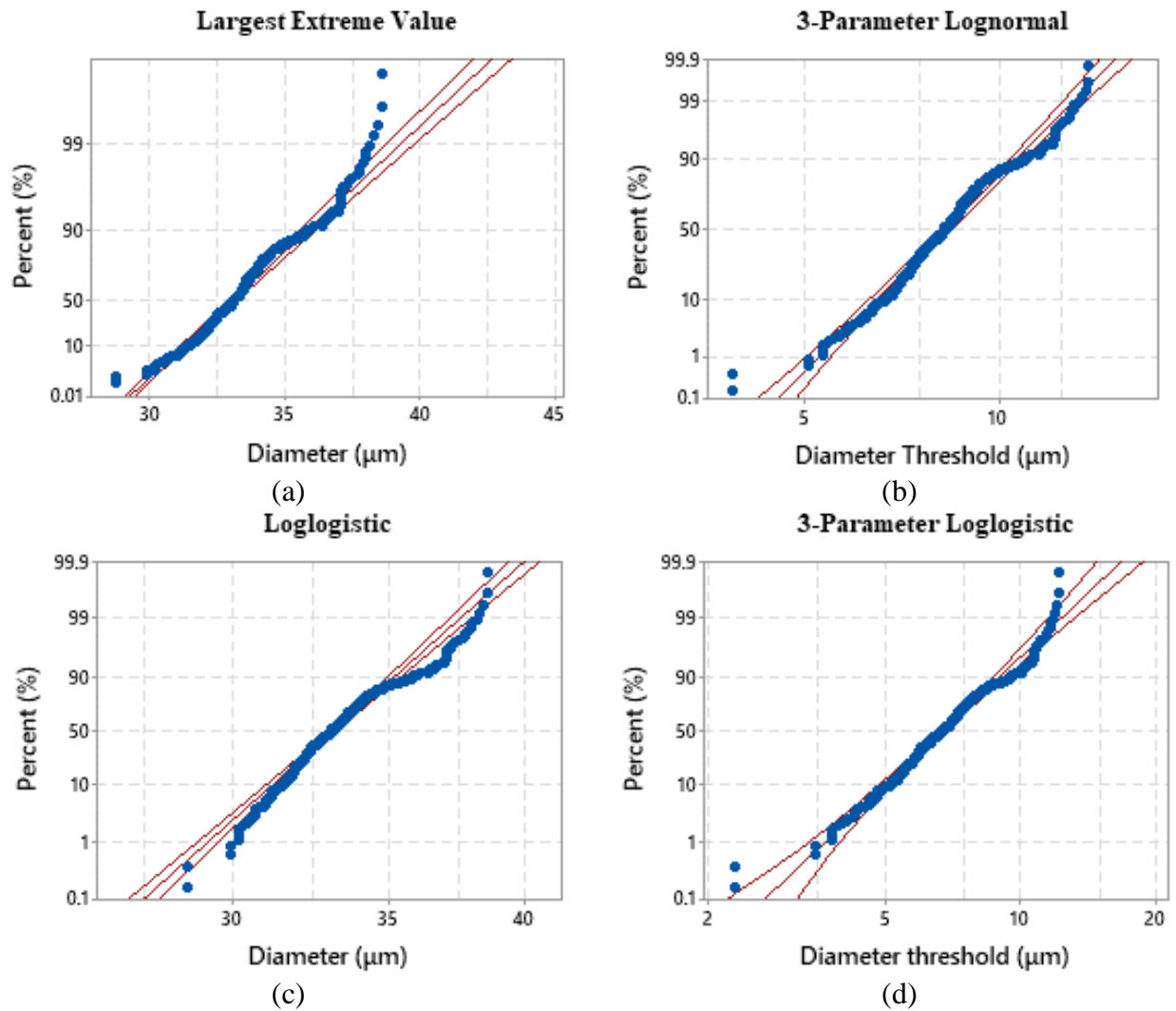
In order to investigate a potential effect of the heating rate, the CNTYs were tested at 1 Hz from 30 to 300 °C, with  $F_{zs} = 18$  mN, using different heating rates. The DMA tensile response of the CNTYs as a function of temperature at different heating rates is shown in Fig. A.5. The curves enclosing those for specimens at 5 °C/min are included for comparison. Unlike the CNTYs tested at 5 °C/min, described in section 3.1.13, the CNTYs tested at slower heating rates (1 and 2 °C/min) show a smaller decrease in  $E'$ . In addition,  $E''$  and  $\tan(\delta)$  remain almost constant throughout the DMA. By decreasing the heating rate, the rate of mass loss due to evaporation from the densifier and moisture, as well as the degradation of amorphous carbon, also decreases. This allows the fibrils/bundles enough time to rearrange, similar to what is observed when the CNTYs are subjected to low strain rates [61]. However, no significant effect has been observed among the CNTYs tested at different heating rates, as they fall within the natural variability of CNTYs.



**Fig. A.5.** DMA tensile response of the CNTYs as a function of temperature ( $T$ ) using different heating rates. (a) Storage modulus ( $E'$ ), (b) loss modulus ( $E''$ ), (c) damping ratio ( $\tan(\delta)$ ).

## B. Diameter distribution of the carbon nanotube yarns

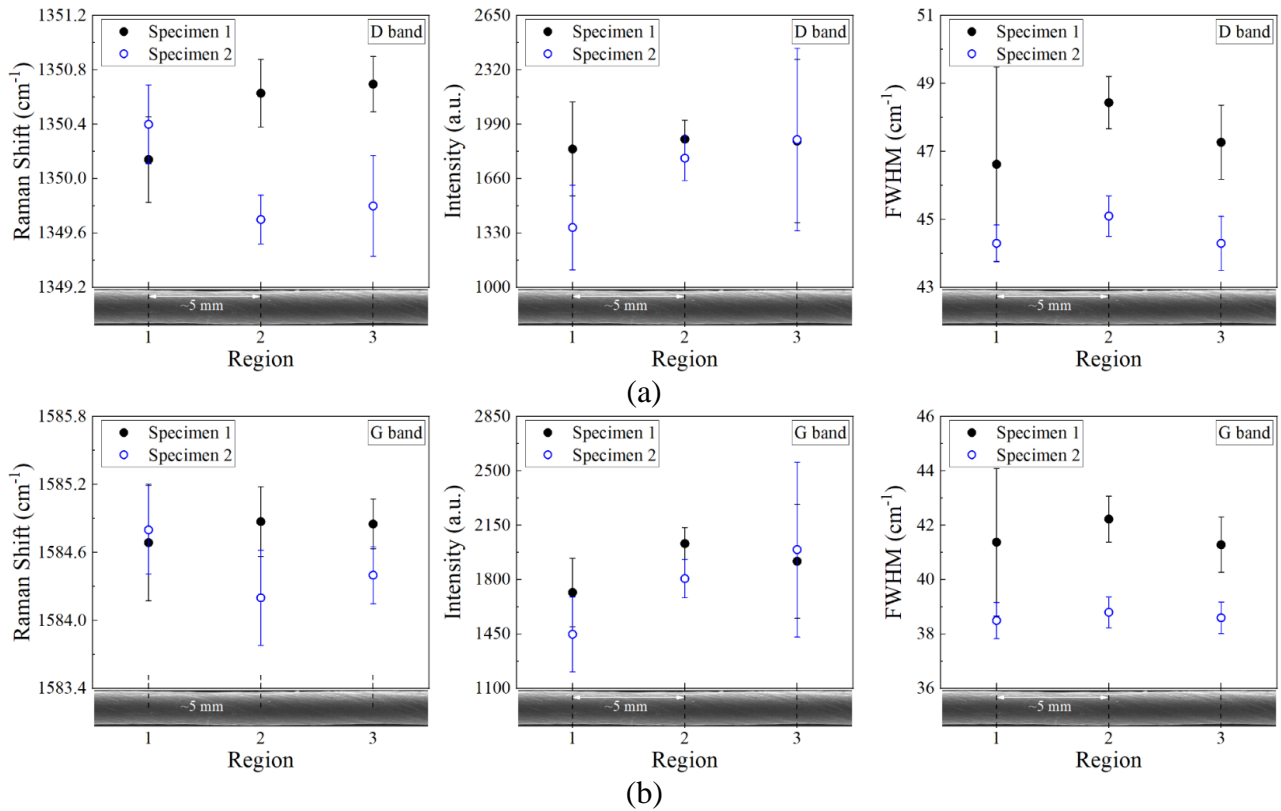
The probability plots of the statistical distributions that best match the diameter distribution of the CNTYs (based on the Anderson-Darling goodness-of-fit test [102]) are shown in Fig. B.1. These plots display the diameter measurements of the CNTYs (blue dots) against the expected values under a specific theoretical distribution within the confidence intervals (red lines). If the data closely follows the theoretical distribution, the points on the plot will align along a straight line. Deviations from this line suggest departures from the assumed distribution. Among the four statistical distributions in Fig. B.1, the 3-parameter loglogistic distribution was identified as the best-fitting diameter distribution, with an Anderson-Darling value of 1.34 (see Table 3.1).



**Fig. B.1.** Probability of the statistical CNTY diameter distributions. (a) Largest extreme value distribution, (b) 3-parameter lognormal distribution, (c) loglogistic distribution, (d) 3-parameter loglogistic distribution.

### C. Variability of Raman spectra in the carbon nanotube yarns as function of location and axial strain

To assess the natural variability of the CNTY in the D band position, a 10  $\mu\text{m}$  line scan (from 0 to 10  $\mu\text{m}$  in steps of 1  $\mu\text{m}$ , resulting in a total of 11 Raman spectra per line scan) was performed along the axial direction of the CNTY ( $z$ ), as described in section 2.2.5. This procedure was repeated in three regions of the CNTY spaced  $\sim 5$  mm, for two different specimens. The variability (mean value and standard deviation) in the peak position, intensity and FWHM of the Raman bands in the CNTYs is shown in Fig. C.1. This variability arises from the non-perfect spatial homogeneity of the CNTY, attributed to their hierarchical structure and current synthesis methods. For the D band peak position (Fig. C.1a), it exhibits a natural uncertainty ranging between 0.18 and 0.37  $\text{cm}^{-1}$ .



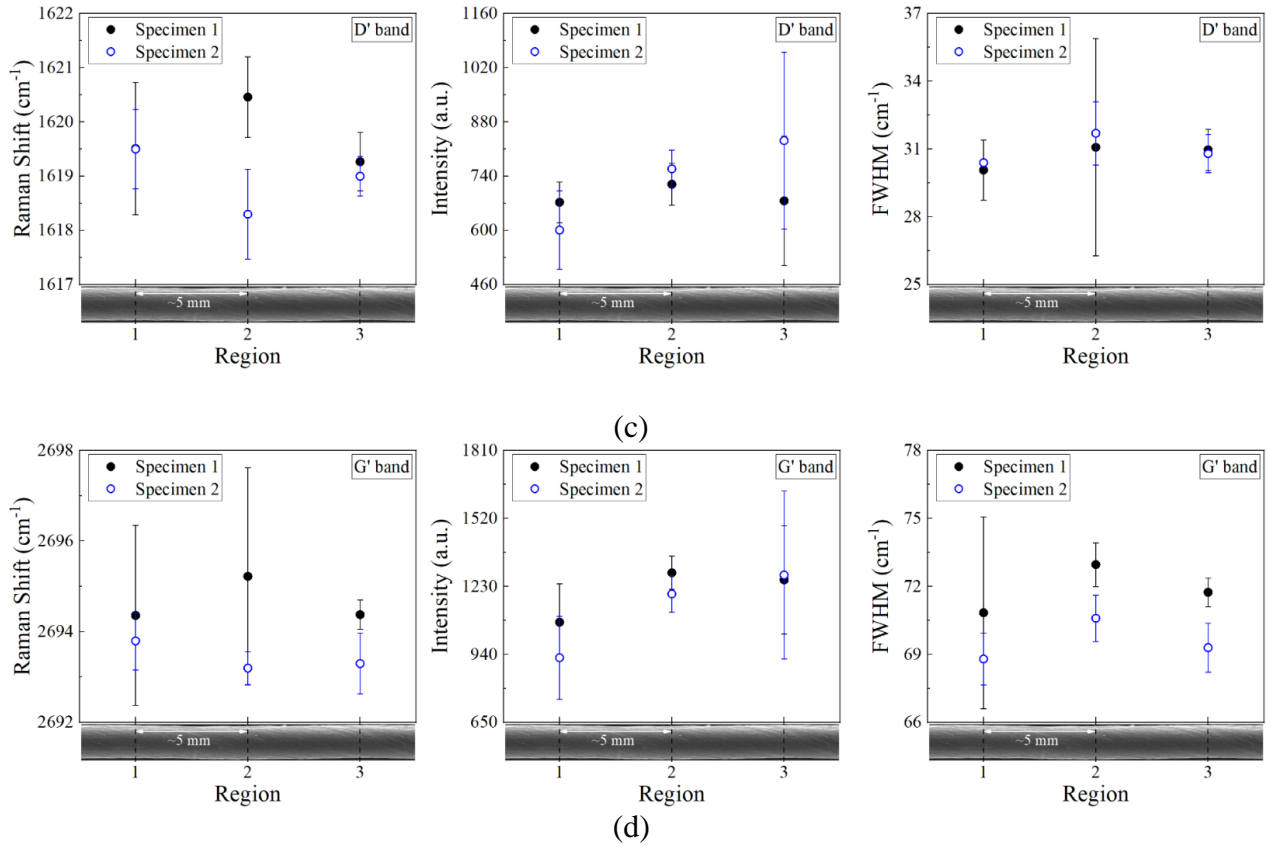


**Fig. C.1.** Variability of the Raman bands' peak position, intensity and FWHM of the CNTYs. (a) D band, (b) G band, (c) D' band, (d) G' band.

The peak position, intensity and FWHM of the Raman bands in the CNTYs as function of  $\varepsilon_z$  are shown in Fig. C.2. Except for the peak position of band D, the other Raman parameters do not exhibit significant changes or a clear trend.

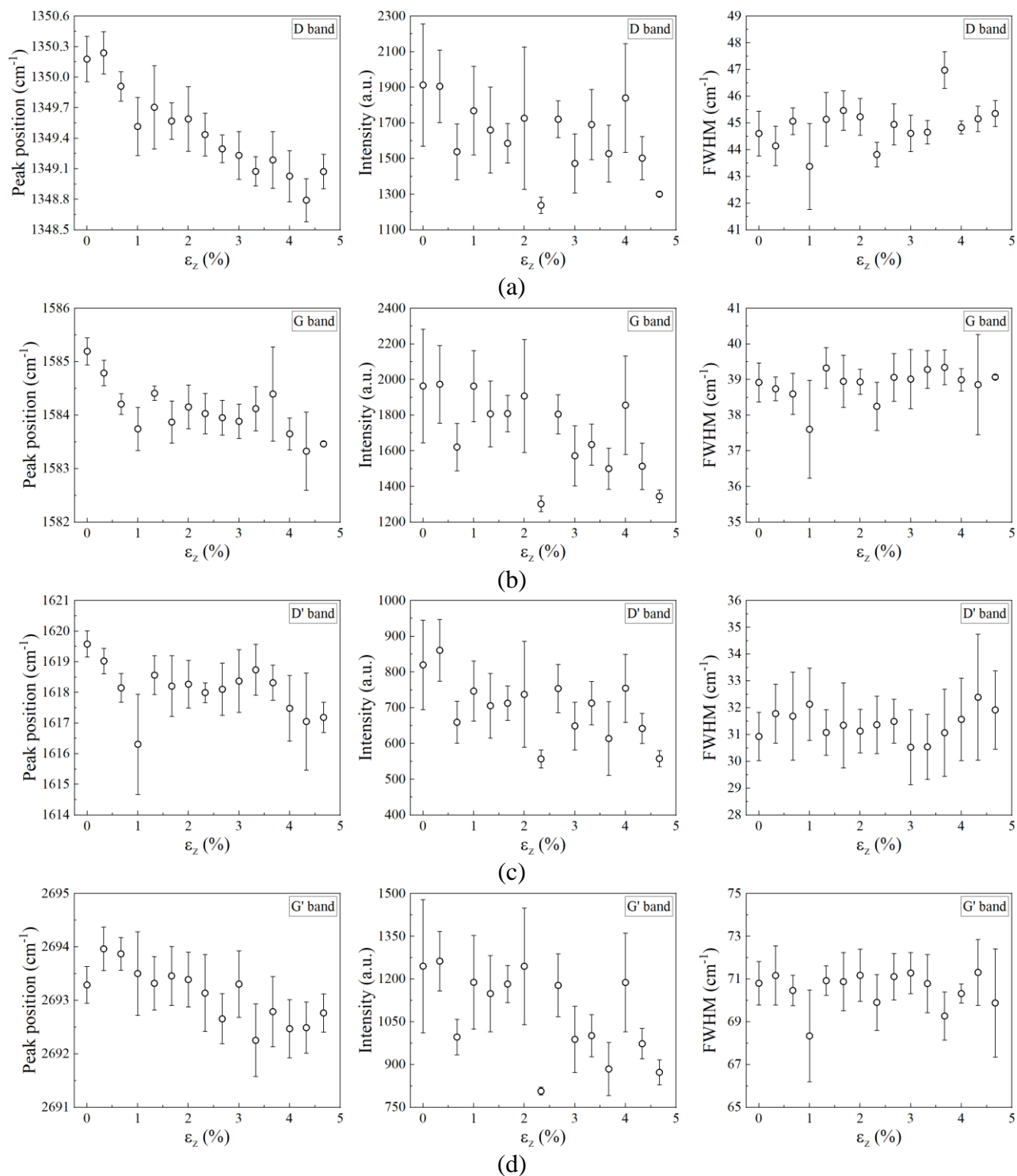


**Fig. C.2.** Raman bands' peak position, intensity and FWHM of the CNTYs as a function of axial strain ( $\epsilon_z$ ). (a) D band, (b) G band, (c) D' band, (d) G' band.

## D. Parametric analysis of the yarn's tensile model

### D.1. Tensile modulus and coefficient of friction of the fibrils

According to Eq. (2.11), the fibril's tensile modulus ( $E_f$ ) depends on the yarn's tensile modulus ( $E$ ), the twist angle at the yarn's surface ( $\theta_{\text{ext}_0} = 29.9^\circ$ ), and the slip factor ( $k$ ). The slip factor can be estimated by considering the radius ( $r_f = 172$  nm), length ( $L_f = 500$   $\mu\text{m}$ ), migration factor ( $Q = 4h$ ), and coefficient of friction ( $\mu$ ) of the fibrils (Eq. (2.11)). However, measuring  $\mu$  can be complex, and it is an important parameter not only for estimating  $k$  but also for determining the slippage ratio (Eq. (2.16)). Therefore, to obtain an accurate value of  $\mu$  (and consequently  $k$ ),  $E_f$  was plotted as a function of  $k$  as shown in Fig. D.1a. It is observed that the increase in  $E_f$  is small for  $k < 0.36$ . However, for  $k > 0.36$ , there is a rapid increase in  $E_f$  which reaches a maximum at  $k = 0.498$ , resulting in  $E_f = 7.89$  TPa (inset in Fig. D.1a). After this point ( $k > 0.498$ ),  $E_f$  immediately drops to unphysical negative values. From that point on, all values of the specific tensile moduli become negative, forming an antisymmetric curve (not shown). Since a negative  $E_f$  holds no physical significance, the value of  $k$  for the CNTY must be below 0.498. It is thus expected that the fibrils of the CNTYs have specific stiffnesses distributed within  $0 \leq k \leq 0.498$ . Several studies have reported the tensile modulus of CNT bundles and fibrils in the range between 30 and 1310 GPa [111–113]. Lower values correspond to fibrils that have larger diameters [111–113]. These values of  $E_f$  fall within the provided range of  $k$ , where the lower limit ( $E_f = 30$  GPa) corresponds to  $k = 0.37$ , and the top limit ( $E_f = 1.31$  TPa) corresponds to  $k = 0.496$ . In this case, as the fibrils used in this study have a relatively large diameter compared to those reported in [111–113], and since the measured elastic modulus of the CNTYs is relatively low ( $E = 5.8$  GPa), the lower bound was selected for the fibril modulus ( $E_f = 30$  GPa), yielding  $k = 0.37$ .

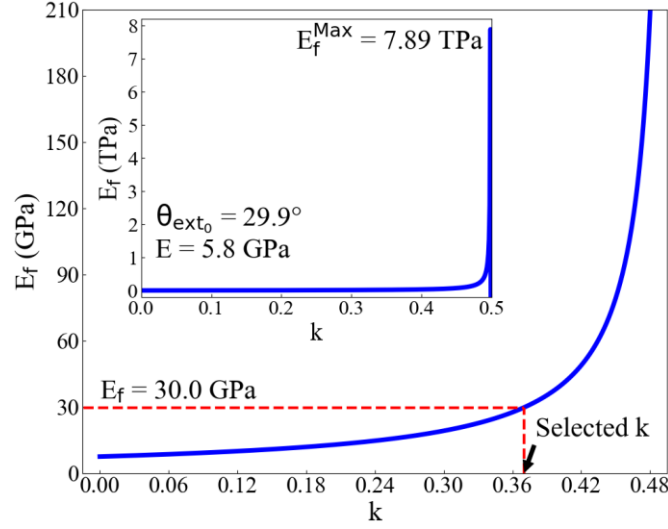


**Fig. D.1.** Effect of the slip factor ( $k$ ) in the fibril tensile modulus ( $E_f$ ) according to Eq. (2.11).

Knowing that  $Q$  depends on the strain and keeping constant the value of  $k$  (and thus  $E_f$ ), Eq. (8) can be rewritten to express  $\mu$  as a function of  $Q$  as,

$$\mu = \left( \frac{2r_f}{9L_f^2 k^2} \right) Q \quad (\text{D.1})$$

Equation (D.1) results in  $\mu = 1.11Q$ , where  $Q$  is in m. These results ( $E_f = 30$  GPa,  $\mu = 1.11Q$ , and  $k = 0.37$ ) were incorporated in the model for the mechanical behavior of CNTYs under tensile loading, Eq. (2.13), as described in section 2.3.

#### D.2. Radial packing density

The normalized packing density ( $\rho_r/\rho_r^{\text{Max}}$ , where  $\rho_r^{\text{Max}}$  is the maximum value of  $\rho_r$ ) as a function of the normalized radial position of the CNTY ( $r/r_{\text{ext}}$ ) for different values of  $\varepsilon_z$  is shown in Fig. D.2. The plots were generated using Eq. (2.14). It is observed that  $\rho_r/\rho_r^{\text{Max}}$  decreases from 1 at the center towards 0 at the yarn's surface. The fibrils at the center experience greater compression and are, therefore, more compacted. In contrast, the outer fibrils experience less compression, resulting in a more dispersed arrangement and, consequently, a lower packing density on the surface. As  $\varepsilon_z$  increases, the CNTY experience radial contraction, due to the rearrangement of the fibrils. This results in a reduction in porosity and consequently an increase in packing density.

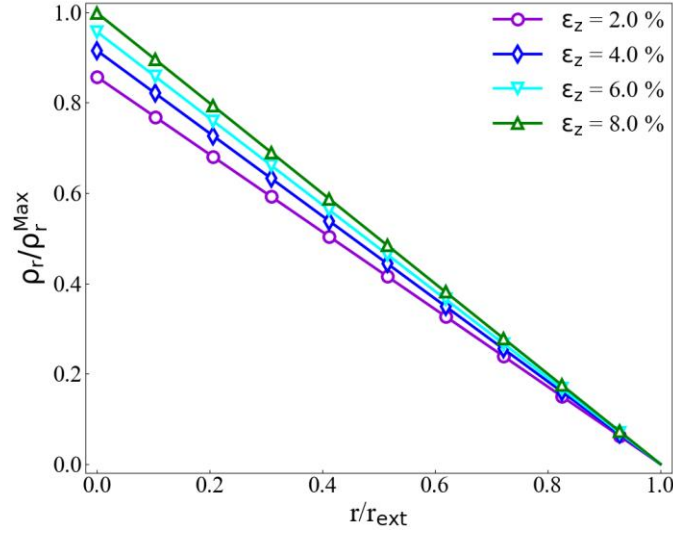


**Fig. D.2.** Distribution of the normalized packing density ( $\rho_r/\rho_r^{\text{Max}}$ ) along the normalized radial position of the CNTY ( $r/r_{\text{ext}}$ ) for different values of axial strain ( $\varepsilon_z$ ).

### D.3. Distribution of compressive transverse stress

The normalized compressive transverse stress in the CNTY ( $P/P_{\text{Max}}$ , where  $P_{\text{Max}}$  is the maximum value of  $P$ ) as a function of  $r/r_{\text{ext}}$  for different values of  $\varepsilon_z$  is shown in Fig. D.3. The plot was generated using Eq. (2.17). It is observed that  $P/P_{\text{Max}}$  decreases from 1 at the center towards 0 at the yarn's surface. When the CNTY is stretched, the radial contraction induces the fibrils of the outer layers of the yarn to exert pressure on the fibrils of the inner layers. This generates higher compressive transverse stress inside the yarn, which is amplified as the strain increases.

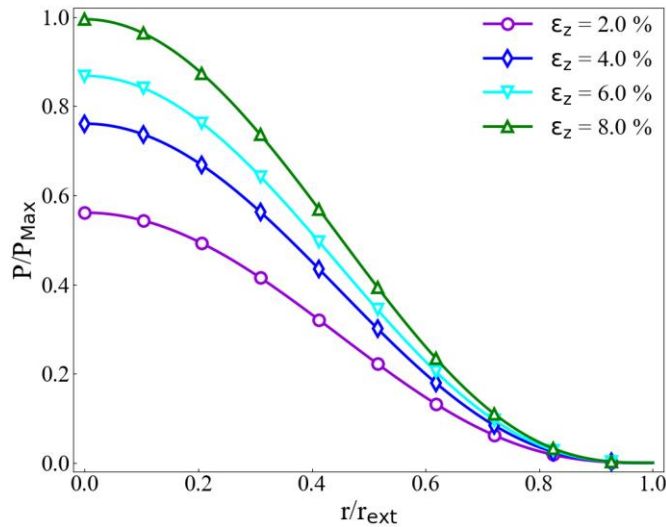


**Fig. D.3.** Distribution of the normalized compressive transverse stress ( $P/P_{\text{Max}}$ ) along the normalized radial position of the CNTY ( $r/r_{\text{ext}}$ ) for different values of axial strain ( $\varepsilon_z$ ).

#### D.4. Distribution of fibril axial strain

The normalized axial strain of the CNT fibrils ( $\varepsilon_{z_f}/\varepsilon_{z_f}^{\text{Max}}$ , where  $\varepsilon_{z_f}^{\text{Max}}$  is the maximum value of  $\varepsilon_{z_f}$ ;  $z_f$  refers to the axial direction,  $z$ , and “f” stands for fibril) comprising the CNTYs as a function of  $r/r_{\text{ext}}$  at different values of  $\varepsilon_z$  is shown in Fig. D.4. The plots were generated using Eq. (2.10), where the radial contraction ratio ( $\nu_{zr}$ ) is given by Eq. (3.1). It is observed that  $\varepsilon_{z_f}/\varepsilon_{z_f}^{\text{Max}}$  decreases nonlinearly with increased CNTY radius, being maximum at the center ( $r = 0$ ). Since the fibrils of the CNTY have a twist angle that varies as a function of  $r$ , it is expected that when the CNTY is strained the outer fibrils with a larger twist angle deform less, as they have more freedom of movement to untwist and pack. On the other hand, the inner fibrils (those closer to the center) have more restricted motion due to entanglement and friction with their neighbors, given the higher packing density.

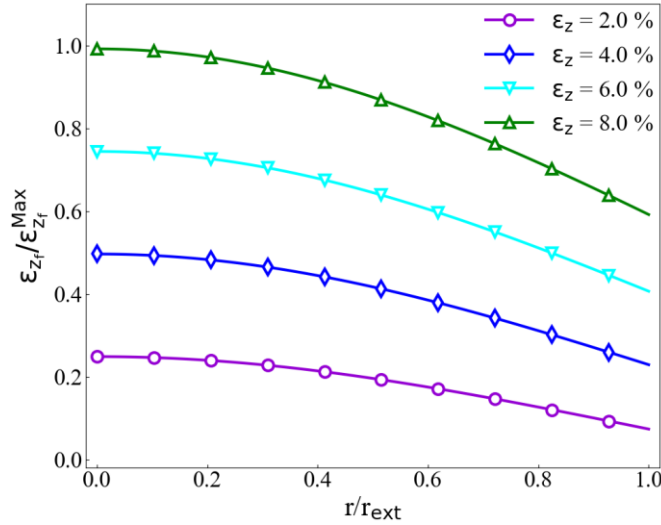


**Fig. D.4.** Distribution of the normalized axial strain of the CNT fibrils ( $\varepsilon_{z_f}/\varepsilon_{z_f}^{\text{Max}}$ ) along the normalized radial position of the CNTY ( $r/r_{\text{ext}}$ ) for different values of axial strain ( $\varepsilon_z$ ).

### E. Critical length for load transfer of the carbon nanotubes and their fibrils

The critical length in a short fiber composite refers to the minimum fiber length required to achieve the maximum allowable fiber strength [183]. This concept can be applied to the CNTs and fibrils comprising the CNTYs. There are several classical models to estimate the critical fiber length, e.g., the Kelly-Tyson model [184], the Cox shear lag model [185], etc. The major differences among them stem from the assumptions regarding the fiber behavior (plastic or elastic), the load transfer between the fiber and matrix, and how the models consider the distribution of normal stress within the fibers and shear stress between the matrix and fibers. The simplest one, which still adequately

captures the mechanics of the problem, is the Kelly-Tyson model [184]. According to this model, adapting it for the CNTs comprising the yarn, the critical length of the CNTs ( $L_c^{\text{CNT}}$ ) can be estimated as [184],

$$L_c^{\text{CNT}} = \left( \frac{\sigma_{z_u}^{\text{CNT}}}{\tau_{\text{Int}}^{\text{CNT}}} \right) r_{\text{CNT}} \quad (\text{E.1})$$

where  $\sigma_{z_u}^{\text{CNT}}$ ,  $\tau_{\text{Int}}^{\text{CNT}}$ , and  $r_{\text{CNT}}$  are the tensile strength, inter-CNT shear strength, and radius of the CNTs, respectively. Knowing that the CNTs examined herein have an external radius ranging from 4.5 to 6.0 nm (see section 3.1.1), considering  $\sigma_{z_u}^{\text{CNT}}$  ranging between 11 and 71 GPa [82,83] (see Table 1.1), and  $\tau_{\text{Int}}^{\text{CNT}}$  ranging between 0.05 and 1.40 GPa [154,155],  $L_c^{\text{CNT}}$  ranges between 35.4 nm and 8.52  $\mu\text{m}$ . The large range of the predicted  $L_c^{\text{CNT}}$  obeys the large variability of the data reported in the literature for  $\sigma_{z_u}^{\text{CNT}}$  and  $\tau_{\text{Int}}^{\text{CNT}}$ . According to this result, a critical length higher than 8.52  $\mu\text{m}$  should be enough for proper load transfer, which should promote breakage of the CNTs. However, as discussed in section 3.1.7, this does not occur in our case, due to the weak interface between CNTs, bundles, and fibrils [151].

The inter-CNT shear strength and the inter-fibril shear strength can be compared by analyzing the ratio between the critical length of the CNTs ( $L_c^{\text{CNT}}$ ) and that of the fibrils ( $L_c^{\text{f}}$ ), i.e.,

$$\frac{L_c^{\text{CNT}}}{L_c^{\text{f}}} = \left( \frac{\sigma_{z_u}^{\text{CNT}}}{\sigma_{z_u}^{\text{f}}} \right) \left( \frac{r_{\text{CNT}}}{r_{\text{f}}} \right) \left( \frac{\tau_{\text{Int}}^{\text{f}}}{\tau_{\text{Int}}^{\text{CNT}}} \right) \quad (\text{E.2})$$

where  $\sigma_{z_u}^{\text{f}}$ ,  $\tau_{\text{Int}}^{\text{f}}$ , and  $r_{\text{f}}$  are the tensile strength, inter-fibril shear strength, and radius of the fibrils, respectively. Considering that the fibrils of the CNTYs exhibit a radius ranging from 68.5 to 414 nm (see section 3.1.1),  $r_{\text{CNT}}/r_{\text{f}}$  is determined to be between 0.01 and 0.09. Regarding  $\tau_{\text{Int}}^{\text{f}}/\tau_{\text{Int}}^{\text{CNT}}$ , the analysis conducted by Deng et al. [151] indicates that  $\tau_{\text{Int}}^{\text{f}}/\tau_{\text{Int}}^{\text{CNT}}$  is between 0.03 and 0.27. For the strength ratio, average values of  $\sigma_{z_u}^{\text{f}}$  and  $\sigma_{z_u}^{\text{CNT}}$  were used, as the range reported in the literature is wide.  $\sigma_{z_u}^{\text{f}}$  has been reported ranging from 1.5 to 52 GPa [112,113,156], while  $\sigma_{z_u}^{\text{CNT}}$  ranging from 11 to 71 GPa [82,83]. Considering average values for both intervals,  $\sigma_{z_u}^{\text{CNT}}/\sigma_{z_u}^{\text{f}}$  is estimated as  $\sim 1.53$ . It is of course expected that the tensile strength of the fibrils is significantly smaller than that of their constituent CNTs (i.e.,  $\sigma_{z_u}^{\text{f}} \leq \sigma_{z_u}^{\text{CNT}}$ ). Thus,  $\sigma_{z_u}^{\text{CNT}}/\sigma_{z_u}^{\text{f}} = 1.53$  is deemed a conservative estimate. As a result, Eq. (E.2) bounds  $L_c^{\text{CNT}}/L_c^{\text{f}}$  between  $45.9 \times 10^{-5}$  and  $37.2 \times 10^{-3}$ . Consequently,  $L_c^{\text{f}}$  is between 27 and 2179 times longer than  $L_c^{\text{CNT}}$ . This result indicates that the load transfer is significantly less efficient at the fibril level than at the CNT level.

## F. Summary of the physical properties of the carbon nanotubes yarns

Table F.1 contains a summary of all the physical properties of the CNTYs obtained in this work.

**Table F.1.** Summary of physical properties of the CNTYs.

Property	Mean value (standard deviation)
Temperature coefficient of resistance in the $0 \leq \Delta T \leq 50$ K range of heating ( $\beta_1$ ).	$-8.63 \times 10^{-4} (\pm 0.79 \times 10^{-4}) \text{ K}^{-1}$
Temperature coefficient of resistance in the $130 \text{ K} \leq \Delta T \leq 250$ K range of heating ( $\beta_2$ ).	$-7.78 \times 10^{-4} (\pm 1.80 \times 10^{-4}) \text{ K}^{-1}$
Temperature coefficient of resistance for the full cooling range ( $\beta_3$ ).	$-7.26 \times 10^{-4} (\pm 0.05 \times 10^{-4}) \text{ K}^{-1}$
Temperature coefficient of resistance of preheated CNTYs for the full range during DMA ( $\beta_{\text{Ph}}^{\text{DMA}}$ ).	$-9.83 \times 10^{-4} (\pm 3.25 \times 10^{-4}) \text{ K}^{-1}$
Temperature coefficient of resistance of pristine CNTYs in the $0 \leq \Delta T \leq 50$ K range during DMA ( $\beta_{\text{Pri}}^{\text{DMA}}$ ).	$-6.92 \times 10^{-4} (\pm 0.55 \times 10^{-4}) \text{ K}^{-1}$
Ultimate (failure) axial tensile strain ( $\varepsilon_{z_u}$ ) at $25^\circ \text{C}$ (obtained by the mechanical testing).	$5.75 (\pm 1.00) \%$
Ultimate (failure) axial tensile strain ( $\varepsilon_{z_u}$ ) at $25^\circ \text{C}$ (obtained by the electromechanical testing).	$4.55 (\pm 1.77) \%$
Ultimate (failure) axial tensile strain ( $\varepsilon_{z_u}$ ) at $80^\circ \text{C}$ (obtained by the electromechanical testing).	$6.08 (\pm 0.47) \%$
Ultimate (failure) axial tensile strain ( $\varepsilon_{z_u}$ ) at $120^\circ \text{C}$ (obtained by the electromechanical testing).	$7.01 (\pm 0.81) \%$
Pristine (undeformed) twist angle ( $\theta_{\text{ext}_0}$ ).	$29.9^\circ (\pm 5.3^\circ)$
Radial contraction ratio ( $\nu_{zr}$ ).	$\nu_{zr} = \nu_{zr_\infty} + c_1 e^{-\frac{\varepsilon_z}{d_1}} + c_2 e^{-\frac{\varepsilon_z}{d_2}};$ $\nu_{zr_\infty} = 0.992, c_1 = 30.1,$ $d_1 = 1.96 \times 10^{-3}, c_2 = 2.33,$ $d_2 = 27.7 \times 10^{-3}$
Electrical conductivity ( $\xi$ ) at $25^\circ \text{C}$ .	$303 (\pm 9) \text{ S/cm}$
Electrical conductivity ( $\xi$ ) at $80^\circ \text{C}$ .	$306 (\pm 9) \text{ S/cm}$
Electrical conductivity ( $\xi$ ) at $120^\circ \text{C}$ .	$309 (\pm 4) \text{ S/cm}$
Specific electrical conductivity ( $\xi/\rho$ ) at $25^\circ \text{C}$	$1211 (\pm 37) \text{ S} \cdot \text{cm}^2/\text{g}$
Specific electrical conductivity ( $\xi/\rho$ ) at $80^\circ \text{C}$	$1225 (\pm 35) \text{ S} \cdot \text{cm}^2/\text{g}$
Specific electrical conductivity ( $\xi/\rho$ ) at $120^\circ \text{C}$	$1237 (\pm 18) \text{ S} \cdot \text{cm}^2/\text{g}$

Volumetric mass density ( $\rho$ ).	0.25 g/cm <sup>3</sup>
Volumetric mass density of the CNTs that make up the CNTYs ( $\rho_{\text{CNT}}$ ).	0.78 g/cm <sup>3</sup>
Linear density ( $\rho_L$ ).	0.21 tex
Axial tensile strength ( $\sigma_{z_u}$ ) at 25 °C (obtained by the mechanical testing).	169 ( $\pm$ 17) MPa
Axial tensile strength ( $\sigma_{z_u}$ ) at 25 °C (obtained by the electromechanical testing).	249 ( $\pm$ 35) MPa
Axial tensile strength ( $\sigma_{z_u}$ ) at 80 °C (obtained by the electromechanical testing).	147 ( $\pm$ 21) MPa
Axial tensile strength ( $\sigma_{z_u}$ ) at 120 °C (obtained by the electromechanical testing).	98.8 ( $\pm$ 18.7) MPa
Specific axial tensile strength ( $\sigma_{z_u}/\rho$ ) at 25 °C (obtained by the mechanical testing).	677 ( $\pm$ 68) mN/tex
Specific axial tensile strength ( $\sigma_{z_u}/\rho$ ) at 25 °C (obtained by the electromechanical testing).	994 ( $\pm$ 140) mN/tex
Specific axial tensile strength ( $\sigma_{z_u}/\rho$ ) at 80 °C (obtained by the electromechanical testing).	586 ( $\pm$ 86) mN/tex
Specific axial tensile strength ( $\sigma_{z_u}/\rho$ ) at 120 °C (obtained by the electromechanical testing).	395 ( $\pm$ 75) mN/tex
Porosity ( $\Phi_p$ ).	0.69
Pristine (undeformed) diameter ( $d_{\text{ext}_0}$ ).	33.3 ( $\pm$ 1.7) $\mu\text{m}$
Diameter of the CNTY's fibrils ( $d_f$ ).	343 nm
Tensile modulus ( $E$ ) in the 0.2 % $\leq \varepsilon_z \leq$ 0.5 % range at 25 °C (obtained by the mechanical testing).	4.30 ( $\pm$ 0.70) GPa
Tensile modulus ( $E$ ) in the 0.2 % $\leq \varepsilon_z \leq$ 0.5 % range at 25 °C (obtained by the electromechanical testing).	5.80 ( $\pm$ 2.24) GPa
Tensile modulus ( $E$ ) in the 0.2 % $\leq \varepsilon_z \leq$ 0.5 % range at 80 °C (obtained by the electromechanical testing).	1.92 ( $\pm$ 0.04) GPa
Tensile modulus ( $E$ ) in the 0.2 % $\leq \varepsilon_z \leq$ 0.5 % range at 120 °C (obtained by the electromechanical testing).	1.64 ( $\pm$ 0.25) GPa
Specific tensile modulus ( $E/\rho$ ) in the 0.2 % $\leq \varepsilon_z \leq$ 0.5 % range at 25 °C (obtained by the mechanical testing).	17.2 ( $\pm$ 2.8) N/tex
Specific tensile modulus ( $E/\rho$ ) in the 0.2 % $\leq \varepsilon_z \leq$ 0.5 % range at 25 °C (obtained by the electromechanical testing).	23.2 ( $\pm$ 8.9) N/tex
Specific tensile modulus ( $E/\rho$ ) in the 0.2 % $\leq \varepsilon_z \leq$ 0.5 % range at 80 °C (obtained by the electromechanical testing).	7.66 ( $\pm$ 0.17) N/tex

Specific tensile modulus ( $E/\rho$ ) in the $0.2 \% \leq \varepsilon_z \leq 0.5 \%$ range at $120\text{ }^\circ\text{C}$ (obtained by the electromechanical testing).	6.55 ( $\pm 0.98$ ) N/tex
Ultimate (failure) axial tensile load ( $F_{z_u}$ ) at $25\text{ }^\circ\text{C}$ (obtained by the mechanical testing).	144 ( $\pm 15$ ) mN
Ultimate (failure) axial tensile load ( $F_{z_u}$ ) at $25\text{ }^\circ\text{C}$ (obtained by the electromechanical testing).	209 ( $\pm 29$ ) mN
Ultimate (failure) axial tensile load ( $F_{z_u}$ ) at $80\text{ }^\circ\text{C}$ (obtained by the electromechanical testing).	123 ( $\pm 18$ ) mN
Ultimate (failure) axial tensile load ( $F_{z_u}$ ) at $120\text{ }^\circ\text{C}$ (obtained by the electromechanical testing).	83.0 ( $\pm 15.7$ ) mN
Gage factor ( $GF$ ) in the $0.2 \% \leq \varepsilon_z \leq 0.5 \%$ range at $25\text{ }^\circ\text{C}$ .	0.36 ( $\pm 0.13$ )
Roughness.	62.2 ( $\pm 12.5$ ) nm

## References

- [1] A. Sivasuriyan, D.S. Vijayan, W. Górski, Ł. Wodzyń, M.D. Vaverková, E. Koda, Practical implementation of structural health monitoring in multi-story buildings, *Buildings*. 11 (2021) 263. <https://doi.org/10.3390/buildings11060263>.
- [2] F. Avilés, A. May-Pat, G. Canché-Escamilla, O. Rodríguez-Uicab, J.J. Ku-Herrera, S. Duarte-Aranda, J. Uribe-Calderon, P.I. Gonzalez-Chi, L. Arronche, V. La Saponara, Influence of carbon nanotube on the piezoresistive behavior of multiwall carbon nanotube/polymer composites, *J. Intell. Mater. Syst. Struct.* 27 (2016) 92–103. <https://doi.org/10.1177/1045389X14560367>.
- [3] M.A. Cullinan, M.L. Culpepper, Carbon nanotubes as piezoresistive microelectromechanical sensors: Theory and experiment, *Phys. Rev. B Condens. Matter Mater. Phys.* 82 (2010) 115428. <https://doi.org/10.1103/PhysRevB.82.115428>.
- [4] J.R. Bautista-Quijano, F. Avilés, J.O. Aguilar, A. Tapia, Strain sensing capabilities of a piezoresistive MWCNT-polysulfone film, *Sensors Actuators A Phys.* 159 (2010) 135–140. <https://doi.org/10.1016/j.sna.2010.03.005>.
- [5] K.L. Lasater, E.T. Thostenson, In situ thermoresistive characterization of multifunctional composites of carbon nanotubes, *Polymer*. 53 (2012) 5367–5374. <https://doi.org/10.1016/j.polymer.2012.09.022>.
- [6] M. Cen-Puc, A.I. Oliva-Avilés, F. Avilés, Thermoresistive mechanisms of carbon nanotube/polymer composites, *Phys. E Low-Dimensional Syst. Nanostructures*. 95 (2018) 41–50. <https://doi.org/10.1016/j.physe.2017.09.001>.
- [7] A. Balam, M. Cen-Puc, A. May-Pat, J.L. Abot, F. Avilés, Influence of polymer matrix on the sensing capabilities of carbon nanotube polymeric thermistors, *Smart Mater. Struct.* 29 (2020) 15012. <https://doi.org/10.1088/1361-665X/AB4E08>.
- [8] E.T. Thostenson, Z. Ren, T.-W. Chou, Advances in the science and technology of carbon nanotubes and their composites: A review, *Compos. Sci. Technol.* 61 (2001) 1899–1912. [https://doi.org/10.1016/S0266-3538\(01\)00094-X](https://doi.org/10.1016/S0266-3538(01)00094-X).
- [9] I. Kang, M.J. Schulz, J.H. Kim, V. Shanov, D. Shi, A carbon nanotube strain sensor for structural health monitoring, *Smart Mater. Struct.* 15 (2006) 737–748. <https://doi.org/10.1088/0964-1726/15/3/009>.
- [10] H. Zhang, E. Bilotti, T. Peijs, The use of carbon nanotubes for damage sensing and structural

- health monitoring in laminated composites: A review, *Nanocomposites*. 1 (2015) 167–184. <https://doi.org/10.1080/20550324.2015.1113639>.
- [11] F. Avilés, A.I. Oliva-Avilés, M. Cen-Puc, Piezoresistivity, strain, and damage self-sensing of polymer composites filled with carbon nanostructures, *Adv. Eng. Mater.* 1701159 (2018) 1–23. <https://doi.org/10.1002/adem.201701159>.
- [12] J. Li, Z. Zhang, J. Fu, Z. Liang, K.R. Ramakrishnan, Mechanical properties and structural health monitoring performance of carbon nanotube-modified FRP composites: A review, *Nanotechnol. Rev.* 10 (2021) 1438–1468. <https://doi.org/10.1515/ntrev-2021-0104>.
- [13] J.C. Fernández-Toribio, A. Íñiguez-Rábago, J. Vilà, C. González, Á. Ridruejo, J.J. Vilatela, A composite fabrication sensor based on electrochemical doping of carbon nanotube yarns, *Adv. Funct. Mater.* 26 (2016) 7139–7147. <https://doi.org/10.1002/adfm.201602949>.
- [14] M. Miao, Yarn spun from carbon nanotube forests: Production, structure, properties and applications, *Particuology*. 11 (2013) 378–393. <https://doi.org/10.1016/j.partic.2012.06.017>.
- [15] M. Miao, Electrical conductivity of pure carbon nanotube yarns, *Carbon*. 49 (2011) 3755–3761. <https://doi.org/10.1016/j.carbon.2011.05.008>.
- [16] W. Lu, M. Zu, J.H. Byun, B.S. Kim, T.W. Chou, State of the art of carbon nanotube fibers: Opportunities and challenges, *Adv. Mater.* 24 (2012) 1805–1833. <https://doi.org/10.1002/adma.201104672>.
- [17] J.L. Abot, Y. Song, M.S. Vatsavaya, S. Medikonda, Z. Kier, C. Jayasinghe, N. Rooy, V.N. Shanov, M.J. Schulz, Delamination detection with carbon nanotube thread in self-sensing composite materials, *Compos. Sci. Technol.* 70 (2010) 1113–1119. <https://doi.org/10.1016/j.compscitech.2010.02.022>.
- [18] H. Zhao, Y. Zhang, P.D. Bradford, Q. Zhou, Q. Jia, F.G. Yuan, Y. Zhu, Carbon nanotube yarn strain sensors, *Nanotechnology*. 21 (2010) 305502. <https://doi.org/10.1088/0957-4484/21/30/305502>.
- [19] X. Ma, Y. Dong, R. Li, Monitoring technology in composites using carbon nanotube yarns based on piezoresistivity, *Mater. Lett.* 188 (2017) 45–47. <https://doi.org/10.1016/j.matlet.2016.10.085>.
- [20] N.D. Alexopoulos, C. Bartholome, P. Poulin, Z. Marioli-Riga, Structural health monitoring of glass fiber reinforced composites using embedded carbon nanotube (CNT) fibers,

Compos. Sci. Technol. 70 (2010) 260–271.  
<https://doi.org/10.1016/j.compscitech.2009.10.017>.

- [21] R. Shoukat, M.I. Khan, Carbon nanotubes: A review on properties, synthesis methods and applications in micro and nanotechnology, *Microsyst. Technol.* 27 (2021) 4183–4192. <https://doi.org/10.1007/s00542-021-05211-6>.
- [22] S. Rathinavel, K. Priyadharshini, D. Panda, A review on carbon nanotube: An overview of synthesis, properties, functionalization, characterization, and the application, *Mater. Sci. Eng. B.* 268 (2021) 115095. <https://doi.org/10.1016/j.mseb.2021.115095>.
- [23] S.K. Tiwari, S. Sahoo, N. Wang, A. Huczko, Graphene research and their outputs: Status and prospect, *J. Sci. Adv. Mater. Devices.* 5 (2020) 10–29. <https://doi.org/10.1016/j.jsamd.2020.01.006>.
- [24] M. He, S. Zhang, J. Zhang, Horizontal single-walled carbon nanotube arrays: Controlled synthesis, characterizations, and applications, *Chem. Rev.* 120 (2020) 12592–12684. <https://doi.org/10.1021/acs.chemrev.0c00395>.
- [25] S. Iijima, Helical microtubules of graphitic carbon, *Nature.* 354 (1991) 56–58. <https://doi.org/10.1038/354056a0>.
- [26] S. Qu, Y. Dai, D. Zhang, Q. Li, T.-W. Chou, W. Lyu, Carbon nanotube film based multifunctional composite materials: An overview, *Funct. Compos. Struct.* 2 (2020) 022002. <https://doi.org/10.1088/2631-6331/ab9752>.
- [27] M. Miao (Ed.), Carbon nanotube fibers and yarns: Production, properties and applications in smart textiles, Woodhead Publishing Ltd, Cambridge, 2020. <https://doi.org/10.1016/C2017-0-04183-6>.
- [28] J.W.S. Hearle, P. Grosberg, S. Backer, Structural Mechanics of Fibers, Yarns, and Fabrics - Volume 1, Wiley-Interscience, New York, 1969.
- [29] M. Zhang, K.R. Atkinson, R.H. Baughman, Multifunctional carbon nanotube yarns by downsizing an ancient technology, *Science.* 306 (2004) 1358–1361. <https://doi.org/10.1126/science.1104276>.
- [30] K.R. Atkinson, S.C. Hawkins, C. Huynh, C. Skourtis, J. Dai, M. Zhang, S. Fang, A.A. Zakhidov, S.B. Lee, A.E. Aliev, C.D. Williams, R.H. Baughman, Multifunctional carbon nanotube yarns and transparent sheets: Fabrication, properties, and applications, *Phys. B Condens. Matter.* 394 (2007) 339–343. <https://doi.org/10.1016/j.physb.2006.12.061>.

- [31] J.J. Vilatela, A.H. Windle, Yarn-Like Carbon Nanotube Fibers, *Adv. Mater.* 22 (2010) 4959–4963. <https://doi.org/10.1002/adma.201002131>.
- [32] Y. Jung, Y.S. Cho, J.W. Lee, J.Y. Oh, C.R. Park, How can we make carbon nanotube yarn stronger?, *Compos. Sci. Technol.* 166 (2018) 95–108. <https://doi.org/10.1016/j.compscitech.2018.02.010>.
- [33] C. Choi, J.A. Lee, A.Y. Choi, Y.T. Kim, X. Lepró, M.D. Lima, R.H. Baughman, S.J. Kim, Flexible supercapacitor made of carbon nanotube yarn with internal pores, *Adv. Mater.* 26 (2014) 2059–2065. <https://doi.org/10.1002/adma.201304736>.
- [34] S.J.S.H. Kim, C.S. Haines, N. Li, K.J. Kim, T.J. Mun, C. Choi, J. Di, Y.J. Oh, J.P. Oviedo, J. Bykova, S. Fang, N. Jiang, Z. Liu, R. Wang, P. Kumar, R. Qiao, S. Priya, K. Cho, M. Kim, M.S. Lucas, L.F. Drummy, B. Maruyama, D.Y. Lee, X. Lepró, E. Gao, D. Albarq, R. Ovalle-Robles, S.J.S.H. Kim, R.H. Baughman, Harvesting electrical energy from carbon nanotube yarn twist, *Science.* 357 (2017) 773–778. <https://doi.org/10.1126/science.aam8771>.
- [35] C. Jiang, L. Li, H. Hao, Carbon nanotube yarns for deep brain stimulation electrode, *IEEE Trans. Neural Syst. Rehabil. Eng.* 19 (2011) 612–616. <https://doi.org/10.1109/TNSRE.2011.2165733>.
- [36] S. Ryu, P. Lee, J.B. Chou, R. Xu, R. Zhao, A.J. Hart, S.-G. Kim, Extremely elastic wearable carbon nanotube fiber strain sensor for monitoring of human motion, *ACS Nano.* 9 (2015) 5929–5936. <https://doi.org/10.1021/acsnano.5b00599>.
- [37] J. Foroughi, G. Spinks, Carbon nanotube and graphene fiber artificial muscles, *Nanoscale Adv.* 1 (2019) 4592–4614. <https://doi.org/10.1039/c9na00038k>.
- [38] Y. Hayashi, Y. Chiba, H. Inoue, M. Hada, T. Nishikawa, A review of dry spun carbon nanotube yarns and their potential applications in energy and mechanical devices, *J. Fiber Sci. Technol.* 76 (2020) 72–78. <https://doi.org/10.2115/fiberst.2020-0013>.
- [39] X. Liu, H. Ji, B. Liu, Q. Yang, All-solid-state carbon-nanotube-fiber-based finger-muscle and robotic gripper, *Int. J. Smart Nano Mater.* 13 (2022). <https://doi.org/10.1080/19475411.2022.2028928>.
- [40] K. Jiang, J. Wang, Q. Li, L. Liu, C. Liu, S. Fan, Superaligned carbon nanotube arrays, films, and yarns: A road to applications, *Adv. Mater.* 23 (2011) 1154–1161. <https://doi.org/10.1002/adma.201003989>.

- [41] Y. Jang, S.M. Kim, G.M. Spinks, S.J. Kim, Carbon nanotube yarn for fiber-shaped electrical sensors, actuators, and energy storage for smart systems, *Adv. Mater.* 32 (2020) 1–14. <https://doi.org/10.1002/adma.201902670>.
- [42] P. Dariyal, A.K. Arya, B.P. Singh, S.R. Dhakate, A review on conducting carbon nanotube fibers spun via direct spinning technique, *J. Mater. Sci.* 56 (2021) 1087–1115. <https://doi.org/10.1007/s10853-020-05304-z>.
- [43] S. Zhang, K.K.K. Koziol, I.A. Kinloch, A.H. Windle, Macroscopic fibers of well-aligned carbon nanotubes by wet spinning, *Small.* 4 (2008) 1217–1222. <https://doi.org/10.1002/smll.200700998>.
- [44] X. Zhang, K. Jiang, C. Feng, P. Liu, L. Zhang, J. Kong, T. Zhang, Q. Li, S. Fan, Spinning and processing continuous yarns from 4-inch wafer scale super-aligned carbon nanotube arrays, *Adv. Mater.* 18 (2006) 1505–1510. <https://doi.org/10.1002/adma.200502528>.
- [45] C. Jayasinghe, S. Chakrabarti, M.J. Schulz, V. Shanov, Spinning yarn from long carbon nanotube arrays, *J. Mater. Res.* 26 (2011) 645–651. <https://doi.org/10.1557/jmr.2010.91>.
- [46] J. Zhao, X. Zhang, Y. Huang, J. Zou, T. Liu, N. Liang, F. Yu, Z. Pan, Y. Zhu, M. Miao, Q. Li, A comparison of the twisted and untwisted structures for one-dimensional carbon nanotube assemblies, *Mater. Des.* 146 (2018) 20–27. <https://doi.org/10.1016/j.matdes.2018.02.068>.
- [47] X.H. Zhong, Y.L. Li, Y.K. Liu, X.H. Qiao, Y. Feng, J. Liang, J. Jin, L. Zhu, F. Hou, J.Y. Li, Continuous multilayered carbon nanotube yarns, *Adv. Mater.* 22 (2010) 692–696. <https://doi.org/10.1002/adma.200902943>.
- [48] A.Y. Li, I. a Kinloch, A.H. Windle, Y. Li, A. Kinloch, Direct Spinning of Carbon Nanotube Fibers from Chemical Vapor Deposition Synthesis, *Science.* 304 (2012) 276–278.
- [49] F. Smail, A. Boies, A. Windle, Direct spinning of CNT fibres: Past, present and future scale up, *Carbon.* 152 (2019) 218–232. <https://doi.org/10.1016/j.carbon.2019.05.024>.
- [50] W. Ma, L. Liu, R. Yang, T. Zhang, Z. Zhang, L. Song, Y. Ren, J. Shen, Z. Niu, W. Zhou, S. Xie, Monitoring a micromechanical process in macroscale carbon nanotube films and fibers, *Adv. Mater.* 21 (2009) 603–608. <https://doi.org/10.1002/adma.200801335>.
- [51] M. Miao, The role of twist in dry spun carbon nanotube yarns, *Carbon.* 96 (2016) 819–826. <https://doi.org/10.1016/j.carbon.2015.10.022>.
- [52] J.C. Anike, K. Belay, J.L. Abot, Effect of twist on the electromechanical properties of carbon

- nanotube yarns, *Carbon*. 142 (2019) 491–503. <https://doi.org/10.1016/j.carbon.2018.10.067>.
- [53] J. Park, K.-H. Lee, Carbon nanotube yarns, *Korean J. Chem. Eng.* 29 (2012) 277–287. <https://doi.org/10.1007/s11814-012-0016-1>.
- [54] O. Suekane, A. Nagataki, H. Mori, Y. Nakayama, Static friction force of carbon nanotube surfaces, *Appl. Phys. Express*. 1 (2008) 064001. <https://doi.org/10.1143/APEX.1.064001>.
- [55] R. Mirzaeifar, Z. Qin, M.J. Buehler, Mesoscale mechanics of twisting carbon nanotube yarns, *Nanoscale*. 7 (2015) 5435–5445. <https://doi.org/10.1039/c4nr06669c>.
- [56] D. Asadollahi, M. Shariati, Investigation of shear forces in twisted carbon nanotube bundles using a structural mechanics approach, *Acta Mech.* 232 (2021) 2425–2441. <https://doi.org/10.1007/s00707-021-02949-y>.
- [57] J.C. Fernández-Toribio, A. Mikhilchan, C. Santos, Á. Ridruejo, J.J. Vilatela, Understanding cooperative loading in carbon nanotube fibres through in-situ structural studies during stretching, *Carbon*. 156 (2020) 430–437. <https://doi.org/10.1016/j.carbon.2019.09.070>.
- [58] M. Miao, J. McDonnell, L. Vuckovic, S.C. Hawkins, Poisson's ratio and porosity of carbon nanotube dry-spun yarns, *Carbon*. 48 (2010) 2802–2811. <https://doi.org/10.1016/j.carbon.2010.04.009>.
- [59] Y. Li, B. Sun, S. Sockalingam, Z. Pan, W. Lu, T.-W. Chou, Influence of transverse compression on axial electromechanical properties of carbon nanotube fibers, *Mater. Des.* 188 (2020) 108463. <https://doi.org/10.1016/j.matdes.2019.108463>.
- [60] P. Lizák, Yarn strength dependence on test length, *Fibres Text. East. Eur.* 10 (2002) 32–34.
- [61] Y. Zhang, L. Zheng, G. Sun, Z. Zhan, K. Liao, Failure mechanisms of carbon nanotube fibers under different strain rates, *Carbon*. 50 (2012) 2887–2893. <https://doi.org/10.1016/j.carbon.2012.02.057>.
- [62] Y. Jung, T. Kim, C.R. Park, Effect of polymer infiltration on structure and properties of carbon nanotube yarns, *Carbon*. 88 (2015) 60–69. <https://doi.org/10.1016/j.carbon.2015.02.065>.
- [63] A. Abu Obaid, D. Heider, J.W. Gillespie Jr., Investigation of electro-mechanical behavior of carbon nanotube yarns during tensile loading, *Carbon*. 93 (2015) 731–741. <https://doi.org/10.1016/j.carbon.2015.05.091>.
- [64] X. Zhang, W. Lu, G. Zhou, Q. Li, Understanding the mechanical and conductive properties of carbon nanotube fibers for smart electronics, *Adv. Mater.* 32 (2020) 1902028.

<https://doi.org/10.1002/adma.201902028>.

- [65] Q. Liu, M. Li, Y. Gu, S. Wang, Y. Zhang, Q. Li, L. Gao, Z. Zhang, Interlocked CNT networks with high damping and storage modulus, *Carbon*. 86 (2015) 46–53. <https://doi.org/10.1016/j.carbon.2015.01.014>.
- [66] J. Zhao, F. Wang, X. Zhang, L. Liang, X. Yang, Q. Li, X. Zhang, Vibration damping of carbon nanotube assembly materials, *Adv. Eng. Mater.* 20 (2018) 1–13. <https://doi.org/10.1002/adem.201700647>.
- [67] J. Zhao, X. Zhang, Z. Pan, Q. Li, Wide-range tunable dynamic property of carbon-nanotube-based fibers, *Adv. Mater. Interfaces*. 2 (2015) 1500093. <https://doi.org/10.1002/admi.201500093>.
- [68] X. Yang, P. He, H. Gao, Modeling frequency- and temperature-invariant dissipative behaviors of randomly entangled carbon nanotube networks under cyclic loading, *Nano Res.* 4 (2011) 1191–1198. <https://doi.org/10.1007/s12274-011-0169-y>.
- [69] Y. Li, M. Kröger, Viscoelasticity of carbon nanotube buckypaper: Zipping-unzipping mechanism and entanglement effects, *Soft Matter*. 8 (2012) 7822–7830. <https://doi.org/10.1039/c2sm25561h>.
- [70] P.H. Mott, C.M. Roland, Limits to Poisson's ratio in isotropic materials, *Phys. Rev. B - Condens. Matter Mater. Phys.* 80 (2009) 132104. <https://doi.org/10.1103/PhysRevB.80.132104>.
- [71] N. Pan, T. Hua, Y. Qiu, Relationship between fiber and yarn strength, *Text. Res. J.* 71 (2001) 960–964. <https://doi.org/10.1177/004051750107101105>.
- [72] I.J. Beyerlein, P.K. Porwal, Y.T. Zhu, K. Hu, X.F. Xu, Scale and twist effects on the strength of nanostructured yarns and reinforced composites, *Nanotechnology*. 20 (2009) 485702. <https://doi.org/10.1088/0957-4484/20/48/485702>.
- [73] J.J. Vilatela, J.A. Elliott, A.H. Windle, A model for the strength of yarn-like carbon nanotube fibers, *ACS Nano*. 5 (2011) 1921–1927. <https://doi.org/10.1021/nn102925a>.
- [74] X. Wei, M. Ford, R.A. Soler-Crespo, H.D. Espinosa, A new Monte Carlo model for predicting the mechanical properties of fiber yarns, *J. Mech. Phys. Solids*. 84 (2015) 325–335. <https://doi.org/10.1016/j.jmps.2015.08.005>.
- [75] E. Gao, W. Lu, Z. Xu, Strength loss of carbon nanotube fibers explained in a three-level hierarchical model, *Carbon*. 138 (2018) 134–142.

<https://doi.org/10.1016/j.carbon.2018.05.052>.

- [76] Y. Zhao, F. Xue, L. Miao, C. Wang, C. Sui, Q. Peng, X. He, Roles of twisting-compression operations on mechanical enhancement of carbon nanotube fibers, *Carbon*. 172 (2021) 41–49. <https://doi.org/10.1016/j.carbon.2020.09.084>.
- [77] A. Pirmoz, J.L. Abot, F. Avilés, Simulation of mechanical response of carbon nanotube yarns under uniaxial tensile loading, *Mech. Mater.* 165 (2022) 104144. <https://doi.org/10.1016/j.mechmat.2021.104144>.
- [78] M.-F. Yu, B.S. Files, S. Arepalli, R.S. Ruoff, Tensile loading of ropes of single wall carbon nanotubes and their mechanical properties, *Phys. Rev. Lett.* 84 (2000) 5552–5555. <https://doi.org/10.1103/PhysRevLett.84.5552>.
- [79] E.T. Thostenson, C. Li, T.W. Chou, Nanocomposites in context, *Compos. Sci. Technol.* 65 (2005) 491–516. <https://doi.org/10.1016/j.compscitech.2004.11.003>.
- [80] N. Hu, Y. Karube, C. Yan, Z. Masuda, H. Fukunaga, Tunneling effect in a polymer/carbon nanotube nanocomposite strain sensor, *Acta Mater.* 56 (2008) 2929–2936. <https://doi.org/10.1016/j.actamat.2008.02.030>.
- [81] Y. Inoue, K. Hayashi, M. Karita, T. Nakano, Y. Shimamura, K. Shirasu, G. Yamamoto, T. Hashida, Study on the mechanical and electrical properties of twisted CNT yarns fabricated from CNTs with various diameters, *Carbon*. 176 (2021) 400–410. <https://doi.org/10.1016/j.carbon.2021.01.139>.
- [82] M.F. Yu, O. Lourie, M.J. Dyer, K. Moloni, T.F. Kelly, R.S. Ruoff, Strength and breaking mechanism of multiwalled carbon nanotubes under tensile load, *Science*. 287 (2000) 637–640. <https://doi.org/10.1126/science.287.5453.637>.
- [83] A. Takakura, K. Beppu, T. Nishihara, A. Fukui, T. Kozeki, T. Namazu, Y. Miyauchi, K. Itami, Strength of carbon nanotubes depends on their chemical structures, *Nat. Commun.* 10 (2019) 3040. <https://doi.org/10.1038/s41467-019-10959-7>.
- [84] Q. Lu, G. Keskar, R. Ciocan, R. Rao, R.B. Mathur, A.M. Rao, L.L. Larcom, Determination of carbon nanotube density by gradient sedimentation, *J. Phys. Chem. B*. 110 (2006) 24371–24376. <https://doi.org/10.1021/jp063660k>.
- [85] T.W. Ebbesen, H.J. Lezec, H. Hiura, J.W. Bennett, H.F. Ghaemi, T. Thio, Electrical conductivity of individual carbon nanotubes, *Nature*. 382 (1996) 54–56. <https://doi.org/10.1038/382054a0>.

- [86] J. Hone, M. Whitney, C. Piskoti, A. Zettl, Thermal conductivity of single-walled carbon nanotubes, *Phys. Rev. B Condens. Matter Mater. Phys.* 59 (1999) R2514. <https://doi.org/10.1103/PhysRevB.59.R2514>.
- [87] P. Kim, L. Shi, A. Majumdar, P.L. McEuen, Thermal transport measurements of individual multiwalled nanotubes, *Phys. Rev. Lett.* 87 (2001) 215502. <https://doi.org/10.1103/PhysRevLett.87.215502>.
- [88] E. Pop, D. Mann, Q. Wang, K. Goodson, H. Dai, Thermal conductance of an individual single-wall carbon nanotube above room temperature, *Nano Lett.* 6 (2006) 96–100. <https://doi.org/10.1021/nl052145f>.
- [89] J.L. Abot, T. Alesh, K. Belay, Strain dependence of electrical resistance in carbon nanotube yarns, *Carbon.* 70 (2014) 95–102. <https://doi.org/10.1016/j.carbon.2013.12.077>.
- [90] J.C. Anike, H.H. Le, G.E. Brodeur, M.M. Kadavan, J.L. Abot, Piezoresistive response of integrated CNT yarns under compression and tension: The effect of lateral constraint, *C.* 3 (2017) 14. <https://doi.org/10.3390/c3020014>.
- [91] J.C. Anike, K. Belay, J.L. Abot, Piezoresistive response of carbon nanotube yarns under tension: Parametric effects and phenomenology, *New Carbon Mater.* 33 (2018) 140–154. [https://doi.org/10.1016/S1872-5805\(18\)60331-2](https://doi.org/10.1016/S1872-5805(18)60331-2).
- [92] J. Terrones, J.A. Elliott, J.J. Vilatela, A.H. Windle, Electric field-modulated non-ohmic behavior of carbon nanotube fibers in polar liquids, *ACS Nano.* 8 (2014) 8497–8504. <https://doi.org/10.1021/nn5030835>.
- [93] O. Rodríguez-Uicab, J.L. Abot, F. Avilés, Electrical resistance sensing of epoxy curing using an embedded carbon nanotube yarn, *Sensors.* 20 (2020) 1–17. <https://doi.org/10.3390/s20113230>.
- [94] Y. Song, A. Hehr, V. Shanov, N. Alvarez, N. Kienzle, J. Cummins, D. Koester, M. Schulz, Carbon nanotube sensor thread for distributed strain and damage monitoring on IM7/977-3 composites, *Smart Mater. Struct.* 23 (2014) 075008. <https://doi.org/10.1088/0964-1726/23/7/075008>.
- [95] A. Hehr, M. Schulz, V. Shanov, Y. Song, Micro-crack detection and assessment with embedded carbon nanotube thread in composite materials, *Struct. Heal. Monit.* 13 (2014) 512–524. <https://doi.org/10.1177/1475921714532987>.
- [96] A. Mikhalchan, J.J. Vilatela, A perspective on high-performance CNT fibres for structural

- composites, *Carbon*. 150 (2019) 191–215. <https://doi.org/10.1016/j.carbon.2019.04.113>.
- [97] M. Jia, Z. Wan, Internal damage analysis of braided composites embedded in carbon nanotube yarn, *Appl. Sci.* 12 (2022) 51. <https://doi.org/10.3390/app12010051>.
- [98] J.W. Kim, G. Sauti, R.J. Cano, R.A. Wincheski, J.G. Ratcliffe, M. Czabaj, N.W. Gardner, E.J. Siochi, Assessment of carbon nanotube yarns as reinforcement for composite overwrapped pressure vessels, *Compos. Part A Appl. Sci. Manuf.* 84 (2016) 256–265. <https://doi.org/10.1016/j.compositesa.2016.02.003>.
- [99] C.E. Evers, B. Vondrasek, C.N. Jolowsky, J.G. Park, M.W. Czabaj, B.E. Ku, K.R. Thagard, G.M. Odegard, Z. Liang, Scalable high tensile modulus composite laminates using continuous carbon nanotube yarns for aerospace applications, *ACS Appl. Nano Mater.* 6 (2023) 11260–11268. <https://doi.org/10.1021/acsanm.3c01266>.
- [100] A. Malekloo, E. Ozer, M. AlHamaydeh, M. Girolami, Machine learning and structural health monitoring overview with emerging technology and high-dimensional data source highlights, *Struct. Heal. Monit.* 21 (2022) 1906–1955. <https://doi.org/10.1177/147592172111036880>.
- [101] V.N. Shanov, A. Gorton, Y.H. Yun, M.J. Schulz, Composite catalyst and method for manufacturing carbon nanostructured materials, WO/2008/105936 A2, 2008. <http://www.wipo.int/pctdb/en/wo.jsp?IA=US2007079528>.
- [102] T.W. Anderson, D.A. Darling, A test of goodness of fit, *J. Am. Stat. Assoc.* 49 (1954) 765–769. <https://doi.org/10.1080/01621459.1954.10501232>.
- [103] M. Safdari, M.S. Al-Haik, Synergistic electrical and thermal transport properties of hybrid polymeric nanocomposites based on carbon nanotubes and graphite nanoplatelets, *Carbon*. 64 (2013) 111–121. <https://doi.org/10.1016/j.carbon.2013.07.042>.
- [104] C. Laurent, E. Flahaut, A. Peigney, The weight and density of carbon nanotubes versus the number of walls and diameter, *Carbon*. 48 (2010) 2994–2996. <https://doi.org/10.1016/j.carbon.2010.04.010>.
- [105] H.F. Brinson, L.C. Brinson, *Polymer engineering science and viscoelasticity: An introduction*, 2nd ed., Springer Science+Business Media, New York, 2015. <https://doi.org/10.1007/978-1-4899-7485-3>.
- [106] M.A. Tapia-Romero, M. Dehonor-Gómez, L.E. Lugo-Urbe, Prony series calculation for viscoelastic behavior modeling of structural adhesives from DMA data, *Ing. Investig. y*

- Tecnol. 21 (2020) 1–10. <https://doi.org/10.22201/fi.25940732e.2020.21n2.014>.
- [107] N.S. Nise, Control systems engineering, 7th ed., John Wiley & Sons, Pomona, 2015.
- [108] X. Shao, Y. Qiu, Y. Wang, Theoretical modeling of the tensile behavior of low-twist staple yarns: Part I - Theoretical model, *J. Text. Inst.* 96 (2005) 61–68. <https://doi.org/10.1533/joti.2004.0002>.
- [109] D. Yilmaz, F. Göktepe, Ö. Göktepe, D. Kremenakova, Packing density of compact yarns, *Text. Res. J.* 77 (2007) 661–667. <https://doi.org/10.1177/0040517507078796>.
- [110] S.K. Sinha, P. Kumar, S. Ghosh, A study on the packing density of structurally modified ring spun yarn, *Fibers Polym.* 17 (2016) 1898–1907. <https://doi.org/10.1007/s12221-016-5940-y>.
- [111] J.P. Salvetat, G.A.D. Briggs, J.M. Bonard, R.R. Bacsa, A.J. Kulik, T. Stöckli, N.A. Burnham, L. Forró, Elastic and shear moduli of single-walled carbon nanotube ropes, *Phys. Rev. Lett.* 82 (1999) 944–947. <https://doi.org/10.1103/PhysRevLett.82.944>.
- [112] M. Naraghi, T. Filleter, A. Moravsky, M. Locascio, R.O. Loutfy, H.D. Espinosa, A multiscale study of high performance double-walled nanotube-polymer fibers, *ACS Nano.* 4 (2010) 6463–6476. <https://doi.org/10.1021/nn101404u>.
- [113] T. Filleter, R. Bernal, S. Li, H.D. Espinosa, Ultrahigh strength and stiffness in cross-linked hierarchical carbon nanotube bundles, *Adv. Mater.* 23 (2011) 2855–2860. <https://doi.org/10.1002/adma.201100547>.
- [114] ASTM International, Designation: D638 – 10 “Standard test method for tensile properties of plastics,” *Annu. B. ASTM Stand.* (2014). <https://doi.org/10.1520/D0638-10.1>.
- [115] ASTM International, Designation: D7137/D7137M – 07 “Standard test method for compressive residual strength properties of damaged polymer matrix composite plates,” *Annu. B. ASTM Stand.* (2007). <https://doi.org/10.1520/D7137>.
- [116] A.A. Kuznetsov, A.F. Fonseca, R.H. Baughman, A.A. Zakhidov, Structural model for dry-drawing of sheets and yarns from carbon nanotube forests, *ACS Nano.* 5 (2011) 985–993. <https://doi.org/10.1021/nn102405u>.
- [117] W. Guo, C. Liu, F. Zhao, X. Sun, Z. Yang, T. Chen, X. Chen, L. Qiu, X. Hu, H. Peng, A novel electromechanical actuation mechanism of a carbon nanotube fiber, *Adv. Mater.* 24 (2012) 5379–5384. <https://doi.org/10.1002/adma.201201845>.
- [118] A.S. Wu, T.W. Chou, Carbon nanotube fibers for advanced composites, *Mater. Today.* 15

- (2012) 302–310. [https://doi.org/10.1016/S1369-7021\(12\)70135-9](https://doi.org/10.1016/S1369-7021(12)70135-9).
- [119] V. Reguero, B. Alemán, B. Mas, J.J. Vilatela, Controlling carbon nanotube type in macroscopic fibers synthesized by the direct spinning process, *Chem. Mater.* 26 (2014) 3550–3557. <https://doi.org/10.1021/cm501187x>.
- [120] V. Țucureanu, A. Matei, A.M. Avram, FTIR Spectroscopy for Carbon Family Study, *Crit. Rev. Anal. Chem.* 46 (2016) 502–520. <https://doi.org/10.1080/10408347.2016.1157013>.
- [121] N. @ A. Mansor, J.-P. Tessonier, A. Rinaldi, S. Reiche, M.G. Kutty, Chemically modified multi-walled carbon nanotubes (MWCNTs) with anchored acidic groups, *Sains Malaysiana.* 41 (2012) 603–609.
- [122] A. Baykal, M. Senel, B. Unal, E. Karaoğlu, H. Sözeri, M.S. Toprak, Acid functionalized multiwall carbon nanotube/magnetite (MWCNT)-COOH/Fe<sub>3</sub>O<sub>4</sub> hybrid: Synthesis, characterization and conductivity evaluation, *J. Inorg. Organomet. Polym. Mater.* 23 (2013) 726–735. <https://doi.org/10.1007/s10904-013-9839-4>.
- [123] R. Yudianti, H. Onggo, Y. Saito, T. Iwata, J. Azuma, Analysis of functional group sited on multi-wall carbon nanotube surface, *Open Mater. Sci. J.* 5 (2011) 242–247. <https://doi.org/10.2174/1874088X01105010242>.
- [124] A.M.F. Lima, A.W. Musumeci, H.W. Liu, E.R. Waclawik, G.G. Silva, Purity evaluation and influence of carbon nanotube on carbon nanotube/graphite thermal stability, *J. Therm. Anal. Calorim.* 97 (2009) 257–263. <https://doi.org/10.1007/s10973-009-0245-7>.
- [125] J.H. Lehman, M. Terrones, E. Mansfield, K.E. Hurst, V. Meunier, Evaluating the characteristics of multiwall carbon nanotubes, *Carbon.* 49 (2011) 2581–2602. <https://doi.org/10.1016/j.carbon.2011.03.028>.
- [126] L.S.K. Pang, J.D. Saxby, S.P. Chatfield, Thermogravimetric analysis of carbon nanotubes and nanoparticles, *J. Phys. Chem.* 97 (1993) 6941–6942. <https://doi.org/10.1021/j100129a001>.
- [127] D. Bom, R. Andrews, D. Jacques, J. Anthony, B. Chen, M.S. Meier, J.P. Selegue, Thermogravimetric analysis of the oxidation of multiwalled carbon nanotubes: Evidence for the role of defect sites in carbon nanotube chemistry, *Nano Lett.* 2 (2002) 615–619. <https://doi.org/10.1021/nl020297u>.
- [128] E.F. Antunes, A.O. Lobo, E.J. Corat, V.J. Trava-Airoldi, Influence of diameter in the Raman spectra of aligned multi-walled carbon nanotubes, *Carbon.* 45 (2007) 913–921.

<https://doi.org/10.1016/j.carbon.2007.01.003>.

- [129] S. Osswald, M. Havel, Y. Gogotsi, Monitoring oxidation of multiwalled carbon nanotubes by Raman spectroscopy, *J. Raman Spectrosc.* 38 (2007) 728–736. <https://doi.org/10.1002/jrs.1686>.
- [130] M.A. Pimenta, G. Dresselhaus, M.S. Dresselhaus, L.G. Cançado, A. Jorio, R. Saito, Studying disorder in graphite-based systems by Raman spectroscopy, *Phys. Chem. Chem. Phys.* 9 (2007) 1276–1291. <https://doi.org/10.1039/b613962k>.
- [131] L.M. Malard, M.A. Pimenta, G. Dresselhaus, M.S. Dresselhaus, Raman spectroscopy in graphene, *Phys. Rep.* 473 (2009) 51–87. <https://doi.org/10.1016/j.physrep.2009.02.003>.
- [132] R. Saito, M. Hofmann, G. Dresselhaus, A. Jorio, M.S. Dresselhaus, Raman spectroscopy of graphene and carbon nanotubes, *Adv. Phys.* 60 (2011) 413–550. <https://doi.org/10.1080/00018732.2011.582251>.
- [133] A.C. Ferrari, D.M. Basko, Raman spectroscopy as a versatile tool for studying the properties of graphene, *Nat. Nanotechnol.* 8 (2013) 235–246. <https://doi.org/10.1038/nnano.2013.46>.
- [134] J.J. Vilatela, L. Deng, I.A. Kinloch, R.J. Young, A.H. Windle, Structure of and stress transfer in fibres spun from carbon nanotubes produced by chemical vapour deposition, *Carbon.* 49 (2011) 4149–4158. <https://doi.org/10.1016/j.carbon.2011.05.045>.
- [135] K.K. Kim, J.S. Park, S.J. Kim, H.Z. Geng, K.H. An, C.M. Yang, K. Sato, R. Saito, Y.H. Lee, Dependence of Raman spectra G' band intensity on metallicity of single-wall carbon nanotubes, *Phys. Rev. B Condens. Matter Mater. Phys.* 76 (2007) 205426. <https://doi.org/10.1103/PhysRevB.76.205426>.
- [136] A.P. Pierlot, A.L. Woodhead, J.S. Church, Thermal annealing effects on multi-walled carbon nanotube yarns probed by Raman spectroscopy, *Spectrochim. Acta Part A Mol. Biomol. Spectrosc.* 117 (2014) 598–603. <https://doi.org/10.1016/j.saa.2013.09.050>.
- [137] C. Pérez-Aranda, Z. Valdez-Nava, F. Gamboa, J. V. Cauich-Rodríguez, F. Avilés, Electro-mechanical properties of thermoplastic polyurethane films and tubes modified by hybrid carbon nanostructures for pressure sensing, *Smart Mater. Struct.* 29 (2020) 115021. <https://doi.org/10.1088/1361-665X/aba9e6>.
- [138] Z. Lei, Y. Wang, F. Qin, W. Qiu, R. Bai, X. Chen, Multi-fiber strains measured by micro-Raman spectroscopy: Principles and experiments, *Opt. Lasers Eng.* 77 (2016) 8–17. <https://doi.org/10.1016/j.optlaseng.2015.07.005>.

- [139] E.K. Gamstedt, M. Skrifvars, T.K. Jacobsen, R. Pyrz, Synthesis of unsaturated polyesters for improved interfacial strength in carbon fibre composites, *Compos. Part A Appl. Sci. Manuf.* 33 (2002) 1239–1252. [https://doi.org/10.1016/S1359-835X\(02\)00077-5](https://doi.org/10.1016/S1359-835X(02)00077-5).
- [140] R.J. Day, J. V. Cauich Rodrigez, Investigation of the micromechanics of the microbond test, *Compos. Sci. Technol.* 58 (1998) 907–914. [https://doi.org/10.1016/S0266-3538\(97\)00197-8](https://doi.org/10.1016/S0266-3538(97)00197-8).
- [141] T.M.G. Mohiuddin, A. Lombardo, R.R. Nair, A. Bonetti, G. Savini, R. Jalil, N. Bonini, D.M. Basko, C. Galiotis, N. Marzari, K.S. Novoselov, A.K. Geim, A.C. Ferrari, Uniaxial strain in graphene by Raman spectroscopy: G peak splitting, Grüneisen parameters, and sample orientation, *Phys. Rev. B Condens. Matter Mater. Phys.* 79 (2009) 205433. <https://doi.org/10.1103/PhysRevB.79.205433>.
- [142] R. Kumar, S.B. Cronin, Raman scattering of carbon nanotube bundles under axial strain and strain-induced debundling, *Phys. Rev. B Condens. Matter Mater. Phys.* 75 (2007) 155421. <https://doi.org/10.1103/PhysRevB.75.155421>.
- [143] S.B. Cronin, A.K. Swan, M.S. Ünlü, B.B. Goldberg, M.S. Dresselhaus, M. Tinkham, Resonant Raman spectroscopy of individual metallic and semiconducting single-wall carbon nanotubes under uniaxial strain, *Phys. Rev. B Condens. Matter Mater. Phys.* 72 (2005) 035425. <https://doi.org/10.1103/PhysRevB.72.035425>.
- [144] M.S. Dresselhaus, G. Dresselhaus, R. Saito, A. Jorio, Raman spectroscopy of carbon nanotubes, *Phys. Rep.* 409 (2005) 47–99. <https://doi.org/10.1016/j.physrep.2004.10.006>.
- [145] A.C. Ferrari, J. Robertson, Interpretation of Raman spectra of disordered and amorphous carbon, *Phys. Rev. B Condens. Matter Mater. Phys.* 61 (2000) 14095. <https://doi.org/10.1103/PhysRevB.61.14095>.
- [146] H. Liang, M. Upmanyu, Axial-strain-induced torsion in single-walled carbon nanotubes, *Phys. Rev. Lett.* 96 (2006) 165501. <https://doi.org/10.1103/PhysRevLett.96.165501>.
- [147] P. Ordejón, E. Artacho, M. Soler, Ab initio structural, elastic, and vibrational properties of carbon nanotubes, *Phys. Rev. B - Condens. Matter Mater. Phys.* 59 (1999) 12678. <https://doi.org/10.1103/PhysRevB.59.12678>.
- [148] Z.L. Wang, R.P. Gao, P. Poncharal, W.A. De Heer, Z.R. Dai, Z.W. Pan, Mechanical and electrostatic properties of carbon nanotubes and nanowires, *Mater. Sci. Eng. C.* 16 (2001) 3–10. [https://doi.org/10.1016/S0928-4931\(01\)00293-4](https://doi.org/10.1016/S0928-4931(01)00293-4).

- [149] W. Guo, Y. Guo, Giant axial electrostrictive deformation in carbon nanotubes, *Phys. Rev. Lett.* 91 (2003) 115501. <https://doi.org/10.1103/PhysRevLett.91.115501>.
- [150] Y. Guo, W. Guo, Mechanical and electrostatic properties of carbon nanotubes under tensile loading and electric field, *J. Phys. D. Appl. Phys.* 36 (2003) 805–805. <https://doi.org/10.1088/0022-3727/36/7/306>.
- [151] W.L. Deng, W. Qiu, Q. Li, Y.L. Kang, J.G. Guo, Y.L. Li, S.S. Han, Multi-scale experiments and interfacial mechanical modeling of carbon nanotube fiber, *Exp. Mech.* 54 (2014) 3–10. <https://doi.org/10.1007/s11340-012-9706-1>.
- [152] J.T. Paci, A. Furmanchuk, H.D. Espinosa, G.C. Schatz, Shear and friction between carbon nanotubes in bundles and yarns, *Nano Lett.* 14 (2014) 6138–6147. <https://doi.org/10.1021/nl502210r>.
- [153] K.M. Liew, C.H. Wong, M.J. Tan, Tensile and compressive properties of carbon nanotube bundles, *Acta Mater.* 54 (2006) 225–231. <https://doi.org/10.1016/j.actamat.2005.09.002>.
- [154] B. Bhushan, X. Ling, Adhesion and friction between individual carbon nanotubes measured using force-versus-distance curves in atomic force microscopy, *Phys. Rev. B - Condens. Matter Mater. Phys.* 78 (2008) 045429. <https://doi.org/10.1103/PhysRevB.78.045429>.
- [155] C. Li, Y. Liu, X. Yao, M. Ito, T. Noguchi, Q. Zheng, Interfacial shear strengths between carbon nanotubes, *Nanotechnology.* 21 (2010). <https://doi.org/10.1088/0957-4484/21/11/115704>.
- [156] D.A. Walters, L.M. Ericson, M.J. Casavant, J. Liu, D.T. Colbert, K.A. Smith, R.E. Smalley, Elastic strain of freely suspended single-wall carbon nanotube ropes, *Appl. Phys. Lett.* 74 (1999) 3803–3805. <https://doi.org/10.1063/1.124185>.
- [157] G.N. Greaves, A.L. Greer, R.S. Lakes, T. Rouxel, Poisson's ratio and modern materials, *Nat. Mater.* 10 (2011) 823–837. <https://doi.org/10.1038/nmat3134>.
- [158] R. Amini, H. Mashroteh, M. Vadood, A novel approach to the Poisson's ratio of the yarn, *J. Text. Inst.* 111 (2020) 999–1007. <https://doi.org/10.1080/00405000.2019.1678236>.
- [159] A.A. Gusev, P.J. Hine, I.M. Ward, Fiber packing and elastic properties of a transversely random unidirectional glass/epoxy composite, *Compos. Sci. Technol.* 60 (2000) 535–541. [https://doi.org/10.1016/S0266-3538\(99\)00152-9](https://doi.org/10.1016/S0266-3538(99)00152-9).
- [160] T.S. Gspann, N. Montinaro, A. Pantano, J.A. Elliott, A.H. Windle, Mechanical properties of carbon nanotube fibres: St Venant's principle at the limit and the role of imperfections,

Carbon. 93 (2015) 1021–1033. <https://doi.org/10.1016/j.carbon.2015.05.065>.

- [161] Y. Li, M. Kröger, A theoretical evaluation of the effects of carbon nanotube entanglement and bundling on the structural and mechanical properties of buckypaper, *Carbon*. 50 (2012) 1793–1806. <https://doi.org/10.1016/j.carbon.2011.12.027>.
- [162] M. Xu, D.N. Futaba, T. Yamada, M. Yumura, K. Hata, Carbon nanotubes with temperature-invariant viscoelasticity from  $-196^{\circ}$  to  $1000^{\circ}\text{C}$ , *Science*. 330 (2010) 1364–1368. <https://doi.org/10.1126/science.1194865>.
- [163] K. Sasikumar, P. Jayesh, N.R. Manoj, T. Mukundan, D. Khastgir, Effect of pristine multiwalled carbon nanotubes on tensile hysteresis in carboxylated nitrile rubber composites, *Polym. Compos.* 39 (2018) E1269–E1279. <https://doi.org/10.1002/pc.24851>.
- [164] F. Ellyin, D. Kujawski, Plastic strain energy in fatigue failure, *J. Press. Vessel Technol.* 106 (1984) 342–347. <https://doi.org/10.1115/1.3264362>.
- [165] N. Yoshihara, H. Ishihara, Structure and properties of segmented poly(urethane-urea) elastic fibers. Part 2: Hysteresis of stress-strain curves, *J. Text. Eng.* 48 (2002) 64–69. <https://doi.org/10.4188/jte.48.64>.
- [166] A. Belaadi, A. Bezazi, M. Maache, F. Scarpa, Fatigue in sisal fiber reinforced polyester composites: Hysteresis and energy dissipation, *Procedia Eng.* 74 (2014) 325–328. <https://doi.org/10.1016/j.proeng.2014.06.272>.
- [167] W. Obitayo, T. Liu, A review: Carbon nanotube-based piezoresistive strain sensors, *J. Sensors*. 2012 (2012) 1–15. <https://doi.org/10.1155/2012/652438>.
- [168] S. Reich, C. Thomsen, P. Ordejón, Electronic band structure of isolated and bundled carbon nanotubes, *Phys. Rev. B - Condens. Matter Mater. Phys.* 65 (2002) 155411. <https://doi.org/10.1103/PhysRevB.65.155411>.
- [169] K. Conley, A.J. Karttunen, Bridging the junction: Electrical conductivity of carbon nanotube networks, *J. Phys. Chem. C*. 126 (2022) 17266–17274. <https://doi.org/10.1021/acs.jpcc.2c03904>.
- [170] F. Avilés, J. V. Cauich-Rodríguez, L. Moo-Tah, A. May-Pat, R. Vargas-Coronado, Evaluation of mild acid oxidation treatments for MWCNT functionalization, *Carbon*. 47 (2009) 2970–2975. <https://doi.org/10.1016/j.carbon.2009.06.044>.
- [171] R. Schönfelder, F. Avilés, A. Bachmatiuk, J. V. Cauich-Rodríguez, M. Knupfer, B. Büchner, M.H. Rummeli, On the merits of Raman spectroscopy and thermogravimetric analysis to

- asses carbon nanotube structural modifications, *Appl. Phys. A Mater. Sci. Process.* 106 (2012) 843–852. <https://doi.org/10.1007/s00339-012-6787-8>.
- [172] S. Santangelo, M. Lanza, C. Milone, Evaluation of the overall crystalline quality of amorphous carbon containing multiwalled nanotubes, *J. Phys. Chem. C.* 117 (2013) 4815–4823. <https://doi.org/10.1021/jp310014w>.
- [173] A. Balam, M. Cen-Puc, O. Rodríguez-Uicab, J.L. Abot, F. Avilés, Cyclic thermoresistivity of freestanding and polymer embedded carbon nanotube yarns, *Adv. Eng. Mater.* 22 (2020) 2000220. <https://doi.org/10.1002/adem.202000220>.
- [174] A.E. Aliev, C. Guthy, M. Zhang, S. Fang, A.A. Zakhidov, J.E. Fischer, R.H. Baughman, Thermal transport in MWCNT sheets and yarns, *Carbon.* 45 (2007) 2880–2888. <https://doi.org/10.1016/j.carbon.2007.10.010>.
- [175] V.T. Dau, C.D. Tran, T.T. Bui, V.D.X. Nguyen, T.X. Dinh, Piezo-resistive and thermo-resistance effects of highly-aligned CNT based macrostructures, *RSC Adv.* 6 (2016) 106090–106095. <https://doi.org/10.1039/C6RA22872K>.
- [176] Y. Gnanou, M. Fontanille, *Organic and physical chemistry of polymers*, John Wiley & Sons, Hoboken, 2008.
- [177] A.M. Beese, X. Wei, S. Sarkar, R. Ramachandramoorthy, M.R. Roenbeck, A. Moravsky, M. Ford, F. Yavari, D.T. Keane, R.O. Loutfy, S.B.T. Nguyen, H.D. Espinosa, Key factors limiting carbon nanotube yarn strength: Exploring processing-structure-property relationships, *ACS Nano.* 8 (2014) 11454–11466. <https://doi.org/10.1021/nn5045504>.
- [178] G. Domokos, P. Holmes, B. Royce, Constrained Euler buckling, *J. Nonlinear Sci.* 7 (1997) 281–314. <https://doi.org/10.1007/BF02678090>.
- [179] A. Goriely, R. Vandiver, M. Destrade, Nonlinear Euler buckling, *Proc. R. Soc. A Math. Phys. Eng. Sci.* 464 (2008) 3003–3019. <https://doi.org/10.1098/rspa.2008.0184>.
- [180] B. Yang, V. Kozey, S. Adanur, S. Kumar, Bending, compression, and shear behavior of woven glass fiber-epoxy composites, *Compos. Part B Eng.* 31 (2000) 715–721. [https://doi.org/10.1016/S1359-8368\(99\)00052-9](https://doi.org/10.1016/S1359-8368(99)00052-9).
- [181] J.M. Whitney, *Structural analysis of laminated anisotropic plates*, 1st ed., Technomic Publishing Company, Lancaster, 1987. <https://doi.org/10.1201/9780203738122>.
- [182] F. López-Santos, A. May-Pat, E.R. Ledesma-Orozco, A. Hernández-Pérez, F. Avilés, Measurement of in-plane and out-of-plane elastic properties of woven fabric composites

using digital image correlation, *J. Compos. Mater.* 55 (2021) 1231–1246.  
<https://doi.org/10.1177/0021998320967073>.

[183] B.D. Agarwal, L.J. Broutman, K. Chandrashekhara, *Analysis and performance of fiber composites*, 3rd ed., John Wiley & Sons, Hoboken, 2006.

[184] A. Kelly, W.R. Tyson, Tensile properties of fibre-reinforced metals: Copper/tungsten and copper/molybdenum, *J. Mech. Phys. Solids.* 13 (1965) 329–338.  
[https://doi.org/10.1016/0022-5096\(65\)90035-9](https://doi.org/10.1016/0022-5096(65)90035-9).

[185] H.L. Cox, The elasticity and strength of paper and other fibrous materials, *Br. J. Appl. Phys.* 72 (1952) 72–79. <https://doi.org/10.1088/0508-3443/3/3/302>.